UNIVERSITÀ DEGLI STUDI DI ROMA "TOR VERGATA"

FACOLTÀ DI SCIENZE MATEMATICHE FISICHE NATURALI

DIPARTIMENTO DI FISICA

DOTTORATO DI RICERCA IN ASTRONOMIA

CICLO XXII

Making the best of Cosmological Perturbations: Theory and Data Analysis

Davide Pietrobon

A. A. 2009/2010

Docente Guida: Dr. Amedeo Balbi

Coordinatore: Prof. Pasquale Mazzotta

Making the Best of Cosmological Perturbations: Theory and Data Analysis

by

Davide Pietrobon

THE THESIS IS SUBMITTED IN PARTIAL FULFILMENT OF THE REQUIREMENTS FOR THE AWARD OF THE DEGREE OF DOCTOR OF PHILOSOPHY OF THE UNIVERSITY OF PORTSMOUTH

September, 2009

Copyright

To my family and friends

Abstract

Cosmology has entered the precision epoch thanks to several very accurate experiments. Cosmologists now have access to an array of tools to test the cosmological concordance model and constrain its parameters; the Cosmic Microwave Background radiation (CMB), in particular, has been playing a crucial role in this ambition. Many questions remain nonetheless unanswered, especially concerning the physics of the early Universe, the inflationary mechanism which set the initial conditions for the Universe expansion on one side, and, on the other, the nature of the late time acceleration of the Universe expansion.

My research contributes to both of these subjects, the common ground being the development of a statistical tool – needlets, a new frame on the sphere – to analyse the CMB. By means of needlets, we measure the Integrated Sachs Wolfe effect by cross-correlating WMAP and NVSS datasets and characterise dark energy properties using a phenomenological fluid model. Motivated by our findings, we study in detail a parameterisation of the dark components, dark matter and dark energy, which makes use of an affine equation of state, constraining the parameters of the model by combining WMAP and SDSS datasets.

We apply needlets to the WMAP 5-year data release testing the Gaussianity of the CMB perturbations. Our approach is twofold: we first focus on the maps, detecting anomalous spots located in the southern hemisphere and check their effect on the angular power spectrum. We next measure the needlet three-point correlation function (bispectrum) and characterise it in terms of its overall amplitude, putting constraints on the primordial $f_{\rm NL}$ parameter, and considering its properties according to the geometry of the triangle configurations which contribute to the total power. We find a significant anomaly in the isosceles configurations, again in the southern hemisphere.

Finally we focus on the construction of an optimal estimator for the (needlets) bispectrum, taking into account foreground residuals.

Preface

The work of this thesis is the result of the agreement signed by the Department of Physics, University of Roma Tor Vergata and the Institute of Cosmology and Gravitation, University of Portsmouth, United Kingdom in the formal context of the "co-tutela" project.

The following chapters are based on published work:

- Chapter 4 - **"Foreground Influence on Primordial non-Gaussianity Estimates: Needlets Analysis of WMAP 5-year Data"**
  P. Cabella, D. Pietrobon, M. Veneziani, A. Balbi, R. Crittenden, G. de Gasperis, C. Quercellini, N. Vittorio
  arXiv:0910.4362 [astro-ph CO]

- Chapter 4 - **"Needlet Bispectrum Asymmetries in the WMAP 5-year Data"**
  D. Pietrobon, P. Cabella, A. Balbi, R. Crittenden, G. de Gasperis, N. Vittorio
  MNRAS(2009) L367
  arXiv:0905.3702 [astro-ph CO]

- Chapter 4 - **"Constraints on Primordial Non-Gaussianity from a Needlet Analysis of the WMAP-5 Data"**
  D. Pietrobon, P. Cabella, A. Balbi, G. de Gasperis, N. Vittorio
  MNRAS(2009) **396** 1682-1688
  arXiv:0812.2478 [astro-ph]

- Chapter 4 - **"Needlet Detection of Features in WMAP CMB Sky and the Impact on Anisotropies and Hemispherical Asymmetries"**
  D. Pietrobon, A. Amblard, A. Balbi, P. Cabella, A. Cooray, D. Marinucci
  Phys. Rev. D (2008) **78** 103504
  arXiv:0809.0010 [astro-ph]

- Chapter 2 - **"Affine parameterization of the dark sector: constraints from WMAP5 and SDSS"**
  D. Pietrobon, A. Balbi, M. Bruni, C. Quercellini

Phys. Rev. D (2008) **78** 083510
arXiv:0807.5077 [astro-ph]

- Chapter 2 - **"Late universe dynamics with scale-independent linear couplings in the dark sector"**
  C. Quercellini, M. Bruni, A. Balbi and D. Pietrobon
  Phys. Rev. D (2008) **78**, 063527
  arXiv:0803.1976 [astro-ph]

- Chapter 3 - **"Spherical needlets for cosmic microwave background data analysis"**
  D. Marinucci, D. Pietrobon, A. Balbi, P. Baldi, P. Cabella, G. Kerkyacharian, P. Natoli, D. Picard, N. Vittorio
  MNRAS(2008) **383**, 539-545
  arXiv:0707.0844 [astro-ph]

- Chapter 2 - **"Integrated Sachs-Wolfe effect from the cross-correlation of WMAP 3 year and NVSS: new results and constraints on dark energy"**
  D. Pietrobon, A. Balbi and D. Marinucci
  Phys. Rev. D (2006) **74**, 043524 [arXiv:astro-ph/0606475]

I contributed to all of the cited papers performing the bulk of the work, with the only exception of Quercellini et al. (2008), where I contributed to the computation of the differential equation solutions and encoded the likelihood analysis of the SNe.

The techniques I developed working on parameter estimation in CMB have been applied to the analysis of the BOOMERANG 2003 experiment dataset, which has been published in:

- **"Properties of Galactic cirrus clouds observed by BOOMERANG"**
  M. Veneziani et al.
  arXiv:0907.5012

- **"Sub-Degree Sunyaev-Zel'dovich Signal from Multi-Frequency BOOMERANG observations "**
  M. Veneziani et al.
  2009 ApJ 702 L61-L65 [arXiv:0904.4313]

I actively contributed also to

- **"Fast transition in Adiabatic Unified Dark Matter models"**
  O. F. Piattella, D. Bertacca, M. Bruni and D. Pietrobon

JCAP 01 (2010) 014
arXiv:0911.2664 [astro-ph CO]

Acknowledgements

This thesis is the result of an ambitious journey through the outskirts of cosmology; and it actually leads just to one more departure. I would like to thank the people who guided me, teaching how to approach research, in particular my supervisors, Amedeo and Robert; Marco, his time and effort to accomplish the co-tutela agreement, which allowed me to spend unforgettable months in Portsmouth. David and Roy, brilliant physicists, being real sport men.

I'm really grateful to my colleagues in Rome, Paolo, always just one call away, Giancarlo and Claudia, happy to share a necessary coffee, Pasquale, Paolo, Domenico and Prof. Nicola Vittorio, who form a great productive group, despite the shortage of money.

To all my Roman friends, in particular Fabio, Regula, Enrico, Emiliano, Francesco, Annalisa, Marina, Elena, Mary, Luca, thanks for making me feel at home. How many crazy days! Thanks to the fantastic friends I met in Portsmouth, Chiara, Antonis, Corrado, Alvise, Guido, YS, Jonas, Tom, Betta and the ICG group all, able to wisely mix research, sports and fun. What about a weird night in London!?

A special thank to my flatmates and friends, Mauro and Roberto first, and now Marcella, who I have shared with some of the most amazing and unforgettable moments ever. To Luca, our friendship has been lasting for more than 15 years, it's a precious gift. We renamed a city too!

A true thank you to my parents and my brother and sister, who have always supported me in my choices, even when they could bring us far away. I'm very proud you are my family.

Finally, I really would like to thank Prof. Sonia Righi, my high school philosophy teacher, who first saw my love for physics and philosophy, and helped me in growing it.

I owe you so much!

Contents

List of Tables

List of Figures

Introduction

"Why in general is there some-thing
rather than no-thing?"[...]
The act of being and the thing are in a
relationship of identity and difference.
This double relationship has to be considered
not to forget either the difference,
whose oblivion determines the loss
of the meaning of being, as the western metaphysics has done,
or the identity, whose oblivion considers
the act of being as trascendent,
making the thing meaningless.

(Freely translated from "Il tramonto dell'occidente", U. Galimberti)

Since his first step on the Earth, man has looked at the sky wondering what governs the marvellous processes which astonished him. The answer to this question has been often found in the context of the natural philosophy or religion. Thanks to the extraordinary improvement both on the theoretical and technical side, cosmology is nowadays able to provide, if not a conclusive answer, certainly a new and complementary prospect, which should be taken into consideration when approaching such a fundamental question.

Since Galileo had the first look through the telescope, astronomy has reached a high degree of over-refinement which provides the scientific community with very accurate measurements of our Universe at many wavelengths, which impress the man of the street and challenge the researcher. By skillfully combining all this information, the cosmologists have derived the current cosmological model. According to this scenario, our Universe began about fourteen billions years ago, out of a tiny, extremely hot and dense energy region. Since then, it has been expanding and cooling, undergoing a series of temporary equilibrium phases between the particles which contribute to the total energy content. The very early phase of the Universe's evolution is still far from being fully understood and it is the subject of intense study. This is the realm where cosmology

merges into high energy physics. Nonetheless we can at least sketch the processes which occurred at this primordial stage, which produced the particle species we can probe in the laboratory. From them, we can reconstruct the chemical evolution of our Universe and the formation of the structures we observe. To this aim, we actually have to combine photon and baryon physics in an homogeneous and isotropic Universe, together with two more ingredients which contribute to the total energy content. These are named dark matter and dark energy. The former creates the gravitational potential wells and determines the growth of the baryon perturbations through gravitational instability; the latter is responsible for the late time acceleration of the Universe expansion.

One reason for the success of the cosmological model is certainly its simplicity: by means of an handful of parameters it is able to account for the complexity we observe. Conversely, this model lacks a solid theoretical basis, not only for what concerns the early stages, but also regarding the explanation of the dark components.

The most powerful tool, which has tightened the constraints on the cosmological parameters, is the Cosmic Microwave Background radiation, the thermal relic of the equilibrium condition in which the Universe was in its first phase of the expansion. We now possess a very precise measurement of this energy emission and we are going to achieve an even better one with the upcoming experiments, which will return a measure very close to the theoretical limit.

During my Ph. D. I have been developing a statistical tool, namely *needlets*, to maximise the amount of information which can be extracted from the cosmic microwave background radiation, and I have applied it to some of the most interesting open questions in cosmology. In particular, I focused on the issue of the nature of the dark energy and on the characterisation of the energy fluctuations distribution, testing its Gaussianity.

This work aims at being a review of my project, explaining coherently the results my collaborators and I obtained. After a brief summary of the cosmological model in Chapter 1, I discuss the dark energy problem and present the approach I followed to probe its properties in Chapter 2. Part of this effort has been performed by means of needlets, a new frame built on the sphere, which I describe in detail in Chapter 3. In Chapter 4, I show the results obtained when applying needlets to the isotropy and Gaussianity issue. Finally, I will draw my conclusions in Chapter 5.

Chapter 1

The Cosmological Model in a Nutshell

Let us suppose that an ichthyologist is exploring the life of the ocean.
He casts a net into the water and brings up a fishy assortment.
Surveying his catch, he proceeds in the usual manner
of a scientist to systematise what it reveals.
He arrives at two generalisations:
(1) No sea-creature is less than two inches long.
(2) All sea-creatures have gills.
These are both true of his catch, and he assumes tentatively that
they will remain true however often he repeats it.

("The Philosophy of Physical Science", Sir A. Eddington)

Looking at the sky through the telescope, we observe a multitude of objects, different in dimension, shape, luminosity, energy emitted. It is natural to look for relationships between the various properties which characterise these structures, and to try to interpret them within an evolutionary theory. Indeed, the laws of physics, which we assume to govern the astrophysical processes, describe the fundamental interactions and suggest dynamical models. However, it is only the last century which has seen the development of a cosmological model which depicts an evolving Universe.

In the next sections we first introduce the theoretical framework within which the cosmological model is built (Sec. 1.1); we then describe the main features which characterise it (Sec. 1.2); finally we discuss a fundamental tool, the cosmic background radiation, to probe our Universe (Sec. 1.3).

1.1 The Metric of the Universe

In the 1929, Edwin Hubble observed a proportionality relation between the distance of the nearby galaxies and their recession velocity, $v = H_0 D$ (Hubble law, Hubble (1929)).

The velocity was inferred from the redshift of the emitted light: interpreting the shift as the Doppler effect due to the motion of the source $z = \Delta\lambda/\lambda \simeq v/c$, Hubble concluded that the sources moved away from the Earth. Obviously this does not mean the Earth, or the Solar system, occupies any special position in the Universe. On the contrary, this is exactly what any observer would measure in an expanding universe.

This measurement can be considered as a milestone on the road to the modern cosmology, and it represents indeed a fundamental tool to measure the expansion rate widely used today. See for example Riess et al. (2009).

The modern cosmology is built on two pillars: i) the Theory of General Relativity, which Einstein developed early in the 20th century, and ii) the Cosmological Principle, which, at least in its first formulation, is due to Einstein as well. See Peebles (1993) for an interesting historical discussion. General relativity describes the mutual interaction between matter (and more generally energy) and space-time, assuming the validity of the special relativity (Einstein, 1905) and postulating the Equivalence Principle (Einstein, 1916)[1].

The cosmological principle states that the Universe is homogeneous and isotropic on large scale ($\gtrsim 100$Mpc). This assumption, which seems pretty reasonable from a theoretical point of view, since it implies that any observer measures the same physics in any direction in the sky, has been indeed confirmed by the observations of the galaxies' distribution such as the 2dF Galaxy Redshift Survey (Cross et al., 2001), the NRAO VLA Sky Survey (Condon et al., 1998) and Sloan Digital Sky Survey (Abazajian et al., 2009).

General relativity begins with the line element defined as

$$ds^2 = \sum_{\mu\nu} g_{\mu\nu}\, \mathrm{d}x^\mu\, \mathrm{d}x^\nu = g_{\mu\nu}\, \mathrm{d}x^\mu\, \mathrm{d}x^\nu \tag{1.1}$$

where $g_{\mu\nu}$ is the 4D (symmetric) metric tensor and the indices run over the range 0-3. The Einstein summation convention has been introduced and it will be assumed in what follows. On a local inertial frame it is possible to express $g_{\mu\nu}$ as the sum of the underlying Minkowski metric, $\eta_{\mu\nu} = \mathrm{Diag}(-1, 1, 1, 1)$, and a perturbation $h_{\mu\nu}$ (Ma & Bertschinger, 1995).

[1]The equivalence principle can be rephrased with the *General Covariance Principle* which requires an equation to hold in absence of a gravitational field and to be invariant under a general transformation of coordinates. It is interesting to notice that the equivalence principle defines somehow the effect of the gravitation: by means of its general covariance, an equation which holds in absence of a gravitational field, holds in the presence of a gravitational field. Assuming a symmetry sets constraints on the equation itself (as in the case of the special relativity), or more properly gives an interpretation to the metric tensor and the affine connections: they are an effect of the gravitational field itself.

Any invariance principle which determines the properties of the interaction of a given field is called a dynamic symmetry. We find other examples of such symmetry in theoretical physics in the Gauge and Chiral symmetries (Weinberg, 1972, 2008).

The cosmological principle allows us to simplify the expression of the line element as

$$ds^2 = -\Big[\,\mathrm{d}t^2 - a(t)^2\big(\,\mathrm{d}\chi^2 + S_\kappa^2(\,\mathrm{d}\theta^2 + \sin^2\theta\,\mathrm{d}\phi^2)\big)\Big], \tag{1.2}$$

which is the Friedmann-Robertson-Walker (FRW) metric (Friedmann, 1922; Lemaître, 1931; Robertson, 1935; Walker, 1937). t is the cosmic time and $\{\chi, \theta, \phi\}$ are the spherical comoving coordinates. Isotropy allows us to choose the maximally symmetric frame and homogeneity requires a to be a function of the cosmic time only. S_κ is defined according to the spatial curvature of the space-time as:

$$S_\kappa = \begin{cases} \sin\chi & \kappa = 1 \\ \chi & \kappa = 0 \\ \sinh\chi & \kappa = -1 \end{cases} \tag{1.3}$$

being respectively closed, flat and open geometries. $a(t)$ is the scale factor and it basically describes the evolution history of the Universe (at the background level). It is then a powerful tool to compare different evolution models. Let us introduce a very useful quantity related to the scale factor: the redshift, which is defined as $z = 1/a - 1$.

Within this formalism it is easy to understand how the Hubble law follows directly from the cosmological principle and the FRW metric. From Eq. 1.2, the proper distance is defined by $r_\mathrm{p} = a(t)\chi$, whereas its velocity is given by $v = \mathrm{d}r_\mathrm{p}/\,\mathrm{d}t = \dot{a}/a\, r_\mathrm{p}$. Defining $H_0 = \dot{a(t)}/a(t)|_0$, we obtain the Hubble law. The Hubble constant turns out to be actually a function evolving in time. Its measured value today is $H_0 = 74 \pm 3.6\mathrm{Km/s/Mpc}$ at 68% confidence level (Riess et al., 2009); it is useful to normalise H_0, expressing it in terms of a dimensionless parameter $h = H_0/100$. The Hubble parameter naturally introduces a characteristic time scale, which sets the order of magnitude of the Universe age, $t_0 = 1/H_0 \simeq 10h^{-1}\mathrm{Gyr}$.

As anticipated, Einstein's equations describe the dynamics of the metric given the matter content of the Universe. The differential equations for the scale factor and the matter density follow from Einstein's equations

$$G^\mu_\nu \equiv R^\mu_\nu - \frac{1}{2}\delta^\mu_\nu R = 8\pi G T^\mu_\nu\,, \tag{1.4}$$

where G^μ_ν is the Einstein tensor, and R^μ_ν is the Ricci tensor, which depends on the metric and its derivatives, R is the Ricci scalar and T^μ_ν is the energy momentum tensor. In the

FRW background (Eq. 1.2) the curvature terms are given by (Kolb & Turner, 1990)

$$R_0^0 = \frac{3\ddot{a}}{a}\,, \tag{1.5}$$

$$R_j^i = \left(\frac{\ddot{a}}{a} + \frac{2\dot{a}^2}{a^2} + \frac{2\kappa}{a^2}\right)\delta_j^i\,, \tag{1.6}$$

$$R = 6\left(\frac{\ddot{a}}{a} + \frac{\dot{a}^2}{a^2} + \frac{\kappa}{a^2}\right)\,, \tag{1.7}$$

where a dot denotes a derivative with respect to t.

Let us consider an ideal perfect fluid as the source of the energy momentum tensor T_ν^μ. In this case we have

$$T_\nu^\mu = \mathrm{Diag}\left(-\rho, p, p, p\right)\,, \tag{1.8}$$

where ρ and p are the energy density and the pressure density of the fluid, respectively. Then Eq. 1.4 gives the two Friedmann equations

$$H^2 \equiv \left(\frac{\dot{a}}{a}\right)^2 = \frac{8\pi G\rho}{3} - \frac{\kappa}{a^2}\,, \tag{1.9}$$

$$\dot{H} = -4\pi G(p+\rho) + \frac{\kappa}{a^2}\,, \tag{1.10}$$

which describe the Hubble parameter and its time evolution. ρ and p denote the total energy density and pressure of all the species present in the universe at a given epoch.

The energy momentum tensor is conserved by virtue of the Bianchi identities, $\nabla_\nu G^{\mu\nu} = 0$, and energy conservation, $\nabla_\nu T^{\mu\nu} = 0$, leading to the continuity equation

$$\dot{\rho} + 3H(\rho + p) = 0\,. \tag{1.11}$$

Equation 1.11 can be derived from Eqs. 1.9 and 1.10, which means that two of Eqs. 1.9, 1.10 and 1.11 are independent. Eliminating the κ/a^2 term from Eqs. 1.9 and 1.10, we obtain

$$\frac{\ddot{a}}{a} = -\frac{4\pi G}{3}\left(\rho + 3p\right)\,. \tag{1.12}$$

Hence the accelerated expansion occurs for $\rho + 3p < 0$. Notice that the derivation of the Friedmann equations within the context of the Newtonian physics would lead to a similar result for the acceleration equation but with the pressure contribution missing. Pressure effects are a peculiar feature of the relativistic equations 1.4, which are able to account for the acceleration of the Universe expansion (Copeland et al., 2006).

It is possible rewrite Eq. 1.9 in the form:

$$\Omega(t) - 1 = \frac{\kappa}{(aH)^2}\,, \tag{1.13}$$

where $\Omega(t) \equiv \rho(t)/\rho_c(t)$ is the dimensionless density parameter and $\rho_c(t) = 3H^2(t)/8\pi G$ is the critical density. The matter and energy distribution clearly determines the spatial geometry of our universe, i.e.,

$$\Omega > 1 \;\text{ or }\; \rho > \rho_c \;\; \rightarrow \kappa = 1\,, \tag{1.14}$$

$$\Omega = 1 \;\text{ or }\; \rho = \rho_c \;\; \rightarrow \kappa = 0\,, \tag{1.15}$$

$$\Omega < 1 \;\text{ or }\; \rho < \rho_c \;\; \rightarrow \kappa = -1\,. \tag{1.16}$$

Observations have shown that the current universe is very close to a spatially flat geometry ($\Omega \simeq 1$) (de Bernardis et al., 2000; Dunkley et al., 2009). This is actually a natural result from inflation in the early universe: see Sec. 1.3.3 and Liddle & Lyth (2000) for a more detailed discussion.

After the first three minutes of the Universe evolution (Weinberg, 1993), the strong and electroweak reactions between particles have frozen due to the Universe expansion (Alpher et al., 1948), and it is reasonable to consider the Universe filled with photons, baryons (mainly hydrogen and helium) and leptons (actually negligible in terms of energy density fraction). Let us consider the evolution of the universe filled with photons and baryons (dust), described as a barotropic perfect fluid. It is common use to define the equation of state parameter

$$w = p/\rho\,. \tag{1.17}$$

w is generally assumed to be constant, and this is a correct statement for radiation and ordinary matter, whereas w can be a function in the case of coupled fluids or more exotic component, such as dark energy. Some examples are described in Chap. 2.

By solving the Einstein equations given in Eqs. 1.9 and 1.10 with $\kappa = 0$, we obtain

$$H = \frac{2}{3(1+w)(t-t_0)}\,, \tag{1.18}$$

$$a(t) \propto (t-t_0)^{\frac{2}{3(1+w)}}\,, \tag{1.19}$$

$$\rho \propto a^{-3(1+w)}\,, \tag{1.20}$$

where t_0 is constant. We note that the above solution is valid for $w \neq -1$. The radiation dominated universe corresponds to $w = 1/3$, whereas the pressure-less matter (dust)

dominated universe corresponds to $w = 0$. In these cases we have

$$\text{Radiation}: \quad a(t) \propto (t - t_0)^{1/2}\,, \quad \rho \propto a^{-4}\,, \tag{1.21}$$

$$\text{Dust}: \quad a(t) \propto (t - t_0)^{2/3}\,, \quad \rho \propto a^{-3}\,. \tag{1.22}$$

Both cases correspond to a decelerated expansion of the universe: from Eq. 1.12 an accelerated expansion ($\ddot{a}(t) > 0$) occurs for the equation of state given by

$$w < -1/3\,. \tag{1.23}$$

As we will extensively discuss in Chap. 2, in order to explain the current acceleration of the Universe, we require an exotic energy, dubbed "dark energy", with equation of state satisfying Eq. 1.23 dominating the energy content of the Universe. Here we mention that from Eq. 1.11 the energy density ρ is constant for $w = -1$. In this case the Hubble rate is also constant from Eq. 1.9, giving the evolution of the scale factor:

$$a \propto e^{Ht}\,, \tag{1.24}$$

which is the de-Sitter universe. This exponential expansion also arises by including a (cosmological) constant, Λ, in the Einstein equations. Such a constant, compatible with requirements of the general relativity formalism (Bianchi identities and conservation law), was first introduced by Einstein, when looking for a stationary solution of the equations. The result was a closed Universe, $\kappa = 1$, with spatial curvature given by Λ and a radius $a = 1/\sqrt{\Lambda}$. For a detailed discussion see Weinberg (1989a); a more recent update on this topic may be found in Copeland et al. (2006).

The description of the static universe was abandoned with the discovery of the redshift of distant stars, but it is intriguing that the cosmological constant should return in the 1990's to explain the observed acceleration of the universe (Riess et al., 1998).

The modified Einstein equations in presence of a cosmological constant are given by

$$R_{\mu\nu} - \frac{1}{2} g_{\mu\nu} R + \Lambda g_{\mu\nu} = 8\pi G T_{\mu\nu}\,. \tag{1.25}$$

Considering Newtonian gravity with metric $g_{\mu\nu} = \eta_{\mu\nu} + h_{\mu\nu}$, it is possible to approximate the Poisson equations as $\Delta\Phi = 4\pi G\rho - \Lambda$. In order to reproduce the classical equation we require that $\Lambda = 0$ or Λ is sufficiently small relative to the $4\pi G\rho$. Since Λ has dimensions of $[\text{Length}]^{-2}$, the scale corresponding to the cosmological constant needs to be much larger than the scale of stellar objects on which Newtonian gravity works well. In other words the cosmological constant becomes important on very large scales.

In the FRW background, the modified Einstein equations (1.25) give

$$H^2 = \frac{8\pi G}{3}\rho - \frac{\kappa}{a^2} + \frac{\Lambda}{3}\,, \tag{1.26}$$

$$\frac{\ddot{a}}{a} = -\frac{4\pi G}{3}\left(\rho + 3p\right) + \frac{\Lambda}{3}\,. \tag{1.27}$$

This clearly demonstrates that the cosmological constant contributes negatively to the pressure term and hence exhibits a repulsive effect.

This description follows the kinematics point of view, which describes Λ as a geometrical quantity; introducing a modified energy density and pressure we can consider Λ as dynamical term, arising from a new energy contribution to the energy tensor:

$$\widetilde{\rho} = \rho + \frac{\Lambda}{8\pi G}\,, \quad \widetilde{p} = p - \frac{\Lambda}{8\pi G}\,,$$

where the negative contribution to the pressure is clearly shown. We find that Eqs. 1.26 and 1.27 reduce to Eqs. 1.9 and 1.12: this is basically the approach behind the explanation of the Universe acceleration by means of auxiliary scalar fields, which appear on the right-hand-side of the Einstein's equations. This scenario has been adopted when trying to solve the fine-tuning problem. For a detailed discussion see Copeland et al. (2006) and references therein. In this context we mention that the main problem connected to the cosmological constant is the huge discrepancy between its measured value, $\Lambda \approx H_0^2 = (2.13h \times 10^{-42}\,\mathrm{GeV})^2$, which correspond to $\rho_\Lambda = \frac{\Lambda m_{\rm pl}^2}{8\pi} \approx 10^{-47}\,\mathrm{GeV}^4$, and its theoretical estimate from quantum considerations of the vacuum energy, which predict $\rho_{\rm vac} = \frac{1}{2}\int_0^\infty \frac{\mathrm{d}^3\mathbf{k}}{(2\pi)^3}\sqrt{k^2+m^2} = \frac{1}{4\pi^2}\int_0^\infty \mathrm{d}k\, k^2\sqrt{k^2+m^2} \approx \frac{k_{\rm max}^4}{16\pi^2}$. Here $k_{\rm max}$ is the cut-off scale of the theory: for the extreme case of General Relativity, we expect it to be valid to just below the Planck scale: $m_{\rm pl} = 1.22 \times 10^{19}\,\mathrm{GeV}$. Hence, if we pick up $k_{\rm max} = m_{\rm pl}$, we find that the vacuum energy density in this case is estimated as $\rho_{\rm vac} \approx 10^{74}\,\mathrm{GeV}^4$ which is about 10^{121} orders of magnitude larger than the observed value. Even if we take an energy scale of QCD for $k_{\rm max}$, we obtain $\rho_{\rm vac} \approx 10^{-3}\,\mathrm{GeV}^4$, which is still much larger than ρ_Λ.

1.2 The Cosmological Model

An evolving homogeneous and isotropic Universe naturally suggests the idea of a beginning of the evolution. Even if, when extrapolating the equation backwards in time, we may enter regimes in which the validity of physics laws breaks down, it is nonetheless reasonable to think of a tiny very hot and dense region of the space-time which the expansion started from, and assuming it as a working hypothesis. In this scenario -

named ironically the Big Bang scenario by Fred Hoyle[2], one of its antagonists - after a very short period of time, in which the fundamental particles, which play a role in the standard model, have formed, we are left with the Universe filled with photons, leptons and a small amount of protons and neutrons constantly transformed through electroweak interaction. Each reaction has a proper time scale set by the particle standard model parameters: in order to be at equilibrium, the time scale has to be shorter than the Hubble time scale at the epoch ($t_{\rm H} \simeq 1/H(t)$).

1.2.1 Primordial Nucleo-synthesis

At high temperature, $\sim 10^{12}$K, when the energy of the radiation was of the order of $k_B T \sim 86$MeV, photons were hard enough to produce electron-positron pairs,

$$e^- + e^+ \leftrightarrow \gamma + \gamma \,, \tag{1.28}$$

which, interacting with neutrons and protons through

$$e^- + p \leftrightarrow n + \nu_e \,, \tag{1.29}$$

allowed the production of the protons and neutrons in a thermal abundance ratio:

$$n/p = e^{-Q/k_{\rm B}T} \simeq 1 \tag{1.30}$$

where $Q = (m_{\rm n} - m_{\rm p})c^2 = 1.2934\,{\rm MeV}$ is the neutron-proton mass difference. The neutrons and protons have a rapid rate for radiative capture

$$n + p \leftrightarrow d + \gamma \tag{1.31}$$

resulting in deuterium production. At high temperature the inverse reaction occurred rapidly too; only when the cooling due to the Universe expansion lowered the temperature, the deuterium could accumulate. At T$\sim 10^{10}$K the time scales of reaction 1.29 exceeded the characteristic Hubble timescale. Moreover the photon energy fell below the 1.022MeV necessary to produce electron-positron pairs and the neutrons were destroyed faster than they were formed. The neutron-to-proton ratio then froze at $n/p \simeq 0.223$. It is only when the temperature dropped below 10^9K, that deuterium could form and then suddenly transform into helium and traces of light elements up to lithium. This chain of reactions fixed indeed the primordial chemical elements abundances, with a helium fraction of the order of 22%, in excellent agreement with observations. The production

[2] http://www.nytimes.com/2001/08/22/obituaries/22HOYL.html?pagewanted=1

of elements up to iron occurred through nuclear fusion in the core of giant stars, while the heavier element production is due to SNe explosions and the reprocessing of the inter-stellar medium.

The thermal equilibrium lasted until the temperature fell below $13.6\,\mathrm{eV}\,(\sim 4000\,\mathrm{K}) \rightarrow z \sim 1100$, which is the hydrogen ionisation energy. This marks the (re)combination epoch and the decoupling of matter and radiation. From that time on, photons travelled in a nearly transparent Universe following the geodesics, while baryons started feeling the gravitational instability, leading to structure formation. Detailed computations show that the actual temperature at which the decoupling occurs is $\sim 0.6\,\mathrm{eV}$. The reason for this is the long tail in the Boltzmann distribution of the photon energy (Planck, 1901): the temperature needs to drop below hydrogen ionisation energy in order to have a low number of photons energetic enough to excite bound electrons.

1.2.2 The Cosmic Microwave Background Radiation

The reactions described above occurred in a Universe where photons drove the expansion, accounting for almost the total energy content; they were in a condition of thermal equilibrium, well described by a blackbody spectrum. The temperature of the radiation, due to the mild interaction with matter and its high heat capacity compared to that of matter, scales with the expansion as $T(t) = T_0/\,a(t)$ (Peebles, 1993), so that the spectral shape of the radiation distribution is then conserved. This is indeed another result of the homogeneity and isotropy, which translate into adiabaticity.

As soon as such computations were attempted, cosmologists realised that a thermal relic of such radiation should be still measurable today in the microwave range, i. e. characterised by a blackbody temperature of $\sim 5\,\mathrm{K}$ (Gamow, 1946; Alpher & Herman, 1948, 1988). Indeed Penzias and Wilson in 1965 reported an excess antenna temperature $T_0 = 3.5 \pm 1.0\mathrm{K}$ (Penzias & Wilson, 1965), which was interpreted as the cosmic relic by Dicke et al. (1965). This discovery was awarded with the Nobel Prize in Physics in 1978. Another milestone on the road to the cosmological standard model had been set.

A further confirmation of the homogeneous and isotropic Universe came in 1992 with the Cosmic Background Explorer (COBE) (Mather et al., 1992), a satellite launched by NASA to measure the cosmic background radiation. COBE was provided with two complementary experiments, the Far Infrared Absolute Spectrophotometer (FIRAS, Mather et al. (1990)) and the Differential Microwave Radiometers (DMR, Smoot et al. (1992)). The former aimed at measuring accurately the blackbody spectrum of the radiation, while the latter was devoted to the detection of anisotropies in the spectrum. Mather and collaborators measured a perfect blackbody spectrum characterised by the temperature of

$T_0 = 2.735 \pm 0.06$K, which definitely corroborated the Big Bang picture and the expanding Universe scenario. In Fig. 1.1 we show the thermal spectrum measured by the COBE satellite, where the agreement between data and theory is excellent.

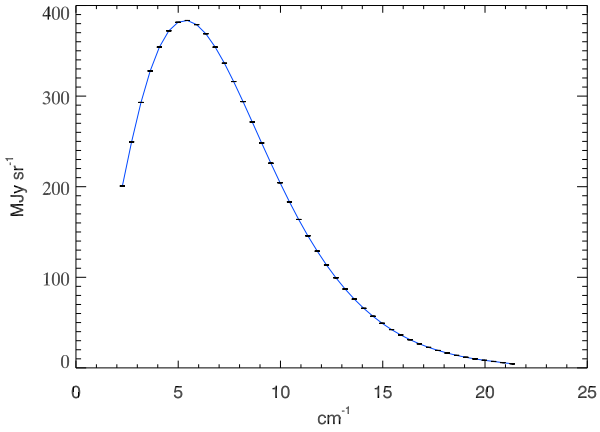

Figure 1.1: Thermal spectrum of the cosmic background radiation as measured by the FIRAS (COBE) satellite. Boxes are the experimental points while the solid line is the theoretical blackbody spectrum for $T = T_0$. The agreement is impressive (Fixsen et al., 1996).

These measurements have been so important as to justify the award of the Nobel prize in 2006 to J. C. Mather and G. F. Smoot.

1.2.3 Structure formation and CMB anisotropies

The previous discussion aimed at introducing the formal context, the general relativity equations, and the global picture, the big bang scenario, in which the cosmological model takes place, under the assumption that the cosmological principle, i. e. the homogeneity and isotropy of the Universe, holds. Obviously this smoothness can be valid on average at large scales only, since in the nearby Universe we observe structures – stars, globular clusters, galaxies and clusters of galaxies – which do not appear homogeneous and isotropic.

The cosmological model provides a natural explanation of the presence of structures in the Universe. Tiny perturbations to the homogeneous background quantities, metric and energy density, were present from the beginning, and they have grown through gravitational instability leading to the large complex objects we observe in the neighbourhood of our Galaxy. Such perturbations would be the quantum energy fluctuations of the very early stages of the Universe, stretched to a classical size by inflation. Inflation is a phase of exponential expansion which the Universe underwent in the first fractions of second of its evolution, which determined the initial conditions of the Big Bang scenario. The

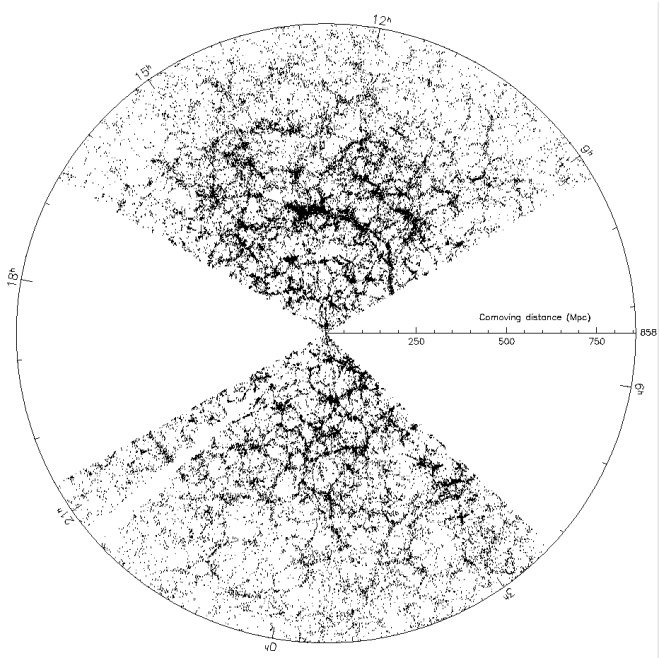

Figure 1.2: Slices through the SDSS 3-dimensional map of the distribution of galaxies. Earth is at the centre, and each point represents a galaxy, typically containing about 100 billion stars. The outer circle is at a distance of two billion light years. The region between the wedges was not mapped by the SDSS because dust in our own Galaxy obscures the view of the distant universe in these directions. Image taken from http://www.sdss.org

details of this phenomenon are not clear yet, and several models compete to draw the correct picture. A full description can be found in Liddle & Lyth (2000).

Unfortunately, there are few exact solutions of general relativity which incorporate spatially inhomogeneous and anisotropic matter and hence geometry. Therefore calculations are usually performed following a perturbative approach, starting from the spatially homogeneous and isotropic FRW model as a background solution with simple properties and increasing the complexity of inhomogeneous perturbations order by order. Metric perturbations can be distinguished into scalar, vector and tensor contributions according to their transformation properties on spatial hypersurfaces (Bardeen, 1980; Stewart, 1990). The reason for splitting the metric perturbation into these three types is that the governing equations decouple at linear order, and hence we can solve each perturbation type separately. At higher order this is no longer true (Nakamura, 2006). For a detailed discussion on this topic see for example Malik & Wands (2009) and Ma & Bertschinger (1995). At the first order, scalar perturbations can be described modifying the metric as

$$\mathrm{d}s^2 = -a(\tau)[(1+2\psi)\,\mathrm{d}\tau^2 - (1+2\phi)\,\mathrm{d}x_i\,\mathrm{d}x^i] \tag{1.32}$$

where we chose the conformal time $\mathrm{d}\tau = \mathrm{d}t/a$ and introduced the two scalar potentials, which are related to the Bardeen potentials (Bardeen, 1980). The energy tensor is

modified as well according to

$$\begin{aligned} T^0{}_0 &= -(\bar{\rho}+\delta\rho)\,, \\ T^0{}_i &= (\bar{\rho}+\bar{P})v_i = -T^i{}_0\,, \\ T^i{}_j &= (\bar{P}+\delta P)\delta^i{}_j + \sigma^i{}_j\,, \qquad \sigma^i{}_i = 0\,, \end{aligned} \tag{1.33}$$

where $\delta\rho$ and δP represent the density and pressure fluctuations respectively, and $\mathbf{v}$ the velocity field. We have allowed an anisotropic shear perturbation $\sigma^i{}_j$ in $T^i{}_j$. Notice that we wrote the equation in the conformal Newtonian gauge, where vector and tensor modes are set to zero from the beginning. See Ma & Bertschinger (1995) and Malik & Wands (2009) for an exhaustive discussion on the gauge problem. This is mainly related to the freedom of choosing a frame in which to perform the perturbation expansion. For instance, the synchronous gauge, defined as the gauge in which the proper time for observers at xed spatial coordinates coincides with cosmic time in the FRW background, i.e. $\mathrm{d}\tau = a\,\mathrm{d}t$ ($\psi = 0$ in Eq. 1.32 and a new scalar perturbation would appear in the spatial part of the metric), is widely used in numerical Boltzmann solvers, such as `cmbfast` [3] (Seljak & Zaldarriaga, 1996) and CAMB[4] (Lewis et al., 2000).

Solving Einstein equations 1.32 and 1.33 in Fourier space, we obtain the Friedmann equations 1.9 and 1.10 for the background quantities at the zeroth order, while at the first order we have the metric fluctuations equations:

$$k^2\phi + 3\frac{\dot{a}}{a}\left(\dot{\phi}+\frac{\dot{a}}{a}\psi\right) = 4\pi G a^2 \delta T^0{}_0\,, \tag{1.34}$$

$$k^2\left(\dot{\phi}+\frac{\dot{a}}{a}\psi\right) = 4\pi G a^2(\bar{\rho}+\bar{P})\theta\,, \tag{1.35}$$

$$\ddot{\phi}+\frac{\dot{a}}{a}(\dot{\psi}+2\dot{\phi})+\left(2\frac{\ddot{a}}{a}-\frac{\dot{a}^2}{a^2}\right)\psi+\frac{k^2}{3}(\phi-\psi) = \frac{4\pi}{3}G a^2 \delta T^i{}_i\,, \tag{1.36}$$

$$k^2(\phi-\psi) = 12\pi G a^2(\bar{\rho}+\bar{P})\sigma\,, \tag{1.37}$$

The energy perturbations are described by:

$$\begin{aligned} \dot{\delta} &= -(1+w)\left(\theta-3\dot{\phi}\right)-3\frac{\dot{a}}{a}\left(\frac{\delta P}{\delta\rho}-w\right)\delta\,, \\ \dot{\theta} &= -\frac{\dot{a}}{a}(1-3w)\theta-\frac{\dot{w}}{1+w}\theta+\frac{\delta P/\delta\rho}{1+w}\,k^2\delta-k^2\sigma+k^2\psi\,. \end{aligned} \tag{1.38}$$

where we defined $\theta = i\mathbf{k}\cdot\mathbf{v}$. w is the equation of state parameter of the total Universe fluid.

[3] http://www.cfa.harvard.edu/∼mzaldarr/CMBFAST/cmbfast.html
[4] http://camb.info/

As we discussed in the previous section, until decoupling occurred at redshift $z \simeq 1100$, the universe was in a condition of thermal equilibrium. The tiny ripples in the energy distribution should then be still present in the distribution of the photons, which have travelled in a almost transparent Universe. This is exactly what Smoot et al. (1992) measured with the DMR experiment, who found $\delta T/T \simeq 10^{-5}$. In Fig. 1.3 the cosmic microwave background anisotropies detected by DMR are shown.

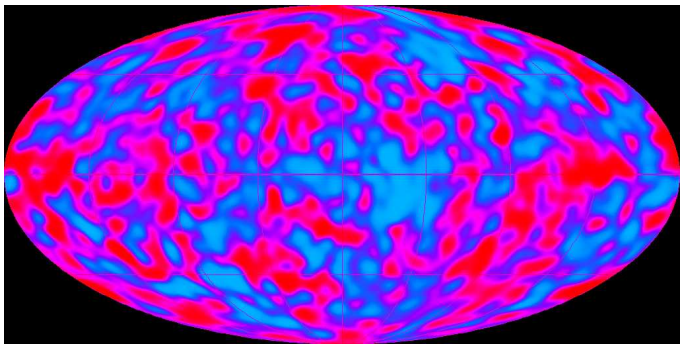

Figure 1.3: Cosmic microwave fluctuations as seen by COBE satellite.

After recombination, the perturbations of ordinary matter could grow via gravitational instability forming galaxies (Jeans, 1943, 1961). Actually self-gravitation would not have allowed baryons to form the structure distribution we observe in the sky (Cross et al., 2001; Condon et al., 1998; Abazajian et al., 2009), in particular baryons would not have had enough time to form large structures. To deal with this, theorists postulated a new kind of pressure-less matter, which interacts gravitationally only. Such dark matter decoupled earlier from radiation: that means that its perturbations started to grow earlier than baryons' ones. After recombination, baryons fell into the potential wells created by dark matter leading to the formation of structure via hierarchical clustering. A very good discussion on cosmic microwave background perturbations can be found in Hu (1995), while for the theory of hierarchical clustering we recall Padmanabhan (1993). A recent review on this topic can be found in Tonini (2009).

Imagining a new species of particles seems a plausible solution, since the particle standard model and its supersymmetric extension offer a plethora of candidates. The challenge today is to (indirectly) measure effects of this non-ordinary matter in the sky. Two interesting and controversial examples are given by Adriani et al. (2009) and Bernabei et al. (2008). Moreover, independent evidence of the presence of a different kind of matter came from the galaxy cluster analysis. The total mass, which can be inferred from the X-ray emission we observe, is larger than the mass in stars and gas we see. From this and other detailed studies of the cluster properties, cosmologists deduced the total amount of mass in the Universe exceeds the baryon mass by a factor of few.

1.3 CMB anisotropies analysis

The cosmic microwave background radiation can be certainly regarded as one of the most fruitful tool we possess to investigate our Universe. Among others, two main reasons are worth mentioning: i) except a minor contribution from re-ionisation at redshift $\simeq 12$, CMB photons have travelled in a nearly transparent Universe from recombination: they carry detailed information of the early stages of the Universe evolution; ii) the bulk of the CMB physics can be described by means of the linear perturbation theory, even though second order effects (Bartolo et al., 2006, 2007; Nitta et al., 2009) are now becoming important in view of the upcoming experiments like Planck (Tauber, 2001). Moreover, the effect on re-ionisation is very important on its own, since it contains details on the processes involving the first generation of stars, the so-called population III stars.

One more advantage of the CMB is that it is naturally defined on the sphere, and then a 2-dimension analysis is computationally more efficient than a full 3-dimensional one. Strictly speaking recombination has not been an instantaneous process, but spanned a redshift interval $\Delta z \simeq 170$; however, this range can be safely considered a fraction compared to the recombination epoch, $z \sim 1100$, so that the surface approximation is correct. Even though the temperature measurement is better performed in real space, the harmonic space is the natural choice for the analysis of the statistical properties of the CMB radiation. We decompose the radiation field onto the spherical harmonics basis

$$T(\gamma) = \sum_{\ell m} Y_{\ell m}(\gamma) a_{\ell m} \tag{1.39}$$

where $a_{\ell m}$ are the spherical harmonic coefficients and ℓ is the multipole considered. An approximated relation useful to keep in mind is $\ell \sim 180/\theta$, which relates the multipole ℓ and angular scale θ, based on the spherical Bessel's functions expansion (in a nearly flat Universe).

We are interested in the angular power distribution described by the quantity $\langle a_{\ell m} a^*_{\ell m} \rangle_{\rm E}$. We can deal with our Universe only and we can not perform such an ensemble average. However, assuming the homogeneity and isotropy of the Universe, we can deduce the rotational invariance of the CMB, and then replace the ensemble average with a sum over m. We end up with an angular power distribution encoded in:

$$\mathcal{C}_\ell = 4\pi \sum_m \frac{a_{\ell m} a^*_{\ell m}}{2\ell + 1} \tag{1.40}$$

characterised by an intrinsic uncertainty – cosmic variance – given by:

$$\Delta_{\mathcal{C}_\ell} = \sqrt{\frac{2}{2\ell+1}}\mathcal{C}_\ell \,. \tag{1.41}$$

Notice how $\Delta_{\mathcal{C}_\ell}$ is proportional to the $\mathcal{C}_\ell$ and monotonically decreasing with the multipole ℓ: this reflects the number of elements, we assume as independent realisations of the same sky, included in the sum 1.40. For a detailed discussion on the derivation of this relation and on the higher angular moments see Hu (2001); Komatsu (2002).

This approach is based on the assumption that the primordial cosmological perturbations were nearly Gaussian as a result of the inflationary phase. It has resisted so far a large number of tests, and its confirmation is one of the main goals of the Planck experiment.

An example of the angular power spectrum measured by the most recent CMB experiments is shown in Fig. 1.4, while the temperature map seen by the Wilkinson Microwave Anisotropy Probe (WMAP) is reported in Fig. 1.5. The improvement with respect to the first image of the CMB taken by the COBE satellite (Fig. 1.3) is impressive and now we are able to detect tiny fluctuations, reaching multipoles $\ell \sim 1500$.

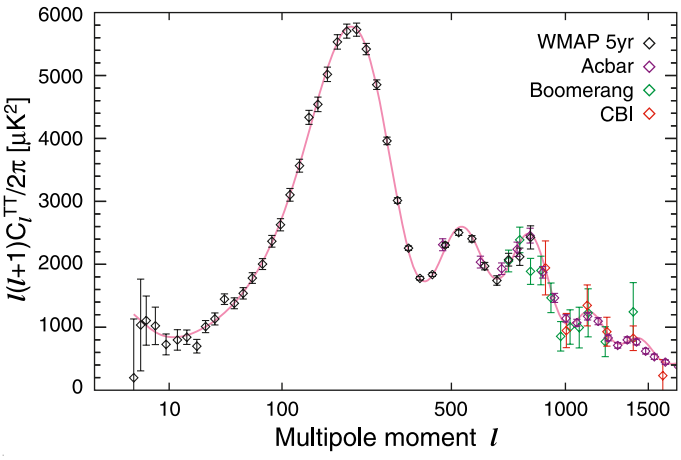

Figure 1.4: Angular power spectrum obtained combining the datasets of several experiments. The image is taken from Nolta et al. (2009).

1.3.1 Acoustic Peaks

The angular power spectrum shows a characteristic peak structure, which perfectly reflects the baryonic acoustic oscillations (BAO), which the photon-baryon plasma underwent before the recombination epoch. Here we briefly comment on the main features of this process, and refer to Hu (1995) for a comprehensive study. We discussed that during the first minutes of the Universe evolution, photons and baryons were tightly coupled

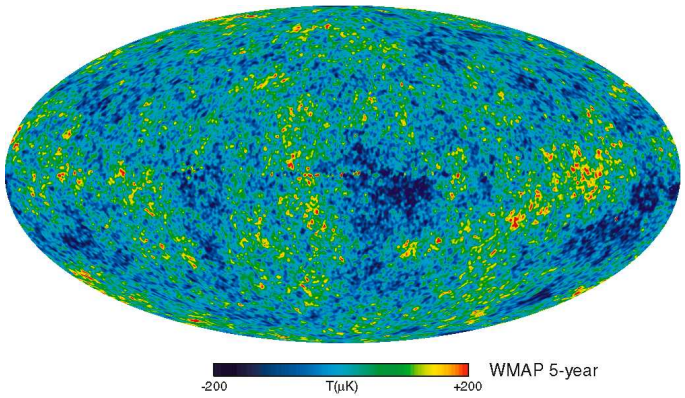

Figure 1.5: Internal linear combination map provided by WMAP team. Image taken from Hinshaw et al. (2009).

through electroweak interaction, in particular, once the nucleo-synthesis had finished, electrons mediated the interactions. We have mentioned that baryon perturbations on their own have vanishing pressure and would grow under the gravitational potential; before recombination, baryons felt the pressure contribution of the radiation, which counterbalanced the gravitational force, producing an oscillatory dynamics of the perturbations. This lasted until decoupling, when the pressure contribution stopped and baryons collapsed, driven by the gravitational potential. These oscillations are those highlighted in the angular power spectrum. The difference in power between peaks can be explained taking into account that the dynamics of the cosmic fluid occurred in an expanding universe. Events in the space-time are connected within a radius $\sim 1/H(t)$, the Hubble horizon, and consequently a perturbation participates in the dynamics sketched above only when entering the horizon, i. e. when its size is smaller than the Hubble radius. This is what happened to small fluctuations, described at large multipoles in the angular power spectrum. The first peak corresponds to the modes which entered the horizon close to the decoupling epoch; they had just started the oscillation, being in the first compression phase and evolved mainly under the gravitational effect. In this oscillation process, the fluctuation at the last scattering surface determines the anisotropy: odd peaks correspond to compression phases, while even ones to rarefaction phases.

The overall matter content sets the global gravitational potential and then the zero point common to the oscillations; if the Universe were filled with pressure-less matter only, the gravitational potential would be constant and this effect would result in a flat plateaux at very large scale we can see in the angular power spectrum at small multipoles, consisting in a nearly constant power (Sachs & Wolfe, 1967). In the case of an evolving potential, as in the case of a radiation or cosmological constant dominated Universe, photon energy is shifted and we observe a bump in the angular power spectrum (Integrated Sachs & Wolfe effect).

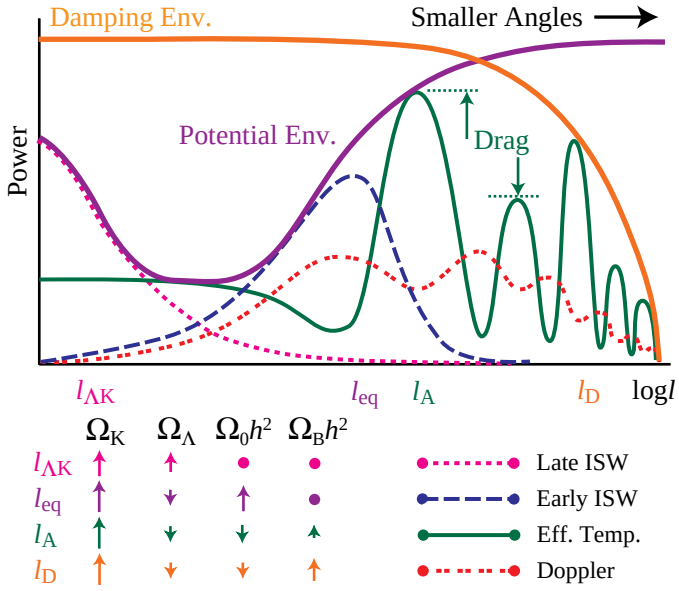

Figure 1.6: Effect of the main contributions to the angular power spectrum. Image taken from Hu (1995).

Another phenomenon, which contributes to the anisotropy pattern, is the Doppler effect due to the motion of the photon-baryon fluid: it results anti-correlated with the compression-rarefaction pattern. All these contributions to the angular power spectrum are schematically summarised in Fig. 1.6.

The position of the first peak sets then a characteristic scale, the horizon size at the recombination, which can be used as a standard ruler in cosmology. Measuring the position of the first peak, and then the angle under which we see it (projection effect), we can infer the global geometry of the Universe. It is from such analysis, measuring the characteristic size of CMB anisotropies, that de Bernardis et al. (2000) claimed the flatness of the Universe. This result has been confirmed later by the *WMAP* team (Spergel et al., 2003) and it represents one of the main, and nonetheless challenging, properties of our Universe (see Sec. 1.3.3).

1.3.2 Cosmological Parameters

The physics of the CMB that we have briefly recalled, has to be studied with rather sophisticated numerical code in order to produce angular power spectra, which can be compared to the observed one. The difficulty consists in properly modelling the photon-baryon fluid properties, fully taking into account the details, and propagating Einstein's equations, which on their own represent a big challenge since they are non-linear. A well-tested numerical code is CAMB (Lewis et al., 2000), which some of the results we will discuss in the work are derived with.

Despite its complexity, since the processes involved are well described by the law of physics, the cosmological model is completely specified by a handful of parameters – and a few assumptions we have already commented on. The basic parameters of the cosmological model, ΛCDM model, are:

- the *baryon density*, normalised to the critical density today, $\Omega_{\rm b} \equiv \rho_{0\rm b}/\rho_{0\rm c} \simeq 0.04$, where $\rho_{0\rm c} = 8\pi G/3H_0 \simeq 1.879 \times 10^{-29} h^2\,{\rm g\,cm^{-3}}$;
- the *cold dark matter density*, $\Omega_{\rm cdm} \equiv \rho_{\rm cdm}/\rho_{0\rm c} \simeq 0.2$;
- the value of the *Hubble parameter* today, $H_0 \simeq 72\,Km/s/Mpc$;
- the *amplitude* of the primordial curvature perturbation power spectrum, $\Delta^2_{\mathcal{R}}(k = 0.002\,{\rm hMpc^{-1}}) \simeq 2.3 \times 10^{-9}$;
- the *spectral index* of the primordial curvature perturbation power spectrum, $n_{\rm s} \simeq 1$;
- the *optical depth*, $\tau \sim 0.09$, which describes the integrated effect of the re-ionisation on the CMB.

The photon density today is sub-dominant with respect to the baryon and cold dark matter ones, and nonetheless crucial: it is set by the blackbody spectrum as $\Omega_{0\gamma}h^2 = 2.38 \times 10^{-5}\Theta_{2.7}$, where $\Theta_{2.7} \equiv T_0/2.7\,{\rm K}$. Since the Universe turns out to be flat, the critical density is achieved by introducing the cosmological constant, parameterised by $\Omega_\Lambda \equiv 1 - \Omega_{0\rm b} + \Omega_{0\rm cdm}$. The cosmological constant fits surprisingly well into the cosmological model, since it allows us to explain the observations of the SNe, which suggest the Universe expansion is now accelerating (Riess et al., 2009; Riess et al., 2004; Riess et al., 1998; Perlmutter et al., 1999; Kowalski et al., 2008; Zhang & Wu, 2009). The initial conditions for the perturbations are set by inflation, which predicts adiabatic nearly Gaussian scale invariant fluctuations. We will outline briefly the single scalar field inflation model in the next section (Sec. 1.3.3).

Accurately measuring the angular power spectrum allows us to set tight constraints on the cosmological parameters (Dunkley et al., 2009). Much more effective are the constraints put by combining CMB, SNe and Baryonic Acoustic Oscillations datasets. See for example Komatsu et al. (2009). In Fig. 1.7 we show the effect which each parameter has on the angular power spectrum. The black solid line represents the ΛCDM fiducial model, the red dashed and blue dotted-dashed lines are obtained by changing each parameter by $\pm 2\,\sigma$ respectively. Increasing the baryon fraction enhances the ratio between the first and the second peak; a greater amount of cold dark matter increases the gravitational potential and lowers the peaks. Increasing the spectral index has a similar effect, since this distributes more power to smaller scales. $\Delta^2_{\mathcal{R}}$ rescales the overall amplitude of

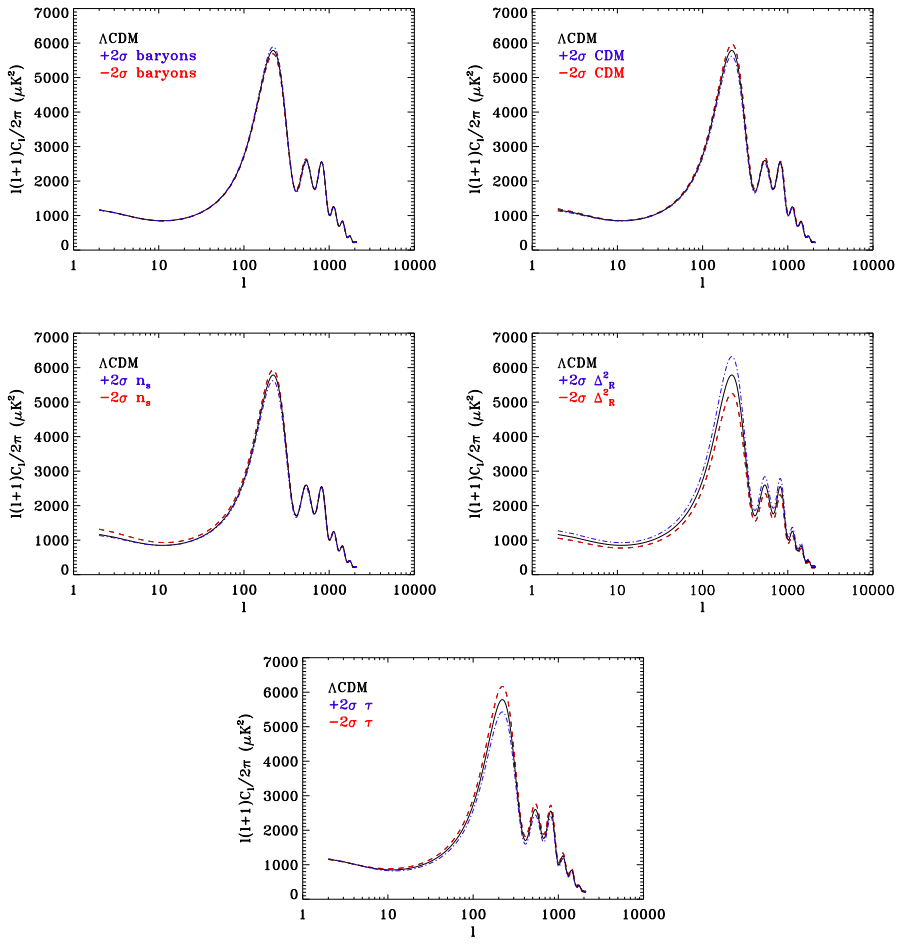

Figure 1.7: Effect of the basic ΛCDM parameters on the angular power spectrum.

the power spectrum, while the optical depth again affects the peak feature with respect to the Sachs & Wolfe plateau.

What clearly emerges from this exercise is that there is a degeneracy also between the basic parameters of the models and a careful combination of many complementary observations is necessary in order to tightly constrain them (CMB,SNe, BAO,...). A way to resolve degeneracies among parameters is to add CMB polarisation information, as discussed in Cabella & Kamionkowski (2004); Kamionkowski et al. (1997).

1.3.3 Inflation

In the previous sections we have presented the cosmological standard model, underlining the big successes it achieved in describing the cosmic elements abundances, the cosmic microwave background radiation – both its smoothness and its tiny roughness – the structure formation, with the basic assumption of the homogeneity and isotropy of the

Universe. We have justified such an assumption as a reasonable, pretty general and simple one, but we already mentioned that it comes naturally as a result of the inflationary phase which occurred at the very early stages of the Universe evolution. Inflation would be also responsible for the amplitude and the spectral index of the primordial curvature perturbations, which are basic parameters of the model.

Basic Idea

Before discussing the main characteristics of inflation, we re-call why a mechanism very similar to inflation is necessary to resolve a few unsatisfactory features of the cosmological model.

According to what we learnt from general relativity, a physical scale λ_0 today would correspond to a proper length of $\lambda_0\, a(t)/a_0$ in the past, scaling with some power of the time, t^n. The characteristic expansion scale of the Universe, on the other hand, is given by the Hubble radius $H^{-1}(t) = (\dot{a}/a)^{-1} = t/n$. In realistic cosmological models, $n < 1$ and hence the ratio $\lambda(t)/H^{-1}(t)$ increases as we go to the earlier epochs. In other words, $\lambda(t)$ would have been larger than the Hubble radius at sufficiently high redshifts. This leads to the major difficulty in the conventional cosmology: normal physical processes act coherently only over sizes smaller than the Hubble radius, so that it is hard to image which process could have seeded the density perturbations necessary to generate structures we see in the Universe, whose scales were much bigger than the Hubble radius at early epochs.

Two more problems affect a Friedmann-Robertson-Walker universe: the so-called *horizon* and *flatness* problems. Let us focus on the former. To any time interval Δt corresponds a proper distance light can have travelled, which sets the particle horizon and the causal connected region to a given event. Without such a communication, there is no *a priori* reason why two regions of the space-time should have a similar environment. Computing the particle horizon at the recombination epoch, we obtain roughly one degree, much smaller than the entire sky on which we observe the CMB, characterised by a nearly perfect blackbody spectrum (which means equilibrium and uniformity). Within the depicted scenario we are not able to justify the homogeneity we detect.

The second problem could be rephrased as a fine-tuning problem. We measure a Universe density today close to the critical one and we derive the flat geometry of the space-time. More quantitatively, we have from Eq. 1.13 for $\kappa \neq 0$

$$\Omega(t) - 1 = \frac{\dot{a}_0^2}{\dot{a}^2}(\Omega_0 - 1)\,. \tag{1.42}$$

Evaluating the expression above in terms of the temperature in the radiation dominated era, we obtain $\Omega - 1 \sim 10^{-60}$ at the Planck scale (Padmanabhan, 1993), which in the absence of any physical mechanism, requires an extreme fine-tuning.

All these difficulties can be solved by introducing a physical process which makes $a(t)$ increase rapidly with t (e. g. exponentially) for a brief period of time. Such a rapid growth is called *inflation*. A universe with an inflationary phase which took place in the radiation dominated era at $t_* \sim 10^{-35}$, characterised by a constant Hubble parameter $H \sim 10^{10}\,\mathrm{GeV}$, lasting a period NH^{-1} with $N \sim 60$ number of e-folds, would make the job (namely a factor e^{60} at $t \sim 10^{-35}$s lasting $\sim 10^{-32}$s). A physical scale λ would grow exponentially with a, while H remains constant; cross the horizon, becoming larger than the Hubble radius, and finally re-enter the horizon during the second radiation dominated phase, when the Hubble radius "catches up" with the proper length λ. Scales of cosmological interest were within the Hubble radius before inflation, so that a physical process could have operated at these scale: such process has to be quantum mechanical by nature, and quantum fluctuations in the matter fields can seed perturbations. Inflation solves the horizon problem by bringing the entire region of the last scattering surface into a causally connected patch; while the flatness problem is eliminated because the exponential growth stretches the space-time, making it almost flat.

Notice that inflation extremely dilutes energy so that some re-heating mechanism has to happen in order to obtain the energy density necessary to the standard cosmological evolution. Inflation suggests a classical solution to problems, which probably find their roots on a pure quantum ground, that, if consistently treated, may resolve those problems coherently. Moreover, both the horizon and the flatness problem are basically postponed, and they may resurface.

A toy model

A very simple model for inflation is provided by a single scalar field, which slowly rolls on a very flat potential towards the true minimum. Deriving the field equations we obtain the density and the pressure of the field in terms of the kinetic term and the potential as

$$\rho_\phi = \frac{1}{2}\dot{\phi}^2 + V(\phi)\,, \qquad p_\phi = \frac{1}{2}\dot{\phi}^2 - V(\phi). \tag{1.43}$$

Under the slow-roll assumption ($1/2\dot{\phi}^2 \ll V(\phi)$), the equation of state parameter, w, results very close to -1; this implies a nearly constant Hubble rate, producing an exponential expansion (see Eq. 1.24). Once the scalar field approaches the minimum of the potential, it oscillates and decays into relativistic particles. This process is called *reheating*. The particle production, together with the Universe expansion damp the oscillations.

The details of the dynamics depend upon the specific model of inflation, but so far none of the single scalar field inflationary model can be considered completely satisfactory. Multiple scalar fields models are now becoming very popular and find inspiration from effective theories deriving from string and brane models. One simple two scalar fields model which has been widely investigated is the curvaton model (Lyth & Wands, 2002).

The generation of the density perturbations can be sketched assuming a de-Sitter metric

$$\begin{aligned} \mathrm{d}s^2 &= -\mathrm{d}t^2 + e^{2Ht}\delta_{ij}\,\mathrm{d}x_i\,\mathrm{d}x_j \\ &= a(\eta)[-\mathrm{d}\eta^2 + \delta_{ij}\,\mathrm{d}x_i\,\mathrm{d}x_j]\,, \qquad a(\eta) = -\frac{1}{H\eta} \end{aligned} \tag{1.44}$$

and defining the fluctuation in terms of the creation and annihilation operators as follows:

$$\delta\phi = \int \frac{\mathrm{d}^3k}{(2\pi)^3}\left[\hat{a}_{\mathbf{k}}\delta\phi_{\mathbf{k}}(t)e^{i\mathbf{k}\cdot\mathbf{x}} + \hat{a}^{\dagger}_{\mathbf{k}}\delta\phi^{*}_{\mathbf{k}}(t)e^{-i\mathbf{k}\cdot\mathbf{x}}\right]. \tag{1.45}$$

Solving the Einstein's equations for the new variable $u_{\mathbf{k}} = a\delta\phi_{\mathbf{k}}$, we obtain, in terms of the original variable, for a light field ($m^2 \ll H^2$)

$$\delta\phi_{\mathbf{k}}(t) = \frac{iH}{\sqrt{2k^3}}(1 + ik\eta)e^{-ik\eta}. \tag{1.46}$$

The density power spectrum is defined as the expectation value on the vacuum state, which reads

$$\langle 0|\delta\phi^2|0\rangle = \int \frac{\mathrm{d}^3k}{(2\pi)^3}P(k) = \begin{cases} (H\eta)^2\frac{k^2}{4\pi^2} & -k\eta \to \infty \\ (\frac{H}{2\pi})^2 & -k\eta \to 0 \end{cases} \tag{1.47}$$

This means that on super-horizon scale the density power spectrum is independent of the scale and function of the Hubble rate only. Once we have the density power spectrum, it is possible to compute the curvature power spectrum using the number-of-efolds formalism under the assumption that the perturbations become classical on super-horizon scales. The curvature is given by

$$\mathcal{R}_c = \delta N|_{t_k} = \frac{\partial N}{\partial\phi}\delta\phi\Big|_{t_k} \tag{1.48}$$

where t_k is the time when the perturbation crosses the horizon and becomes classical. By using the definition of the number of e-folds, $N = \int H\,\mathrm{d}t$, we derive $\frac{\partial N}{\partial\phi} = \frac{H}{\dot{\phi}}$, which leads to

$$\langle\mathcal{R}_c^2\rangle = \left(\frac{H}{\dot{\phi}}\right)^2\langle\delta\phi^2\rangle \qquad \to \qquad P_{\mathcal{R}} = \left(\frac{H}{2\pi\dot{\phi}}\right)^2\Big|_{t_k}. \tag{1.49}$$

The details of the computation depend upon the specific inflationary model under investigation, however the basic concepts we outlined above are common to any early universe scenario. Observationally it is not yet possible to set tight constraints on the inflaton potential; what it is generally done is to bound two derived inflationary parameters, which describe the slow-roll condition:

$$\begin{aligned} \epsilon &\equiv \frac{M_{\rm p}^2}{16\pi}\left(\frac{V'}{V}\right)^2 \ll 1 \\ \eta &\equiv \frac{M_{\rm p}^2}{8\pi}\left(\frac{V''}{V}\right) \ll 1 \end{aligned} \tag{1.50}$$

These parameters are useful because, within the slow-roll paradigm, there exist consistency relations between inflation derived quantities, which can be tested. One of these is:

$$n_{\rm s} \simeq 1 - 6\epsilon + 2\eta \tag{1.51}$$

Finally, we have discussed the scalar perturbations only, but very interesting is the treatment of tensor perturbations, which should translate into a stochastic gravitational wave background. Properties of the tensor modes can be expressed in the slow-roll scenario as

$$\begin{aligned} &n_{\rm t} \simeq -2\epsilon, \\ &\frac{T}{S} = 16\epsilon = 8|n_{\rm t}| \end{aligned} \tag{1.52}$$

The determination of the inflation parameters is very important to understand the inner nature of our Universe and to start probing more exotic early Universe scenarios, such as the ekpyrotic one (Lehners & Steinhardt, 2008), which get inspiration from high dimensional theories. The Planck mission has considered this aspect as one of the main goals (Popa et al., 2009).

Conclusions

In this chapter we briefly outlined the cosmological model, presenting the main experiments which have confirmed or inspired the theoretical progress. The ΛCDM model describes an evolving Universe, that began about 14 billion years ago out of a very hot and dense region of the space-time. After a brief exponential expansion, which set the initial conditions of homogeneity and isotropy and seeded the cosmological perturbations, an interacting photon-baryon fluid governed the evolution, producing the light chemical elements, hydrogen, helium, lithium. When the photon temperature dropped below the

hydrogen ionisation value, protons and electrons combined and decoupled from radiation. The small fluctuations in the baryon density grew through gravitational instability forming galaxies, clusters of galaxies and the structures we observe in the Universe. Two more ingredients are necessary to properly reproduce the cosmological observations: dark matter and cosmological constant (or dark energy). The former creates the gravitational wells in which baryons fell; the latter is responsible for the late time acceleration of the Universe expansion.

All the processes which take place in the ΛCDM model are described by means of the fundamental laws of physics and the addition of a few parameters, which are now well constrained by very accurate experiments. However, open questions remain, in particular concerning the nature of inflation, dark matter and dark energy. In the next chapters we will discuss some recent works, which can help in solving these fascinating questions.

Chapter 2

The Dark Energy Problem: Theory and CMB Data analysis

If there is something that appears
to lie beyond the natural world
as it is now imperfectly understood,
we hope eventually to understand it
and embrace it within the natural.

("The god delusion", R. Dawkins)

The most outstanding problem in modern cosmology is understanding the mechanism that led to a recent epoch of accelerated expansion of the universe. The evidence that we live in an accelerating universe is now compelling. The luminosity distance at high redshift ($z \sim 1$) measured from distant type Ia supernovae is consistent with a negative deceleration parameter ($q_0 < 0$ at $\sim 3\sigma$) and shows strong evidence of a recent transition from deceleration to acceleration (Riess et al., 2009; Riess et al., 2004; Riess et al., 1998; Perlmutter et al., 1999; Kowalski et al., 2008; Zhang & Wu, 2009). The amount of clustered matter in the universe, as detected from its gravitational signature through a variety of large scale probes (redshift surveys, clusters of galaxies, etc.) cannot be more than $\sim 1/3$ of the total content of the universe (Springel et al., 2006). Observations of the cosmic microwave background (CMB) anisotropy have constrained the value of cosmological parameters with high precision (Hinshaw et al., 2009; Brown et al., 2009; Reichardt et al., 2009; Curto et al., 2008; Sievers et al., 2007; Masi et al., 2006). The recent WMAP data (Hinshaw et al., 2009; Komatsu et al., 2009; Dunkley et al., 2009) have shown that the total density of the universe is very close to its critical value. Taken together, these results are a strong indication in favour of a non-null cosmological term, which would at the same time explain the accelerated expansion of the universe and provide the remaining $\sim 2/3$ of its critical density.

The precise nature of the cosmological term which drives the accelerated expansion, however, remains mysterious. The favoured working hypothesis is to consider a dynamical, almost homogeneous component (termed *dark energy*) with negative pressure (or, equivalently, repulsive gravity) and an equation of state $w \equiv p/\rho < -1/3$ (Peebles & Ratra, 1988; Caldwell et al., 1998; Wang et al., 2000; Peebles & Ratra, 2003). See Sec. 1.1. Such a framework helps alleviating a number of fundamental problems arising when a constant cosmological term is interpreted as the energy density of the vacuum (Weinberg, 1989b; Copeland et al., 2006).

Very recently, Shafieloo et al. (2009) refined the SNe analysis finding evidence for a slow-down of the acceleration of the Universe. If confirmed, this would surely favour a dark energy based explanation, since a cosmological constant would not be able to account for such a decelerating behaviour. This result is however controversial as discussed in Serra et al. (2009).

In this chapter we address the dark energy problem from different standpoints. In Sec. 2.1 we discuss the ISW effect and how it can be used to pin down the dark energy properties. In Sec. 2.2 we attempt a global explanation of the dark sector, in terms of the two coupled fluids. We deduce that a very common scenario is an affine behaviour, that we tested against observations in Sec. 2.3.

2.1 Integrated Sachs-Wolfe effect from the cross-correlation of WMAP 3 year and NVSS: new results and constraints on dark energy

One key indication of an accelerated phase in cosmic history is the signature from the integrated Sachs-Wolfe (ISW) effect (Sachs & Wolfe, 1967) in the CMB angular power spectrum. This is directly related to variations in the gravitational potential: in particular, it traces the epoch of transition from a matter-dominated universe to one dominated by dark energy. This effect (which is usually called *late ISW*, as opposed to an *early ISW* generated during the radiation-matter transition), shows up as a contribution in the low multipole region of the CMB spectrum. A detection of a late ISW signal in a flat universe is, in itself, a direct evidence of dark energy. Furthermore, the details of the ISW contribution depend on the physics of dark energy, and are therefore a powerful tool to better understand its nature. Unfortunately, the low multipole region of the angular power spectrum is also the most affected by cosmic variance (Eq. 1.41), making the extraction of the ISW signal a difficult task.

A useful way to separate the ISW contribution from the total signal is to cross-correlate the CMB anisotropy pattern (imprinted during the recombination epoch at $z \sim 1100$) with tracers of the large scale structure (LSS) in the local universe (Crittenden & Turok, 1996). Detailed predictions of the ability to reconstruct the ISW using this technique were obtained by a number of authors (Cooray, 2002; Hu & Scranton, 2004; Afshordi, 2004; Corasaniti et al., 2003; Pogosian et al., 2005; Giannantonio et al., 2008; Ho et al., 2008). This kind of analysis has been performed several times during the past few years, using different CMB data sets and various tracers of clustering. The first detection of the ISW (Boughn & Crittenden, 2004; Boughn & Crittenden, 2005) was obtained by combining the WMAP 1st year CMB data with the hard X-ray background observed by the High Energy Astronomy Observatory-1 satellite (HEAO-1 (Boldt, 1987)) and with the radio galaxies of the NRAO VLA Sky Survey (NVSS (Condon et al., 1998)). The positive correlation with NVSS was later confirmed by the WMAP team (Nolta et al., 2004). Other large scale structure tracers that led to similar positive results were the APM galaxy survey Maddox et al. (1990), the Sloan Digital Sky Survey (SDSS (York et al., 2000)) and the near infrared 2 Micron All Sky Survey eXtendend Source Catalog (2MASS XSC (Jarrett et al., 2000)) (Fosalba et al., 2003; Scranton et al., 2003; Fosalba & Gaztanaga, 2004; Afshordi et al., 2004; Padmanabhan et al., 2005; Cabre et al., 2006).

A somewhat different strategy to attack the problem was recently adopted by other authors, who attempted to seek the ISW signal in spaces other than the pixel space of the maps or the harmonic space of the angular power spectrum (Vielva et al., 2006; McEwen et al., 2007). This approach relies on spherical wavelets as a tool to exploit the spatial localisation of ISW (at large angular scales) in order to get a more significant detection of the effect.

The purpose of the present section is twofold. On one side, we want to perform a further analysis of the CMB-LSS cross-correlation, in order to obtain an independent check on previous results. We combine the recent 3-year release of WMAP CMB sky maps with the radio galaxy NVSS catalogue, and carry out our investigation in the new spherical needlets frame whose properties will be extensively discussed in Chap. 3. This then represents at the same time a check on previous results (Vielva et al., 2006; McEwen et al., 2007) and a significant improvement of the statistical and technical aspects of the problem. On the other side, we follow a rather general approach to dark energy modelling, as first proposed by Hu (1998). Within this framework the phenomenology of dark energy is characterised by three physical parameters: its overall density Ω_{DE}, its equation of state w, and the sound speed c_s^2. This parameterisation has the advantage of being model independent, allowing one to encompass a rather broad set of fundamental models, and of giving a more realistic description of the dark energy fluid, for example accounting for its clustering properties, a feature that was shown to have quite a strong

effect on theoretical predictions (Weller & Lewis, 2003). As shown by Hu & Scranton (2004); Bean & Dore (2004) and Corasaniti et al. (2003) the ISW signature can in principle be able to set constraints on the parameters of this generalised dark energy scenario: however, previous analyses of the ISW from CMB-LSS cross-correlation made a number of unrealistic simplified assumptions on the dark energy component and were only able to either find confirmations for its existence by constraining its density, or to set limits on its equation of state under restrictive hypotheses on its clustering properties (one notable exception being the analysis performed by Corasaniti et al. (2005) which applied a parameterisation similar to ours to make a likelihood analysis of the cross-correlation data points estimated by Gaztanaga et al. (2006)). Our approach is more ambitious, as we attempt a more realistic description of dark energy and derive constraints on the combined set of three above mentioned parameters.

2.1.1 Data

We trace the local distribution of matter in the universe by using the NVSS radio galaxy catalogue (Condon et al., 1998). This dataset contains roughly 1.8×10^6 point sources observed at 1.4 GHz. The flux limit of the catalogue is at ~ 2.5 mJy, resulting in a completeness of about 50%. The survey covers about 80% of the sky, at $\delta > -40°$. We construct a point source map (after removal of about 3×10^5 resolved sources) using the $N_{\rm side} = 64$ HEALPix pixelization (Górski et al., 2005). Such a map has $49\,152$ pixels of about 1 degree side, and guarantees a good sampling of source counts in each pixel. We conservatively exclude from the map all sources with $\delta > -37°$ since the coverage becomes very poor when approaching that value of declination. The final map we use has roughly 35 sources per pixel on average. It was pointed out by Boughn & Crittenden (2002) that there is a declination dependence of the mean source density in the catalogue, since the survey had different integration time in some well-defined constant-declination bands on the sky. As suggested in previous analyses (Nolta et al., 2004; Vielva et al., 2006) we correct for this spurious effect by subtracting the average source count in each constant-declination band.

Our CMB dataset consists of the internal linear combination (ILC) temperature map from the 3 year release of WMAP [1]. This map is produced by combining 5 smoothed temperature maps, with weights chosen in such a way to produce minimal Galactic foreground contamination while maintaining the CMB signal. According to the WMAP team (Hinshaw et al., 2007; Nolta et al., 2004) the ILC map gives a reliable estimate of the CMB signal at low multipoles with negligible instrumental noise. We believe this is appropriate with respect to our goals, since the late ISW effect is expected to peak exactly

[1] Available at http://lambda.gsfc.nasa.gov/

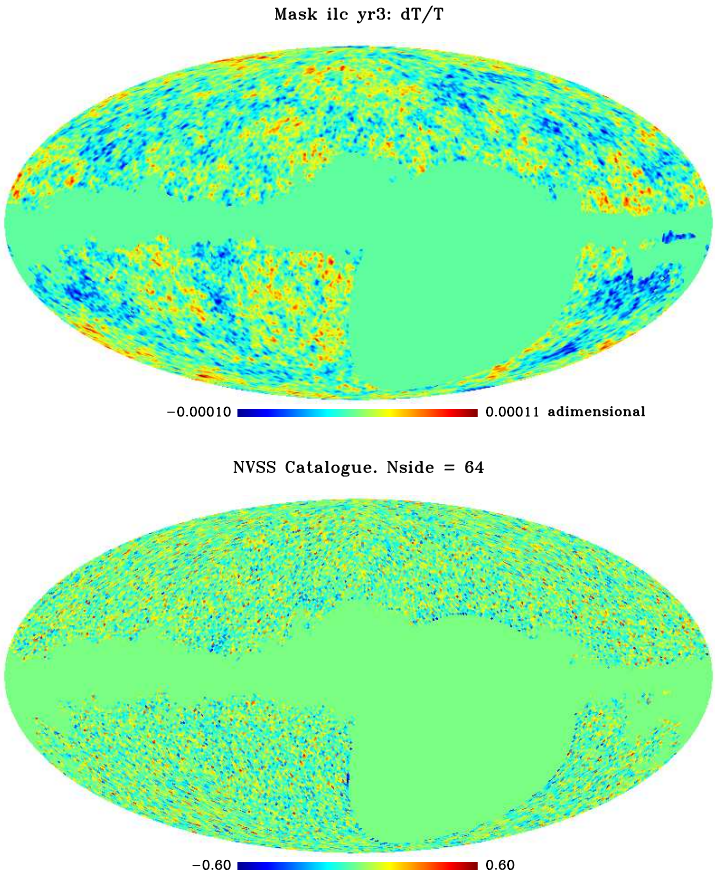

Figure 2.1: CMB and galaxy map used in the analysis.

at such large angular scales. As an additional caution, we mask out the Galactic plane region of the map and bright point sources using one of the templates produced by the WMAP team, namely the conservative KP0 intensity mask.

While the original map ILC was produced at a resolution $N_{\rm side} = 512$ in the HEALPix pixelization scheme (consisting of $12N_{\rm side} = 3,145,728$ pixels) we degrade it to a resolution of $N_{\rm side} = 64$ to match the resolution of the NVSS. This resolution is appropriate for the CMB as well, since we are not interested in the fine-scale details of the map.

A joint mask, including both the KP0 mask and the NVSS declination limit, is applied to both maps used in the analysis. The CMB and galaxy maps are shown in Fig. 2.1.

There is no redshift information for the individual sources in the catalogue. Nonetheless, some knowledge of the dN/dz function is needed to connect the observed source count fluctuation δn to the underlying matter fluctuation $\delta\rho$ (as we will show later). We then use a fit to the dN/dz estimated by Dunlop & Peacock (1990) and already applied to previous analysis of the NVSS catalogue Nolta et al. (2004). Since the fit by Dunlop & Peacock (1990) breaks down at low redshifts, we have approximated it with a Gaussian dN/dZ centred around $z \simeq 0.9$ with a width $\Delta z \simeq 0.8$, and normalised in order to give a

unit integral. The resulting dN/dz used in our analysis is shown in Figure 2.2. We have verified that the difference at low z has negligible effect on the final results.

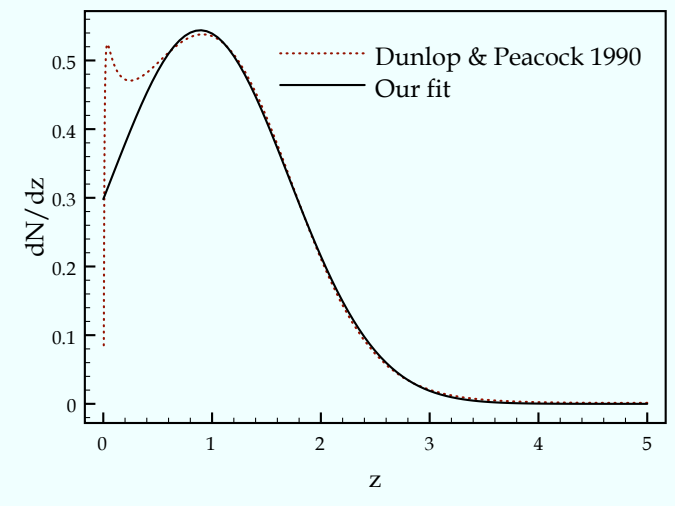

Figure 2.2: The function dN/dz used for the sources in the NVSS in our analysis. The dotted curve is the theoretical model from Dunlop & Peacock (1990), which has a spurious feature due to the breakdown of the fit at low z. The continuous line is the fit adopted in our analysis.

2.1.2 Cross-correlation between CMB and LSS

It is common practice to expand the map of the CMB temperature fluctuations into spherical harmonics (Y_{lm}) as:

$$\delta T = \sum_{lm} a^T_{\ell m} Y_{\ell m}(\theta, \phi) \tag{2.1}$$

in order to extract the angular power spectrum:

$$C^{TT}_\ell = \langle |a^T_{\ell m}|^2 \rangle \tag{2.2}$$

which enters in the two-point auto-correlation function of the CMB as:

$$\begin{aligned} C^{TT}(\alpha) &\equiv \langle \delta T_1 \delta T_2 \rangle = \\ &= \sum_\ell \frac{(2\ell+1)}{4\pi} \omega^2_{T,\ell} C^{TT}_\ell P_\ell(\cos\alpha) \end{aligned} \tag{2.3}$$

where P_l are the Legendre polynomials, α is the angular separation between two given points, and the function $\omega_{T,\ell}$ models the experimental beam response and the pixel window function of the map.

In an equivalent way, given a projected source count map:

$$\delta n = \int dz\, b(z) \frac{dN}{dz} \delta(z) \tag{2.4}$$

(where δ is the underlying matter fluctuation in a given direction, b is the bias parameter, and dN/dz was discussed previously) we can define the source count auto-correlation function:

$$\begin{aligned} C^{NN}(\alpha) &\equiv \langle \delta n_1 \delta n_2 \rangle = \\ &= \sum_\ell \frac{(2\ell+1)}{4\pi} \omega_{N,\ell}^2 C_\ell^{NN} P_\ell(\cos\alpha). \end{aligned} \tag{2.5}$$

Finally, the cross-correlation between CMB and source counts is defined as:

$$\begin{aligned} C^{TN}(\alpha) &\equiv \langle \delta T_1 \delta n_2 \rangle = \\ &= \sum_\ell \frac{(2\ell+1)}{4\pi} \omega_{T,\ell} \omega_{N,\ell} C_\ell^{TN} P_\ell(\cos\alpha) \end{aligned} \tag{2.6}$$

with the usual definition

$$C_\ell^{TN} \equiv \langle a_{\ell m}^T a_{\ell m}^{*\mathrm{N}} \rangle \tag{2.7}$$

The theoretical auto and cross-correlation functions in a given cosmological model can be calculated by numerically integrating the Boltzmann equation for photon brightness coupled to the other relevant equations, including the linear evolution of matter density perturbations and the evolution of gravitational potential fluctuations. We did this by suitably modifying the CMBFast code (Seljak & Zaldarriaga, 1996) in order to output the needed angular power spectra. In particular, we can write the angular cross-spectrum in terms of CMBFast temperature and matter transfer functions (T_l and N_l) as:

$$C_\ell^{TN} = 4\pi \int \frac{dk}{k} \Delta^2(k) T_\ell(k) N_\ell(k) \tag{2.8}$$

where $\Delta^2(k) \equiv k^3 P(k)/2\pi^2$ and $P(k)$ is the primordial power spectrum of fluctuations. Our CMBFast modification also includes a full treatment of a generalised model of dark energy.

Having extracted the needlets coefficients β_{jk} from the CMB and source count maps, which are nothing but the analogous of the spherical harmonics coefficients $a_{\ell m}$ for the expansion on the needlet basis, the cross-correlation estimator in needlets space, β_j, can

be calculated simply through Eq. 3.12:

$$\beta_j^{\rm TN} \equiv \sum_k \frac{1}{N_{\rm pix}(j)} \beta_{jk}^T \overline{\beta}_{jk}^N \tag{2.9}$$

where $N_{\rm pix}(j)$ is the number of pixels in the pixelization scheme. The theoretical predictions for $\beta_j^{\rm TN}$ and the corresponding error bars can be computed from the expected C_l^{TN} and their variance which lead to:

$$\beta_j^{\rm TN} = \sum_\ell \frac{(2\ell+1)}{4\pi} \left[b\left(\frac{\ell}{B^j}\right)\right]^2 B_{T,\ell} B_{N,\ell} C_\ell^{TN} \tag{2.10}$$

$$\Delta\beta_j^{\rm TN} = \left(\sum_\ell \frac{(2\ell+1)}{16\pi^2} \left[b\left(\frac{\ell}{B^j}\right)\right]^4 \left(\left(C_\ell^{TN}\right)^2 + C_\ell^T C_\ell^N \right) \right)^{1/2} \tag{2.11}$$

More details on needlet estimators and their properties are provided in Chapter 3.

2.1.3 Results

ISW detection

In Figure 2.3 we show the cross-correlation signal in needlet space extracted from the WMAP and NVSS data. The data points shown in the Figure were obtained following the above described procedure, applying Equation 2.9. We chose the value $B = 1.5$ in the wavelet construction for our analysis. The excess signal peaks at value $6 < j < 9$, corresponding to angular scales between 2° and 10°, as expected from theoretical studies (Afshordi, 2004). We recall that the conversion between j and the actual angular scale can is easily made through the relation $\ell_{\rm c} = B^j$.

In order to check that the observed signal was not produced by casual alignment of sources in the NVSS catalogue with the CMB pattern at decoupling, we produced $1,000$ Monte Carlo simulations of the CMB sky with an underlying theoretical fiducial LCDM model corresponding to the WMAP 3 year best fit. The resulting maps were processed through our analysis pipeline, and the cross-correlation with the real NVSS map was calculated for each simulated data set. Figure 2.3 shows the resulting average cross-correlation signal (continuous line), which is basically zero on all scales. The standard deviation of the simulations is also shown in the same Figure (shaded area). These errors, calculated through the Monte Carlo procedure, are consistent with the analytical estimates of Eq. 2.11. We want to stress that the error bars computed through CMB Monte Carlo simulations only are accurate enough to our purpose as demonstrated by Giannantonio et al. (2008) who produced mock galaxy distribution maps.

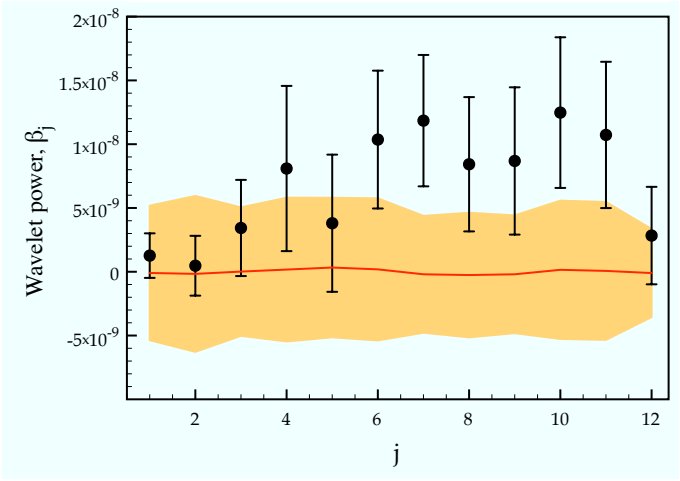

Figure 2.3: The needlet cross-correlation power spectrum β_j of the WMAP and NVSS maps. The points represent the signal extracted from the real data, with error bars given by Eq. 2.11. The continuous line is the average of the cross-correlation power spectra obtained when 1,000 simulated CMB fiducial data sets are correlated with the real NVSS map: this measures the level of correlation expected from casual alignment. The shaded area is the 1σ dispersion of the simulated spectra.

The cross-correlation signal extracted from the data is significantly higher than the expectation value of the simulated data. To quantify the statistical significance of the detection, we computed the quantity $X^2 \equiv \sum_j (\beta_j^{\rm obs} - \langle \beta_j^{\rm sim} \rangle)^2 / \Delta\beta_j^2$. We found $X^2 = 29.8$. Assuming X^2 is distributed as a χ^2 with 12 degrees of freedom (corresponding to our 12 data points), we can exclude that the β_j were produced under the null hypothesis with 99.7% confidence. We stress again the fact that the very nature of needlets guarantees that the correlation between adjacent data points is very low, even in the presence of sky cuts. See Sec. 3.2 and Tab. 3.1-3.2 for an detailed explanation.

Consequences for dark energy models

We have compared the cross-correlation estimated from the data with the theoretical predictions in order to set constraints on dark energy models. Following the phenomenology described in Hu (1998), we have modelled the dark energy component as a fluid characterised by its density parameter, Ω_{DE}, its equation of state, $w = p/\rho$, and the sound speed $c_s^2 = \delta p / \delta\rho$. The latter, needs not be the usual adiabatic one, but also accounts for an entropic sound speed, so that $c_s^2 \neq \dot{p}/\dot{\rho}$. For a more detailed discussion see Sec. 2.3. We have considered the above three quantities as the free parameters of our analysis. All the other cosmological parameters were held fixed at the best fit values estimated using the WMAP 3 year data: $\Omega = 1$, $H_0 = 73$ km/s/Mpc, $\Omega_{\rm b} = 0.042$, $\tau = 0.088$, $A = 0.68 \rightarrow \Delta^2_{\mathcal{R}} \simeq 2.35 \times 10^{-9}$ (or $\sigma_8 = 0.74$), $n_s = 0.951$ (Spergel et al., 2007). When modeling the NVSS catalogue, we adopted a constant bias parameter $b = 1.6$, a

value suggested in Dunlop & Peacock (1990) and already used in previous analysis, e.g. Boughn & Crittenden (2004); Boughn & Crittenden (2005); Nolta et al. (2004); Vielva et al. (2006).

We have computed the theoretical expectation for the cross-correlation by using Eq. 2.9 and the output of our modified `cmbfast` code. Our calculation fully takes into account the clustering properties of dark energy. We restricted our analysis to two different values of c_s^2 corresponding to the limiting cases describing a scalar field behaviour ($c_s^2 = 1$) and a matter behaviour ($c_s^2 = 0$).

The main results of our analysis are summarised in Figure 2.4 where we plot the joint constraints on the dark energy parameters Ω_{DE} and w for the two cases of sound speed considered here, and in Figure 2.5, where we show the separate marginalized likelihoods for Ω_{DE} and w. The likelihood were computed under the Gaussian hypothesis: we argue that even though it may be fail in representing the true likelihood for the dark energy model, it is nonetheless a first reasonable approximation useful to extract the parameters of the model and infer dark energy properties.

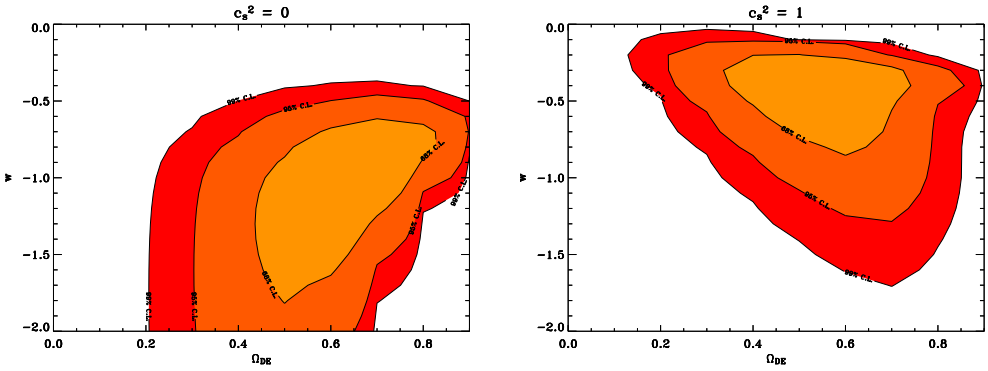

Figure 2.4: Constraints at 68%, 95% and 99% confidence level in the Ω_{DE}—w plane. The left panel was obtained under the hypothesis that the dark energy speed of sound is $c_s^2 = 0$; the right panel was obtained for $c_s^2 = 1$.

The first conclusion we can draw from our analysis is that the evidence for non zero dark energy density is rather robust: we find $0.32 \leq \Omega_{DE} \leq 0.78$ for $c_s^2 = 1$ and $0.36 \leq \Omega_{DE} \leq 0.81$ for $c_s^2 = 0$, both at 95% confidence level. A null value of Ω_{DE} is excluded at more than 4σ (see Figure 2.5, upper panel), independently of c_s^2. When we model the dark energy as a cosmological constant (i.e. we assume the value $w = -1$ for its equation of state), the bounds on its density shrinks to $0.41 \leq \Omega_{DE} \leq 0.79$ at 95% confidence level.

On the other hand, the constraints on w are strongly influenced by the assumed value of c_s^2, because of the different clustering behaviour of dark energy (Figure 2.5, right panel). In particular, we find that the value of the equation of state which corresponds to

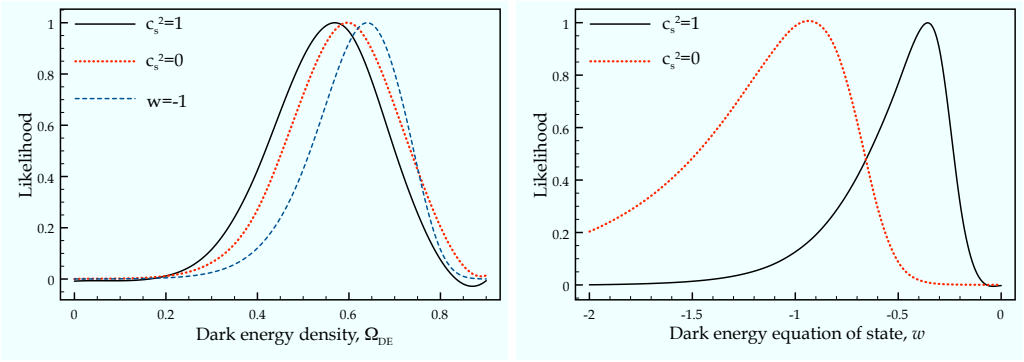

Figure 2.5: Marginalized likelihood function for the dark energy density Ω_{DE} (left panel) and equation of state w (right panel). In each panel, the continuous curve was obtained under the hypothesis that $c_s^2 = 1$, while the dotted curve is for $c_s^2 = 0$.

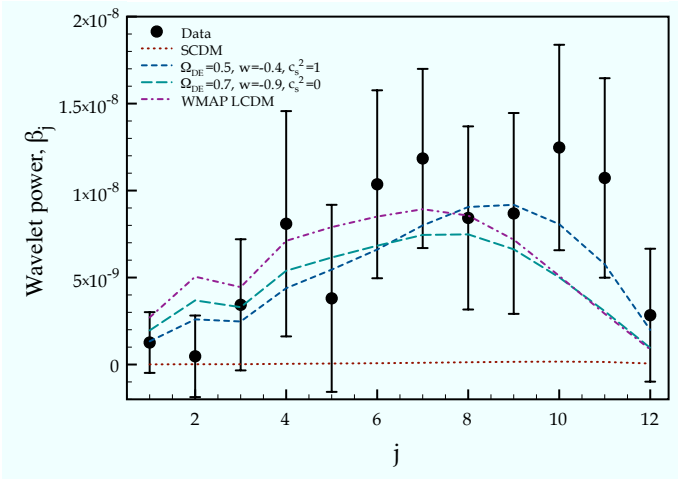

Figure 2.6: The cross-correlation data points estimated in our analysis (big dots), with their errors, are shown together with the theoretical predictions for a standard CDM model (without dark energy, dotted curve), the best fit under the hypothesis that $c_s^2 = 1$ (short-dashed curve), the best fit under the hypothesis that $c_s^2 = 0$ (long-dashed curve) and the LCDM ($w = -1$) that best fits the WMAP 3 year data (dot-dashed curve).

a cosmological constant ($w = -1$) is well within the 95% c.l. when we assume $c_s^2 = 0$. In this case, we can only put an upper bound at 95% c.l.: $w \leq -0.54$. When $c_s^2 = 1$ is assumed, we find that phantom models are excluded and that the cosmological constant case performs comparatively worse than models with larger values of w. Our bounds at 95% c.l. are $-0.96 \leq w \leq -0.16$. However, we emphasise that, for values of $\Omega_{DE} \sim 0.7$, models with $w = -1$ are a good fit to the data, as it is evident from Figure 2.4 (lower panel). In fact, the LCDM WMAP best fit (with $\Omega_{DE} = 0.76$ and $w = -1$) has $\chi^2 = 9.35$, with 12 data points. The predicted cross-correlation for some dark energy models is shown together with our data points in Figure 2.6.

We have analysed the WMAP 3 year CMB temperature data, in conjunction with the NVSS radio galaxy survey, and found further evidence of a correlation between the

CMB fluctuation pattern and the local distribution of matter, consistent with an ISW effect taking place at a late epoch of cosmic evolution. Our findings are based on a new construction of spherical wavelets that has a number of advantages with respect to previous studies. The presence of a correlation between the CMB and the LSS is established with a high level of confidence.

We have also improved the treatment of the dark energy component, introducing a more general parameterisation than those used in similar earlier analyses. Quite interestingly, we find that although the case for a non zero dark energy contribution to the total density is compelling and robust, the constraints on w do depend on the assumed clustering properties of the dark energy component, namely its sound speed c_s^2. Phantom models, and also the ordinary cosmological constant case $w = -1$, perform worse when a quintessence behaviour $c_s^2 = 1$ is assumed. This is due to the fact that there exist models with $w \sim -0.4$ which predict more correlation at larger angular scales ($\theta \sim 2^\circ$).

Whether this is an indication of interesting physics taking place between the dark energy and dark matter components is a subject that requires further investigation. Clearly, the observation of ISW is proving quite promising as a tool to answer the questions arising from the mysterious nature of dark energy. While the CMB data have reached a great degree of accuracy on the angular scales that are more relevant for the detection of ISW, deeper redshift surveys and better catalogues can, in the future, improve the tracing of the local matter distribution, thus allowing us to reduce the errors on the cross-correlation determination.

An exhaustive updated analysis of the correlation between CMB and LSS is provided by Giannantonio et al. (2008) and Ho et al. (2008). We want to stress that a key ingredient still missing in these analyses is the correct treatment of the galaxy bias. The bias is a parameter, or more generally a function dependent both on redshift and scale, which describes how the baryons trace the dark matter, and then incorporates all the complexity of the baryons interactions. Raccanelli et al. (2008) have addressed this issue studying the effect of a time dependent bias on the cross-correlation function for an underlying ΛCDM model. A step further would imply a complete MCMC analysis, allowing both dark energy and bias parameter to vary. A preliminary study has been performed by Schaefer et al. (2009). The bias investigation is one of the hottest topics in cosmology since it has been proven to be extremely important in the context of non-Gaussianity too (Smith et al., 2009; Wands & Slosar, 2009; Slosar et al., 2008)

Motivated by our findings, which confirm at a high significance level the presence of a mysterious component which drives the acceleration of the Universe expansion, we study in the next two sections a couple of models which try to describe in a unified manner both dark matter and dark energy. In Sec. 2.2 this is achieved by means of a coupling between

the two components, whereas in Sec. 2.3 we propose a unique description based on a peculiar equation of state for the fluid.

2.2 Late universe dynamics with scale-independent linear couplings in the dark sector

As discussed in the introduction to this chapter, several cosmological observations such as SuperNovae (SNe) (Riess et al., 2009; Riess, 2007; Riess et al., 1998; Perlmutter et al., 1999), baryon acoustic oscillations (BAO) (Percival et al., 2009, 2007a; Eisenstein et al., 2005), Integrated Sachs-Wolfe (ISW) measurements (Giannantonio et al., 2008; Pietrobon et al., 2006; Ho et al., 2008), suggest the Universe expansion is accelerating. To explain this acceleration, cosmologists invoke the existence of an unknown dark component (Copeland et al., 2006), whose general properties have to be inferred by observations, i.e. a procedure which relies on indirect evidences. One possibility is that the dark sector is accounted for, partly or in full, by a modified gravity theory[2], while a more conventional approach is to assume that gravity is well described by general relativity, with the dark sector made up of an unusual energy momentum tensor.

In the currently prevailing scenario, the dark sector consists of two distinct contributions. One component, *cold dark matter* (CDM), accounts for about one third of the critical density (Percival et al., 2007b, 2009) and is needed to explain the growth of inhomogeneities that we observe up to very large scales, as well as a host of other cosmological observations which goes from galactic scales, to clusters of galaxies, to redshift surveys. The other contribution, dubbed *dark energy*, accounts for the remaining two thirds of the critical density, and it is required to explain the observed late time acceleration of the universe expansion (Perlmutter et al., 1999; Riess, 2007; Riess et al., 2009). CDM can be modelled as a pressureless perfect fluid, representing unknown heavy particles, collisionless and cold, i.e. with negligible velocity dispersion. In its simplest form, dark energy consists of vacuum energy density, i.e. a cosmological constant Λ. Taken together, Λ and CDM make up the the so-called concordance ΛCDM model (Spergel et al., 2003; Tegmark et al., 2004). This simple model fits observations reasonably well, but lacks a sound explanation in terms of fundamental physics, and a number of alternatives have been proposed. In general, dark energy can be modelled as a perfect fluid with an equation of state (EoS from now on) that violates the strong energy condition (namely $\rho + 3p > 0$) (Visser, 1997), such that it can dominate at late times and have sufficiently negative pressure to drive the observed accelerated expansion. Scalar fields can also be formally represented as perfect fluids (see e.g. Bruni et al. (1992) and refs. therein). In a more exotic version, dubbed *phantom energy* (Caldwell, 2002; Caldwell et al., 2003), the EoS also violates the null energy condition ($\rho + p > 0$) (Visser, 1997), leading to the growth in time of the energy density with the cosmic expansion. Finally,

[2] See e.g. Durrer & Maartens (2008); Durrer & Maartens (2008) and other articles in the same special issue on dark energy.

another rather radical alternative to ΛCDM is to assume a single unified dark matter (UDM), able to mimic the essential features of ΛCDM which are necessary to build a viable cosmology. For example, in Balbi et al. (2007) we have considered observational constraints on a UDM model with an "affine" EoS, i.e. such that the pressure satisfies the affine [3] relation $P = P_o + \alpha\rho$ with the energy density (Ananda & Bruni, 2006; Ananda & Bruni, 2006). This model is a one parameter (α) generalisation of ΛCDM, with the latter recovered for $\alpha = 0$. There is no need to assume *a-priori* a Λ term in Einstein equations, because the EoS $P = P_o + \alpha\rho$ leads to an effective cosmological constant with $\Omega_\Lambda = -8\pi G P_o/[3H_o^2(1+\alpha)]$. The problem is thus shifted from justifying a Λ term in Einstein equations to that of justifying the assumed EoS: a possible justification of this affine model can be given in terms of scalar fields, either of quintessence or k-essence type (Quercellini et al., 2007). This type of model escapes typical constrains on many UDM models (Sandvik et al., 2004) (but cf. e.g. Gorini et al. (2008)) because, for a given homogeneous isotropic background expansion, it allows multiple phenomenological choices for the speed of sound of the perturbations (Pietrobon et al., 2008) (see also for detailed discussion Sec. 2.3).

In models of the dark sector consisting of two components, dark matter and dark energy are usually assumed to interact only through gravity, but they might exhibit other interactions without violating observational constraints (Kunz, 2007). Exploiting this degeneracy, here we depart from the standard scenario, and assume a cosmological model where the dark sector is made up of two coupled dark components, each described as a perfect fluid with its own constant EoS parameter w. This choice allows for the possibility that the observed evolution of the universe, although reasonably well explained by the ΛCDM model, is actually due to the dynamics of two rather general coupled components, possibly alleviating the so-called "coincidence problem", $\Omega_\Lambda \approx \Omega_{CDM}$, typical of the standard model (Copeland et al., 2006).

We first characterise the dynamics of our cosmological model with the two general coupled components, taking into account general forms of interaction, parameterised in terms of a late time function Q linear in the energy densities, Eqs. (2.16-2.17). To this end we will use standard dynamical system techniques (Arrowsmith & Place, 1992; Wainwright & Ellis, 1997), which are now rather common in the analysis of cosmological models, see e. g. Wands et al. (1993); Bruni (1993); Amendola et al. (1993); Bruni & Piotrkowska (1994); Bruni et al. (1995a,b) and Copeland et al. (1998); Ananda & Bruni (2006); Ananda & Bruni (2006); Böhmer et al. (2008). To our knowledge, such an exhaustive analysis has not been carried out yet, although several sub-cases have been considered Majerotto et al. (2004); Olivares et al. (2006); Guo et al. (2007); Böhmer et al.

[3] The term *affine* is a technical word used in maths to define a general linear coordinate transformation.

(2008); Quartin et al. (2008); Pettorino & Baccigalupi (2008); Barrow & Clifton (2006). In our study, we restrict ourselves to the evolution of a homogeneous, isotropic cosmological background, leaving aside the question of what the effects of coupling could be in anisotropic models (Ananda & Bruni, 2006), or when general perturbations are present (Valiviita et al., 2008; Dunsby et al., 1992). It is however worth noticing that, thanks to the particular form of coupling we choose, our analysis of the dynamics of the two components is valid in any theory of gravity, because it is based only on the conservation equations, and not on specific field equations.

Secondly, as a way to gain some physical insight on the likelihood of some specific coupling models, we also explore the constraints on the predicted luminosity distance modulus derived from type Ia Supernovae observations, using a Monte Carlo Markov Chain (MCMC) approach. Needless to say, this is not intended as a full-fledged cosmological parameter estimation for these models, but only as a first exploration of the parameter space to rule out those models which are manifestly in contrast with observations. This analysis requires the use of the Friedmann equation, hence general relativity is assumed as the valid theory of gravity.

2.2.1 Dynamics of dark components

Linear scale-free coupling

In general relativity, assuming a a flat Robertson-Walker universe, the dynamics is subject to the Friedmann constraint

$$H^2 = \frac{8\pi G}{3}\,\rho_T\,, \tag{2.12}$$

where ρ_T is the total energy density of the various components. Beside baryons and radiation, ρ_T includes any other component contributing to the dark sector, i.e. that part of the total energy-momentum tensor that in the context of general relativity is needed to explain the observed universe, in particular the CMB (Spergel et al., 2007; Dunkley et al., 2009), structure formation (Springel et al., 2006; Khalil & Munoz, 2002) and the late time acceleration of the expansion (Riess et al., 1998; Perlmutter et al., 1999; Riess, 2007; Riess et al., 2009; Eisenstein et al., 2005; Percival et al., 2007a; Pietrobon et al., 2006; Ho et al., 2008; Giannantonio et al., 2008). The dynamics itself is described by the evolution of the Hubble expansion scalar $H = \dot{a}/a$, given by the Raychaudhuri equation

$$\dot{H} = -H^2 - \frac{4\pi G}{3}(1 + 3\,w_T)\rho_T. \tag{2.13}$$

This is coupled to the evolution equations for the energy density of each of the matter components contributing to ρ_T. Since $\dot{H} + H^2 = \ddot{a}/a$, with $a(t)$ the usual metric

scale-factor (which we assume normalised to its present value), acceleration is achieved whenever $w_T = P_T/\rho_T < -1/3$, as it is well known.

The standard ΛCDM model assumes two dark components: the pressureless cold dark matter (CDM), with $w_{DM} = 0$, and the cosmological constant Λ with $w_\Lambda = -1$. CDM is needed to fill the gap between the baryon abundance and the amount of matter that is needed to explain the rotation curves of galaxies and structure formation in general, as well as to allow for a vanishing curvature model. In the context of general relativity, and under the Robertson-Walker homogeneous and isotropic assumption (see e.g. Célérier (2007) for alternatives), a cosmological constant Λ is the simplest possible form of dark energy (DE) needed to generate the observed low redshift acceleration. While this simple scenario is preferred from the point of view of model comparison and selection (Balbi et al., 2007), because of the low number of parameters, from a theoretical perspective it is oversimplified, and it is worth exploring alternatives, even if purely phenomenological.

Here we shall consider two general coupled dark components with energy densities ρ_A and ρ_B. Since we want to introduce a rather general type of coupling, focusing our analysis on its effects, we shall assume the simplest possible form for the EoS of these two dark components, i.e. we will assume that the EoS parameters w_A and w_B are constant. On the other hand, we shall not *a priori* restrict our study to the sub-class of models where one of the two components represents CDM with, for instance, $w_B = 0$.

Due to the presence of the coupling, the two dark components satisfy the balance equations

$$\dot{\rho_A} + 3H(1+w_A)\rho_A = Q \tag{2.14}$$

$$\dot{\rho_B} + 3H(1+w_B)\rho_B = -Q\,. \tag{2.15}$$

Even assuming the linear form for the coupling Q given in Eqs. 2.16 and 2.17 below, this model allows us to explore a large number of alternatives. Here we will focus on models for the homogeneous and isotropic background expansion, assuming that for those models that will fit current observational data it might always be possible to construct an appropriate perturbative scheme allowing for structure formation, for instance by assuming a vanishing effective speed of sound in one component.

The coupled dark components ρ_A and ρ_B could be in principle be taken to represent DE only, i.e. they could be two extra dark components contributing to ρ_T in (2.12), *in addition* to CDM. Leaving aside this possibility, and ignoring baryons and radiation as we will do in this Section, the sum of Eqs. (2.14-2.15) gives the conservation equation for $\rho_T = \rho_B + \rho_A$. A positive coupling term Q corresponds to a transfer of energy from ρ_B to ρ_A, and vice versa, but in general Q doesn't need to have a definite sign.

An interaction term between two components has been considered several times in the literature, starting from Wetterich (1988, 1995), Wands et al. (1993); Copeland et al. (1998) in scalar field models, and has been analysed in dark energy models by Amendola (2000); Amendola & Tocchini-Valentini (2001); Amendola & Quercellini (2003, 2004), and for example recently in Majerotto et al. (2004); Olivares et al. (2006); Guo et al. (2007); Böhmer et al. (2008); Quartin et al. (2008); Pettorino & Baccigalupi (2008); de la Macorra (2008); Manera & Mota (2006).

The coupling term Q can take any possible form $Q = Q(H, \rho_A, \rho_B, t)$. Here we shall consider the case of an autonomous (t independent) coupling with a factorized H dependence

$$Q = \frac{3}{2} H q(\rho_A, \rho_B). \tag{2.16}$$

As we shall see below, with this assumption the effects of the coupling on the dynamics of ρ_A and ρ_B become effectively independent of the evolution of the Hubble scale H. For this reason, we may call this a "scale-independent" coupling. This choice has been often adopted in literature mainly because it simplifies the computation and allows to investigate several phenomenological models which display a coupling between the dark components. Furthermore, with the decoupling of the dynamics of the two dark components from that of H, the analysis of the next section is valid in any theory of gravity, because it is based on the conservation equations only: we don't need to use Eqs. 2.12-2.13, i.e. the field equations of general relativity. Finally, we note that any coupling of this type can be approximated at late times by a linear expansion:

$$q = q_0 + q_A \rho_A + q_B \rho_B \ , \tag{2.17}$$

where q_A, q_B are dimensionless coupling constants, and q_0 is a constant coupling term with dimensions of an energy density[4]. In the following we shall analyse the dynamics arising from this general linear scale-independent coupling. Obvious sub-cases are: $q \propto \rho_T$ ($q_0 = 0, q_A = q_B$); $q \propto \rho_A$ ($q_0 = 0, q_B = 0$); etc. We will come back to this in more detail in the next Section. Linear couplings have been frequently analysed in literature (Wetterich, 1995; Amendola, 2000; Majerotto et al., 2004; Guo et al., 2007),Multamaki et al. (2007); Mainini & Bonometto (2007); Böhmer et al. (2008); Quartin et al. (2008) both for mathematical simplicity, since they retain the linearity of system 2.14-2.15 with no coupling, and because they can arise from string theory or Brans-Dicke-like Lagrangians after a conformal transformation of the metric.

[4]Strictly speaking, an expansion about today would lead to $q = \hat{q}_0 + \hat{q}_A(\rho_A - \rho_{A0}) + \hat{q}_B(\rho_B - \rho_{B0})$, but constants can always be re-defined in order to put the coupling q in the form 2.17.

2.2.2 Analysis of the scale-free linear dynamics

The linear dynamical system

In order to proceed with the analysis of the dynamics of the dark components, let us change variables, using the total density $\rho_T = \rho_B + \rho_A$ and the difference $\Delta = \rho_B - \rho_A$. We also set

$$w_+ = (w_B + w_A)/2\,, \qquad w_- = (w_B - w_A)/2\,, \tag{2.18}$$

$$q_+ = (q_B + q_A)/2\,, \qquad q_- = (q_B - q_A)/2\,. \tag{2.19}$$

One reason for this choice is that ultimately the evolution of ρ_T is the one that governs the general expansion law through Eq. 2.12 and 2.13. In addition, thanks to the particular form of the coupling (Eq. 2.16) and assuming $H > 0$, the dynamics can be made explicitly scale-independent, eliminating H by adopting $N = \ln(a)$, the *e*-folding, as the independent variable. Then, denoting with a prime the derivative with respect to N, the system (2.14-2.15) is transformed into

$$\rho_T' + 3\rho_T(1 + w_+) + 3w_-\Delta = 0 \tag{2.20}$$

$$\Delta' + 3\Delta(1 + w_+) + 3w_-\rho_T = -3(q_+\rho_T + q_-\Delta + q_0). \tag{2.21}$$

An effective EoS parameter w_{eff} is implicitly defined from Eq. 2.20: when $w_- = 0$ the two EoS coincide giving rise to a constant $w_{eff} = w_+ = w_A$ and ρ_T scales accordingly, as a standard barotropic perfect fluid, but in general

$$w_{eff} = w_+ + w_-\frac{\Delta}{\rho_T} \tag{2.22}$$

changes with time. Notice that we can also define, using (2.16-2.17) in (2.14), the effective EoS parameters for the two components:

$$w_{Aeff} = w_A - \frac{q_0 + q_B\rho_B}{2\rho_A} - \frac{q_A}{2}\,, \tag{2.23}$$

$$w_{Beff} = w_B + \frac{q_0 + q_A\rho_A}{2\rho_B} + \frac{q_B}{2}\,. \tag{2.24}$$

From now on we will characterise the cosmological evolution of any of the energy densities as standard/phantom behaviour. As mentioned in the introduction, standard/phantom respectively correspond to an energy density which is either a decreasing or an increasing function of time (the scale factor or the *e*-folding *N*). The phantom behaviour arises in the presence of coupling from an effective EoS parameter < -1, which corresponds to the violation of the null energy condition (Visser, 1997) for that given energy density.

Thus, it follows from Eq. 2.22 and 2.23-2.24 that we can have a phantom behaviour in the total energy density ρ_T as well as in one or both of the single components ρ_A and ρ_B, and that in principle the effective EoS parameter of each of these can pass through the -1 value, from phantom to standard or vice versa. On the other hand, we will also refer to constant parameters such as w_A and w_B as having a standard/phantom value, respectively $w_{A/B} > -1$ or $w_{A/B} < -1$, because the corresponding fluid would evolve in that way in the case of no coupling.

We will also refer to an "affine" evolution. As said in the introduction, for an uncoupled component with energy density ρ this arises from an affine EoS of the form $P = P_o + \alpha\rho$. Inserted in the energy conservation equation this leads to

$$\rho = \rho_\Lambda + \rho_{0M} a^{-3(1+\alpha)} \,. \tag{2.25}$$

Therefore, starting from the Friedmann equations 2.12-2.13 with no cosmological constant term, the affine EoS and energy conservation lead to an effective cosmological constant ρ_Λ plus an effective matter-like component with constant EoS parameter α (a barotropic perfect fluid) and today's density ρ_{0M} (cf. Ananda & Bruni (2006); Ananda & Bruni (2006); Balbi et al. (2007); Quercellini et al. (2007) for a detailed analysis of the cosmological dynamics arising in this case). As we will see, it turns out that there are solutions of the system (2.20-2.21) that evolve according to Eq. 2.25.

In order to proceed with the analysis of Eqs. 2.20-2.21 using standard dynamical system techniques (Arrowsmith & Place, 1992), it is convenient to write it as

$$\mathbf{X}' = \mathbf{J}\,\mathbf{X} + \mathbf{C}\,, \tag{2.26}$$

where the phase-space state vector $\mathbf{X}$ and the constant $\mathbf{C}$ are

$$\mathbf{X} = \begin{pmatrix} \rho_T \\ \Delta \end{pmatrix}, \quad \mathbf{C} = \begin{pmatrix} 0 \\ -3q_0 \end{pmatrix}, \tag{2.27}$$

and the matrix of coefficients $\mathbf{J}$ is given by

$$\mathbf{J} = \begin{pmatrix} -3(1+w_+) & -3w_- \\ -3(w_- + q_+) & -3(1+w_+ + q_-) \end{pmatrix}. \tag{2.28}$$

Fixed points, if they exist, are solutions $\mathbf{X}_*$ of the equation $\mathbf{J}\,\mathbf{X}_* + \mathbf{C} = \mathbf{0}$ and, given that the system (2.26) is linear, $\mathbf{J}$ is also the Jacobian of the system at these fixed points. These fixed points correspond to constant values of ρ_T and Δ and in turn of ρ_A and ρ_B, that is to the emergence of an effective cosmological constant (when $\rho_T \neq 0$, see below). Every constant form of energy is indeed alike the cosmological constant Λ, and plays

exactly the same cosmological role: when it dominates the evolution of the background, it drives an exponentially accelerated expansion, with an effective EoS parameter close to -1. Notice that - unlike the case with no coupling - there is no *a priori* guarantee from the equations above that ρ_A and/or ρ_B, as well as ρ_T, will always be non-negative. However, one has to keep in mind that ρ_T must be non-negative because of the Friedmann constraint (Eq. 2.12). This means that if ρ_T is vanishing for some value of N (a), then at that point the assumption $H > 0$, on the basis of which Eq. 2.26 is derived, is violated, and the solutions of Eq. 2.26 no longer correspond to solutions of the original coupled system of Eqs.2.13 and 2.14-2.15.

We refer to App. **??** for the solution of the linear system and a detailed discussion of its properties. An insight of the physical consequences of the stability properties of the system Eq. 2.26 may be achieved considering the solution of the second order differential equation for $\rho_{\rm T}$, which can be easily derived from the linear system. The details of the computation are fully described in App. **??**; here we report the main results, useful to understand the investigation of the parameter space of the model discussed in the following sections. The total energy density can be described as:

$$\rho_T'' - \mathrm{tr}(\mathbf{J})\,\rho_T' + \det(\mathbf{J})\,\rho_T = 9 w_- q_0,$$
$$\rho_T = \rho_{T+} a^{-3(1+\beta_+)} + \rho_{T-} a^{-3(1+\beta_-)} + \rho_\Lambda,$$

where $\beta_\pm = \beta_0 \pm \sqrt{D}/3$, with $\beta_0 = w_+ + q_-/2$ and $D = 9\left[\left(\frac{q_-}{2}\right)^2 + w_-(q_+ + w_-)\right]$. The total energy density is made up of two evolving components and an effective cosmological constant, ρ_Λ, function of the parameters of the model, which may arise according to the dynamics of the system.

Here we focus on a less general solution, for which we perform a parameter space viability study through a Monte Carlo approach.

2.2.3 Analysis of specific couplings

Dynamics of density parameters

Introducing an interaction between two fluids can lead to interesting solutions for the energy densities, like attractor points in the phase space where the contributions of the two fluids to the total energy density are constants. In these points the value of the normalised energy densities depends only on the parameters of the model and, since they are attractors, they are reached from a wide range of initial conditions, thereby alleviating the coincidence problem. These are usually called “scaling solutions” (Wands et al., 1993; Copeland et al., 1998) and are characterised by constant fractions of the energy density parameters, namely $\Omega_{A,B} = \rho_{A,B}/(3H^2)$ (in units $8\pi G = 1$, $c = 1$).

In order to analyse the dynamics of the system, let us define the new variables:

$$x = \frac{\rho_A}{3H^2}; \qquad y = \frac{\rho_B}{3H^2}; \qquad z = \frac{\rho_\Lambda}{3H^2}, \tag{2.29}$$

where together with the coupled fluids we also include radiation to include the era when it's the dominating component, when initial conditions are usually set. Note that $x = \Omega_A$, $y = \Omega_B$ and Ω_γ are constrained by $x + y + \Omega_\gamma = 1$; z is the energy density parameter of the total effective cosmological constant, and we neglect the baryons contribution, which is always subdominant. The system (2.14-2.15) then becomes

$$\begin{aligned} x' &= -x\Big[3(1 + w_+ - w_-) + 2\frac{H'}{H}\Big] \qquad (2.30)\\ &+ \frac{3}{2}\Big[(q_+ - q_-)x + (q_+ + q_-)y + \frac{\det(\mathbf{J})}{9w_-}z\Big] \\ y' &= -y\Big[3(1 + w_+ + w_-) + 2\frac{H'}{H}\Big] \qquad (2.31)\\ &- 3\Big[(q_+ - q_-)x + (q_+ + q_-)y + \frac{\det(\mathbf{J})}{9w_-}z\Big] \\ z' &= -2z\frac{H'}{H}, \qquad (2.32) \end{aligned}$$

where

$$\begin{aligned} \frac{H'}{H} &= -1 - \frac{1}{2}\left[x(1 + 3(w_+ - w_-))\right. \\ &\left. + y(1 + 3(w_+ + w_-)) + 2(1 - x - y)\right] \end{aligned} \tag{2.33}$$

is a rewriting of the Raychaudhuri equation (2.13) for the Hubble expansion scalar.

The fixed points, namely the points satisfying $x' = y' = z' = 0$, are presented in Table 2.1, labelled by capital letters, together with the corresponding eigenvalues. To the best of our knowledge, this is the first complete analysis of the dynamics of a three components cosmological system where two of the barotropic fluids are coupled via a general linear coupling function of the form (2.17). The effective EoS parameters at each of the fixed points $w_{eff} = p_{tot}/\rho_{tot}$ is also listed, where $\rho_{tot} = \rho_A + \rho_B + \rho_\gamma$ and therefore $w_{eff} = (w_+ - w_-)x + (w_+ + w_-)y + \Omega_\gamma/3$.

All the fixed points shown in Table 2.1 exist for $w_- \neq 0$, when the EoS parameters of the two fluids are the different. The only physically reasonable fixed point for system (2.20-2.21) corresponding to $w_- = 0$ is Case 2a (see Sec. **??**), where $\det(\mathbf{J}) = 0$, and we end up with an infinite number of solutions, characterised by $w_A = w_B = -1$.

The fixed points A corresponds to the radiation dominated era, while B, C and D represent epochs that are dominated by the two fluids, as can be inferred by looking at the values of the effective equation of state parameter, w_{eff}. In particular, at the fixed

Points	x	y	z	w_{eff}	λ_x	λ_y	λ_z
A	0	0	0	$\frac{1}{3}$	4	$1-3\beta_+$	$1-3\beta_-$
B	$-\frac{q_--2w_-+2\sqrt{D}/3}{4w_-}$	$\frac{(q_--2w_-+2\sqrt{D}/3)(q_++2w_-+2\sqrt{D}/3)}{4w_-(q_++q_-)}$	0	β_+	$3(1+\beta_+)$	$-\frac{1-3(\beta_+-2\beta_-+q_-)+\sqrt{F_+}}{2}$	$-\frac{1-3(\beta_+-2\beta_-+q_-)-\sqrt{F_+}}{2}$
C	$-\frac{q_--2w_--2\sqrt{D}/3}{4w_-}$	$\frac{(q_--2w_--2\sqrt{D}/3)(q_++2w_--2\sqrt{D}/3)}{4w_-(q_++q_-)}$	0	β_-	$3(1+\beta_-)$	$-\frac{1-3(\beta_--2\beta_++q_-)+\sqrt{F_-}}{2}$	$-\frac{1-3(\beta_--2\beta_++q_-)-\sqrt{F_-}}{2}$
D	$\frac{1+w_-+w_+}{2w_-}$	$-\frac{1-w_-+w_+}{2w_-}$	1	-1	-4	$-3(1+\beta_+)$	$-3(1+\beta_-)$

Table 2.1: Fixed points of system (2.30-2.32), the corresponding effective EoS and eigenvalues, where $F_\pm = 9q_-^2/2 - 3q_-(1\pm\sqrt{D}-3w_+) + 9q_+w_- + 9w_-^2 - (1\pm 2\sqrt{D}-3w_+)(-1+3w_+)$.

point D the constant energy densities of x and y ($\rho_{A\Lambda}$ and $\rho_{B\Lambda}$) cause the accelerated expansion with $w_{eff} = -1$. From the expression for x and y at this latter fixed point it is easy to see that $y = -x(1 + w_A)/(1 + w_B)$: this represents an example of the so-called *scaling solutions*, by virtue of the proportionality relation between the energy density of the two fluids see Case 1 and Case 2c discussed at the end of App. **??**). This point is characterised by the final domination of an effective cosmological constant, either driven by q_0 (Case 1, see Fig. 2.8) or not (Case 2c, see Fig. 2.9). In the first case whenever $|\beta_\pm| < 1$ D is always an attractor, while in the second case it is not because one of the eigenvalues is null. Notice that its existence is completely independent of q_+ and q_-. Whenever the system settles into the fixed points B or C the role of β_+ and β_- is exactly that of effective EoS parameters (see Table 2.1) which allows for phantom line crossing at late time (see Fig. 2.7), i.e. the line for which the effective total EoS parameter is $w_{eff} = -1$.

In the following we will examine in more detail three special classes of the coupling function and in Sec. 2.2.4 we will make a first comparison of the models to the data using MCMC applied to type Ia SNe distance modulus.

I. $q_+ = q_-$

Imposing $q_+ = q_-$ is equivalent to choosing $q_A = 0$ and $q_B = q$; therefore among the range of possible couplings represented by Eq. 2.17 we are restricting to the class of models where Q/H is proportional solely to the energy density of one fluid (in our case e.g. ρ_B), and it reads

$$\frac{Q}{H} = \frac{3}{2}(q\rho_B + q_0). \tag{2.34}$$

This assumption also includes models with $q_+ = -q_-$ since the coefficients q_A and q_B can be either negative of positive. In this case the dynamics is the same as for $q_+ = q_-$, the roles of x and y being simply interchanged. We will refer to this subclass of models as model I.

In this model $\sqrt{D}$ is automatically real, since $D = 9(q/2 + w_B - w_A)^2/4$; as a consequence the scaling function (**??**) always drives a power law expansion, with $\beta_+ = q/2 + w_B$ and $\beta_- = w_A$ if $\beta_0 > 0$ (i.e. $(w_B + w_A + q/2) > 0$), vice versa if $\beta_0 < 0$. Hence the total fluid ends up as if it was made up of: *i)* a component scaling as the original fluid ρ_A with no coupling, *ii)* a second component characterised by a new EoS parameter and *iii)* an effective cosmological constant term ρ_Λ. Moreover a pure affine behaviour (2.25), or its improper modification (**??**), is obtained in three cases: *i*) $q = -2(w_B - w_A)$, which gives (**??**); *ii*) $q = -2(1 + w_B)$, that corresponds to $\beta_{+/-} = -1$ (even for $\rho_\Lambda = 0$, i.e. $q_0 = 0$, an effective cosmological constant is generated); *iii*) $w_A = -1$, where one of the two fluids is *ab initio* a constant term. Notice however that generally, because

$\beta_+ = \beta_- + 2\sqrt{D}/3$, models with $\beta_+ = -1$ and $\beta_- > -1$ are not feasible. In particular, the ΛCDM evolution is exactly recovered in case *ii*) for $w_A = 0$, that is if one of the fluids *is* dust; in case *iii*) for $q_B = -2w_B$.

The fixed point D is characterised by the domination of the constant part of the total energy density ρ_Λ; along it, the values of x and y are both positive only if either w_A or w_B have phantom values, i.e. $w_A < -1$ or $w_B < -1$. This statement holds true also for models II and III. However, if $w_A < -1$ D is no longer an attractor, as $\lambda_y = -3(1 + w_A)$ is greater than zero. On the other hand $w_B < -1$ requires $q > -2(1 + w_B)$ to let the fixed point be an attractor: in this case q is positive. A strong and positive q corresponds to a transfer of energy from ρ_A to the other fluid with $w_B < -1$. Therefore in order to fall at late time into the cosmological constant dominated era a fluid with a phantom EoS parameter w_B must absorb energy from the other non-phantom fluid. It is worth stressing that the effective cosmological constant, i.e. q_0, is somewhat redundant whenever the fixed point D is not an attractor (see Fig. 2.7). In Fig. (2.7) an example of this dynamics of the background is shown; the effective cosmological constant is not noticeable, since, after the evolution on the saddle point B, the system is trapped in the attractor point C.

II. $q_- = 0$

If $q_- = 0$ the resulting coupling function Q/H is linearly dependent on the sum of the energy densities of the two fluids, approximately equivalent to the total energy density (these models have been examined for example in Olivares et al. (2006) and Abdalla et al. (2009)) and is as follows

$$\frac{Q}{H} = \frac{3}{2}(q\rho_T + q_0). \tag{2.35}$$

With this assumption $q_A = q_B = q_+ = q$ and $\beta_\pm = w_+ \pm \sqrt{D}/3$ where $D = 9(w_B - w_A)(2q + w_B - w_A)/4$. If q is positive these effective EoS are real for $w_B > w_A$ or $w_B \leq w_A - 2q$, while if q is negative the same relations hold but with opposite inequality signs. We will label this model II.

In this model the affine evolution is recovered for $w_B = (qw_A + 2w_A + 2)/(q - 2w_A - 2)$, corresponding to $\beta_- = -1$. In this case, which is indeed Case 2c of Section **??**, an effective cosmological constant arises even for $\rho_\Lambda = 0$. Again, because $\beta_+ = \beta_- + 2\sqrt{D}$, models with $\beta_+ = -1$ and $\beta_- > -1$ are not feasible. From a cosmological point of view this means that a matter-like evolution cannot be generated together with a cosmological constant. The ΛCDM limit is achieved if $w_A = (-1 + q \pm \sqrt{q^2 + 1})/2$ and $w_B = -1 - w_A$. The evolution of the energy densities for a special choice of the parameters is illustrated in Fig. 2.8: the effective cosmological constant (**??**) arises at late time, driving the acceleration, and ρ_Λ is caused by a non-zero q_0 ($\Omega_\Lambda \neq 0$).

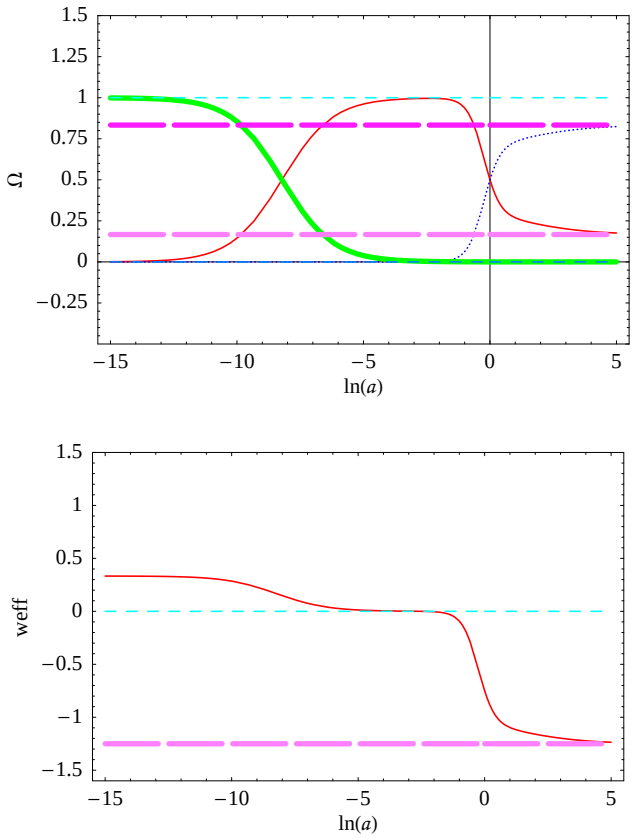

Figure 2.7: Upper panel: evolutions of the energy density parameters Ω_A (thin solid line), Ω_B (dotted line) and Ω_γ (thick solid line) for a model with $q_+ = q_- = 0.25$; for comparison, the dashed lines are the values of x and y at the fixed points B (thin short-dashed lines) and C (thick long-dashed lines). For this model the parameters are: $\Omega_{0A} = \Omega_\Lambda = 0.5$, $w_A = 0$, $w_B = -1.5$, $\beta_+ = 0$ and $\beta_- = -1.25$. Lower panel: the total effective EoS parameter for the same model : w_{eff} evolves from the value $1/3$ in the radiation dominated era, approaches the value 0 in the matter dominated era and then asymptotically evolves toward a constant phantom value, in this case $\beta_- = -1.25$.

III. $q_+ = 0$

The subgroup of models with $q_+ = 0$ (from now on model III) includes the couplings that are proportional to the difference of the energy densities Δ (for example recently analysed in Chimento et al. (2009)). With this assumption $q_- = q_B = -q_A = q$ and the discriminant $D = 9(q^2 + (w_B - w_A)^2)/4$ is always positive, so that oscillating solutions (**??**) are never permitted. The coupling function reads

$$\frac{Q}{H} = \frac{3}{2}(q\Delta + q_0). \tag{2.36}$$

As before, the affine expansion (2.25) may only be generated if one of the two effective EoS parameters assumes the value of the EoS of a cosmological constant, that is either

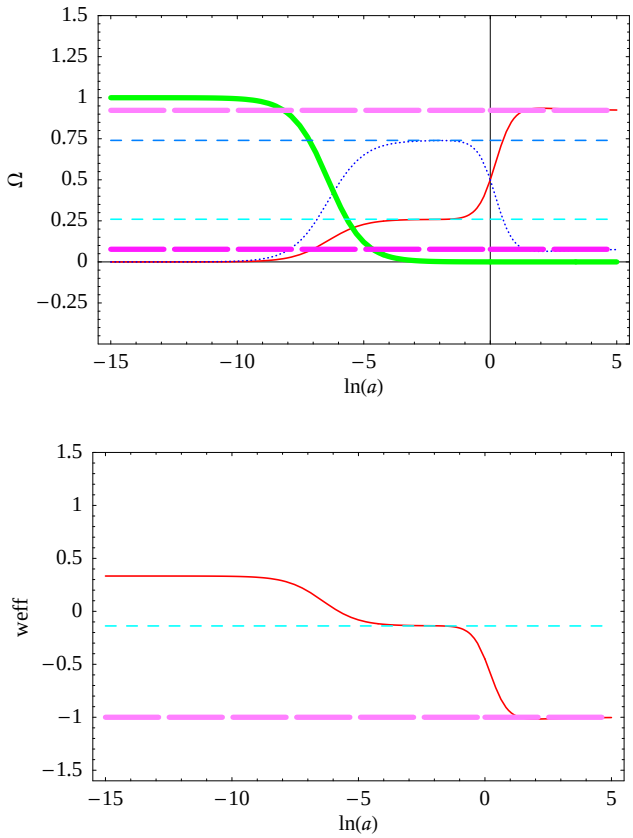

Figure 2.8: Upper panel: evolutions for the energy density parameters for a model with $q_- = 0$ and $q_+ = -0.5$; for comparison, the dashed lines are the values of x and y at the fixed points B (thin short-dashed lines) and D (thick long-dashed lines). For this model the parameters are: $\Omega_{0A} = \Omega_\Lambda = 0.5$, $w_A = -1.1$, $w_B = 0.2$. Lower panel: effective EoS for the same model; for comparison, we plot the EoS parameter of the fixed point B, $\beta_+ = -0.14$.

$\beta_+ = -1$ or $\beta_- = -1$. In particular if $\beta_+ = -1$, $\beta_- = -1 - 2\sqrt{D}/3$ is always phantom. In this case none of the terms in Eq. (**??**) can play the role of matter. On the other hand if $\beta_- = -1$ (corresponding to $w_A = (-1 - q \pm \sqrt{1 - q^2})/2$), $\beta_+ = -1 + 2\sqrt{D}/3$ is always grater than -1, i.e. always standard. An example of this dynamics is shown in Fig. 2.9, where the effective cosmological constant (**??**) arises at late time with no need of q_0, driving the acceleration (Case 2c). Then typically for $w_B = -q - w_A - 1$ we have that $\beta_+ = 0$ and the ΛCDM model is recovered.

2.2.4 Markov chains with supernovae

Methods

Given the large number of parameters, the task of finding the minimum χ^2 and mapping its distribution in the entire parameter space can be computationally expensive. To this end we adopt a MCMC approach. In this work we only want to test our models as a

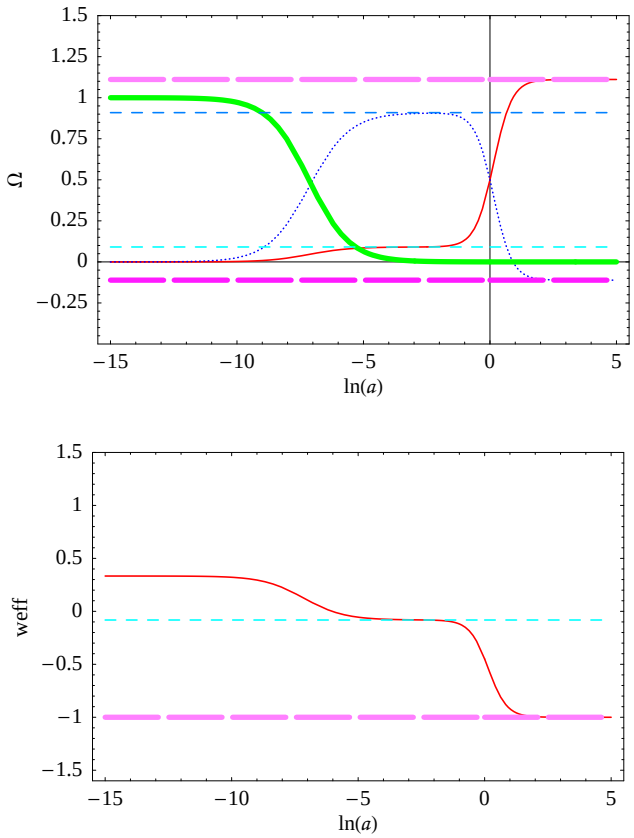

Figure 2.9: Upper panel: evolutions for the energy density parameters for a model with $q_+ = 0$ and $q_- = -0.18$; for comparison, the dashed lines are the values of x and y at the fixed point B (thin short-dashed lines) and D (thick long-dashed lines). For this model the parameters are: $\Omega_{0A} = 0.5$, $\Omega_\Lambda = 0$, $w_A = -0.9$, $w_B = 0$. (dust). The EoS parameters at B are $\beta_+ = -0.08$ and $\beta_- = -1$. Lower panel: effective EoS for the same model.

description of the homogeneous isotropic background expansion (regardless of perturbations), hence supernovae are ideal for this purpose. We use the 192 type Ia SNe distance modulus data set provided in Davis et al. (2007). In particular we want to see whether supernovae can qualitatively distinguish different kind of couplings, included what we called model I, II and III.

Type Ia SNe light curves allow a determination of an extinction-corrected distance moduli,

$$\mu_0 = m - M = 5 \log (d_L/\mathrm{Mpc}) + 25 \tag{2.37}$$

where $d_L = (L/4\pi F)^{1/2} = (1+z) \int_0^z dz'/H(z')$ is the luminosity distance. We compare our theoretical predictions to the values of μ_0 with $H^2 = 8\pi G/3(\rho_A+\rho_B+\rho_\gamma+\rho_b)$, where we account also for the baryon energy density ρ_b. We fix the value of the dimensionless Hubble constant to be $h = 0.72$ (Freedman et al., 2001) and the baryon energy density at present $\Omega_b h^2 = 0.02229$ according to Spergel et al. (2007). The smaller is the EoS

parameter of a single fluid the later can be the domination era for this fluid. Hence, counting the role of $\beta_\pm$ as effective EoS parameters, whenever $\beta_\pm > 0$ a baryonic era might emerge at recent time. The absolute distance modulus M is intrinsically affected by uncertainty; therefore we treat it as a nuisance parameter and marginalize over it. The distance modulus for the models shown in Fig. 2.7-2.9 together with the 192 SNe data points are displayed in Fig. 2.10.

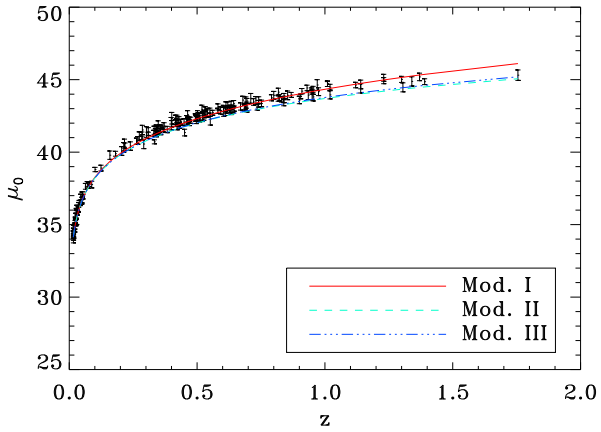

Figure 2.10: Comparison of the distance modulus for the three coupling models in Fig. 2.7-2.9 to the 192 SNe dataset used in the MCMC analysis.

The parameters that are representative of the models are $\{\Omega_{0A}, \Omega_\Lambda, q_A, q_B, w_A, w_B\}$, or otherwise $\{\Omega_{0A}, \Omega_\Lambda, q_+, q_-, w_+, w_-\}$ and, as functions of these, the two effective EoS introduced in Eq. (**??**): β_+ and β_-. For the ensuing analysis it is worth recalling our classification of models: I) model with a coupling function proportional to only one of the two energy densities; II) model with a coupling function proportional to the sum of the energy densities; III) model with a coupling function proportional to the difference of the energy densities.

We shall now focus our analysis on the case $w_B = 0$, i.e. ρ_B would represent standard CDM if it wasn't for the coupling with the DE component.

Results: CDM - DE coupled models

The first result we obtain is that Ω_Λ is completely unconstrained, independently of which model we consider. This means that SNe are not sensitive to the constant term of the coupling. The dynamics of the system can easily generate the acceleration settling on fixed points D, where $w_{eff} = -1$ (see Tab. 2.1), even for $\Omega_\Lambda = 0$ (see Fig. 2.9), or B and C, where the total energy density can also exhibit phantom evolutions.

In Fig. 2.11 and 2.12 we present MCMC chains in a two-dimensional diagram $[q_+, q_-]$ ($[q_A, q_B]$ on the right hand side). As said above, we consider a model where one of the two

fluids represents a CDM component, i.e. $w_B = 0$, a reasonable assumption considering all the other cosmological probes pointing towards the existence of a form of cold dark matter (see e.g. Khalil & Munoz (2002)), and we let w_A assume three different values that characterise ρ_A as a DE component (phantom-like behaviour is shown in the top panels, cosmological constant-like in the second row panels and non-phantom model in the bottom panels).

Note that the case where $w_A = 0$ and ρ_B is DE can be easily derived from the previous one, corresponding in the diagram to a reflection with respect to the line $q_B = -q_A$. In fact, interchanging the two EoS and swapping the roles of the two energy densities, and applying the transformation ($q_A \to -q_B$, $q_B \to -q_A$, i.e. $q_+ \to -q_+$, $q_- \to q_-$), one recovers the aforementioned model.

In addition, the straight lines corresponding to models I, II and III are drawn, and diagrams of Fig. 2.12 are derived from the same choice of parameters as in Fig. 2.11 except for $\Omega_\Lambda \neq 0$ (it is by eye easily verifiable that there is no dependence on Ω_Λ). Finally, the short-dashed curves represent the improper affine evolution (**??**), while the short-dashed straight line represents affine models (2.25) with $\beta_{+/-} = -1$ (Case 2c).

As a first step we derived the unidimensional likelihood for $\{\Omega_{0A}, q_+, q_-\}$. The best fit of the energy density parameter for the three classes of models presented in Fig. 2.11 and 2.12 is respectively $\Omega_{0A} = 0.63, 0.65, 0.76$ with an error of $2\sigma = 0.1$; this best fit does not change including Ω_Λ. In the diagrams Ω_{0A} is therefore fixed to these best fit values. It is worth stressing that here we are not just analysing the typical models considered in the literature (namely I, II and III) but the results incorporate *all* the possible linear couplings, and, we might say, all the possible expansions at recent times of a generic coupling function Q (Eq. 2.16). Hence we are not interested in deriving constraints on single parameters, a route that might be hard to follow with SN Ia in view the high number of parameters and their degeneracies. We instead want to see what kind of linear couplings are preferred by the data and provide a qualitative way to distinguish the type and the direction of the interaction.

The first noticeable thing in the $[q_A, q_B]$ diagram is that the points lie almost on a horizontal branch of the diagram, close to the line representing model I, in particular with $Q \propto \rho_A$. So if we allow the interaction term to be strong and move out of the weak coupling regime (i.e. $|q_{A,B}| > 1$), the most "frequent" linear coupling function emerging from the chains is the one proportional to the DE density (ρ_A). In addition, strong couplings are favoured for positive value of q_A (see Fig. 2.11 and 2.12): the energy is transferred from dark matter to DE (as a consequence of the sign in Eqs. 2.14-2.15). Increasing the value of w_A, that is moving from phantom-like values towards quintessence-like ones (going downwards in the right hand side column of fig. (2.11)), this horizontal branch tends to negative values of q_B. Models with a phantom w_A show an increasing

energy density with the scale factor, a, while for a DE model characterised by $w_A > -1$ the energy density is diluted with the universe expansion: this second kind of model requires a lower transfer of energy from CDM to DE. Apart from a small spot in the origin of the axis (weak couplings), the coupling or type II does not seem to be favoured by SN data, the effect increasing with higher values of w_A, i.e. for non-phantom values. Another piece of evidence that arises from diagrams Fig. 2.11 and 2.12 is that for non-phantom values of w_A (third row in figures) the uncoupled case (namely $[q_A, q_B] = [0, 0]$) falls almost outside the border of the likelihood.

Since today $\rho_{0B} \simeq \rho_{0A}$ we can say that the sign of the coupling function ($Q \simeq q_A\rho_{0A} + q_B\rho_{0B}$) changes along the straight line $q_B = -q_A$ (long dashed line): above this line the exchange term reverses the energy transfer from CDM to DE (i.e. positive Q), while below it is the opposite (negative Q). Again, the higher w_A, the bigger is the number of points that we can find below this line. Therefore for DE components with $w_A < -1$ an exchange of energy from DE to CDM is less probable, independently of the type of linear coupling. This reflects the fact that an increasing energy density (characteristic of phantom behaviour) favours more and more absorbing and positive DE couplings at present, while non-phantom values of w_A seem to need a negative exchange term, most of all for weak couplings, to explain supernovae data. It is worth stressing that eventually the likelihood seems to exclude the uncoupled case.

The connection between where the points lie in the diagrams, i.e. the region favoured by the likelihood, and where the cosmological background evolution is affine is an interesting issue; this directly connects coupled DE models to an effective evolution of the total energy density that is completely equivalent to a cosmological constant plus a component with constant EoS parameter α, Eq. (2.25). If one looks at the left side diagrams of Fig. 2.12, a short-dashed curve and a short-dashed straight line are drawn on it. The former corresponds to the improper affine evolution (**??**), obtained for $q_- = \pm\sqrt{-4w_-(q_+ + w_-)}$. Hence the only affine models are those that correspond to the straight line for which $\beta_{+/-} = -1$ (for the model with $w_A = -1$ this coincides with the line representing model II, the only possibility to recover the affine evolution with no coupling). For a DE model with a phantom w_A the affine evolution coexisting with a non-zero Ω_Λ is somewhat ruled out and, among the models indicated in the last Section, is more compatible with a coupling function proportional to ρ_A (DE, model I) and possibly to Δ (model III). For DE models with $w_A > -1$ the situation is different: the data seem to favour an affine evolution generated in models with a coupling function proportional to ρ_B (matter, model I) and again model III. In addition, for DE models with standard w_A an improper affine evolution together with a non-vanishing q_0 (Ω_Λ) is allowed, in a region where the coupling function shifts towards negative sign, thus representing a transfer of energy from DE to CDM.

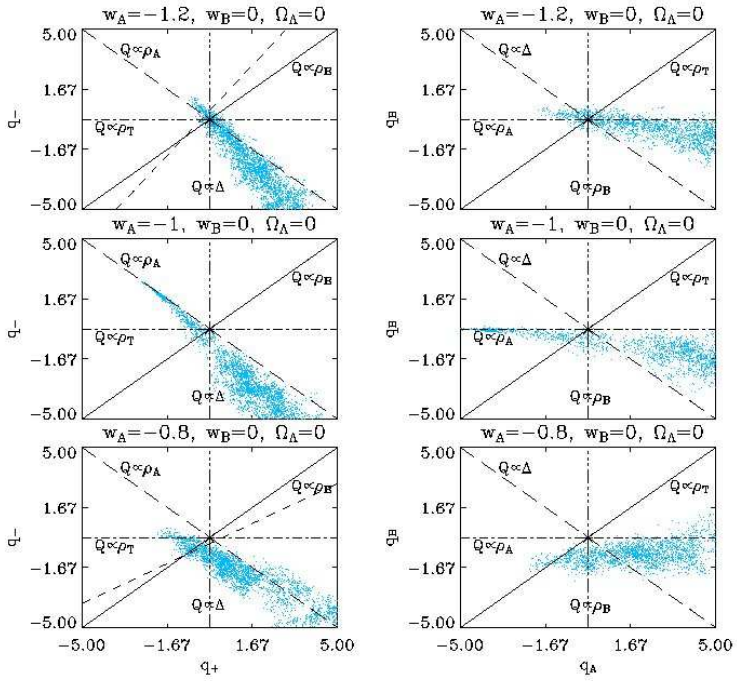

Figure 2.11: Coupling diagrams with two-dimensional likelihood for models with $\Omega_\Lambda = 0$. Apart from the short-dashed line that represents an affine evolution with $\beta_{+/-} = -1$, all the other lines are labelled with the corresponding type of coupling function (e.g. the solid line on the left side diagrams represents a coupling function $Q \propto \rho_B$ (model I), while on the right side diagrams it represents $Q \propto \rho_T$ (model II)). The energy density parameter at present is fixed at its best fit value, respectively $\Omega_{0A} = 0.63, 0.65, 0.76$.

2.2.5 Conclusions

We have analysed the dynamics of two coupled dark components represented by two barotropic perfect fluids characterised by constant EoS parameters w_A and w_B. We have assumed a flat, homogeneous and isotropic cosmology and a general linear coupling between the two barotropic perfect fluids. This scale-independent coupling takes a linear form proportional to the single energy densities plus a constant term: any coupling of this type can approximate at late time a more general coupling function. We have studied the stability of the system and shown that an effective cosmological constant can arise both from the constant part q_0 of the function Q and from an effective cosmological constant-like EoS. We have also examined the dynamics of the energy density parameters, and evaluated the fixed points and the corresponding eigenvalues, for the most general form of linear coupling. We have then restricted the analysis to some specific linear couplings previously considered in the literature (model I, II, III). Since we are restricting to the background expansion and we have modelled the coupling function as a late time first order Taylor expansion, a comparison with distance modulus from SN Ia data appeared as our natural step further. We have presented a MCMC analysis for a model with dark

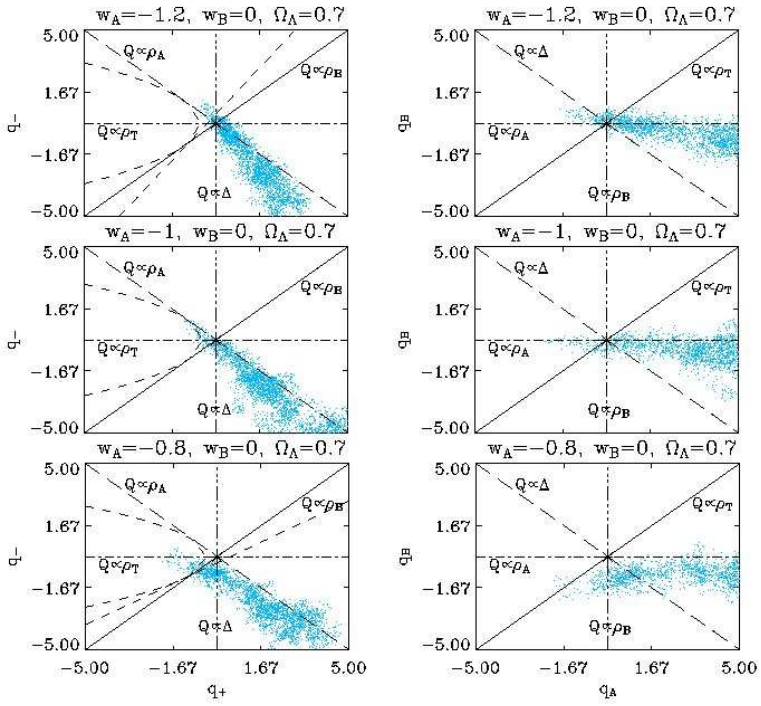

Figure 2.12: Coupling diagrams with two-dimensional likelihood for models with $\Omega_\Lambda = 0.7$. All the lines are labelled with the corresponding type of coupling function (e.g. the solid line on the left side diagrams represents a coupling function $Q \propto \rho_B$ (model I), while on the right side diagrams it represents $Q \propto \rho_T$ (model II)). The short-dashed line represents affine evolution with $\beta_{+/-} = -1$ and the short-dashed curve represents affine evolution with $\beta_+ = \beta_-$. The energy density parameter at present is fixed at its best fit value, respectively $\Omega_{0A} = 0.63, 0.65, 0.76$.

matter plus DE using the data set provided in Davis et al. (2007). Considering two representative specific values of the DE parameter w_A, one standard ($w_A > -1$) and the other phantom ($w_A < -1$), we have condensed our results in coupling diagrams, where the points arising from the MCMC chains are drawn together with lines for model I, II and III and for the improper affine (**??**) affine (2.25) evolutions, the latter including the ΛCDM model as a subcase. Couplings proportional to the DE density seem favoured, mostly for strong couplings $|q_A| > 1$. The total sign of the exchange term sets the direction of the interaction: models with phantom w_A definitely prefer positive coupling, i.e. an energy transfer from dark matter to DE. On the other hand, models with non-phantom w_A not only allow for negative Q, but force the uncoupled model to fall at the border of the likelihood. For further and stronger constraints more complementary data are required, like CMB spectra or matter power spectra. These observables necessitate an accurate relativistic perturbation analysis which is neither obvious nor uniquely defined in phenomenological coupled models as those considered here. Moreover, simplified observables that make no use of perturbation analysis, like the CMB shift parameter, can be strongly model-dependent and, although straightforward, should not be used in models

where the evolution, even just that of the unperturbed background, detaches significantly from that of the ΛCDM model. These extended investigations can only be settled with future work.

2.3 Affine parameterisation of the dark sector: constraints from WMAP5 and SDSS

In the previous section we have introduced a generic coupling between two dark components, which may eventually account for dark matter and dark energy. We studied the fluid dynamics and put constraints on the coupling parameters from SNe data. We also concluded that an affine EoS model is likely to arise for a wide range of the parameters. The affine model has been constrained by Balbi et al. (2007) using SNe, BAO and CMB datasets. The peculiarity of this model is its parameterisation of the equation of state (Ananda & Bruni, 2006):

$$p_X = P_0 + \alpha\rho_X, \tag{2.38}$$

where p_X is the pressure, ρ_X is the energy density, and P_0 and α are constant parameters; this leads to a time dependent equation of state parameter

$$w_X = \frac{P_0}{\rho_X} + \alpha. \tag{2.39}$$

An interesting property of this parameterisation is that it results in a constant energy density term mimicking an effective cosmological constant, with $\Omega_\Lambda = -P_0/\left[\rho_c(1+\alpha)\right]$, plus an evolving term that can reproduce a dark matter behaviour for certain choices of the parameter α. This allows one to either treat the affine fluid as a single unified dark component, or to use it to model dark energy alone.

As shown in Quercellini et al. (2007), when α is negative, this description can be seen as the attractor solution for a quintessence scalar field dynamics. Alternatively, when treating perturbations, a barotropic affine fluid can be interpreted as a k-essence scalar field (naturally describing an effective cosmological constant plus dark matter), while a scalar field with sound speed $c_s^2 = 1$ acts as a dark energy component. In addition, an affine fluid description can also be interpreted as the result of two interacting dark components (one of them being a cold dark matter component), as we discussed in detail in the previous section (Quercellini et al., 2008). In order to be realistic, every model must include the perturbation theory and fit well enough the structure formation history we can reconstruct from galaxy surveys (Abazajian et al., 2009; Cross et al., 2001; Condon et al., 1998). The aim of this section is to complete the study performed by Balbi et al. (2007); Quercellini et al. (2007) and Quercellini et al. (2008) by addressing the perturbations issue in the framework of the affine EoS. Since it has been proven that several scalar field models may lead to such EoS dynamics, we follow a more phenomenological approach, modelling the dark sector as a perfect fluid characterised by the EoS parameter w and the sound speed, c_s^2. We consider two classes of models: one where the affine fluid describes

a unified dark component, the other containing a cold dark matter component as well. For each class, we also study three separate subcases, identified by the value of the speed of sound: the barotropic case, with $c^2_{\rm eff} = \alpha$, the case $c^2_{\rm eff} = 1$, and the "silent" case (Bruni et al., 1995b,a) with $c^2_{\rm eff} = 0$.

To study the properties of the model, we calculate the evolution of scalar perturbations in the affine fluid by modifying the publicly available CAMB code, and set constraints to the parameters of the model by performing a Monte Carlo Markov Chain analysis using the cosmic microwave background anisotropy WMAP 5 year data (Komatsu et al., 2009) and the large-scale matter distribution derived from the Sloan Digital Sky Survey (SDSS) Luminous Red Galaxy (LRG) 4 year data (Tegmark et al., 2004).

2.3.1 Affine fluid model

General framework

We perform our calculations in the context of a flat, homogeneous and isotropic universe, whose unperturbed evolution is described by the Friedman equation

$$H^2 \equiv \left(\frac{\dot{a}}{a}\right)^2 = \frac{8\pi G}{3}\rho \tag{2.40}$$

where ρ is the total energy density, the sum of the densities of all the components in the universe, each of them satisfying a continuity equation that, in the case of non-interacting components, reads

$$\dot{\rho}_{(i)} + 3H(\rho_{(i)} + p_{(i)}) = 0. \tag{2.41}$$

According to the specific properties of each component one has different scaling behaviour: for example, for photons and baryons $\rho_\gamma \propto a^{-4}$ and $\rho_B \propto a^{-3}$, respectively. We will refer to the decaying in time of the energy density as "standard" behaviour; when the energy density grows in time, i.e. when $\rho_{(i)} + p_{(i)} < 0$ (the null energy condition is violated), the behaviour is called "phantom" (Caldwell et al., 2003).

When treating perturbations of the background line element, we adopt the synchronous gauge (Ma & Bertschinger, 1995). The perturbed metric then reads:

$$ds^2 = a(\tau)^2(d\tau^2 - (\delta_{ij} + h_{ij}(\mathbf{x}, \tau))dx^i dx^j) \tag{2.42}$$

where τ is the conformal time and $|h_{ij}| \ll 1$ is the metric perturbation. We then compute the Einstein's equations at first order from the metric given above and from the perturbed

energy-momentum tensor

$$T_{\mu\nu} = \sum_i T^{(i)}_{\mu\nu} \tag{2.43}$$

where the index i runs over the components in the universe, photons, baryons, and dark components. The perturbed energy-momentum tensor components are

$$\begin{aligned} T^{(i)0}{}_0 &= \rho_b^{(i)}(1+\delta^{(i)}), \\ T^{(i)0}{}_k &= \rho_b^{(i)}(1+w^{(i)})V_k^{(i)}, \\ T^{(i)j}{}_k &= (p_b^{(i)} + \delta p^{(i)})\delta^j_k, \end{aligned} \tag{2.44}$$

where $\delta^{(i)}$ is the density contrast for the i component, $V^{(i)}$ is the velocity, $w^{(i)}$ is the equation of state parameter (not necessarily constant) and the subscript b refers to the background (i.e. unperturbed) quantities.

Background evolution

The basic property of the phenomenological model we consider is the affine form of the pressure as a function of the density of the dark component, Eq. (2.38). Even if the EoS parameter of the dark component is not constant, a simple solution for the Eq. (2.41) exists and it is given by

$$\rho_X = \rho_\Lambda + (\rho_{X0} - \rho_\Lambda)a^{-3(1+\alpha)}, \qquad \alpha \neq -1; \tag{2.45}$$

$$\rho_X = \rho_{X0} - 3P_0 \ln a, \qquad \alpha = -1. \tag{2.46}$$

where ρ_{X0} is the density of the dark component at the present time (i.e. $a = 1$) and $\rho_\Lambda \equiv -P_0/(1+\alpha)$, with α and P_0 free parameters of the model. This density evolves in time in a way that can be either standard or phantom, depending on the particular choice of the parameters. A full description of the background properties of such a dark component is given in Balbi et al. (2007). Here we want to stress that, in the absence of cold dark matter, this component should both be able to create the gravitational potential necessary to form structures at high redshifts, and to drive the late time acceleration of the universe. With respect to a flat ΛCDM model, we have an additional degree of freedom, α, which is the square of the barotropic sound speed, that allows us to investigate the effective equation of state of the clustering part of the component.

Since the perturbation equations of the dark component will be written in terms of its equation of state parameter, Eq. (2.39), it is interesting to explicitly consider the time evolution of w_X.

We first comment on the case $\rho_{X0} - \rho_\Lambda > 0$ (Fig. 2.13). In this case, if $\alpha > -1$, $w_X(a)$ evolves from the value α approaching the value -1; conversely, if $\alpha < -1$, it approaches

the value α moving away from $w = -1$. In the former situation, $-3(1+\alpha) < 0$ and the dynamical part of the affine component dominates at early times. When $\alpha < -1$, then $-3(1+\alpha) > 0$, so that the evolving dark component increases in time, i.e. it has a phantom behaviour, becoming dominant at late times. The slope of the curve obviously depends on ρ_{X0}, P_0 and α.

Let us now consider the case when $\rho_{X0} - \rho_\Lambda < 0$ (Fig. 2.14). The behaviour is opposite to the previous case, with the phantom evolution appearing when $\alpha > -1$. In this case there is a divergence of w in the past, making this choice of parameters more problematic. In this paper we will restrict the analysis only to cases with $\rho_{X0} - \rho_\Lambda > 0$.

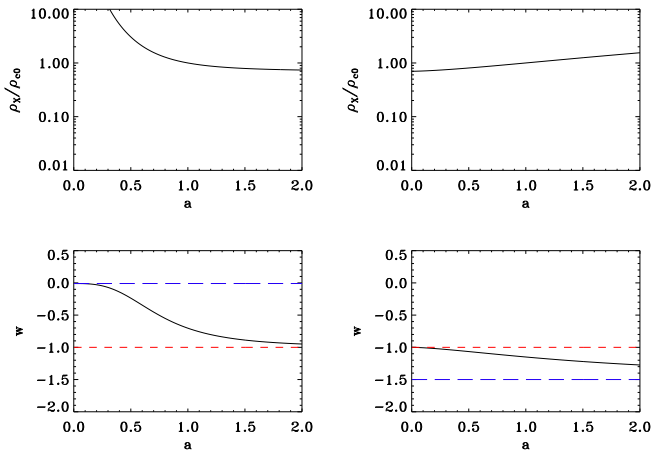

Figure 2.13: Evolution of the dark component energy density (top) and equation of state parameter (bottom), for two values of α: $\alpha = -0.01$ (left) and $\alpha = -1.5$ (right). In both cases, $\rho_{X0} - \rho_\Lambda > 0$: in this case, $\alpha < -1$ results in a phantom regime, characterised by an energy density which increases in time.

Fluid perturbations

Einstein's equations in the synchronous gauge and in Fourier space give the following system of coupled equations

$$\dot{\delta}_{(i)} = -(1+w_{(i)})\Big(\theta_{(i)} + \frac{\dot{h}}{2}\Big) + 3H\Big(\frac{dp_{(i)}}{d\rho_{(i)}} - w_{(i)}\Big)\delta_{(i)}, \tag{2.47}$$

$$\dot{\theta}_{(i)} = -H(1-3w_{(i)})\theta - \frac{\dot{w}_{(i)}}{1+w_{(i)}}\theta_{(i)} + \frac{dp_{(i)}/d\rho_{(i)}}{1+w_{(i)}}k^2\delta_{(i)}, \tag{2.48}$$

where we defined $ikV_{(i)} \equiv \theta_{(i)}$.

A pure barotropic fluid with a negative EoS parameter has imaginary adiabatic sound speed that causes a runaway growth of perturbations. Not only does this have unpleasant

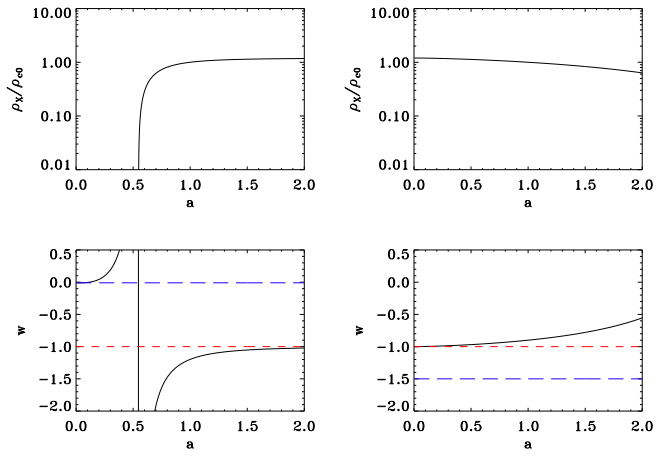

Figure 2.14: Evolution of the dark component energy density (top) and equation of state parameter (bottom): for two values of α: $\alpha = -0.01$ (left) and $\alpha = -1.5$ (right). In both cases, $\rho_{X0} - \rho_\Lambda < 0$: in this case, $\alpha > -1$ results in a phantom regime, characterised by an energy density which increases in time.

consequences for structure formation, but it also creates an instability in the set of coupled perturbation equations (2.47), (2.48). A viable way to overcome this inconvenience is to allow for entropy perturbations in the dark component, assuming that the effective speed of sound, the sum of the adiabatic and entropic one, is positive or null. We follow the formalism developed in the context of generalised dark matter (Hu, 1998), where

$$c^2_{X,\mathrm{eff}} \equiv \frac{\delta p_X}{\delta \rho_X} = c^2_{X,\mathrm{ad}} + \frac{w_X}{\delta_{X,\mathrm{rest}}}\Gamma_X \,, \tag{2.49}$$

$$c^2_{X,\mathrm{ad}} \equiv \frac{\dot{p}_X}{\dot{\rho}_X} = \alpha. \tag{2.50}$$

Here Γ_X is a constant parameter we will not use since we prefer to specify the more fundamental quantity c^2_{eff}; $\delta_{X,rest}$ is the density contrast in the rest frame of the dark component, defined as

$$\delta_{X,\mathrm{rest}} = \delta_X + 3\frac{\dot{a}}{a}\frac{\theta_X}{k^2}. \tag{2.51}$$

The fact that, in our fluid description, the effective speed of sound is a free parameter not tied to the behaviour of equation of state parameter w_X, allows us to evade the tight constraints on unified dark matter models pointed out in Sandvik et al. (2004) and arising from the runaway growth of perturbations.

To perform numerical predictions for the evolution of perturbations, we modified the publicly available code CAMB[5] adding a new component whose perturbations are

[5] http://camb.info/

described by the following equations in the synchronous gauge:

$$\begin{aligned}\dot{\delta}_X &= -(1+w_X)(\theta_X+\frac{\dot{h}}{2}) - 3\frac{\dot{a}}{a}(c^2_{X,\mathrm{eff}}-\alpha)\delta_{X,\mathrm{rest}} \\ &+ \frac{\dot{w}}{(1+w)}\delta_X, \qquad (2.52)\\ \dot{\theta}_X &= -\frac{\dot{a}}{a}\theta_X + \frac{c^2_{X,\mathrm{eff}}}{(1+w)}k^2\delta_{X,\mathrm{rest}}. \qquad (2.53)\end{aligned}$$

We adopt adiabatic initial conditions for the dark component (Doran et al., 2003; Amendola, 2004). We first investigate the constraints coming from the CMB anisotropy power spectrum on a single dark component governed by an affine equation of state. As we already mentioned, this can account for both dark matter with a non-vanishing EoS parameter and a cosmological constant; we label this unified model as αDM model. The affine component can also be employed as a pure dark energy component, if standard CDM is present. We denominate this model as αCDM model. In addition to comparing our CMB anisotropy predictions with actual data from the WMAP 5 year observations, we improve our results by adding the SDSS dataset in order to remove degeneracies among parameters. In fact, α affects the CMB angular power spectrum in two ways: it shifts the peak position by modifying the Universe evolution through the Hubble rate, and, as barotropic sound speed, it influences the relative amplitude of the peaks, by changing the balance between the pressure and gravitational forces (according to its sign). These effects occur mainly before decoupling, when photons feel the gravitational potential through the interaction with baryons. It is by measuring the matter power spectrum at much lower redshift, which we can indeed improved the constraints on the sound speed, since even a tiny negative or positive sound speed is clearly visible as a rapidly increasing or decreasing matter power spectrum. This effect is shown in Figg. 2.16 and 2.17.

In the next section we discuss the results obtained for both αDM and αCDM models.

2.3.2 Results

Methods

We performed a full analysis of the two classes of models arising from an affine equation of state (i.e. the αDM and αCDM models) using the Monte Carlo Markov Chain (MCMC) approach implemented in a modified version of the public CosmoMC software[6] (Lewis & Bridle, 2002). We span the parameter space defined by the baryon density, $\Omega_b h^2$, the cold dark matter density, $\Omega_c h^2$, the current expansion rate of the universe, H_0,

[6] http://cosmologist.info/cosmomc/

the reionization optical depth, τ, the spectral index n_s and the normalisation amplitude A_s that parametrise the primordial curvature fluctuation power spectrum

$$P(k) = A_s(k/k_0)^{n_s}. \tag{2.54}$$

This results in a galaxy power spectrum $P_g(k) = b_L^2 9/25 P(k)$, where b_L is the galaxy bias set constant and the factor $9/25$ comes form the relation between density and curvature fluctuations. The affine dark component is characterised by the two parameters Ω_Λ (defined, as usual, as $8\pi G\rho_\Lambda/3H_0^2$) and α. Its effective sound speed squared has been fixed to three different values, namely 0, 1 and α, in order to consider the three possible clustering possibilities, namely cold dark matter-like behaviour, scalar field limit and barotropic fluid. We assumed a flat universe and set a Gaussian prior on the Hubble parameter with mean value and standard deviation consistent with the Hubble Space Telescope Key Project, 72 ± 8 km/sec/Mpc (Freedman et al., 2001). See Riess et al. (2009) for a recent Hubble constant measure.

We computed the likelihood function of the data using the public code provided by WMAP team[7] that includes both the temperature and the polarisation CMB power spectrum (the main effect of the latter being a tighter constraint on the optical depth τ).

Even if at the background level the αDM model is equivalent to a dark matter with non-vanishing EoS parameter plus a cosmological constant, there are differences at the perturbation level; moreover, the difference is conceptual, since the αDM model treats the dark sector as a whole, and can even be the result of interacting dark components (Quercellini et al., 2008).

αDM Models

In this section we investigate the properties of a single dark component described by an affine equation of state. The parameters of this model are $(\Omega_b h^2, \theta, \tau, \ln 10^{10} A_s, \Omega_\Lambda, \alpha)$. We expect the model with sound speed $c^2_{\rm eff} = 1$ to be ruled out by the current cosmological datasets: a quintessence scalar field able to drive the late time acceleration of the universe expansion prevents structure formation (Quercellini et al., 2007). We tested our pipeline in the limit of standard ΛCDM model, i.e. for the choice $\alpha = 0$, obtaining results that are in excellent agreement with the 5-year WMAP release (Komatsu et al., 2009; Dunkley et al., 2009). In the following we describe the results obtained for the three sub-classes of models we analysed.

[7] http://lambda.gsfc.nasa.gov/product/map/dr2/likelihood_get.cfm

αDM - $c^2_{\rm eff} = \alpha$ We investigated the barotropic model, namely the one with $c^2_{\rm eff} = c^2_{\rm ad} = \alpha$, which does not require any assumption concerning entropy perturbations. As we mentioned earlier, this model has an equivalent description in terms of a k-essence scalar field. Our findings are shown in Fig. 2.15.

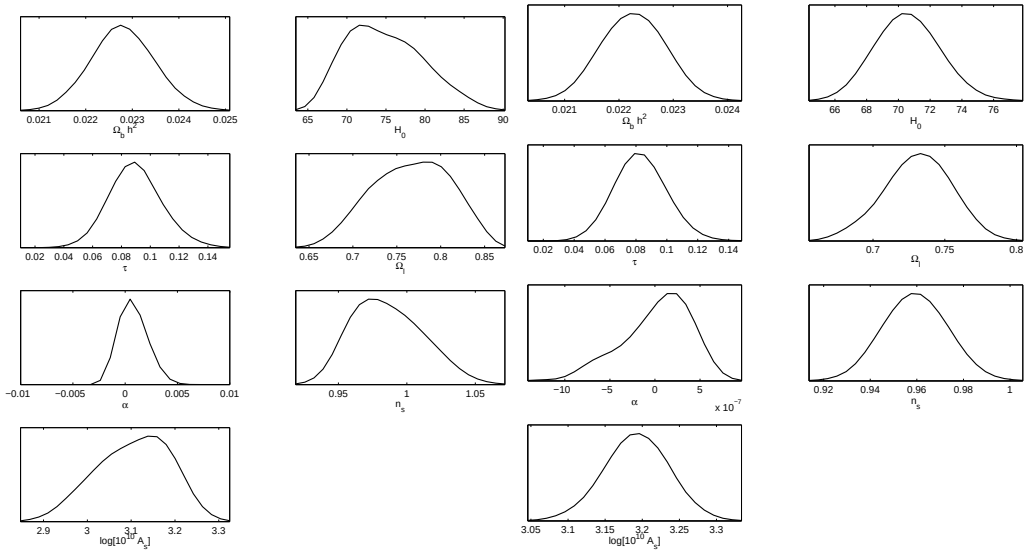

Figure 2.15: **αDM - $c^2_{\rm eff} = \alpha$**: Parameter likelihoods computed for the αDM model under the assumption of barotropic fluid, i.e. a fluid that fulfils the relation $c^2_{\rm eff} = \alpha$. The left panel is CMB alone, the right panel is CMB combined with the matter power spectrum. When the matter power spectrum is taken into account the constraints on the equation of state parameter are much tighter. The other parameters are fully consistent with the results of 5 years WMAP release.

With this choice of the sound speed we tested the equation of state of dark matter. Our best fit model from the 5 year WMAP CMB data has $\alpha = (8 \pm 11) \times 10^{-4}$ and $\Omega_\Lambda = 0.76 \pm 0.04$: we confirm that an almost pressureless component is the most likely one. Since we know that the effect of a non-vanishing sound speed is to strongly modify the clustering properties, we investigated the constraints which the matter power spectrum data put on this specific model. As expected, the constraint on α shrinks to $|\alpha| \lesssim 10^{-7}$, in excellent agreement with what found in Muller (2005). For Ω_Λ we find $\Omega_\Lambda = 0.73 \pm 0.02$. In Figs. 2.16 and 2.17 the effect of even such a tiny barotropic EoS parameter is shown.

αDM - $c^2_{\rm eff} = 0$ The parameter likelihoods for the case of $c^2_{\rm eff} = 0$ are shown in Fig. 2.18. The main difference with respect to the barotropic model is a weaker constraint on α, due to the presence of a vanishing effective sound speed that cancels the pressure term in the perturbation equations, guaranteeing the clustering properties of the dark component.

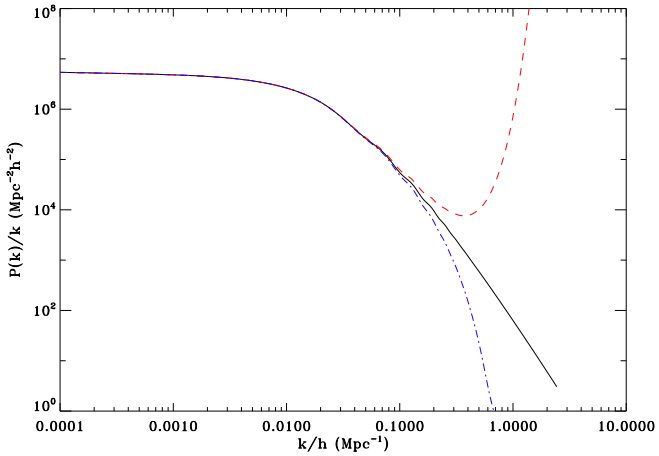

Figure 2.16: Matter power spectrum dependence on α. The black solid line is the matter power spectrum computed for $\alpha = 0$, i.e. for the concordance ΛCDM model. The dashed curve is for the value $\alpha = -1 \times 10^{-6}$; the dot-dashed curve is for $\alpha = 1 \times 10^{-6}$. The perturbation instability is clear when a negative EoS parameter is chosen.

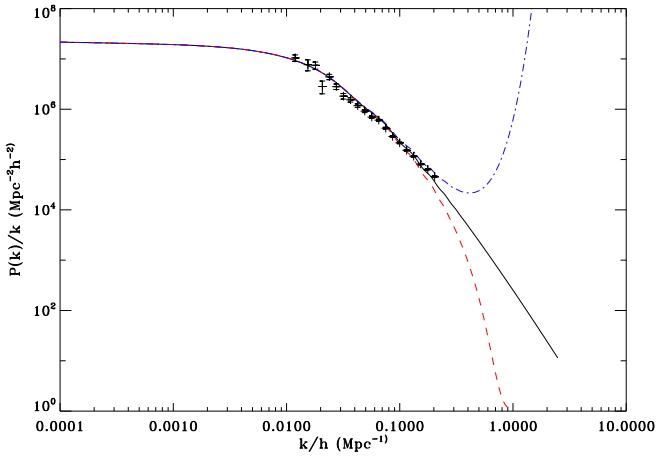

Figure 2.17: To further illustrate the point, for the barotropic αDM model we plot against real data the power spectra for values of α at 2σ from the best fit. It is clear that the data constrain the value of α in two ways: 1) the theoretical curve has to fit the overall shape of the data distribution; 2) the data points at smaller scales pin down the value of $|\alpha|$, constraining it to be small enough to *i)* give a small enough Jeans scale λ_J for $\alpha > 0$, such that enough power is produced for $\lambda > \lambda_J$, and *ii)* for $\alpha < 0$, to produce an explosive growth of perturbations only at small enough scales, again such that above the Jeans length, where gravity dominates against the pressure effects, the spectrum is undisturbed. It is clear from the figure that the second effect is dominant, in that it is extremely sensitive to the value of α.

We get $\alpha = (-1.5 \pm 3) \times 10^{-3}$ and $\Omega_\Lambda = 0.70 \pm 0.09$. When the matter power spectrum is considered, the limit on the square of the barotropic sound speed α shrinks to $(-2 \pm 2) \times 10^{-3}$ at 1σ level, and $\Omega_\Lambda = 0.69 \pm 0.05$.

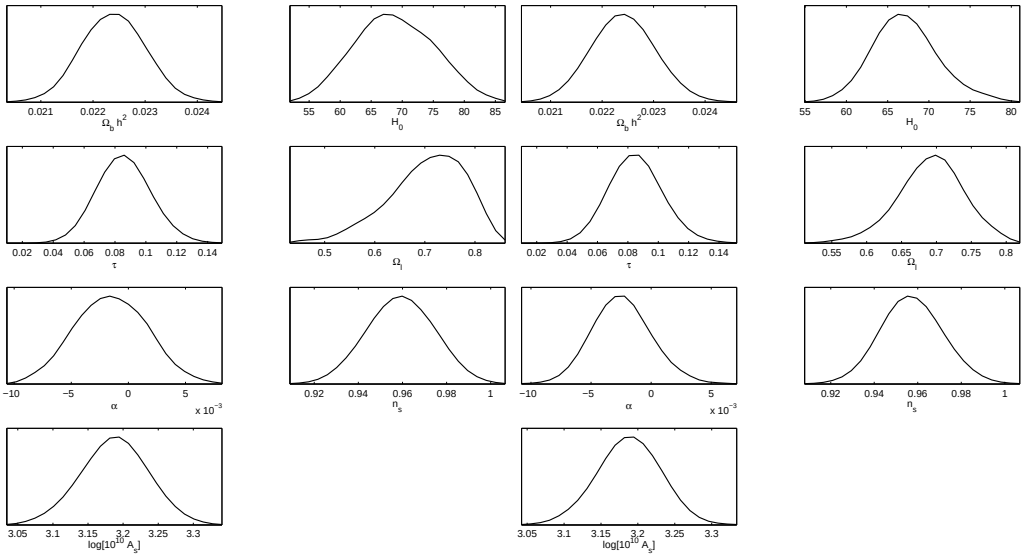

Figure 2.18: α**DM - c$^2_{\rm eff} = 0$**: Parameter likelihoods for the αDM model with sound speed $c^2_{\rm eff} = 0$. The left panel is for CMB alone, the right panel is for CMB combined with the matter power spectrum. The barotropic sound speed squared α is still consistent with 0, but the constraints are weaker than in the case of a pure barotropic fluid. The other parameters do not change significantly with respect to the concordance model.

αDM - c$^2_{\rm eff} = 1$ For completeness, we also performed the analysis in the weakly clustering limit, described by $c^2_{\rm eff} = 1$; as expected, the model fails completely in fitting the observational data. A fluid with a luminal speed of sound prevents the clustering at scales even close to the horizon (Quercellini et al., 2007).

αCDM Models

In what follows we present the results we obtained for the αCDM model, i.e. when we consider a flat universe filled with baryons, cold dark matter and a dark energy component described by the affine equation of state Eq. (2.38). The choice can help to distinguish the cosmological constant from a more general dynamical field. In this framework the most natural value for the speed of sound is $c^2_{\rm eff} = 1$: with this choice, our fluid description represents well the attractor dynamics of a quintessence scalar field, when $\alpha < 0$ Quercellini et al. (2007).

αCDM - c$^2_{\rm eff} = 1$ In Fig. 2.19 we show the results for the αCDM model with $c^2_{\rm eff} = 1$. Also this case, as the previous one, has an equivalent description in terms of a scalar field, but with a standard kinetic term. The main effect of dark energy is to modify the low multipoles region of the CMB power spectrum, unfortunately the one where high cosmic variance prevents a precise determination of the cosmological parameters.

Even worse, the model suffers from intrinsic degeneracies. At zeroth order, i.e. in the background, 1) if $\alpha \sim 0$ the dynamical part of the affine component behaves like dark matter, while, 2) if $\alpha \sim -1$ it can replace the cosmological constant. Since we fixed the speed of sound equal to 1, the first degeneracy is not present because dark matter and the affine component are different at the perturbation level. We are left with the second degeneracy, that is clearly visible in the flat likelihood for Ω_Λ and the broad likelihood for α. We obtain a rather loose constraint on α, i.e. $\alpha = -1.2 \pm 0.4$, while $\Omega_\Lambda = 0.5 \pm 0.2$. When we add the matter power spectrum, the $\Omega_\Lambda - \alpha$ degeneracy is partially removed. The result is a slightly tighter constraint on α, which is $\alpha = -1.1 \pm 0.2$.

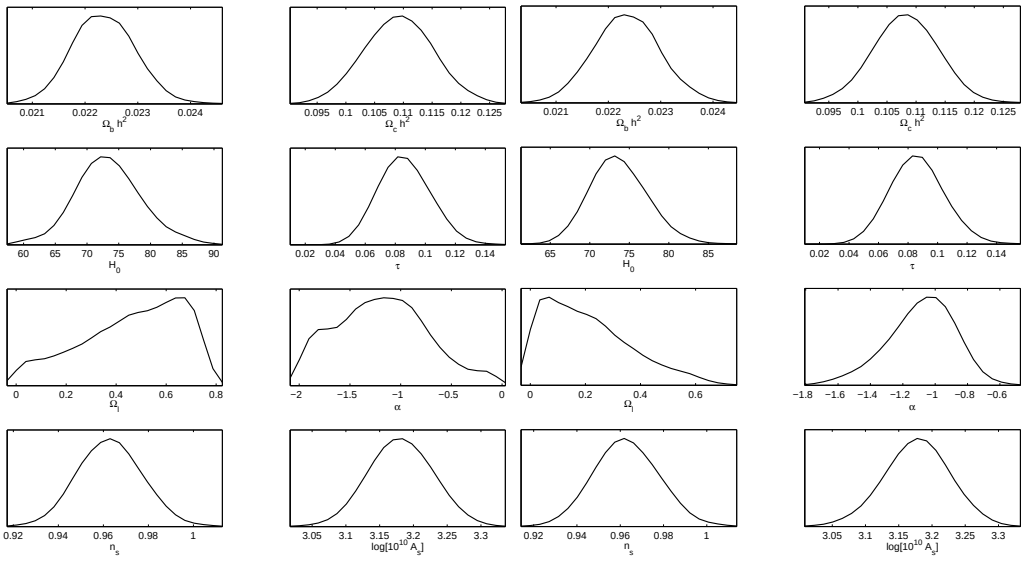

Figure 2.19: α**CDM - c$^2_{\rm eff} = 1$**: Parameter likelihoods computed for the αCDM model when the sound speed is fixed to $c^2_{\rm eff} = 1$. The left panel is CMB alone, the right panel is CMB combined with the matter power spectrum. The almost flat likelihood for Ω_Λ together with the broad one for α reflect the degeneracies of the model. Adding matter power spectrum data helps to break this degeneracy since it forces $\Omega_c h^2$ to be of the order of 0.11 and $\alpha \sim -1$. However, Ω_Λ remains essentially unconstrained.

αCDM - c$^2_{\rm eff} = 0$ The results are only marginally affected by the value of the sound speed of the dark component (fig. 2.20), since the CMB is basically insensitive to the sound speed of dark energy. We find $\alpha = -1.1 \pm 0.4$ and $\Omega_\Lambda = 0.5 \pm 0.2$. When the matter power spectrum is included in the analysis these change to $\alpha = -1.0 \pm 0.3$ and $\Omega_\Lambda = 0.3 \pm 0.2$

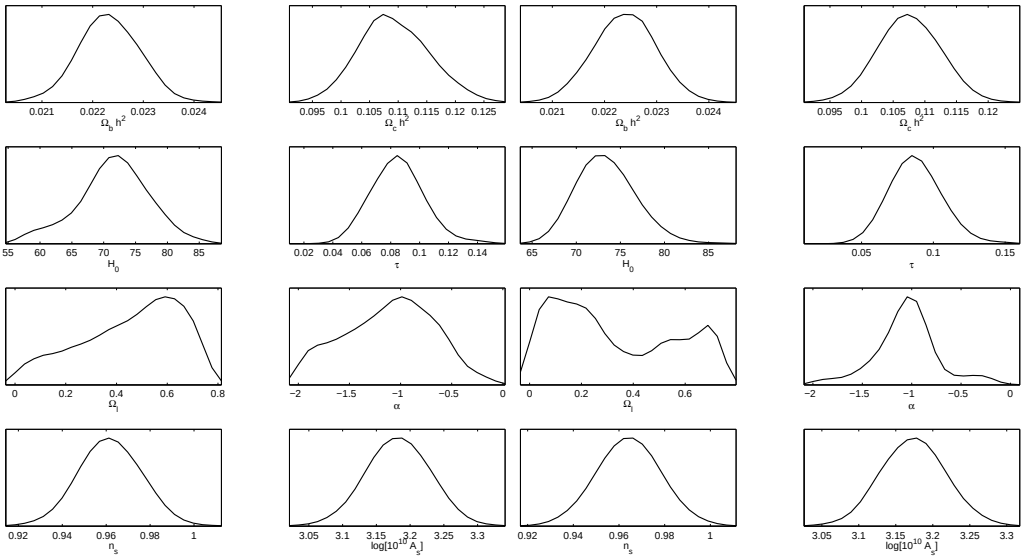

Figure 2.20: α**CDM - c$^2_{\rm eff}$ = 0**: Parameter likelihoods for the αCDM model when the sound speed is fixed to $c^2_{\rm eff} = 0$. The left panel is from CMB alone, the right panel is from CMB combined with the matter power spectrum. The results are very close to those obtained in the case of sound speed equal to 1.

αCDM - c$^2_{\rm eff} = \alpha$ When the dark component is forced to be barotropic the only degeneracy we are left with is the first degeneracy mentioned above, since $\alpha \sim 0$. The result is $\Omega_\Lambda = 0.76 \pm 0.03$ while Ω_c and α are badly constrained ($\alpha = (6 \pm 9) \times 10^{-3}$): a lower value of Ω_c can be balanced by the dynamical part of the affine component. When the matter power spectrum is added we obtain a slightly tighter constraint on Ω_Λ ($\Omega_\Lambda = 0.74 \pm 0.02$), while Ω_c is determined by the shape of the spectrum. This implies actually a broad likelihood for the parameter α, since the coefficient $(\rho_{X0} - \rho_\Lambda) \simeq 0$. We obtain $\alpha = (1.9 \pm 1.4) \times 10^{-2}$. The figure 2.21 summarises the results described above.

2.3.3 Conclusions

We studied the effect of an affine EoS fluid model applied to the dark sector, both as a unified description of dark matter and an effective cosmological constant, and as a pure dark energy component. Our model makes use of a dynamical parameterisation relating p and ρ, as opposed to the usual kinematics description of the EoS parameter in terms of its current value and its first derivative. In a previous paper Balbi et al. (2007) we carried out a comparison of the background evolution of this model with existing cosmological observations. In the present work, we focused on the behaviour of cosmological perturbations, and compared the theoretical predictions with the CMB WMAP 5 year data, and with the SDSS large scale structure data.

Table 2.2: Best fit parameter values for αDM.

models/params	ΛCDM +	αDM - bar		αDM - $c^2_{\text{eff}} = 0$	
	SNe & BAO (WMAP5)	CMB	MPS	CMB	MPS
$\Omega_b h^2$	0.02265 ± 0.00059	0.0223 ± 0.0007	0.0223 ± 0.0006	0.0224 ± 0.0006	0.0224 ± 0.0003
$\Omega_c h^2$	0.1143 ± 0.0034	-	-	-	-
H_0	70.1 ± 1.3	75 ± 5	71 ± 2	69 ± 6	67 ± 4
τ	0.084 ± 0.016	0.090 ± 0.018	0.083 ± 0.016	0.086 ± 0.017	0.085 ± 0.017
n_s	0.960 ± 0.014	0.99 ± 0.03	0.960 ± 0.014	0.959 ± 0.015	0.957 ± 0.014
$\log(10^{10} A_s)\|_{k=0.002}$	3.20 ± 0.08	3.10 ± 0.08	3.19 ± 0.04	3.19 ± 0.05	3.19 ± 0.04
Ω_Λ	0.721 ± 0.015	0.76 ± 0.04	0.73 ± 0.02	0.70 ± 0.09	0.69 ± 0.05
α	-	$(8 \pm 11) \times 10^{-4}$	$(0.2 \pm 4) \times 10^{-7}$	$(-1.5 \pm 3) \times 10^{-3}$	$(-2 \pm 2) \times 10^{-3}$

Table 2.3: Best fit parameter values for αCDM.

models/params	αCDM - bar		αCDM - $c^2_{\text{eff}} = 0$		αCDM - $c^2_{\text{eff}} = 1$	
	CMB	MPS	CMB	MPS	CMB	MPS
$\Omega_b h^2$	0.0224 ± 0.0007	0.0220 ± 0.0007	0.0223 ± 0.0006	0.0224 ± 0.0006	0.0224 ± 0.0006	0.0224 ± 0.0006
$\Omega_c h^2$	0.07 ± 0.03	0.106 ± 0.004	0.109 ± 0.006	0.107 ± 0.006	0.109 ± 0.006	0.107 ± 0.006
H_0	74 ± 4	72 ± 2	71 ± 6	73 ± 3	73 ± 5	74 ± 3
τ	0.087 ± 0.017	0.083 ± 0.017	0.085 ± 0.018	0.088 ± 0.017	0.086 ± 0.016	0.085 ± 0.018
n_s	0.975 ± 0.019	0.964 ± 0.015	0.962 ± 0.014	0.964 ± 0.014	0.963 ± 0.014	0.963 ± 0.015
$\log(10^{10} A_s)\|_{k=0.002}$	3.15 ± 0.06	3.19 ± 0.05	3.18 ± 0.05	3.17 ± 0.04	3.18 ± 0.05	3.17 ± 0.05
Ω_Λ	0.76 ± 0.03	0.74 ± 0.02	0.5 ± 0.2	0.3 ± 0.2	0.5 ± 0.2	0.2 ± 0.2
α	$(6 \pm 9) \times 10^{-3}$	$(1.9 \pm 1.4) \times 10^{-2}$	-1.1 ± 0.4	-1.0 ± 0.3	-1.2 ± 0.4	-1.1 ± 0.2

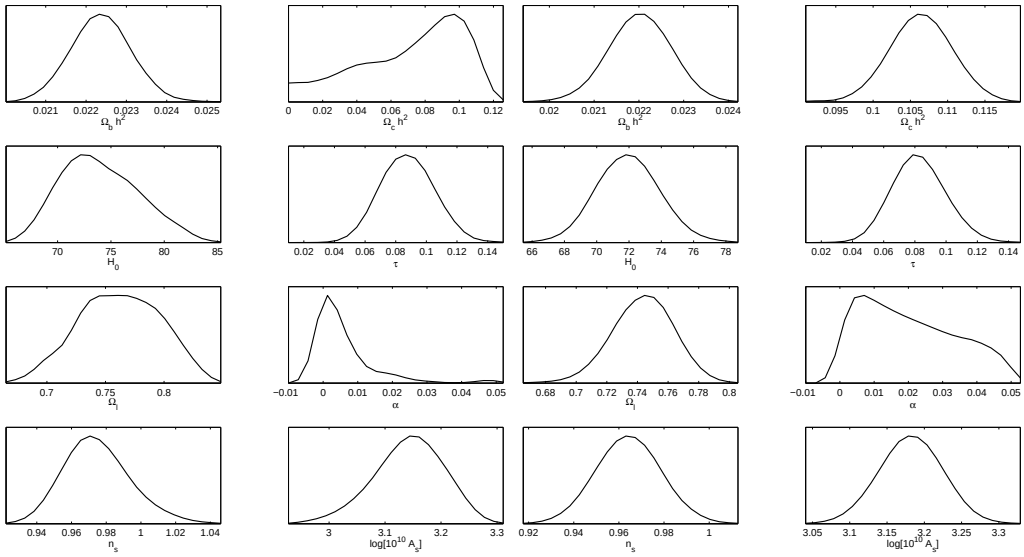

Figure 2.21: α**CDM - c$^2_{\rm eff}$** $= \alpha$: CMB alone, left panel, and CMB combined with MPS, right panel, likelihoods for the pure barotropic αCDM model ($c^2_{\rm eff} = \alpha$). The CMB alone likelihoods show the degeneracy between $\Omega_c h^2$ and Ω_Λ, being α close to 1. Adding the matter power spectrum $\Omega_c h^2$ and Ω_Λ are better constrained, but we lost any information on α (this is because we assume a flat universe).

As a first result, we obtained much tighter constraints on the parameters of the model with respect to the analysis carried out the background observables in Balbi et al. (2007), confirming that perturbations should be properly included in the calculations when developing effective models for the dark sector Valiviita et al. (2008).

In the case when the fluid is treated as a unified dark component, we get values of the effective cosmological constant $\Omega_\Lambda \simeq 0.7$, essentially independent of the speed of sound. For the equation of state parameter α, the constraints vary when the fluid is treated as barotropic (resulting in a slightly positive α) or a vanishing speed of sound is assumed (resulting in a slightly negative α). Both cases are however compatible with $\alpha = 0$ at one sigma confidence level. The inclusion of the matter power spectrum in the analysis has generally the effect of shrinking the confidence interval on the parameters, in particular in the barotropic case, due to the effect of α on the Jeans length of the perturbations Quercellini et al. (2007).

When standard dark matter is included, the effects of α on the clustering process is less relevant, because the matter-like component of the unified fluid is forced to mimic the cosmological constant behaviour. This is apparent from the fact that the α best fit value moves to $\alpha \sim -1$ which is typical of a cosmological constant. The constraints in the barotropic case remain quite tight, but get larger when the sound speed is set to zero. We also considered the case with a sound of speed equal to unity, which describes a scalar field behaviour. Also in this case the constraints on α are rather loose.

It is important to remember that these results are achieved within the context of a constant speed of sound. This represents a strong constraint and it is the main reason why we obtained nearly pressure-less components. We need a vanishing sound speed during the structure formation epoch. An extension of this scenario is attempted in Piattella et al. (2010) where time-dependent sound speed models are discussed.

Conclusions

In this chapter we have discussed in detail some issues related to the dark energy problem. Dark energy is a new component of the Universe, surprisingly the largest one, which theorists have introduced to explain the late time acceleration of the Universe expansion. The evidence for such behaviour is now compelling. We found further evidence for dark energy by measuring the ISW effect cross-correlating CMB and LSS datasets at a high confidence level. Although there are no significant evidences of departures from the simplest kind of dark energy, i. e. a cosmological constant, it is tempting to explore other scenarios, with more complicated models, since this can help to solve the coincidence problem and possible candidates can be found in fundamental particle theories. We discussed an example involving two coupled scalar fields and constrained the model parameters using several observables. Nonetheless the nature of the dark energy remains a mystery and more accurate experiments are required when trying to rule out models.

Chapter 3

Statistical Toolbox: Needlets Frame

...reality is not external.
Reality exists in the human mind,
and nowhere else.
Not in the individual mind,
which can make mistakes,
and in any case soon perishes:...

("Nineteen Eighty-Four", G. Orwell)

Cosmic microwave background radiation represents a fundamental tool to probe the Universe and test our theories. Its analysis is naturally performed both in real space, where we measure the temperature anisotropies and it is easier to deal with the partial sky coverage and the experimental noise, and in the harmonic domain, where beam treatment and cosmological parameters estimation are more effective. Both spaces have advantages and disadvantages. In this chapter we introduce a new wavelet basis on the sphere, more properly a frame, called *needlets*, which combines the virtues of the two spaces on which the temperature anisotropies decomposition is particularly fruitful.

Astronomical data generally give rise to complex hierarchical structures, eventually described as fractals, which require a multi-scale investigation. The wavelet transform represents then a very useful tool to CMB and astrophysical data analysis in general, since it provides a frequency decomposition of the field, keeping trace of the local features in pixel space where the field is defined. For this reason wavelets perform very well in constraining statistical properties of a given field (such as isotropy and Gaussianity), as well as its morphology; moreover they can be used for reconstruction algorithms such as *shrinkage* or *thresholding*. See for example Wiaux et al. (2005); Anestis (2007) and references therein.

Over the last few years, wavelets have emerged as one of the most powerful tools of CMB data analysis, finding applications in virtually all areas where statistical methods are required; a very incomplete list of references should include testing for non-Gaussianity (see Vielva et al. (2004); Cabella et al. (2004)), foreground subtraction (Hansen et al. (2006)), point source detection (Sanz et al. (2006)), component separation (Moudden et al. (2005); Starck et al. (2006)), polarisation analysis (Cabella et al. (2007)), denoising (Sanz et al., 1999) and many others. The reason for such a strong interest is easily understood. As it is well-known, CMB models are best analysed in the frequency domain, where the behaviour at different multipoles can be investigated separately; on the other hand, partial sky coverage and other missing observations make the evaluation of exact spherical harmonic transforms troublesome. The combination of these two features makes the time-frequency localisation properties of wavelets most valuable.

In Sec. 3.1 we introduce the needlets formalism, while in Sec. 3.2 we discuss in detail their properties, comparing them with other filter constructions. In Sec. 3.3 we develop the estimators we will use in the following analysis, and finally we conclude presenting the numerical implementation we adopt.

3.1 Operative Definition of a Spherical Needlets Frame

Despite the wide agreement on their importance as a data analysis instrument, the derivation of a wavelets basis on the sphere is still an open issue for research. Many efforts have been undertaken in this area, most of them being based upon the so-called tangent plane approach (Antoine & Vandergheynst, 1999). In this framework, a flat sky approximation is entertained locally, and then some form of standard plane wavelets are implemented. Directional wavelets have been advocated by McEwen et al. (2006, 2007), again by means of a tangent plane approximation. An interesting attempt to overcome the tangent plane approximation is due to Sanz et al. (2006). A detailed study of the wavelets construction in terms of group theory is discussed in Wiaux et al. (2007, 2008).

A new approach to spherical wavelets was introduced in the statistical literature by Baldi et al. (2006), adapting tools proposed in the functional analysis literature by Narcowich et al. (2006); the first application to CMB data is due to Pietrobon et al. (2006), where needlets are used to estimate (cross-)angular power spectra in order to search for dark energy imprints on the correlation between large scale structures and CMB (Sachs & Wolfe, 1967). A detailed description of the results obtained are discussed in Sec. 2.1. Guilloux et al. (2007) investigates the effect of different window functions in needlets constructions; whereas Baldi et al. (2007) provides further mathematical results on their behaviour for partially observed sky-maps. Needlets applications have been applied to

angular power spectrum estimation in the presence of noise (Fay et al., 2008; Faÿ & Guilloux, 2008), estimation of the bispectrum (Lan & Marinucci, 2008b) applied to the WMAP 5-year data release by Pietrobon et al. (2009) and Rudjord et al. (2009a) to constrain the primordial non-Gaussianity parameter (see Sec.4.2). The bispectrum formalism has been further exploited by Pietrobon et al. (2009) and Rudjord et al. (2009b) who addressed the sky asymmetry issue within the three-point correlation function (see Sec. 4.3) and the primordial non-Gaussianity parameter. Foreground component separation has been studied by Delabrouille et al. (2009), while analysis of directional data are described in Baldi et al. (2008). Recently, the needlet formalism has been extended to the polarisation field, as discussed by Geller & Marinucci (2008); Geller et al. (2008) and Geller et al. (2009).

Needlets enjoy several features which are not in general granted by other spherical wavelets construction; we anticipate some of these features, which we shall investigate more deeply in the Sections to come. More precisely:

a) they do not rely on any tangent plane approximation (compare Sanz et al. 2006), and take advantage of the manifold structure of the sphere;

b) being defined in harmonic space, they are computationally very convenient, and natively adapted to standard packages such as HEALPix[1] (Górski et al., 2005);

c) they allow for a simple reconstruction formula (see Eq. 3.5), where the same needlets functions appear both in the direct and the inverse transform (see also Kerkyacharian et al. (2007)). This property is the same as for spherical harmonics but it is *not* shared by other wavelets systems such as the well-known Spherical Mexican Hat Wavelet (hereafter SMHW);

d) they are quasi-exponentially (i.e. faster than any polynomial) concentrated in pixel space, see Eq. 3.6 below;

e) they are exactly localised on a finite number of multipoles; the width of this support is explicitly known and can be specified as an input parameter (see Eq. 3.1);

f) random needlets coefficients can be shown to be asymptotically uncorrelated (and hence, in the Gaussian case, independent) at any fixed angular distance, when the frequency increases. This capital property can be exploited in several statistical procedures, as it allows us to treat needlets coefficients as a sample of independent and identically distributed coefficients on small scales, at least under the Gaussianity assumption.

[1] http://healpix.jpl.nasa.gov

The following discussion can be found in Marinucci et al. (2008) and Pietrobon (2009) where a numerical code is provided. Complementary mathematical analyses can be found in Geller & Mayeli (2007); Lan & Marinucci (2008a) and Mayeli (2008).

We start by outlining briefly the construction of a needlets basis. More details can be found in Narcowich et al. (2006), and in Baldi et al. (2006). We shall discuss the details of the construction step by step, in order to provide to potential users a clear recipe for needlets implementation.

We first recall that the spherical needlet (function) is defined as

$$\psi_{jk}(\hat{\gamma}) = \sqrt{\lambda_{jk}} \sum_{\ell} b(\frac{\ell}{B^j}) \sum_{m=-\ell}^{\ell} \overline{Y}_{\ell m}(\hat{\gamma}) Y_{\ell m}(\xi_{jk}); \tag{3.1}$$

where γ and ξ_{jk} are directions on the sphere, $Y_{\ell m}$ is a spherical harmonic function, with $\overline{Y}_{\ell m}$ identifying its complex conjugate, and $b(x)$ is a filter function defined for $x \in [1/B, B]$, which the entire needlet construction relies on. Here, we use $\{\xi_{jk}\}$ to denote a set of *cubature points* on the sphere, corresponding to frequency j; in practice, we shall identify these points with the pixel centres in HEALPix. Also, λ_{jk} denotes the cubature weights, which for simplicity can be envisaged as $1/N_p$, N_p denoting the number of pixels for the chosen *HEALPix* resolution (see Pietrobon et al. (2006) and Sec. 2.1).

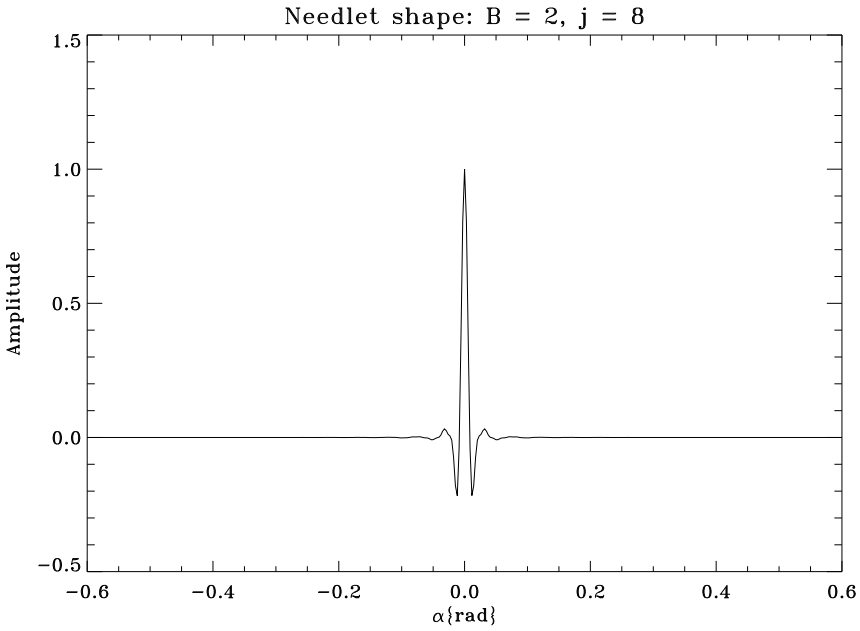

Figure 3.1: Needlets in pixel space. $B = 2$, $j = 8$

Intuitively, needlets should be viewed as a convolution of the projection operator $\sum_{m=-\ell}^{\ell} \overline{Y}_{\ell m}(\hat{\gamma}) Y_{\ell m}(\xi_{jk})$ with a suitably chosen window function $b(.)$. Special properties of $b(.)$ ensure that the needlets enjoy quasi-exponential localisation properties in pixel space. Formally, we must ensure that (Narcowich et al., 2006; Baldi et al., 2006):

- $b^2(.)$ has support in $[\frac{1}{B}, B]$, and hence $b(\frac{\ell}{B^j})$ has support in $\ell \in [B^{j-1}, B^{j+1}]$
- the function $b(.)$ is infinitely differentiable in $(0, \infty)$.
- we have

$$\sum_{j=1}^{\infty} b^2(\frac{\ell}{B^j}) \equiv 1 \text{ for all } \ell > B. \tag{3.2}$$

It is immediate to see that property (i) ensures the needlets have bounded support in the harmonic domain; property (ii) is the crucial element in the derivation of the localisation properties, which we shall illustrate in the following section. Finally, property (iii) is necessary to establish the reconstruction formula which we shall discuss below; functions such as $b^2(.)$ are called *partitions of unity*.

There are of course many possible constructions satisfying (i-iii); indeed an interesting theme for future research is the derivation of optimal windows satisfying these three conditions (compare Guilloux et al. 2007). We expect, however, that the choice of $b(.)$ will only exert second-order effects on the final estimates (Lan & Marinucci, 2008a). An explicit recipe for the construction of $b(.)$ is as follows.

1. Construct the function

$$f(t) = \begin{cases} \exp(-\frac{1}{1-t^2}), & -1 \leq t \leq 1 \\ 0, & \text{otherwise} \end{cases}.$$

   It is immediate to check that the function $f(.)$ is C^∞ and compactly supported in the interval $(-1, 1)$

2. Construct the function

$$\psi(u) = \frac{\int_{-1}^{u} f(t)dt}{\int_{-1}^{1} f(t)dt}.$$

   The function $\psi(.)$ is again C^∞; it is moreover non-decreasing and normalised so that $\psi(-1) = 0$, $\psi(1) = 1$

3. Construct the function

$$\varphi(t) = \begin{cases} 1 & \text{if } 0 \leq t \leq \frac{1}{B} \\ \psi(1 - \frac{2B}{B-1}(t - \frac{1}{B})) & \text{if } \frac{1}{B} \leq t \leq 1 \\ 0 & \text{if } t > 1 \end{cases}$$

Here we are simply implementing a change of variable so that the resulting function $\varphi(.)$ is constant on $(0, B^{-1})$ and monotonically decreasing to zero in the interval $(B^{-1}, 1)$. Indeed it can be checked that

$$1 - \frac{2B}{B-1}(t - \frac{1}{B}) = \begin{cases} 1 & \text{for } t = \frac{1}{B} \\ -1 & \text{for } t = 1 \end{cases}$$

and

$$\begin{aligned} \varphi(\frac{1}{B}) &= \psi(1) = 1 \\ \varphi(1) &= \psi(-1) = 0 \end{aligned}$$

4. Construct

$$b^2(\xi) = \varphi(\frac{\xi}{B}) - \varphi(\xi)$$

The expression for $b^2(.)$ is meant to ensure that the function satisfies the partition-of-unity property of Eq. 3.2. Needless to say, for $b(\xi) = \left\{\varphi(\frac{\xi}{B}) - \varphi(\xi)\right\}^{1/2}$ we take the positive root.

In Fig. 3.2 we show the set of filter functions in ℓ space for the choice $B = 2$. They result in a homogeneous binning in $\log \ell$.

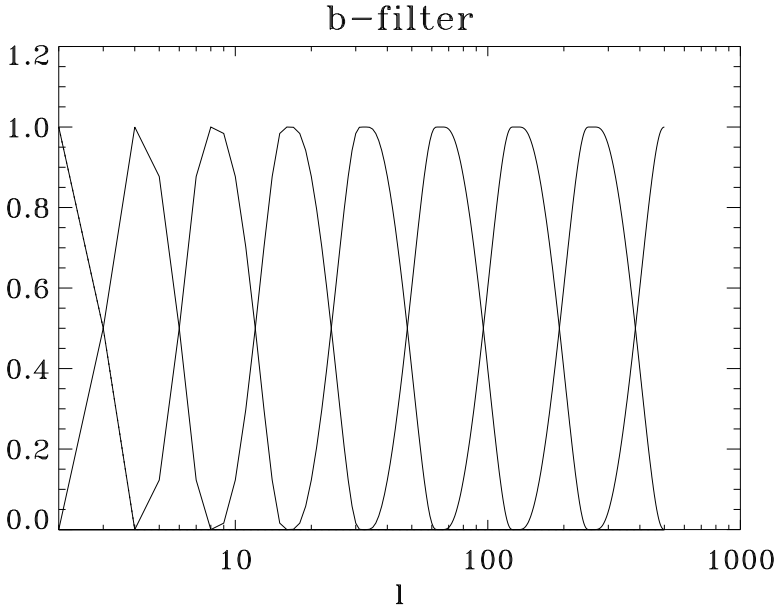

Figure 3.2: Filter function in ℓ-space which the needlet construction relies on. Set computed for $B = 2$.

Needlets coefficients for an arbitrary temperature field on the sky are hence given by

$$\begin{aligned}
\beta_{jk} &= \int_{\mathbb{S}^2} T(x)\psi_{jk}(x)dx \\
&= \int_{\mathbb{S}^2} \left\{ \sum_{\ell=1}^{\infty} \sum_{m=-\ell}^{\ell} a_{\ell m} Y_{\ell m}(x) \right\} \psi_{jk}(x)dx \\
&= \int_{\mathbb{S}^2} \sum_{\ell=1}^{\infty} \sum_{m=-\ell}^{\ell} a_{\ell m} Y_{\ell m}(x) \times \\
&\times \left\{ \sum_{\ell'=[B^{j-1}]}^{[B^{j+1}]} b\left(\frac{\ell'}{B^j}\right) \sum_{m'=-\ell'}^{\ell'} \overline{Y}_{l'm'}(x) Y_{\ell' m'}(\xi_{jk}) \right\} dx \\
&= \sum_{\ell'=[B^{j-1}]}^{[B^{j+1}]} b\left(\frac{\ell'}{B^j}\right) \sum_{\ell=1}^{\infty} \sum_{m=-\ell}^{\ell} a_{\ell m} \times \\
&\times \sum_{m'=-\ell'}^{\ell'} \overline{Y}_{\ell' m'}(\xi_{jk}) \left\{ \int_{\mathbb{S}^2} Y_{\ell m}(x) \overline{Y}_{\ell' m'}(x) dx \right\} \\
&= \sum_{\ell=[B^{j-1}]}^{[B^{j+1}]} b\left(\frac{\ell}{B^j}\right) \sum_{m=-\ell}^{l} a_{\ell m} Y_{\ell m}(\xi_{jk}) \, ; \qquad (3.3)
\end{aligned}$$

It is very important to stress that, although the needlets do *not* make up an orthonormal basis for square integrable functions on the sphere, they do represent a *tight frame.* In general, a tight frame on the sphere is a countable set of functions $\{e_j\}$ such that, for all square integrable functions on the sphere $f \in L^2(S^2)$, we have

$$\sum_j \langle f, e_j \rangle^2 \equiv \int_{S^2} f(\hat{\gamma})^2 d\Omega,$$

so that the norm is preserved. Of course, this norm-preserving property is shared by all orthonormal systems; however, frames do not in general make up a basis, as they admit redundant elements. They can be viewed as the closer system to a basis, for a given redundancy, see Hernández & Weiss (1996), Baldi et al. (2006) and Baldi et al. (2007) for further definitions and discussion.
In our framework, the norm-preserving property becomes

$$\sum_{j,k} \beta_{jk}^2 \equiv \sum_{\ell=1}^{\infty} \frac{2\ell+1}{4\pi} \widehat{C}_\ell \,, \tag{3.4}$$

where

$$\widehat{C}_\ell = \frac{4\pi}{2\ell+1} \sum_m |a_{\ell m}|^2$$

is the raw angular power spectrum of the map $T(\hat{\gamma})$. Identity 3.4 has indeed been verified by means of numerical simulations and implicitly provides the correct normalisation for needlets. It is basically a consequence of the peculiar partition-of-unity property of $b(\cdot)$ (Eq. 3.2). Of course this property is not generally shared by other constructions such as SMHW, where the wavelets functions are normalised to unity in the real domain. Eq. 3.4 is related to a much more fundamental result, i.e. the reconstruction formula

$$T(\hat{\gamma}) \equiv \sum_{j,k} \beta_{jk} \psi_{jk}(\hat{\gamma}) \tag{3.5}$$

which in turn is a non-trivial consequence of the careful construction leading to Eq. 3.2. As mentioned before, the simple reconstruction formula of Eq. 3.5 is typical of tight frames but does not hold in general for other wavelets systems. It is easy to envisage many possible applications of this result when handling masked data and we hence view Eq. 3.5 as a clear advantage of the needlets over their competitors.

3.2 Localisation properties

The following quasi-exponential localisation property of needlets is due to Narcowich et al. (2006) and motivates their name:

For any $M = 1, 2, ...$ there exists a positive constant c_M such that for any point $x \in S^2$ we have

$$|\psi_{jk}(\hat{\gamma})| \leq \frac{c_M B^j}{(1 + B^j \arccos(< x, \xi_{jk} >)^M} \,. \tag{3.6}$$

We recall that $\arccos(< x, \xi_{jk} >)$ is just the natural distance on the unit sphere between the points (x, ξ_{jk}). The meaning of Eq. 3.6 is then clear: for any fixed angular distance, the value of $\psi_{jk}(\hat{\gamma})$ goes to zero quasi-exponentially in the parameter B. This clearly establishes an excellent localisation behaviour in pixel space. Note that the constants c_M do depend on the form of the weight function $b(\cdot)$, and in particular on the value of the bandwidth parameter B; typically a better localisation in multipole space (i.e., a value of B very close to unity) will entail a larger value of c_M, that is, less concentration in pixel space for any fixed j. The resulting trade-off in the behaviour over the harmonic and real spaces is expected: smaller values of B correspond to a tighter localisation in harmonic space (less multipoles entering into any needlet), whereas larger values ensure a faster decay in real space.

Due to their localisation properties, needlets are especially useful in the analysis of partial sky coverage. In fact, in view of Eq. 3.6 we expect the value of needlets coefficients to be mildly affected by the presence of gaps in the maps. To illustrate this important feature, we plot the quantity

$$\chi_{jk} = \frac{< (\beta_{jk,mask} - \beta_{jk})^2 >}{< \beta_{jk}^2 >} \tag{3.7}$$

in Fig. 3.3, where the Kp0 mask [2], that is used to remove Galactic emission and point sources from WMAP data (roughly 75% of the sky), is applied. The expected values of Eq. 3.7 are again evaluated by means of 100 Monte Carlo simulations; in particular we focus on needlets coefficients corresponding to $B = 2.72$ and $j = 5$, which amounts to a range in multipoles space in the order of $58 < \ell < 398$. To put our results in perspective, in the same Figure we show analogous findings with the use of a top-hat binning filter and SMHW. We recall the SMHW formula

$$\Psi(y, R) \;=\; \frac{1}{\sqrt{2\pi} N(R)} \left[1 + \left(\frac{y}{2}\right)^2\right]^2 \cdot \left[2 - \left(\frac{y}{R}\right)^2\right] \exp\left(-y^2/2R^2\right)$$

[2] See LAMBDA website, http://lambda.gsfc.nasa.gov/

where $y = 2\tan\theta/2$ (θ is the polar angle), R is the scale of convolution and $N(R)$ a normalisation factor (Martínez-González et al., 2002). Under these circumstances, needlets

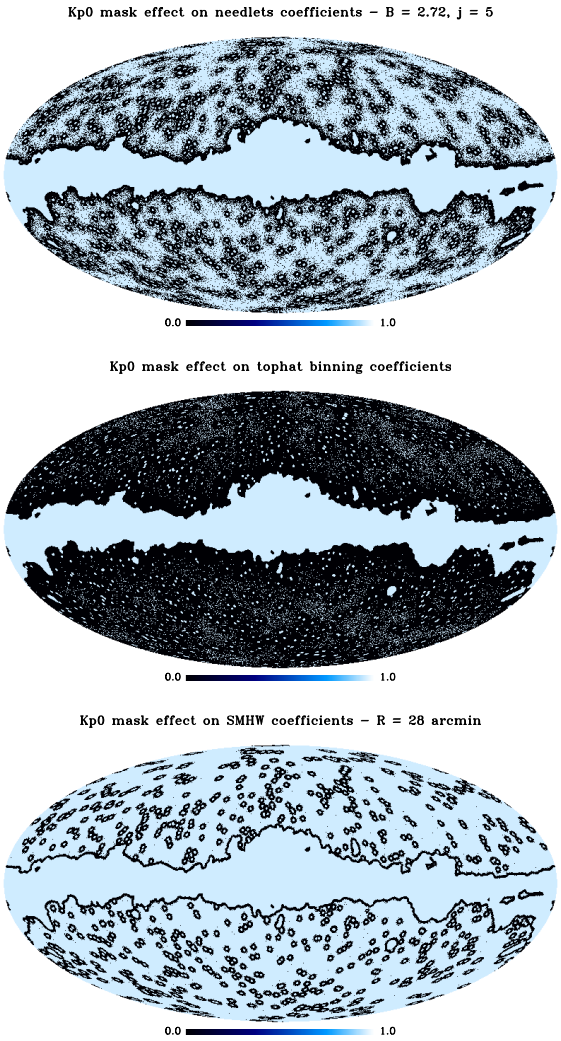

Figure 3.3: Effect of Kp0 on needlets coefficients, visualised by plotting on a sky map the quantity defined in Eq. 3.7. From top to bottom, the result for needlets, flat binning, and SMHW (28arcmin).

coefficients are well localised, but slightly sensitive to the mask. Indeed, only 56% of the pixel are changed by less than 0.1; SMHW coefficients perform a bit better (73%) while a simple top-hat binning fails completely (only 6%). The difference between the two wavelets bases can be due to the different power that they give to multipoles (see fig. 3.5). In fact the performance of needlets can be improved choosing the appropriate B^j, that defines the optimal shape for the window $b(\cdot)$, given the multipoles range of interest. For details see Guilloux et al. (2007). In the same paper, the authors argue that an optimal filter can be adapted to deconvolve a specific mask: this property provides a further degree of flexibility to the needlets toolbox.

In Baldi et al. (2006), another relevant property of needlets coefficients was discussed, namely their asymptotic uncorrelation at any fixed angular distance, for growing frequencies j. More explicitly, at high frequency needlets coefficients can be approximated as a sample of identically distributed and independent (under Gaussianity) coefficients, and this property opens the way to a huge toolbox of statistical procedures for CMB data analysis (for instance, for testing Gaussianity, Sec. 4.3 and isotropy, Sec. 4.1). Also, in view of Eq. 3.3, for full sky maps and in the absence of any mask we should expect the theoretical correlation to be identically zero whenever $|j_1 - j_2| \geq 2$.

The probabilistic properties of the coefficients β_{jk} have been established in Baldi et al. (2007); in that paper, it is shown that for any two (sequence of) pixels $\xi_{jk}, \xi_{jk'}$ such that their angular distance is larger than a positive ε, for all j, we have

$$\frac{\langle \beta_{jk}\beta_{jk'}\rangle}{\sqrt{\langle \beta_{jk}^2\rangle \langle \beta_{jk'}^2\rangle}} \leq \frac{c_M}{(s^j\varepsilon)^{M-1}} \text{ for all } M = 1, 2, 3, \ldots \tag{3.8}$$

thus proving wavelets coefficients are asymptotically uncorrelated as $j \to \infty$ for any fixed angular distance; Eq. 3.8 is clearly a probabilistic counterpart of Eq. 3.6. To the best of our knowledge, this is the first example of such kind of results for any type of spherical wavelets: asymptotic uncorrelation (i.e. independence in the Gaussian case) simplifies enormously any statistical inference procedure. In particular, Eq. 3.8 is used in Baldi et al. (2007) to derive analytically the asymptotic behaviour of a number of procedures based on needlets, including tests on angular power spectra or tests for Gaussianity and isotropy.

In order to test this property, let us define the realized correlation between two different scales j_1, j_2 as

$$\rho_{j_1 j_2} = \frac{\sum_k \langle \beta_{j_1 k}\beta_{j_2 k}\rangle}{\sqrt{\sum_k \langle \beta_{j_1 k}^2\rangle \sum_k \langle \beta_{j_2 k}^2\rangle}}. \tag{3.9}$$

By using Eq. 3.3 one has that:

$$\langle \beta_{j_1 k}\beta_{j_2 k}\rangle = \sum_\ell b(\ell/B^{j_1})\, b(\ell/B^{j_2})\, C_\ell \sum_m K_{\ell\ell mm} \tag{3.10}$$

$$\tag{3.11}$$

where C_ℓ is the underlying CMB angular power spectrum and the coupling kernel $K_{\ell\ell' mm'}$ is defined in terms of the observed mask $W(\hat{\gamma})$ (see e.g. Hivon et al. (2002)):

$$K_{\ell\ell' mm'} = \int_{S^2} Y_{\ell m}(\hat{\gamma}) Y_{\ell' m'}(\hat{\gamma}) W(\hat{\gamma}) d\Omega$$

Note that, in the absence of gaps (i.e. $W(\hat{\gamma}) = 1$), $\sum_m K_{\ell\ell mm}$ reduces simply to $(2\ell+1)$.

Table 3.1: Needlets correlation parameter. $B = 2.72$ without gaps

j/j'	1	2	3	4	5
1	1.000	0.275	0.001	0.001	0.003
2	-	1.000	0.248	0.001	0.001
3	-	-	1.000	0.268	0.001
4	-	-	-	1.000	0.242
5	-	-	-	-	1.000

Table 3.2: Needlets correlation parameter. $B = 2.72$ with gaps

j/j'	1	2	3	4	5
1	1.000	0.420	0.140	0.040	0.060
2	-	1.000	0.335	0.023	0.001
3	-	-	1.000	0.291	0.004
4	-	-	-	1.000	0.252
5	-	-	-	-	1.000

Equation 3.9 can not be expected to be reproduced exactly, due to numerical approximations; in particular, we should stress that theoretical results are derived under the assumption that needlets coefficients are evaluated at *exact* cubature points, so that the $\{a_{lm}\}$ are precisely reconstructed from the maps. Of course, this is not the case in practice; however, we do expect small and vanishing values for $j_1 \ll j_2$. At the same time, we expect this correlation to increase on the presence of sky cuts, but less so than for other bases. Here, we want to illustrate the practical relevance of this mathematical results by means of simulations on the correlation coefficient. More precisely, we computed the quantity 3.9 by performing a Monte Carlo over 100 simulations. Our findings are shown in Tables 3.1, 3.2.

We view these results as very encouraging. In the absence of a mask, the correlation coefficient is by any practical means virtually negligible for all frequency distances greater or equal than 2, while at distance $\Delta j = 1$ the correlation is around ~ 0.25 in good agreement with Eq. 3.9 which predicts 0.22 for our input parameters. In the presence of sky cuts, the performance deteriorates as expected only at low j where it exceeds a few percentage points, as shown for our simulations in the case of the Kp0 mask. A computation analogous to 3.9 yields for SMHW the theoretical results reported in Table 3.3; note how we have no-zero values at all distances. Numerical results to support the theoretical findings are provided by Tables 3.4, 3.5. We believe these compared results strongly

Table 3.3: Theoretical correlation for Needlets and SMHW

corr/Δj	0	1	2	3	4
Needlets	1.000	0.220	0.000	0.000	0.000
SMHW	1.000	0.500	0.100	0.014	0.002

Table 3.4: SMHW correlation parameter without gaps. The scale R is given in arcmin.

R/R'	1792	896	448	224	112	56	28
1792	1.000	0.503	0.109	0.016	0.002	0.0002	0.00003
896	-	1.000	0.500	0.099	0.014	0.002	0.0002
448	-	-	1.000	0.510	0.103	0.014	0.002
224	-	-	-	1.000	0.511	0.104	0.014
112	-	-	-	-	1.000	0.513	0.107
56	-	-	-	-	-	1.000	0.519
28	-	-	-	-	-	-	1.000

support the potential of needlets for the implementations of statistical procedures, where uncorrelation properties are clearly a very valuable asset.

As a further comparison, we evaluated the domains in harmonic and real spaces for needlets, top-hat binning and SMHW. In particular we normalised the three bases to have roughly an equal area in the harmonic domain, paying attention to have the maximum of the power in a similar range of multipoles. Results are plotted in Fig. 3.5, 3.6. It is evident how SMHW and needlets outperform top-hat binning by two orders of magnitude in terms of localisation in real space: indeed in this domain the two wavelets constructions perform quite similarly. Moreover, in Fig. 3.8, we computed the angle where the integral of the filter functions in pixel space reaches 68%, 95% and 99% of the total

Table 3.5: SMHW correlation parameter with gaps. The scale R is given in arcmin.

R/R'	1792	896	448	224	112	56	28
1792	1.000	0.496	0.113	0.022	0.005	0.002	0.0007
896	-	1.000	0.520	0.115	0.021	0.005	0.002
448	-	-	1.000	0.523	0.114	0.021	0.005
224	-	-	-	1.000	0.520	0.114	0.020
112	-	-	-	-	1.000	0.522	0.116
56	-	-	-	-	-	1.000	0.527
28	-	-	-	-	-	-	1.000

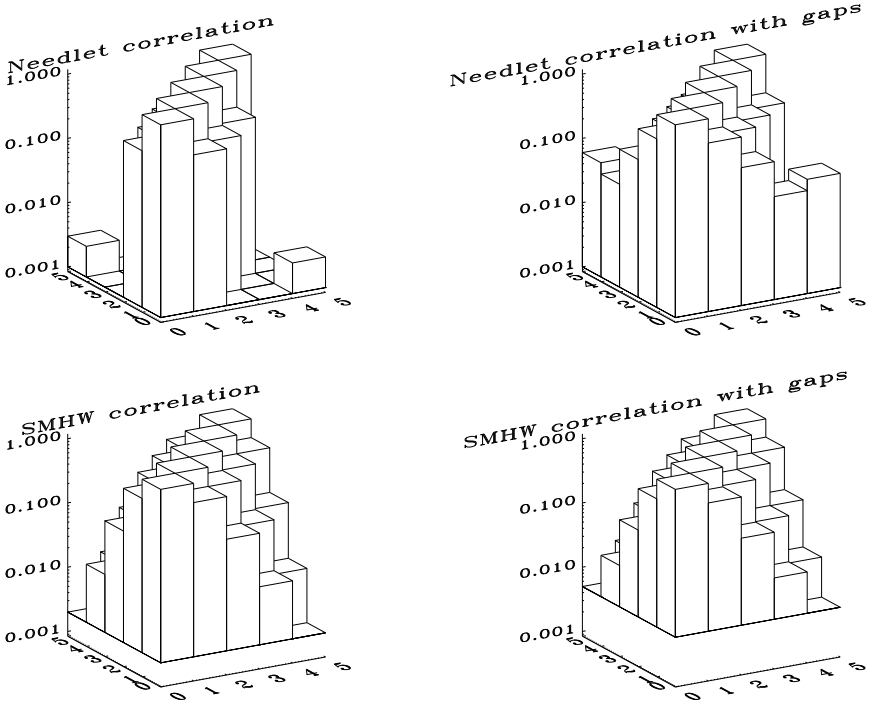

Figure 3.4: The correlation for needlets (top panels) and SMHW (bottom panels) is plotted as a function of the scale, in absence (left panels) and in presence (right panel) of sky cuts (Kp0 mask).

area, respectively. Again, it is immediate to check how at every scale needlets outperform very clearly a simple binning approach; on the other hand, SMHW seems slightly more concentrated in this setting. The linear trend for needlets in the log-log plot is a direct consequence of their construction, and in particular of the functional dependence on ℓ/B^j.

On the other hand the advantage of needlets over SMHW emerges quite clearly in the harmonic domain. More precisely, after normalising the two methods to be centred at the same angular scale, with roughly the same total power, the needlets support seems clearly more concentrated than SMHW. In particular we stress how SMHW suffer from "leakage" by the very low multipoles, i.e. exactly those most affected by sky cuts and cosmic variance. No such leakage occurs for needlets.

3.3 Building Needlets Estimators: 2- and 3- point correlation functions

In the previous sections we have introduced the spherical needlets frame, and discussed its properties which we tested by means of simulations. We also compared needlets to alternative binning choices (top-hat, SMHW) concluding that there is a wide number of

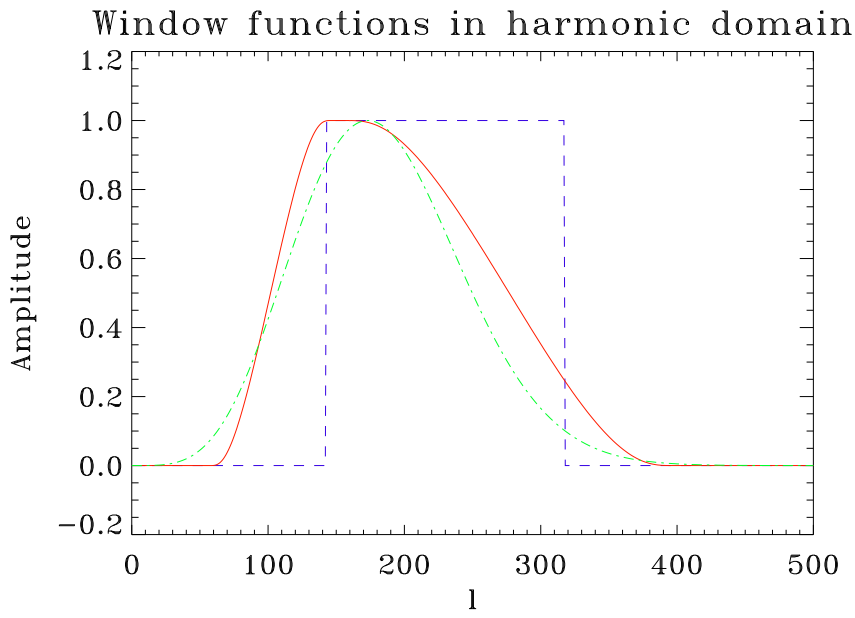

Figure 3.5: The red solid line represents needlets window function, $b(\frac{\ell}{B^j})$ in harmonic space for $B = 2.72$, $j = 5$. The blue dashed and green dot-dashed lines provide the top-hat and the SMHW window functions, respectively. The SMHW corresponds to a scale $R = 28\prime$ in pixel space.

applications in CMB data analysis where needlets perform extremely well. We now want to describe the statistical techniques which lay behind CMB data analysis achievable with needlets. We will discuss specific problems and the results we obtained in more details in the following chapters (see Chap. 2 Sec. 2.1 and Chap. 4).

The needlet coefficients of a field $T(\hat{\gamma})$ defined on the sphere are given by the projection of the field itself on the corresponding needlet $\psi_{jk}(\hat{\gamma})$, as stated by Eq. 3.3:

$$\beta_{jk} = \sqrt{\lambda_{jk}} \sum_{\ell} b(\frac{\ell}{B^j}) \sum_{m=-\ell}^{\ell} a_{\ell m} Y_{\ell m}(\xi_{jk})$$

where $a_{\ell m}$s are the spherical harmonics expansion coefficients. In Fig. 3.9 we show the needlet coefficients of WMAP 5-year temperature map for the specific choice $B = 2$ and $j = 4$. A remarkable aspect of this construction is that the needlet coefficients can be represented easily as a mollweide projection in the *HEALPix* framework. This makes dealing with needlets particularly handy, since it is easy to encode a needlets analysis using *HEALPix* routines (Pietrobon, 2009). We assume $\mathcal{X}_j = \{\xi_{jk}\}_{k=1,2,...,}$ to be the pixelization of the unit sphere $\mathbb{S}^2$ provided by *HEALPix* , with $N_{\rm side}$ such that $l_{\rm max} \equiv [B^{j+1}] \leq 2N_{\rm side}$ (with $[\cdot]$ denoting the integer part and $B > 1$). We then computed the β_{jk} coefficients for each k position given by the *HEALPix* scheme evaluating the projection operators, namely the product of $\sum_{\ell\ell'} Y_{\ell m} \overline{Y}_{ell'm'}$ for each pair of pixels ξ_{jk}, by means of the *HEALPix* software package.

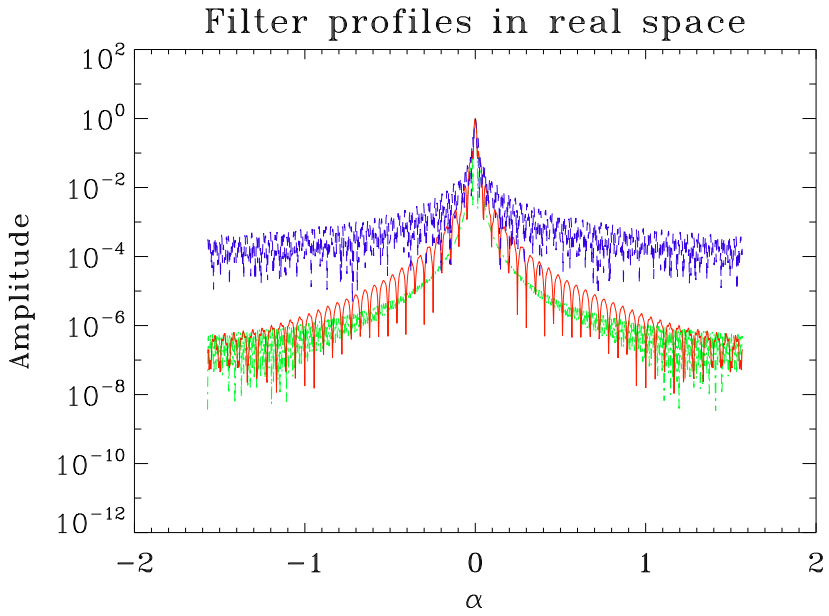

Figure 3.6: Behaviour of needlets (solid red), SMHW (dot-dashed green) and top-hat binning (blue dashed) in pixel space. The angle in horizontal axis is measured in radians.

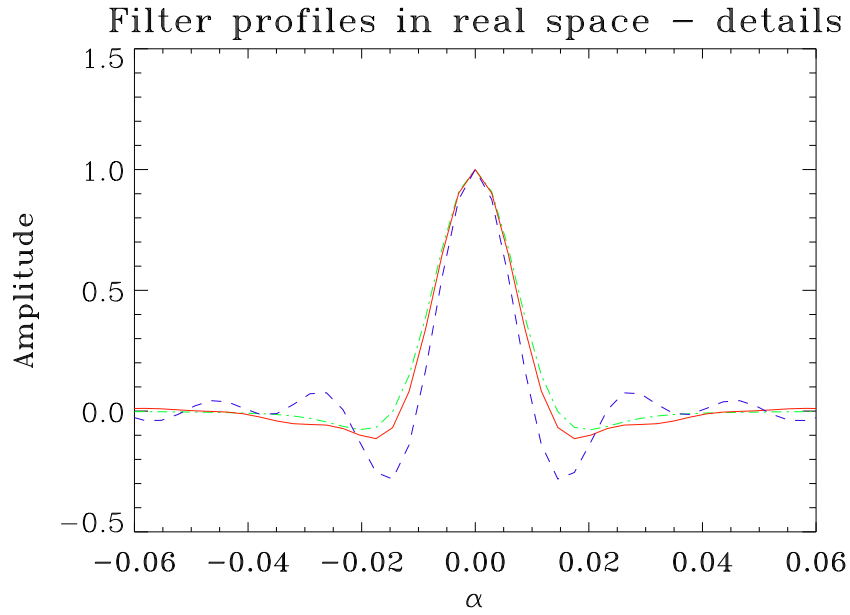

Figure 3.7: Here in this figure we provide details of the behaviour in pixel space over the relevant range, i.e. the region where the three functions exceed 0.001. Lines have the same meaning as in the previous figures.

(Cross-) Power Spectrum

Having extracted the needlets coefficients β_{jk} from a map (e. g. the CMB or source count map), we can use Eq. 3.4 to build a (cross-)correlation estimator in wavelet space,

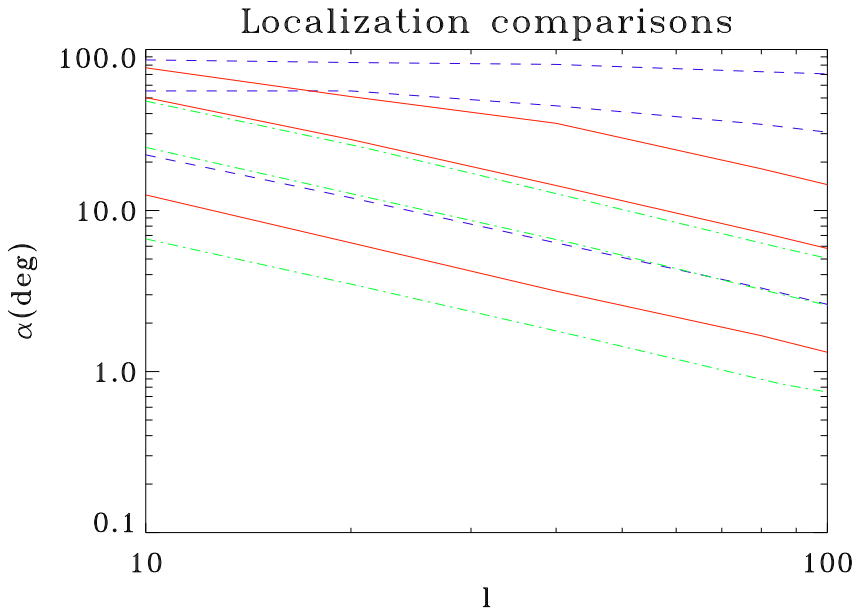

Figure 3.8: The three lines represent the angle at which the area of needlet, in red, or the top-hat, in blue, filter reaches the 99%, 95%, 68% of the total area as a function of the peak multipole in each window function. The latter corresponds directly to a given j for needlets and to the scale R for SMHW; for the top-hat window the central ℓ in the band is given.

β_j, as:

$$\beta_j^{\rm IJ} \equiv \sum_k \frac{1}{N_{\rm pix}(j)} \beta_{jk}^{\rm I} \overline{\beta}_{jk}^{\rm J} \tag{3.12}$$

where $N_{\rm pix}(j)$ is the number of pixels in the pixelization scheme (given by $N_{\rm pix} = 12N_{\rm side}^2$) with I and J denoting the two chosen maps. The theoretical prediction for β_j can be computed from the expected $C_l^{\rm IJ}$ as:

$$\beta_j^{\rm IJ} = \sum_\ell \frac{(2\ell+1)}{4\pi} \left[b\left(\frac{\ell}{B^j}\right)\right]^2 C_\ell^{\rm IJ} \tag{3.13}$$

where we recall $C_\ell^{\rm IJ} \equiv \langle a_{\ell m}^{\rm I} a_{\ell m}^{\rm J*} \rangle = \sum_m \frac{4\pi}{2\ell+1} a_{\ell m}^{\rm I} a_{\ell m}^{\rm J*}$.

β_j provides then an unbiased estimator for the (cross-) angular power spectrum within the needlets framework. The analytic relation between β_j and C_ℓ underlines a few more advantages in using needlets with respect to other wavelets constructions. Indeed this can be used as a check for the simulations and the *HEALPix* implementation we gave, and it makes extremely easy and straightforward dealing with beam profiles and experimental window functions, which have to be taken into account when analysing real data (see Pietrobon et al. (2006) and Sec. 2.1). The duality which needlets embed, namely the localisation both in pixel and harmonic domain, allows us to handle the noise too

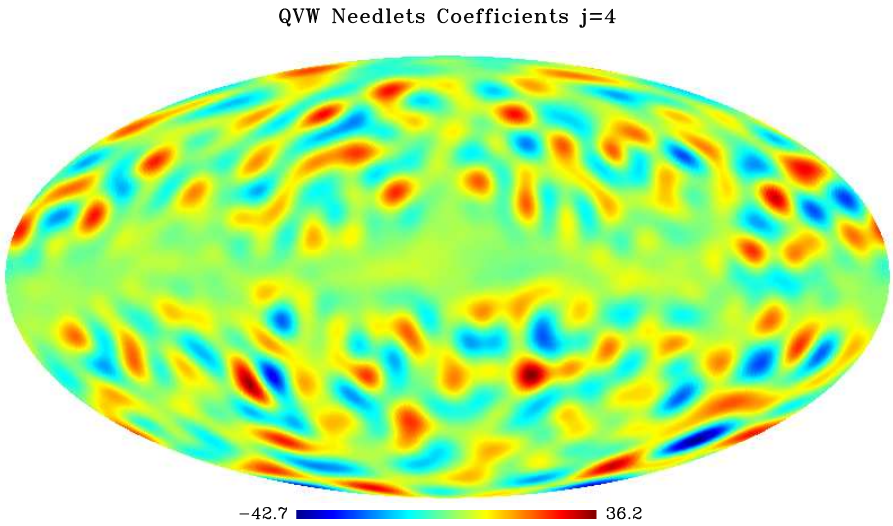

Figure 3.9: Needlet coefficients of the combined Q, V, W map at the resolution $j = 4$. The B parameter is fixed to 2. Notice the anomalous bright spots found by Pietrobon et al. (2008) are clearly visible.

(see Sec. 4.2, Sec. 4.3 and Pietrobon et al. (2009) and Pietrobon et al. (2009) for direct applications to *WMAP* 5-year data.)

Computing the 4-point correlation function for the $a_{\ell m}$, it can be easily shown that the analytical expression for the dispersion of the estimated cross-correlation power spectrum in needlet space is:

$$\Delta\beta_j^{\mathrm{IJ}} = \left(\sum_\ell \frac{(2\ell+1)}{16\pi^2} \left[b\left(\frac{\ell}{B^j}\right) \right]^4 \left(\left(C_\ell^{\mathrm{IJ}}\right)^2 + C_\ell^{\mathrm{I}} C_\ell^{\mathrm{J}} \right) \right)^{1/2} \tag{3.14}$$

which, of course, must be only taken as an approximation when dealing with real data, when the window functions, noise and partial sky coverage have to taken into proper account.

It is important to stress that Eq. 3.12 generalises for a any pair of j_1 j_2 into

$$\beta_{j_1 j_2} = \frac{1}{N_{\mathrm{pix}}} \sum_k \beta_{j_1 k} \beta_{j_2 k}, \tag{3.15}$$

which describes the needlets coefficients covariance and it has been used in Pietrobon et al. (2008) to determine the degree of anomaly of the few hot and cold spots found in the CMB temperature map (see Sec. 4.1).

We have shown that the needlets formalism may be suitable for the angular power spectrum estimation and therefore the parameters estimation. In particular the application of needlets to the *WMAP* 3-year data led to interesting constraints on the dynamics

of dark energy (see Sec. 2.1 and Pietrobon et al. (2006)) and to the measure of the difference in power between the two estimates of the power spectrum computed on the north and south CMB skies (Pietrobon et al., 2008). A detailed discussion on the needlets application to power spectrum can be found in Fay et al. (2008).

Needlets Bispectrum

In the previous section we described how needlets can naturally be applied to the estimation of the 2-point correlation function and how, thanks to the reconstruction formula (Eqs. 3.2 and 3.4), it relates to the usual angular power spectrum. It is easy to extend the formalism to the higher order correlation functions.

In this section we focus on the 3-point correlation function, more often called bispectrum, which plays a crucial role in CMB data analysis to detect any departure from the Gaussian assumption, pointing towards new physics of inflation. We will discuss widely this topic in Chap. 4.We next briefly review the properties of the needlet bispectrum and how it relates to the usual bispectrum. An extensive discussion is provided in Lan & Marinucci (2008b); Rudjord et al. (2009a). See also Pietrobon et al. (2009).

The needlet estimator is defined as follows:

$$\begin{aligned} S_{j_1 j_2 j_3} &= \frac{1}{N_{\rm pix}} \sum_k \beta_{j_1 k} \beta_{j_2 k} \beta_{j_3 k} \\ &= \sum_{\ell_1 \ell_2 \ell_3} b_{\ell_1}^{(j_1)} b_{\ell_2}^{(j_2)} b_{\ell_3}^{(j_3)} \sqrt{\frac{(2\ell_1+1)(2\ell_2+1)(2\ell_3+1)}{4\pi}} \\ &\times \begin{pmatrix} \ell_1 & \ell_2 & \ell_3 \\ 0 & 0 & 0 \end{pmatrix} \hat{\rm B}_{\ell_1 \ell_2 \ell_3} \end{aligned} \tag{3.16}$$

where

$$\hat{\rm B}_{\ell_1 \ell_2 \ell_3} \equiv \langle a_{\ell_1 m_1} a_{\ell_2 m_2} a_{\ell_3 m_3} \rangle = \sum_m a_{\ell_1 m_1} a_{\ell_2 m_2} a_{\ell_3 m_3} \tag{3.17}$$

is the estimated bispectrum, averaged over m_is. $S_{j_1 j_2 j_3}$ can be seen as a *binned bispectrum*, a smooth and combined component of the angular bispectrum.

The bispectrum is supposed to be vanishing for a Gaussian distribution. The standard inflation mechanism (Guth, 1981; Sato, 1981; Linde, 1982; Albrecht & Steinhardt, 1982) predicts a tiny non-Gaussianity in the cosmological perturbations: this is why a great effort has been spent to measure a bispectrum amplitude different from zero in the CMB data which would provide an extraordinary handle on the early universe physics (Smith et al., 2009; Curto et al., 2008; Komatsu et al., 2009; De Troia et al., 2007). This kind of study is usually performed in terms of the non-linear parameter $f_{\rm NL}$ (see for example (Komatsu & Spergel, 2001; Bartolo et al., 2004)). A more detailed discussion will be

provided in Chap. 4. Here we want to introduce that the bispectrum allows a richer analysis: by splitting for example equilateral and isosceles configurations it is possible to distinguish two kinds of non-Gaussianity, equilateral and local respectively, according to the triangle shapes which they affect (Creminelli et al., 2006).

We will use largely this feature in Sec. 4.3 where we address the bispectrum asymmetries. For the purpose of this section it is enough to define the quantities we are interested in. The bispectrum can be divided into four classes based on their geometries: equilateral (*equi*) configurations have three equal j values, isosceles configurations (*iso*) have two legs equal (e.g. $j_1 = j_2 \neq j_3$), while scalene configurations (*scal*) have three different legs. Finally we also consider *open* configurations, for which j_1, j_2 and j_3 do not form a triangle (e.g. $j_1 > j_2 + j_3$); naively these might be expected to be zero, but since each j includes a range of ℓ values, these could include signals arising from ℓ_1, ℓ_2 and ℓ_3 which just satisfy the triangle relations. Thus open configurations correspond to the most co-linear geometries. In principle, since the analytic relation between j and ℓ is given for each B, it would be possible to select the non-vanishing configurations only. However, keeping them represents a strong consistency check of our numerical implementation. The link between the angular scale ℓ and the needlet resolution must be kept in mind for all the configurations; e.g., while the equilateral j-configurations will be dominated by triangles roughly equilateral in ℓ, they will also have contributions from other geometries. Separating the needlet bispectrum by the above described configurations may provide insight into the physical origin of possible anomalies. For instance Ackerman et al. (2007) and Erickcek et al. (2008) suggest early Universe models which could produce a statistically anisotropic CMB sky.

Before discussing some needlets applications in CMB data analysis, it is important to recall that the skewness of the needlets coefficients can be computed via Eq.3.16 as

$$S_j = \frac{1}{N_{\rm pix}} \sum_k \frac{\beta_{jk}^3}{\sigma_j^3}. \tag{3.18}$$

One of the key properties of a needlets frame is that the sum of the squared filter functions in harmonic space, $b_{\ell j}$, is 1 (see Eq. 3.2). This means that, even if we group multipoles and each needlet peaks at a certain multipole range, the total power is conserved: this property is peculiar to the needlets and it is not shared by other wavelet constructions. Therefore, in the case of full sky maps, the needlets power spectrum analysis can be in principle performed with any choice of the parameter B, with the total power conserved, and only the correlation and localisation properties affected by different width of $b_{\ell j}$. Obviously when dealing with real data, this is not completely true due to the presence of the beam, noise and sky cuts.

This does not hold any more when the the cubic power of the filter functions contributes to the estimator used, which is indeed the case of the skewness expression and more generally of the bispectrum one. This fact is displayed in Fig. 3.10, where we plot the sum of square and cube of the filters functions. The not uniform sampling of the multipoles for a n-power estimator suggests that the choice of the B parameter is crucial for the analysis and must be driven by insight on the range of multipoles to be probed.

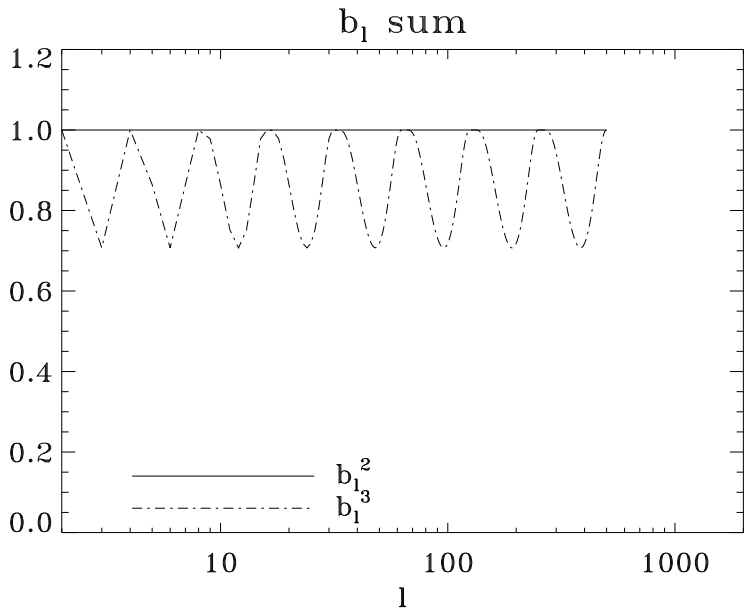

Figure 3.10: Solid line sum of the b_ℓ^2; dot-dashed line sum of the b_ℓ^3. While the former is equal to 1 for the entire range of multipole, the latter is not.

3.4 The Numerical Implementation of Needlets

We have released a public numerical code, which computes the needlets filter functions in harmonic space and the needlets coefficients, given a set of parameters. The code implements the construction described in this chapter and is based on the public available *HEALPix* package[3] (Górski et al., 2005), which is required for the installation. The needlets software is composed by two programs, "*syneed*" and "*ananeed*", which, following the *HEALPix* structure, respectively deconvolves a given map to obtain a needlets frame decomposition, and reconstructs the original map, if a needlets basis is given as input.

Both programs accept the same parsing file in which the fundamental parameters are provided by the user. A list of such parameters is given in Tab. 3.6. The maximum

[3] http://healpix.jpl.nasa.gov/

Table 3.6: Parameters required by the codes "syneed" and "ananeed".

Parameter	Test value
$\ell_{\max}$	250
B	2.0
compute_needlets	T
mapfile	input/test_ilc_RING_512.fits
mapnside	512
maskfile	input/wmap5_kq75_mask_RING_512.fits
bl2_root	test_bl2
need_root	!test_needlet
factor	1

number of multipoles ($\ell_{\max}$) and the B parameter are required. Those given, the codes computes the maximum j necessary to keep all the information in the map. The $N_{\rm side}$ of the needlets coefficients is then determined according to the relation $\ell_{\max} \leq 2N_{\rm side}$. The filter functions $b_{\ell j}$ are computed by default, while it is possible to choose whether to perform the needlets coefficients, which actually is the most time consuming part, by setting the keyword "*compute_needlets*". It is necessary then to specify the map and its resolution. A sky mask can be applied filling the "*maskfile*" variable. The last two keywords set the output files. It is possible to re-scale the map by setting "*factor*" different from 1.
The code currently accepts "RING" ordering only.

All the analysis described in this chapter and in the following ones has been performed by using this software.

Conclusions

In this chapter we have introduced and studied in detail a novel wavelet construction, called needlets, which distinguishes from the others mainly because it is has a finite support in harmonic domain. This translates to a sharp localisation in pixel space, shared by other wavelets renditions, and to excellent properties of non-correlation among the functions of the set. This aspect is crucial when building estimators for CMB data analysis as we discussed extensively. Needlets result then in a very promising tool for the next generation of cosmological experiments; waiting for the future data releases, we applied the formalism we developed to the WMAP dataset and a large scale structure surveys, namely NVSS, as we discussed in the previous chapter. We will exploit further needlet application in the following chapter, focusing on the isotropy and Gaussianity issues.

Chapter 4

Non-Gaussianity in the CMB Sky: a WMAP 5-year data analysis

Sometimes, after long absence, you return to a place
which has painful associations,
and this can be an unpredictable experience.
You have certain expectations:
that a particular street, or room, or café,
once visited, will inspire a particular feeling,
and you are surprised when it fails to do so.

("A touch of love", J. Coe)

In this chapter we discuss the non-Gaussianity of cosmological perturbations from different and complementary points of view. As discussed in the introduction, nearly Gaussian fluctuations are a general prediction of a broad class of early Universe models. A detailed study of the statistical properties of the cosmological fluctuations is necessary to discriminate between several plausible models and get an insight to the physics which drives the first stages of the Universe evolution. Focusing first on the CMB temperature map on large scales, we find anomalous spots barely compatible with the Gaussian hypothesis and describe their impact on the CMB power spectrum, Sec. 4.1.

Then we address the primordial non-Gaussianity issue focusing on the bispectrum analysis. We constrain the primordial non-Gaussianity parameter $f_{\rm NL}$ in Sec. 4.2 while Sec. 4.3 is devoted to the study of the bispectrum itself and its asymmetries.

Finally we perform an analysis of the impact of the foreground residuals in the CMB maps which may dilute the $f_{\rm NL}$ signal (Sec. 4.4). The application of needlets is the rationale behind these complementary studies.

4.1 Needlet Detection of Features in WMAP CMB Sky and the Impact on Anisotropies and Hemispherical Asymmetries

Beyond the angular power spectrum of the cosmic microwave background (CMB) anisotropies, the high sensitivity all-sky CMB maps produced by the Wilkinson Microwave Anisotropy Probe (WMAP)[1] (Hinshaw et al., 2009) have enabled detailed statistical studies to extract higher-order information. These studies include characterisation of asymmetries in the CMB sky (Groeneboom & Eriksen, 2009a) and the search for anomalous features in the anisotropy field. Previous analyses have shown evidences for alignments (Copi et al., 2007), asymmetry in the CMB statistics between northern and southern Galactic hemispheres (Eriksen et al., 2007), and features such as the "cold spot", a significant negative feature in the CMB map first identified with wavelets (Cruz et al., 2005).

In this section, we make use of needlets to further study features in the WMAP CMB maps. We focus on the large angular scales or equivalently, on multipoles smaller than 200. We recover the cold spot that was previously detected in WMAP data with wavelets, and we also detect other features, including two hot spots, that have so far received less attention. By masking these features, we study how the angular power spectrum of CMB anisotropies is modified. Given that these features are located in the southern hemisphere, we also discuss the extent to which these features could be responsible for the north-south asymmetry in WMAP data Lew (2008); Groeneboom & Eriksen (2009a); Hansen et al. (2004). As well-known, this asymmetry has also drawn much interest in the theoretical community, since it could entail strong implications on the physical nature of primordial perturbations, including inflation Erickcek et al. (2008). By masking the low-ℓ features, we find that the difference in the CMB anisotropy variance between the two hemispheres is reduced by a factor 2, reducing the significance of previous detections.

We finally explore the evidence that statistically significant bumps and dips in the CMB anisotropy power spectrum at multipoles of 20 and 40 could be related to features in the CMB sky. We did not locate any particular feature in the sky that dominates the power spectrum at these multipoles; masking the significant features detected by needlets tuned to these multipoles did not change the power spectrum more than $\sim$5%.

4.1.1 Maps

We decomposed the Internal Linear Combination (ILC) WMAP 5-year temperature map by means of needlet functions corresponding to $B = 1.8$. The choice of B must be driven

[1] http://lambda.gsfc.nasa.gov/product/map/current/

by the insight on the range of multipoles to be probed: this specific choice provides us needlets at eleven frequencies j, which span properly the low multipoles we are interested in. Eight frequencies span multipoles up to $\ell = 200$, while the information at smallest scales is concentrated on just three frequencies. The range of multipoles covered by each needlet is given by the relation $\ell \in [B^{j-1}, B^{j+1}]$ and it is summarised in Tab. 4.1.

Three clarifying examples of the WMAP 5-year ILC map decomposition on $j = 3$, $j = 4$ and $j = 5$ needlets by making use of the functions b_ℓ depicted in Figure 4.1 are shown in Fig. 4.3.

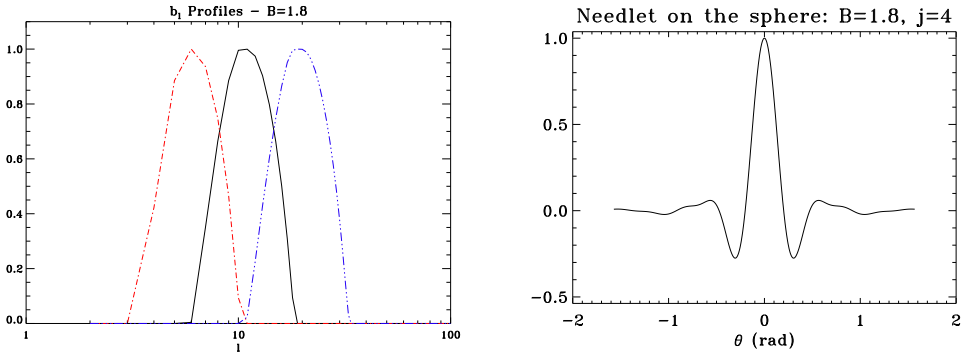

Figure 4.1: Left: Profile of the function $b(x)$ in ℓ-space for the choice $B = 1.8$. The black solid line represents $j = 4$, the red dot-dashed line $j = 3$ and the blue dot-long-dashed line $j = 5$. Right: needlets on the sphere for $j = 4$. At each cubature point, ξ_{jk}, the needlet is sharply localised.

j	ℓ-range
1	2
2	2-5
3	4-10
4	6-18
5	11-33
6	20-60
7	35-108
8	63-196
9	113-352
10	203-635
11	365-1143

Table 4.1: Range of multipoles spanned by needlets for $B = 1.8$.

We first applied our procedure to the WMAP map with the extended mask KQ75 from the WMAP team. Such a large mask, however, entails a greater correlation for multipoles corresponding to large angular scales; for low values of j, this could potentially impact the needlets coefficients as well. Any detection of significant features in

the CMB anisotropy map using the large mask, however, can be reconfirmed at a higher significance level with a smaller mask. After studying the temperature map using KQ75, we repeated all the analysis applying KQ85, which is the mask currently favoured for cosmological data analysis, including power spectrum measurements. We find that our results related to statistically significant features on the WMAP map are fully consistent in the two cases.

Hot/Cold spot maps

In Figure 4.3, we represent the needlet coefficients for the cases of $j = 3$ to $j = 5$. These three frequencies are particularly interesting since they probe the low-multipole region, highlighting a peculiar pattern of anisotropies in the southern hemisphere. When $j = 4$, we recognise two spots, one hotter and one colder than the average CMB fluctuations. While the latter is a detection of the so-called *cold spot*, a feature studied in detail in the literature as a source of non-Gaussianity in the CMB map (Vielva et al., 2004; Larson & Wandelt, 2004; Cruz et al., 2005; Vielva et al., 2007; Cruz et al., 2007, 2008; Smith & Huterer, 2008), the hot spot has not had the same scrutiny with only a minor description in Naselsky et al. (2007) and Vielva et al. (2007).

In fact, the $j = 3$ and $j = 5$ needlet coefficients represent a cross-validation of the existing literature, as they also highlight a second hot spot centred at $(g_l = 173, g_b = -46)$ (as pointed out in Naselsky et al. (2007)) and a minor cold spot centred at $(g_l = 80, g_b = -33)$ (observed in Vielva et al. (2007)), that actually appears with an adjacent hot spot. In figure 4.2 the three spots we will use in the angular power spectrum analysis are shown. We stress that our identification follows uniform criteria with the same technique, quite differently from some of the existing literature. Moreover, as explained above we are also able to identify exactly the range of multipoles where these features contribute to the angular power spectrum of CMB anisotropies, due to the specific needlet properties. To establish the significance of the features we detected, we consider a Monte-Carlo analysis by performing a large set simulations (1,000) of a Gaussian CMB sky with the same angular power spectrum as the WMAP 5-year best-fit cosmological parameters (Komatsu et al., 2009); we then compute the average and the standard deviation of the distribution for each needlet coefficient. The expected distribution is Gaussian with zero mean, (see Baldi et al. (2006)), in good agreement with our simulations. We focus on the statistic

$$S_{jk} = \frac{|\beta_{jk} - < \beta_{jk} >|}{\sigma_{\beta_{jk}}}. \tag{4.1}$$

where $\sigma_{\beta_{jk}}$ is the usual standard deviation of the distribution. In Figure 4.3, we show that the hot and cold spots exceed three sigma level at $j = 4$. The cold spot appears

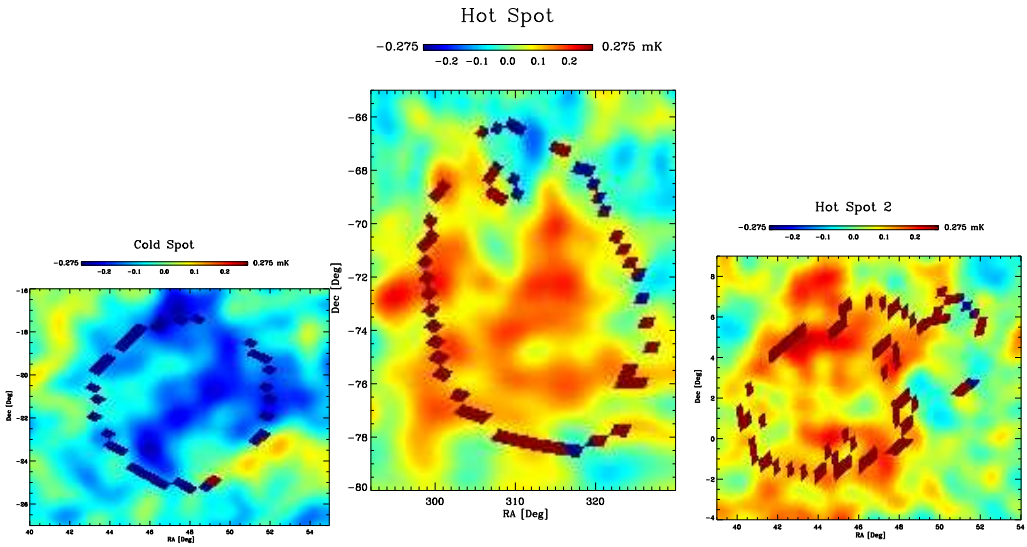

Figure 4.2: Detail of the spots. From the left, the cold spot at $(g_l = 209, g_b = -57)$, the hot spot at $(g_l = 320, g_b = -34)$ present at $j = 4$, and the second hot one at $(g_l = 173, g_b = -46)$ measure at $j = 3$. The true colours are altered by the use of the masks we employed in the analysis to highlight the region above three sigma level.

Property / Spots	**Cold Spot**	**Hot Spot**	**Hot Spot**
(g_l, g_b)	$(209, -57)$	$(320, -34)$	$(173, -46)$
j	4	4	3
S_{jk}^{max}	$(-)3.72$	3.56	3.24

Table 4.2: Main properties of the spots highlighted in our analysis.

significantly both in the needlet coefficients for $j = 4$ and $j = 5$, and thus its impact can be reckoned to span the range between $\ell = 6$ and $\ell = 33$ (Table 1). In Table 4.2 the significance values of the three anomalous spots are quoted.

It may be suspected that the hot spot we located could be a spurious effect due to oscillations in the needlet function. See Fig. 4.1, right panel. We considered this explanation, but we concluded that the angular distance at which the hot and cold spot appear is greater than the needlet oscillation range.

As a test for the joint significance of needlet coefficients, we consider the statistic

$$\Gamma_k^{jj'} = \frac{\beta_{jk}\,\beta_{j'k} - < \beta_{jk}\,\beta_{j'k} >}{\Sigma_k^{jj'}} \tag{4.2}$$

where $\Sigma_k^{jj'}$ is the second moment of the distribution. Of course, the statistical distribution of Γ cannot be taken as Gaussian. Hence, to analyse its statistical significance we used again a set of Monte Carlo simulations with the underlying ΛCDM best fit model

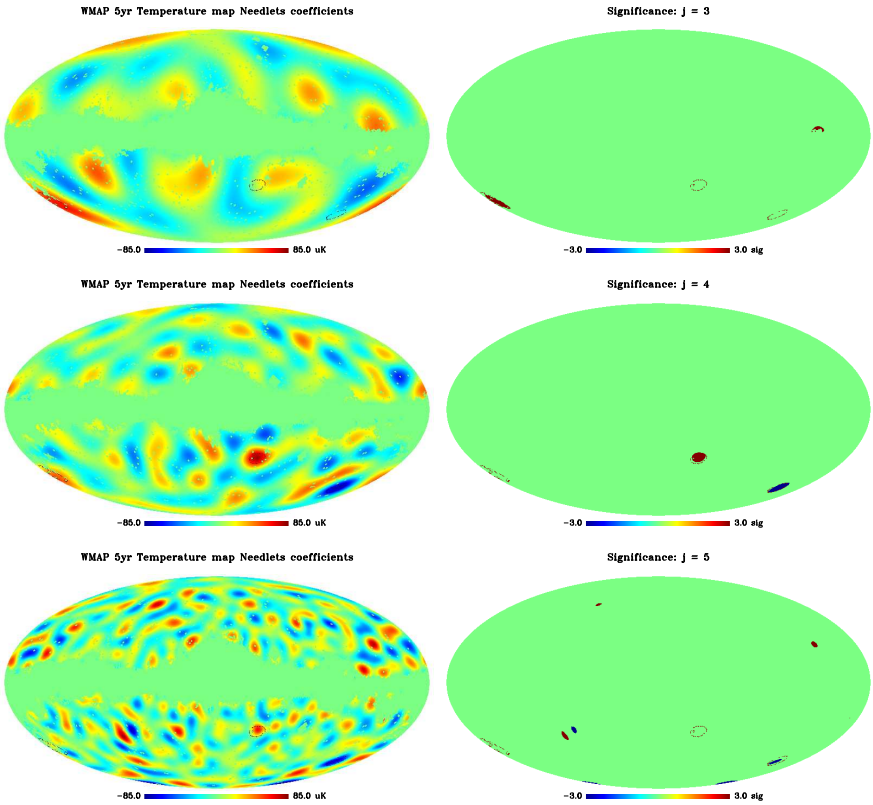

Figure 4.3: Needlet coefficients of the WMAP 5-year CMB temperature map. On the left, from top $j = 3$, $j = 4$ and $j = 5$ are plotted. The set of needlets is characterised by $B = 1.8$. Each pixel represents the coefficient for the needlet function computed at ξ_{jk}, where k identifies the pixel in the Healpix ordering. The effect of the applied KQ75 mask is clearly visible, setting to zero the value of each pixel that belongs to the mask. It is interesting to notice that needlet coefficients highlight the presence of the well known cold spot in the Southern hemisphere, as well as a hot spot localised in the Southern hemisphere closer to the mask. Needlet coefficients for $j = 5$ show the cold spot pretty well, while the hot spot is weaker. Another couple of hot-cold spots appear above the Galactic plane. On the right, from the top, significance of the needlet coefficients for $j = 3$, $j = 4$ and $j = 5$. The three maps show the significance S_{jk} above the threshold of 3. This allows us to localise in ℓ-space the contribution of the hot spot that results to be in the range of multipoles between $\ell = 6$ and $\ell = 18$. Computing the coefficients for $j = 6$ and observing that the cold spot, if present, does not have a high statistical significance, we can deduce the range of multipoles covered by the cold spot: between $\ell = 6$ and $\ell = 33$.

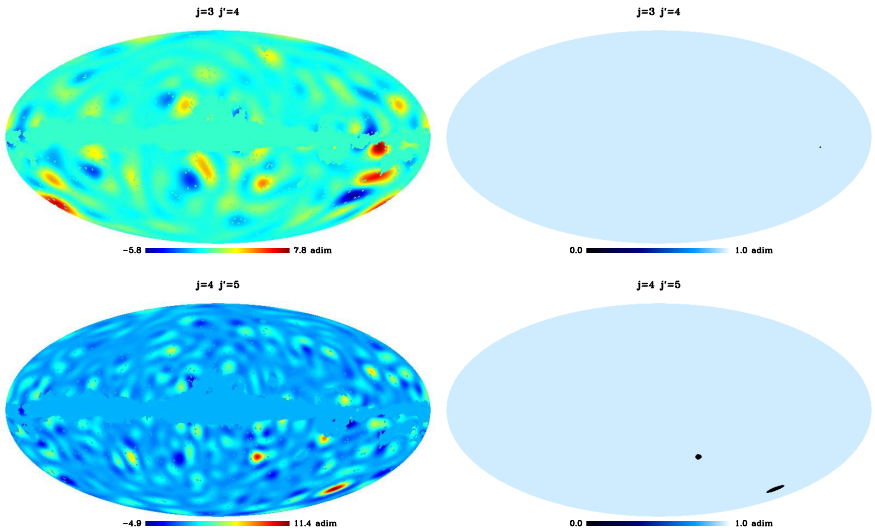

Figure 4.4: Γ statistics for $j = 3$ and $j = 4$ (left-hand side) and with $j = 4$ and $j = 5$, (right-hand side). Both the cold spot and the hot spot are clearly visible in the maps, but when a threshold of $\Gamma_k^{jj'} > 7.5$ is applied their signal is strong only on the $j = 4 - j = 5$ maps.

(Komatsu et al., 2009) and derive the statistics described in Eq. 4.2. Figure 4.4 shows the values of $\Gamma_{jj'}$ for the pair $j = 3$ and $j' = 4$, upper panels, and for $j = 4$ and $j' = 5$, lower panels. Results are expressed directly in terms of the statistic defined in Eq. 4.2 in the upper panels; in the lower panels a threshold of 7.5 for $\Gamma_k^{jj'}$ is adopted to underline the fact that the hot and cold spots identified by the mask $j = 4$ are the most significant.

III.B North-South Asymmetry

We now wish to investigate the extent to which masking the previously found features affects the asymmetry between the northern and the southern hemisphere of the CMB sky. To see this, we recall that in Baldi et al. (2006); Pietrobon et al. (2006); Marinucci et al. (2008) it is shown that

$$\langle \sum_k \beta_{jk}^2 \rangle = \sum_\ell \frac{(2\ell+1)}{4\pi} b^2 \Big(\frac{\ell}{B^j} \Big) \mathcal{C}_\ell$$

whence $\beta_j \equiv \sum_k \beta_{jk}^2$ is an unbiased estimator for the weighted angular power spectrum (see Sec. 3.3). In Baldi et al. (2006), Section 7 it is also shown that this statistic is approximately Gaussian (after centring and normalisation) at high frequencies, see also

Delabrouille et al. (2009); Faÿ & Guilloux (2008) for extensions and related work. Developing this idea, we computed here the total power in each hemisphere by taking the sum of squares of the needlet coefficients at $j = 3$ and $j = 4$ extracted from the masked ILC temperature map

$$C_{3,4} = \sum_{j=3}^{4} \sum_{k} \beta_{jk}^2 = \sum_{j=3}^{4} \beta_j. \tag{4.3}$$

We label the mask associated with the $j = 3$ and $j = 4$ features we found as "$j3j4$", and we include it in addition to standard WMAP masks.

The difference is measured by computing

$$D \equiv \frac{1}{V} \left(C_{3,4}^S - C_{3,4}^N \right) , \tag{4.4}$$

where $C_{3,4}^i$, $i = S, N$ is the quantity in Eq. 4.3, where the needlet coefficients are restricted to either the northern or the southern hemisphere (in the Galactic coordinate system), normalised to the variance V of the whole sky. The latter actually turn out to be the cosmic variance of the CMB power spectrum binned with $b_{\ell,34}^2$. In some sense, D is measuring the difference between two local versions of the power spectrum estimator; such local estimators can indeed be rigorously justified, in view of the uncorrelation properties of needlets in pixel space (see Baldi et al. (2007)). In practice, we defined the pixels in the northern hemisphere as those outside the mask characterised by $\theta < \pi/2$ and pixels in the southern hemisphere as those outside the mask, with $\theta > \pi/2$.

In Fig. 4.5 we plot β_j as defined in Eq. 4.3 extracted from the whole sky as well those measured in each hemisphere, both including the spots and masking them. The southern hemisphere shows an excess of power compared to the northern one that is reduced by a factor 2 when the "j3j4" mask is applied. Notice that, as expected, the power measured in the north region is not affected by the masking procedure. In the lower panel of Fig. 4.5 we quantify this effect computing the difference $\beta_j^S - \beta_j^N$, normalised to the variance of the estimator. The results are summarised in Tab. 4.3. Our findings are sensitive to the chosen sky-cut: when the KQ85 mask is used, the asymmetry, measured in terms of a difference in the variance of power, decreases from 4.26 without the $j3j4$ needlet mask to 1.97 with needlet mask. When the more aggressive mask KQ75 is applied to CMB data (together with the $j3j4$ mask), the difference is larger and the global asymmetry is further reduced: from 4.37 to 2.0. Note that the north-south power variance difference with just the WMAP team's masks, KQ75 and KQ85, is rather small (4.26 vs. 4.37); this suggests that the hemispherical asymmetry cannot be explained by simply extending the galactic plane mask. With the $j3j4$ mask we introduced (which cuts roughly 0.5% of the sky), we find a significant reduction of a factor 2.

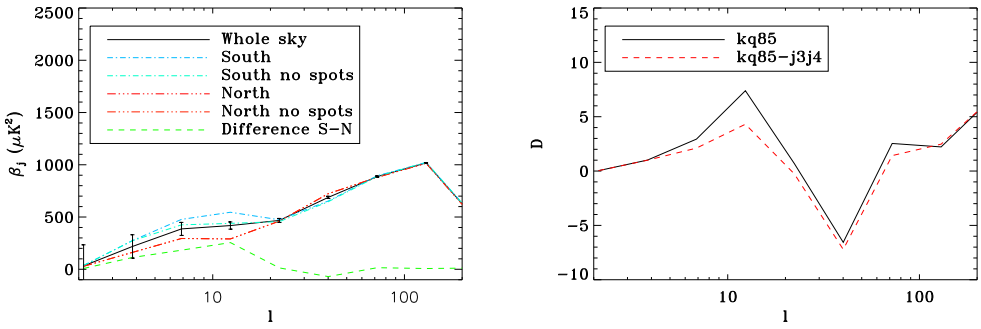

Figure 4.5: In the left panel β_j extracted from WMAP data when different sky cuts are applied are shown. The black solid line shows the signal for the whole CMB sky (kq85 is applied). The blue and red dashed lines show how the power is split between the two hemispheres. When the cold and hot spots detected are masked the excess of power in the southern region is decreased (light blue and orange dot-dashed lines). In the right panel the significance of the difference D is plotted.

Mask	$C_{3,4}$	$C^N_{3,4}$	$C^S_{3,4}$	**D**
kq85	766	556	974	4.26
kq85**+j3j4**	673	544	802	1.97
kq75	703	502	908	4.37
kq75**+j3j4**	655	492	728	2.0

Table 4.3: We report the values of total power (Eq. 4.3) carried by needlets at $j = 3$ and $j = 4$ extracted on the ILC map. Four cases, corresponding to the different masks we applied in this analysis. The last column reports the significance D as defined in Eq. 4.4. It is interesting to notice how masking the hot and cold spots reduces the asymmetry by a factor greater than two, being the $j3j4$ mask the 0.5% of the sky only.

Given that we mask a smaller area on the sky than the 10% difference between KQ85 and KQ75, it seems rather likely that the hemispherical asymmetry can be credited to features in the southern hemisphere. While we have localised (some of) these features, this does not establish by itself whether the asymmetry is primordial or associated with fluctuations in our local universe. There exist already several extended studies on the nature of the cold spot (Masina & Notari (2009); Sakai & Inoue (2008); Granett et al. (2008); Cembranos et al. (2008); Génova-Santos et al. (2008); Cruz et al. (2008); Hansen et al. (2007)); for further statistical studies we make publicly available the $j3j4$ mask.

III.C Further statistical analysis

As a further statistical cross-check, we chose randomly needlet coefficients at different locations on the map and fit their distribution to the one derived from 1000 simulations where the KQ85 mask was applied. The simulated results are in excellent agreement

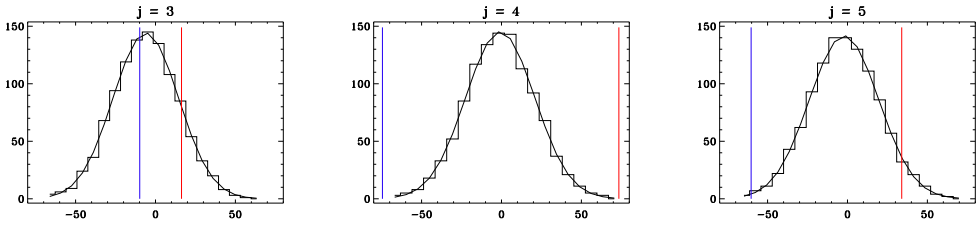

Figure 4.6: From left to right, distribution of the needlet coefficient for $j = 3$, $j = 4$ and $j = 5$. The blue (on the left-hand side) and red (on the right-hand side) vertical lines mark the values of the cold and hot spot respectively. They are both well beyond three sigma level for $j = 4$. At $j = 3$ the significance is basically zero, while at $j = 5$ only the cold spot is still visible.

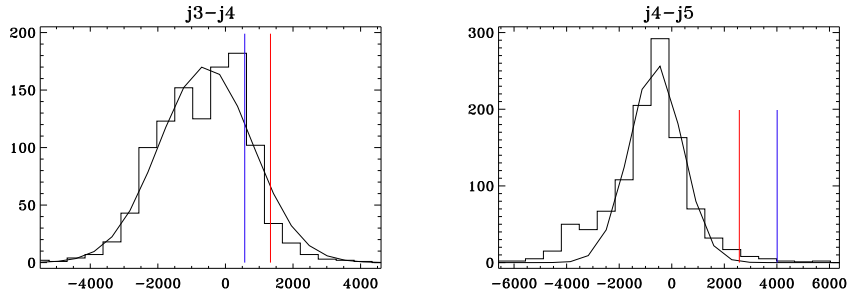

Figure 4.7: Distribution of Γ statistic for $(j, j') = (3, 4)$ (left) and $(j, j') = (4, 5)$ (right). The two vertical lines mark the values of the hot and cold spot, being the latter the more significant. As expected, this is non-Gaussian, and is characterised by large non-Gaussian tails.

with a zero-mean Gaussian distribution, as shown in Figure 4.6. This result is of course expected, as the needlet coefficients are a linear functional of the underlying temperature map. However, we report the figure as a further check to ensure that the procedure we followed to compute the significance of the spots is well justified.

We followed the same procedure also to quantify the significance of $\Gamma_k^{jj'}$. Of course, in this case simulations are indeed necessary, because $\Gamma_k^{jj'}$ is a non-linear statistic and hence non-Gaussian. In Figure 4.7 we provide some evidence on the significance of the statistics we measured in the regions where the anomalous spots are located. The curve is the fit to the distribution of needlet coefficients in simulated maps, while the vertical lines mark the value measured in the WMAP temperature needlet coefficients. The simulated distribution has rather large tails; the statistical significance of $\Gamma_k^{jj'}$ at the locations corresponding to the spots is nevertheless rather high, with an estimated p-value of 0.5% for the cold spot and of 1.65% for the hot spot. We can still confirm that the signal is mostly peaked in the correlation between $j = 4$ and $j = 5$.

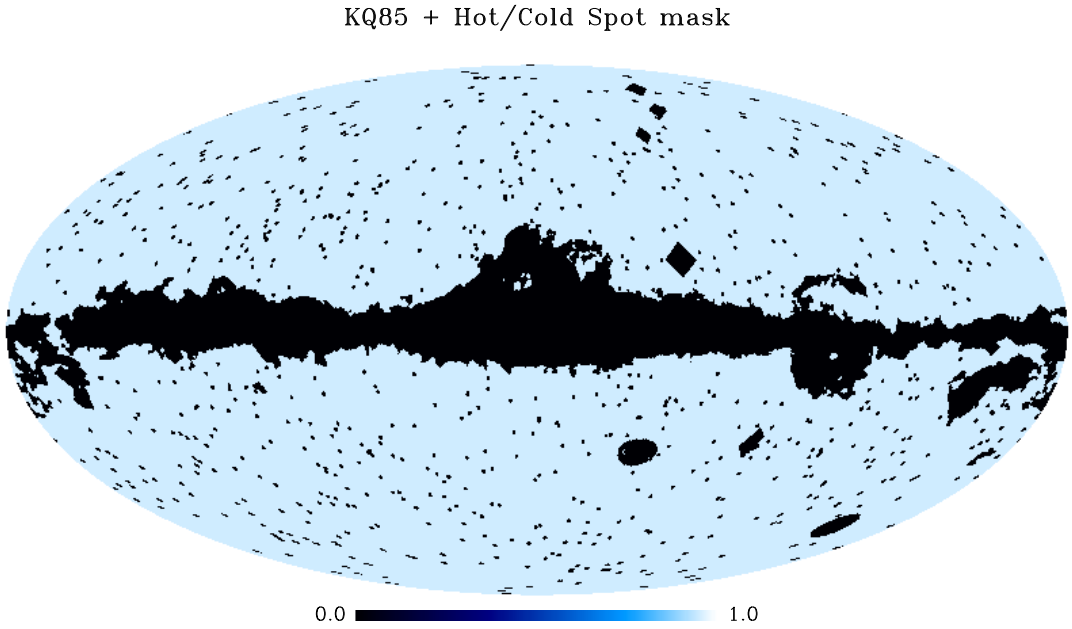

Figure 4.8: Joint KQ85 and hot/cold spots mask applied to the WMAP ILC temperature map.

4.1.2 Impact on the CMB power spectrum

The purpose of this section is to investigate the extent to which masking the hot and cold regions we found affects the CMB power spectrum (Masina & Notari, 2009). To address this issue, we first estimate the angular power spectrum from the ILC WMAP 5 year map after applying the KQ85 mask. We then compare this result with the angular power spectrum resulting from a wider mask: the sum of KQ85 plus the regions above three sigma level we discovered when performing our temperature analysis. We report in Figure 4.8 the resulting mask.

The effect of the different masking is not negligible, reaching the value of 12% at low multipoles. To check against systematics, we performed a Monte Carlo simulation of 200 CMB maps with the underlying WMAP 5 year best fit model (Komatsu et al., 2009), in order to estimate the mean effect of the joint mask. We computed the average and the standard deviation to quantify the hot/cold spots effect. The results are shown in Figure 4.9.

Quite remarkably, the region where the signal is stronger is exactly the one where the cold spot is localised. This may be interpreted as a confirmation of the localisation properties of needlets in pixel and harmonic spaces. We believe the use of the ILC map is justified here, because our signal peaks at low multipoles; however for completeness we computed the same quantity from both the W and V bands of WMAP 5 year, as well as

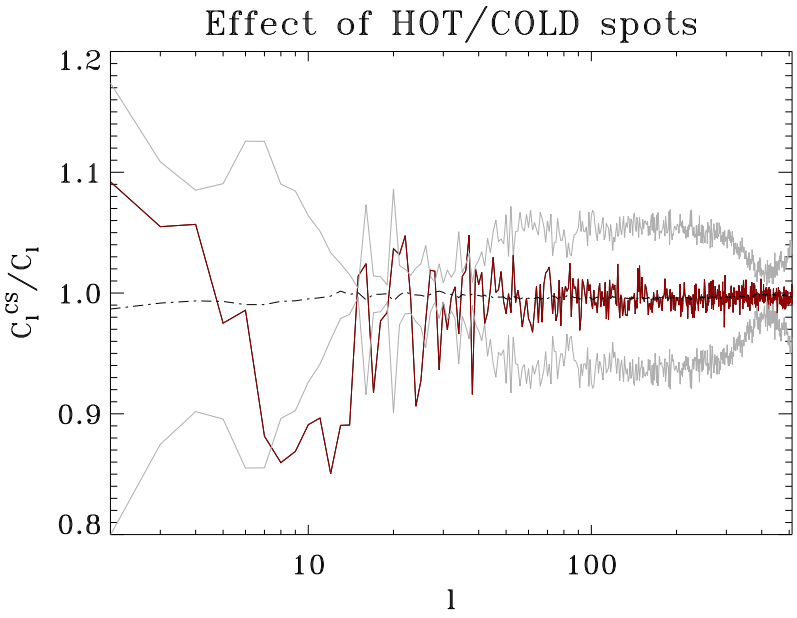

Figure 4.9: Effect on the angular power spectrum due to the subtraction of the hot and cold spots in the CMB temperature map. The red solid line shows the difference in the $\mathcal{C}_\ell$, the gray dashed-dotted line represents the average modification of the simulation, while the solid lines mark the one sigma level. In the region between $\ell = 8$ and $\ell = 30$ the effect exceeds one sigma level: that region is the one where the effect of the cold spot is stronger.

using the map obtained by de Oliveira-Costa et al. (2008)[2]. The result is fully consistent with what we found using ILC, thus validating the procedure we followed. The signal is shown in Figure 4.10

The next step has been to evaluate the effect that the change in the angular power spectrum induces on cosmological parameter estimates. Since the low multipole region is affected by the largest variation, we expect that changes might occur on the spectral index, n_s, the optical depth, τ and possibly on the primordial fluctuation normalisation amplitude A_s. Actually, since the variation is at maximum 12% in a handful of multipoles, we expect a global variation on the power spectrum of roughly few parts in one thousand.

The WMAP team performed the temperature analysis splitting the low multipoles and the high multipoles regions. The former is probed by a Gibbs-sampling based Monte Carlo analysis (Eriksen et al., 2004). The high moments are instead investigated fitting the angular power spectrum extracted from the W and V bands. To take into account the modifications due to the new masking we replaced the KQ85 mask used at low resolution with the joint mask KQ85 plus the hot and cold spots (Fig. 4.8), and multiplied the angular power spectrum used for the analysis by the ratio between the $\mathcal{C}_\ell$ computed with

[2]http://space.mit.edu/home/angelica/gsm/

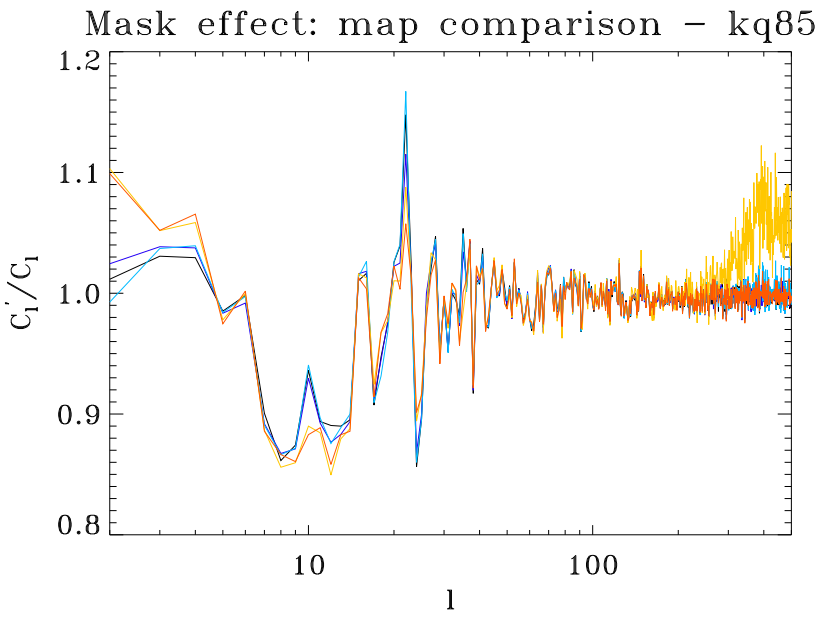

Figure 4.10: Ratio of two CMB power spectra computed from a given map with the kq85 and kq85+j3j4: ILC the yellow curve, W the black curve, V the blue one, WV the light blue curve, and that extracted by the map reconstructed in de Oliveira-Costa et al. (2008) in orange. Except for the WMAP ILC map at $\ell > 200$, the difference on the angular power spectrum is consistent among a variety of maps. Beyond $\ell = 200$ ILC power spectrum shows features not compatible with other spectra, probably due to the way the different WMAP channels are combined.

parameter	WMAP5	Hot/Cold spot masked ($j4$)	$j3$-$j4$ mask
$\mathbf{\Omega_b h^2}$	$\mathbf{0.0227 \pm 0.0006}$	$\mathbf{0.0228 \pm 0.0006}$	$\mathbf{0.0228 \pm 0.0006}$
$\mathbf{\Omega_c h^2}$	$\mathbf{0.110 \pm 0.006}$	$\mathbf{0.109 \pm 0.006}$	$\mathbf{0.109 \pm 0.006}$
θ_A	1.040 ± 0.003	1.040 ± 0.003	1.040 ± 0.003
τ	$\mathbf{0.089 \pm 0.018}$	$\mathbf{0.091 \pm 0.017}$	$\mathbf{0.089 \pm 0.017}$
$\mathbf{n_s}$	$\mathbf{0.965 \pm 0.014}$	$\mathbf{0.966 \pm 0.014}$	$\mathbf{0.966 \pm 0.014}$
$\mathbf{\ln(10^{10} A_s)}$	$\mathbf{3.18 \pm 0.05}$	$\mathbf{3.17 \pm 0.05}$	$\mathbf{3.17 \pm 0.05}$

Table 4.4: Effect of the wider mask on the ΛCDM six parameters. The difference due to the sum of KQ85 mask plus HOT/Cold spot mask is small.

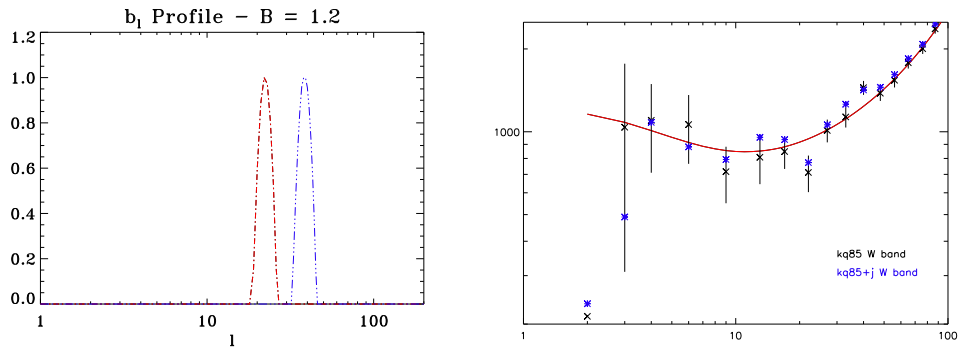

Figure 4.11: Left panel, profile of the function $b(x)$ in ℓ-space for the choice $B = 1.2$. The red dot-dashed line represents $j = 17$ and the blue long dashed line $j = 20$. Right panel, power spectrum modification due to the structures measured using the set of needlets shown in Fig. 4.12.

the wider mask and $\mathcal{C}_\ell$ obtained with the unmodified KQ85 mask applied to ILC, in the range of multipoles $2 - 200$ (see Fig. 4.10).

The results are shown is Table 4.4. In short, we do not observe a significant variation in any of the cosmological parameters.

It is well known that the angular power spectrum measured by the WMAP collaboration shows some interesting features at low multipoles; in particular the range between $\ell = 20$ and $\ell = 24$ has a deficit in power with respect to the prediction of the best-fit ΛCDM theoretical model, while that between $\ell = 37$ to $\ell = 44$ shows excess power. To investigate these issues, we chose needlets corresponding to frequencies that match those two intervals and we looked for coefficients exceeding the threshold of three sigma. More precisely, we select $B = 1.2$ and we take $j = 17$, $j = 20$ to span the relevant ranges of multipoles. Figure 4.11 (upper panel) and figure 4.12 show (respectively) the b_ℓ profile employed for this purpose and the corresponding needlet coefficients.

We find that the effect on the angular power spectrum is actually rather small (overall less than one sigma). However it does follow the expected sign, decreasing the deficit and the excess of power in the selected ranges. The effect is shown in the lower panel of Figure 4.11.

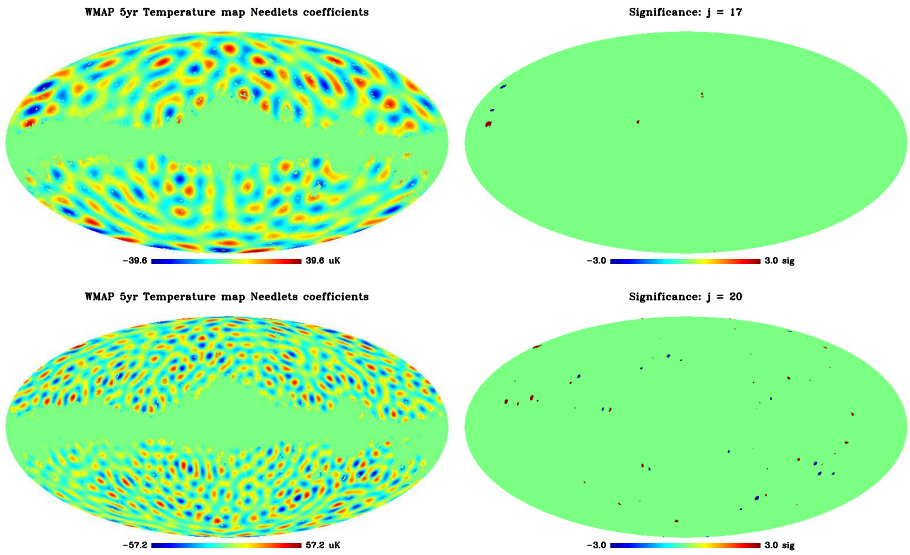

Figure 4.12: Needlet coefficients and their significance at $j = 17$ and $j = 20$ for $B = 1.2$.

4.1.3 Conclusions

We apply spherical needlets to the Wilkinson Microwave Anisotropy Probe 5-year cosmic microwave background (CMB) dataset, to search for imprints of non-isotropic features in the CMB sky.

After calibration by means of a large set of mock simulations to compute the expected correlation for a ΛCDM model, the analysis of needlet coefficients highlights the presence of the now well-known "cold spot" of the CMB map in the southern hemisphere, and in addition two hot spots at significance greater than 99% confidence level, again in the southern hemisphere and closer to the Galactic plane. While the cold spot primarily contributes to the anisotropy power spectrum in the multipoles between $\ell = 6$ to $\ell = 33$, the hot spots are found to be dominating the anisotropy power in the range between $\ell = 6$ and $\ell = 18$.

We also studied the effect the two spots have on the CMB power spectrum, by building $1,000$ mock CMB simulations. We conclude that, especially at low multipoles, the effect is measurable: masking both the cold and the two hot spots results in an increase in the quadrupole amplitude of 10%, while at $\ell = 10$ power is reduced by 12%. To investigate the effect of this difference on the value of cosmological parameters, we modified the WMAP 5-year CMB fiducial power spectrum and the KQ85 mask used to perform the analysis by cutting out the contribution of the two spots, and we repeated the parameter estimation analysis. The results we obtain are slightly different, but fully consistent

within the 1σ errors on parameters published by the WMAP team. We may incidentally notice that we found a significant anomaly localised at large angular scales, but the overall CMB power spectrum is consistent with the standard cosmological model.

Since all three spots appear in the southern hemisphere, we also studied the power spectrum asymmetry between the two hemispheres, which has been previously found to be statistically significant. When the features detected by needlets are masked, we find that the difference in the power, measured in terms of the anisotropy variance between $\ell = 4$ and $\ell = 18$, is reduced by a factor 2. This decreases the significance of the previously claimed north-south asymmetry. We make the mask resulting from needlet features available for future, more detailed studies on the asymmetries in the CMB anisotropy sky[3].

[3] http://www.fisica.uniroma2.it/∼cosmo/masks

4.2 Constraints on Primordial Non-Gaussianity from a Needlet Analysis of the WMAP-5 Data

With the increasing amount of high-quality observations performed in the last decade (Hinshaw et al. (2009); Reichardt et al. (2009); Sievers et al. (2007); Wu et al. (2009); Pryke et al. (2009); Hinderks et al. (2009); Masi et al. (2006); Johnson et al. (2007)), statistical tests of the CMB temperature anisotropy pattern are getting more and more accurate. This has made it possible to test one of the basic tenets of the standard cosmological scenario, i.e. that the primordial density perturbations follow a Gaussian distribution. This is a definite prediction of the simplest inflationary models (Guth, 1981; Sato, 1981; Linde, 1982; Albrecht & Steinhardt, 1982): the detection of primordial deviations from Gaussianity would be a smoking gun for more complicated implementations of the inflationary mechanism, such as those of multi-fields (Lyth & Wands, 2002; Linde & Mukhanov, 2006; Alabidi & Lyth, 2006), ekpyrotic (Mizuno et al., 2008; Khoury, 2002) or cyclic scenarios (Steinhardt & Turok, 2002; Lehners & Steinhardt, 2008).

When dealing with the search for non-Gaussian statistics in real data, two major issues have to be addressed. One has to do with the statistical tools used to analyse the data and detect deviations from Gaussianity: not only can these deviations be very subtle and elusive, but they could be generated by processes that are not directly related to the primordial density perturbations — such as unremoved astrophysical foregrounds (Cooray et al., 2008; Serra & Cooray, 2008) or instrumental systematics. The other issue is theoretical, and relates to the way the non-Gaussianity is parameterised: while there is only one way to realize a Gaussian distribution, non-Gaussian statistics can be produced in countless ways. One then has to assume a non-Gaussian parameterisation which relates in some sensible way to an underlying early universe scenario.

The latter issue is usually addressed by introducing a parameter $f_{\rm NL}$, which quantifies the amplitude of non-Gaussianity as a quadratic deviation with respect to the primordial Gaussian gravitational potential $\Phi_{\rm L}$, i.e.:

$$\Phi(x) = \Phi_{\rm L}(x) + f_{\rm NL}\left[\Phi^2_{\rm L}(x) - \langle\Phi^2_{\rm L}(x)\rangle\right] \tag{4.5}$$

The major advantage of this parameterisation is that, regardless of the specific underlying early universe model, it can represent the second-order approximation of any non linear deviation from Gaussianity. For an excellent review on this topic see Bartolo et al. (2004).

From the point of view of data analysis, a number of techniques have been proposed in the past few years to quantify the level of deviation from Gaussian statistics in the data. The most used one in harmonic space is the bispectrum (Luo, 1994; Heavens, 1998;

Spergel & Goldberg, 1999; Komatsu & Spergel, 2001; Cabella et al., 2006). The bispectrum is defined as the three-point correlation function, and an estimate of $f_{\rm NL}$ through the bispectrum requires the sum over all the triangle configurations. Since this is extremely time-consuming, regardless whether the computation is performed in harmonic space or pixel space, Komatsu et al. (2005) have proposed a fast cubic estimator based on the Wiener filter matching, which reduces considerably the computational challenge. This estimator has been further developed by Creminelli et al. (2006) introducing a linear correction which allows the correct treatment of the anisotropic noise, and finally optimised (Yadav et al., 2007) and extended to polarisation measurements (Yadav et al., 2008). Recently, Yadav & Wandelt (2008) applied the cubic estimator to the WMAP 3-year data, finding a detection of a primordial non-Gaussian signal at more than 2.5 sigma. An indication of a primordial non-Gaussian signal has been also found by the WMAP collaboration in the analysis of the 5-year dataset, although with a lower confidence level (Komatsu et al., 2009). An interesting discussion on optimal and sub-optimal estimators can be found in Smith & Zaldarriaga (2006). See for further details Yu & Lu (2008) and Babich (2005).

Concerning the methods in pixel space, De Troia et al. (2007); Reichardt et al. (2009); Hikage et al. (2006); Curto et al. (2008, 2007); Natoli (2009) applied Minkowski functionals to several CMB datasets; Cabella et al. (2005) applied local curvature on WMAP 1-year data and Monteserín et al. (2006) developed scalar statistics using the Laplacian as a tool to test Gaussianity. Alternative indicators based on skewness and kurtosis have been proposed by Bernui & Reboucas (2009). Tests based on wavelets were applied to WMAP 1-year data (Vielva et al., 2004; Mukherjee & Wang, 2004), and WMAP 5-year data by Curto et al. (2009) and McEwen et al. (2008). Wavelets have been also used in CMB studies (Martínez-González et al., 2002) to identify anomalies in WMAP data (McEwen et al., 2008; Wiaux et al., 2008; Cruz et al., 2008, 2007; Vielva et al., 2007; Wiaux et al., 2006; Cruz et al., 2005; Vielva et al., 2004; Pietrobon et al., 2008), denoising (Sanz et al., 1999; Hammond et al., 2009), point sources extraction (Cayón et al., 2000; González-Nuevo et al., 2006). Very recently Vielva & Sanz (2008) constrained primordial non-Gaussianity by means of N-point probability distribution functions.

The signature of non-Gaussianity appears in the higher moments of a distribution, which are no longer completely specified by the first moment (i.e. the mean value of the distribution) and the second moment (i.e. the standard deviation). For a Gaussian distribution, all odd moments are vanishing, while the even ones can be expressed in terms of the first two only. We then look for a non-vanishing skewness of the distribution of the needlet coefficients, applying a cubic statistic.

4.2.1 WMAP-5 needlet analysis

In the following we describe the statistical techniques and simulations used in order to constrain $f_{\rm NL}$.

We started by producing simulations of non-Gaussian CMB maps with the WMAP-5 characteristics, for varying $f_{\rm NL}$. For each channel [Q1, Q2, V1, V2, W1, W2, W3, W4], we used as input a realization of a simulated primordial non-Gaussian map (Liguori et al., 2007); these maps were convolved with the respective beam window functions for each channel and a random noise realization was added to each map adopting the nominal sensitivities and number of hits provided by the WMAP team[4] (Hinshaw et al., 2009). From these single-channel maps we constructed an optimal map via Jarosik et al. (2007):

$$T(\gamma) = \sum_{ch} T_{ch}(\gamma) w_{ch}(\gamma) \tag{4.6}$$

where γ represents a direction on the sky (which, in practice, is identified with a specific pixel in the Healpix scheme (Górski et al., 2005)), and $w_{ch} = n_h(\gamma)/\sigma^2_{ch}/\sum_{ch} w_{ch}$. where n_h is the number of observations of a given pixel and σ_{ch} the nominal sensitivity of the channel, estimated by WMAP team. We finally applied the WMAP mask Kq85 and degraded the resulting map to the resolution of $N = 256$. At the end of this procedure we were left with realistic Monte Carlo simulations of the CMB sky as seen from WMAP-5, containing different levels of primordial non-Gaussianity parameterised by the value of $f_{\rm NL}$.

Then, we extracted the needlet coefficients β_{jk} from the simulated maps for a given B. For each j resolution, the needlet coefficients can be visualised as a sky map, where k is the pixel number. We calculated the skewness of the reconstructed coefficients maps over the unmasked region, as:

$$S_j = \frac{1}{\tilde{N}_p} \sum_{k'} \frac{(\beta_{jk'} - \langle \beta_{jk'} \rangle)^3}{\sigma_j^3} \tag{4.7}$$

where $\tilde{N}_p$ denotes the number of pixels outside the mask and σ_j is the variance of the needlet coefficients at the j resolution. This procedure allows us to build an empirical statistical distribution of the skewness as a function of $f_{\rm NL}$. Finally, we calculated the skewness from the real data of the foreground-reduced WMAP 5-year Q, V and W channels data, using the same procedure applied to the simulated maps. The comparison of the real data skewness to the simulated distributions allowed us to set limits on the non-Gaussian signal in the data.

[4] http://lambda.gsfc.nasa.gov/product/map/dr3/m_products.cfm

A non-vanishing skewness represents a deviation from a Gaussian distribution and could give a fundamental handle on the physics responsible for inflation and the generation of primordial fluctuations. In general we expect the needlet coefficients to pick up signal at different angular scales as a function of both j and B, making different sets sensitive to non-Gaussianity in specific ways. This could be indeed a powerful tool when looking for imprint of specific models of non-Gaussianity. This feature is enhanced by the statistics itself we consider in our analysis. As described in Chap. 3, since $S \propto \beta_{jk}^3$ we have an intrinsic modulation in the power of the cube of the needlet coefficients. Figure 3.10 shows this effect compared to the square of the b_ℓ function.

For this reason it does make sense to compute the statistics defined in Eq. 4.7 for several sets of needlets. In particular we employed values of B from 1.8 to 4.5, choosing the step in order to span as homogeneously as possible the entire range of multipoles $\ell = 2$ to $\ell = 500$. The set of B we have considered is [1.8, 1.9, 2.0, 2.15, 2.5, 3.0, 3.5, 4.0, 4.5]. We also tried finer samplings of B, but no additional information resulted for the sampling considered.

χ^2 analysis

In order to estimate $f_{\rm NL}$ we minimised the quantity:

$$\chi^2(f_{\rm NL}) = (X^d - \langle X(f_{\rm NL})\rangle)^T C^{-1} (X^d - \langle X(f_{\rm NL})\rangle). \tag{4.8}$$

Here X is a vector composed by the set of skewness of our set (B, j). The averages $\langle X(f_{\rm NL})\rangle$ were calculated via Monte Carlo simulation over 100 primordial non-Gaussian maps. Formally, C^{-1} is dependent on $f_{\rm NL}$ as well but it has been shown (Spergel & Goldberg, 1999; Komatsu & Spergel, 2001) that for the mild level of non-Gaussianity we expect this dependence is weak and can be estimated by Gaussian simulations. We found that calculating C^{-1} from 10,000 Monte Carlo simulations gives a very stable estimate.

The result is shown in Fig. 4.13: the curves deviating from zero corresponds to the effect due to the primordial non-Gaussianity for positive (dashed lines) and negative (dotted lines) values of $f_{\rm NL}$, while the yellow and orange bands correspond to the 1σ and 2σ levels respectively. Diamonds represent the results of WMAP 5-year data. $f_{\rm NL}$ is estimated to be 20 with $-30 < f_{\rm NL} < 70$ and $-80 < f_{\rm NL} < 120$ at 1 and 2σ respectively. These results show no significant deviation from the Gaussian hypothesis. This is not in contrast with the values found by Yadav & Wandelt (2008), since we have performed our analysis on maps with the maximum multipole corresponding to $\ell_{\rm max} = 500$, whereas Yadav & Wandelt (2008) clearly showed that their results crucially depend on the maximum multipole considered. The reduced χ^2 of WMAP data is 1.53 with 85 degrees of freedom.

As a further consistency check, we performed a goodness-of-fit test by calculating the quantile of the WMAP data from the non-Gaussian realizations with $f_{\rm NL} = 20$. We found that 21% of the simulations had a larger χ^2 of the WMAP χ^2, confirming that the specifications of our Monte Carlo simulations well describe the experimental setting of WMAP 5-year data.

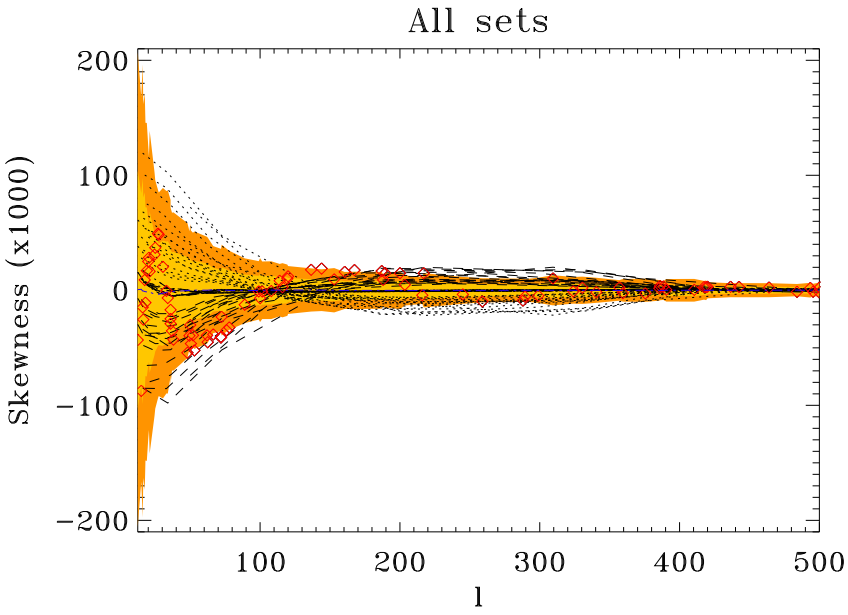

Figure 4.13: Skewness of needlet coefficients for the entire set of parameter B as a function of multipole ℓ. Shaded areas represents 1 and 2 σ confidence levels calculated from 10000 Gaussian Monte Carlo simulations with beam, noise level, and marks of WMAP 5-year data. Dashed (dotted) lines correspond to the averages over 100 primordial non-Gaussian maps with $f_{\rm NL} = 200, 400$ $(-200, 400)$. Diamond are the WMAP 5-year data.

A skewness based $f_{\rm NL}$ estimator

Since the primordial non-Gaussianity is a second order effect, it contributes linearly to the skewness through $f_{\rm NL}$. This means that it is possible to compute from the non-Gaussian simulations the skewness $S(j)$ for $f_{\rm NL} = 1$ and use it as a template to build a filter-matching estimator of the non-linear coupling parameter. Assuming that $S_j^{\rm obs} = f_{\rm NL}\ S_j^{\rm th}|_{f_{\rm NL}=1}$, where "th" means the average over the non-Gaussian simulations, we obtain

$$f_{\rm NL} = \frac{\sum_{jj'} S_j^{\rm obs} \mathbf{Cov}_{jj'}^{-1} S_{j'}^{\rm th}}{\sum_{jj'} S_j^{\rm th} \mathbf{Cov}_{jj'}^{-1} S_{j'}^{\rm th}} \tag{4.9}$$

where we dropped the subscript $f_{\rm NL} = 1$. This estimator is built following the same approach as Komatsu et al. (2005), i. e. a filter matching one, translated into the needlet

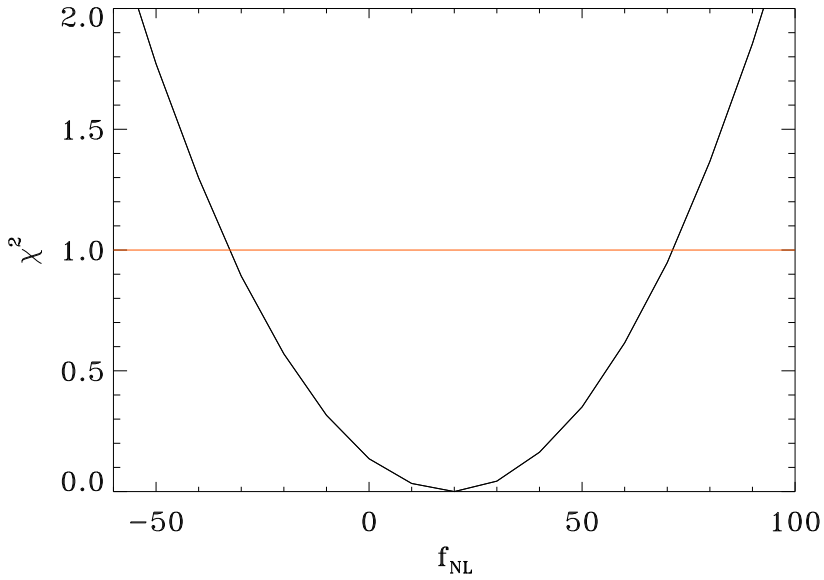

Figure 4.14: The $\Delta\chi^2$ of WMAP 5-year data as a function of $f_{\rm NL}$. $f_{\rm NL}$ is estimated to be $f_{\rm NL} = 20 \pm 50$ and $f_{\rm NL} = 20 \pm 100$ at 1 σ and 2 σ level respectively.

framework: we bispectrum of the data and we hit it on the theoretical prediction, weighting it with the covariance of the primordial signal, which also takes into account the instrumental noise. The theoretical skewness computed for $f_{\rm NL} = 1$ is shown in Fig. 4.15. We checked that the pipeline applied to simulated non-Gaussian CMB maps does not affect the linear relation: in particular we verified that the average signal we obtain for a given $f_{\rm NL}$ scales linearly with $f_{\rm NL}$ itself, meaning for example that we can mimic the signal for $f_{\rm NL} = \pm 400$ by taking the double of that for $f_{\rm NL} = \pm 200$.

The main contribution to the covariance matrix $\mathbf{Cov}_{jj'}$ comes from the Gaussian part of gravitational potential; this allows us to estimate the covariance from random Gaussian simulations. According to this assumption, we estimate the error bars on the primordial non-linear coupling parameter computing the standard deviation of the 10000 $f_{\rm NL}$ estimates resulting from a fresh set of Gaussian simulations, via Eq. 4.9. We find $f_{\rm NL} = 21 \pm 54$ at 1 sigma confidence level, which is fully consistent with what we found applying the χ^2 statistic. This corroborates the robustness of our procedure and confirms needlets as a suitable tool to study primordial non-Gaussianity.

Our limits on primordial non-Gaussianity are slightly larger than those achieved by Curto et al. (2009) being our 1σ confidence level ($-30 < f_{\rm NL} < 70$) slightly broader than $-8 < f_{\rm NL} < -111$ at 95% confidence level. However we were limited in our analysis to multipoles lower than $\ell_{max} = 500$, while the strongest constraints on primordial non-Gaussianity make use of higher angular scales.

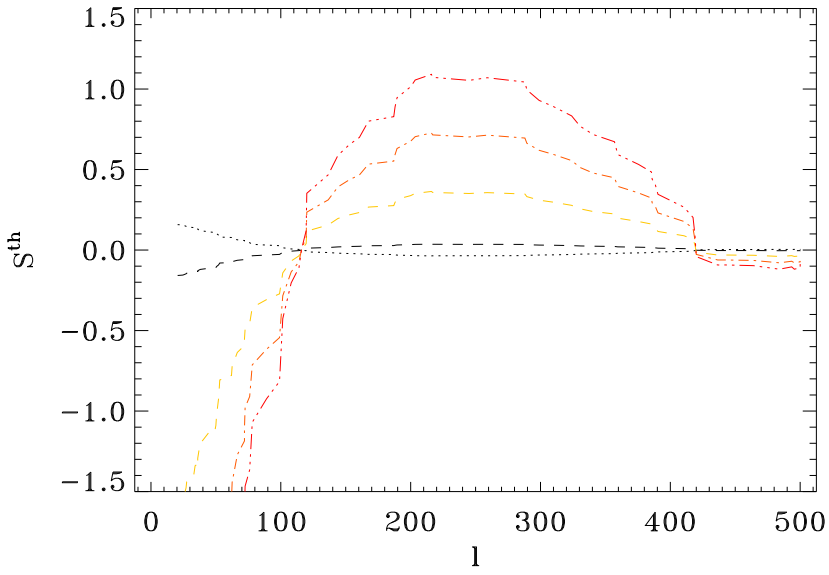

Figure 4.15: Skewness for $f_{\rm NL} = \pm 1$, respectively dashed and dotted line, derived from non-Gaussian simulations. Theoretical curves for $f_{\rm NL} = 10, 20, 30$ (from bottom to top) are shown too.

Our limits on $f_{\rm NL}$ are quite promising for future experiments such as Planck[5], where sensitivity and angular resolution will be enormously improved.

Further analysis: binned bispectrum

The analysis we performed in the previous sections, based on the skewness of the needlets coefficients β_{jk}, is mainly sensitive to the equilateral configurations, since it is proportional to the primordial bispectrum computed for $\ell_1 \simeq \ell_2 \simeq \ell_3$ summed over all the multipoles up to $\ell_{\rm max} = 500$. This can be easily understood by direct inspection of Eq. 4.7 as discussed in Chap. 3.

A qualitative improvement in constraining the parameter $f_{\rm NL}$ can be achieved by adding in the estimator the effect of the squeezed configurations, considering the product of three β_{jk} with $j_1 \neq j_2 \neq j_3$. The skewness of needlet coefficients can be generalised into

$$S_{j_1 j_2 j_3} = \frac{1}{\tilde{N}_p} \sum_k \frac{\beta_{j_1 k} \beta_{j_2 k} \beta_{j_3 k}}{\sigma_{j_1} \sigma_{j_2} \sigma_{j_3}} \tag{4.10}$$

We repeated the needlet analysis applying this new estimator to the same set of WMAP 5-year data and simulations for the choice of the needlet parameter $B = 3.5$,

[5]http://www.rssd.esa.int/SA/PLANCK/docs/Bluebook-ESA-SCI(2005)1.pdf

which has the highest signal-to-noise ratio among the set chosen in the previous analysis. The minimisation of the χ^2 gives $f_{\rm NL} = 30 \pm 40$, which is consistent with what we found applying S_j. The χ^2 for WMAP 5-year data is shown in Fig. 4.16

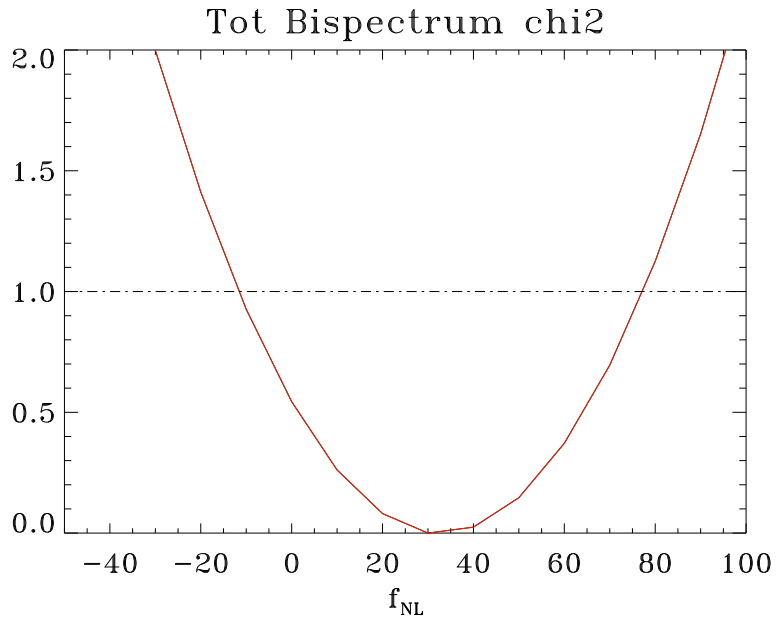

Figure 4.16: The $\Delta\chi^2$ of WMAP 5-year data as a function of $f_{\rm NL}$ computed from the binned bispectrum. B is chosen 3.50 which had the highest signal-to-noise ratio among those chosen in the previous analysis. $f_{\rm NL}$ is estimated to be $f_{\rm NL} = 30 \pm 40$ and $f_{\rm NL} = 30 \pm 80$ at 1 σ and 2 σ level respectively.

Recently an analysis based on a cubic estimator analogous to $S_{j_1 j_2 j_3}$ has been performed by Curto et al. (2009,?) who include the effect of squeezed configurations in the Spherical Mexican Hat Wavelet; and by Rudjord et al. (2009a) using a set of needlets characterised by a different B parameter obtaining $f_{\rm NL} = 84 \pm 40$. While the difference in the value of $f_{\rm NL}$ can be due to the higher number of multipoles considered in the analysis, $\ell_{\rm max} = 1000$, and it is consistent with the result of Yadav & Wandelt (2008), it is important that the estimated error bars are fully consistent with ours.

In a following paper Rudjord et al. (2009b) checked the dependence of the $f_{\rm NL}$ parameter on the direction in the sky. They computed the needlets bispectrum on 48 different regions of the CMB sky finding no significant deviation from the full-sky measurement, as expected for a primordial signal such as the local non-Gaussianity. Very recently Smidt et al. (2009) improved the constraints on $f_{\rm NL} = 11 \pm 23$ by using the skewness power spectrum on WMAP 5-year data.

4.2.2 Conclusions

Primordial non-Gaussianity is becoming one of the keys to understand the physics of the early Universe. Several tests have been developed and applied to WMAP data to constrain the non-linear coupling parameter $f_{\rm NL}$. Recently, different methods (Yadav & Wandelt, 2008; Curto et al., 2009) found different constraints on $f_{\rm NL}$ using similar datasets, WMAP 3-year and WMAP 5-year respectively. The two approaches have been shown to have the same power in constraining primordial non-Gaussianity, while they obtained different best fit values for $f_{\rm NL}$. Whereas this might be due to the masks applied to the datasets, it certainly underlines the complexity and difficulty of measuring $f_{\rm NL}$. The next generation of experiments will provide data with excellent angular resolution and signal-to-noise ratio which will be decisive to confirm or confute the measurements of $f_{\rm NL}$ of the references above. In this respect, it will be even important to constrain $f_{\rm NL}$ with different methods in order to get a more robust detection or to spot spurious presences of non-Gaussian signal. Moreover, integrated estimators, not based on Wiener filters, are differently sensitive to the non-linear coupling and can be useful to address exotic non-Gaussian models which predict high values of $f_{\rm NL}$ and whose bispectrum evaluation, for instance, may require prohibitive computational time due to the convolution in the bispectrum formula.

We constrained the primordial non-Gaussianity parameter $f_{\rm NL}$ by developing the needlets formalism and applying it to the WMAP 5-year CMB data. We estimated $f_{\rm NL}$ to be 20 with $-30 < f_{\rm NL} < 70$ and $-80 < f_{\rm NL} < 120$ at 1 and 2 sigma respectively, then consistent with the Gaussian hypothesis. We performed two different analyses, the χ^2 statistics and an estimator based on the skewness of the primordial non-Gaussian sky, finding an excellent agreement between the two results. Needlets have been proven to be a well understood tool for CMB data analysis, sensitive to the primordial non-Gaussianity. Since the skewness of the needlets coefficients is mainly sensitive to the equilateral triangle configurations, we improved our estimator computing the three point correlation function in needlet space which indeed recovers the signal due to squeezed triangle configurations. We obtain $f_{\rm NL} = 30 \pm 40$ at 68% confidence level, consistent with the previous analysis. Our constraints are slightly broader than those achieved by Curto et al. (2009,?) and not in contrast with the values found by Yadav & Wandelt (2008) since we were limited by a smaller range of multipoles due to the non-Gaussian simulations we had, whereas the tighter constraints on $f_{\rm NL}$ crucially depend on the maximum multipole considered.

Our limits on $f_{\rm NL}$ are quite promising for future experiments like Planck, whose sensitivity and angular resolution will be enormously improved.

4.3 Needlet Bispectrum Asymmetries in the WMAP 5-year Data

Since the first release of the WMAP satellite data (Bennett et al., 2003b), there have been many claims of anomalies in the statistical distribution of CMB temperature fluctuations in the sky (see e.g. Eriksen et al. (2004)). For example, there appear to be localised areas which are hotter or colder than would be expected in the concordance ΛCDM cosmological model with Gaussian statistics (see Cruz et al. (2005)). Also, power seems to be preferentially aligned along a certain direction (dubbed the 'axis of evil,' Land & Magueijo (2007)) and the quadrupole and octopole power appears to be correlated (de Oliveira-Costa et al., 2004). These anomalies were subsequently confirmed with new releases of the WMAP data (Spergel et al., 2007; Nolta et al., 2009).

Many other studies have highlighted a marked difference in the statistics of the northern and southern galactic skies. Park (2004) found an asymmetry in the Minkowski functionals values in the northern and southern galactic hemispheres. Eriksen et al. (2005) detected anomalies at large angular scales comparing the amplitudes of temperature power spectra in the two hemispheres and confirmed the anomalies are present in the n-point correlation function. Vielva et al. (2004) studied the kurtosis of Spherical Mexican Hat Wavelets coefficients, discovering a strong non-Gaussian signal in the southern hemisphere. Hansen et al. (2004) reported that the local curvature of the CMB sky exhibited asymmetric behaviour as well. McEwen et al. (2008) and Pietrobon et al. (2008) applied two different wavelets constructions to the 5-year WMAP data, confirming many of these results; they have also been seen using scaling indices (Rossmanith et al., 2009). Copi et al. (2007) pointed out a lack of power in the north hemisphere in the two point correlation function. The presence of these anomalies has been tested against mask effect and foreground contamination by Bernui et al. (2007). Lew (2008) constrains the direction of the anomaly axis using a generic maximum a posteriori method. Very recently, Hansen et al. (2008) reported that the power asymmetry spans a very large range of angular scales (corresponding to multipoles $2 \leq \ell \leq 600$): this result is based on an angular power spectrum analysis of the WMAP sky maps. A summary of most of these anomalies can be found in Bernui & Reboucas (2009).

Here, we investigate the CMB anomalies using the needlets bispectrum(Lan & Marinucci, 2008b) to the WMAP 5-year data; this technique was recently used to constrain primordial non-Gaussianity in the same dataset by Pietrobon et al. (2009) and Rudjord et al. (2009a). For the first time, we analyse the contribution of different triangle configurations, grouped according to their size and shape.

4.3.1 Statistical Analysis and Results for WMAP 5-year Data

We processed the WMAP 5-year data and the simulations in the same way discussed in Sec. 4.2.1. To test the Gaussianity of WMAP 5-year data, we compare the distribution of the $\chi^2 = XC^{-1}X^T$ of the simulated dataset to the value obtained from data, where X is the array consisting of the needlet bispectrum values calculated via Eq. 3.16. We consider the needlet bispectrum values (indicated by "*all*" in the tables)' and, to identify where the anomalies are concentrated, we split the analysis in different branches according to the geometry of the triangles. For the chosen $B = 2.0$, we have 115 which satisfy the requirements: 9 equilateral, 56 isosceles, 50 scalene. We define the remaining 50 configurations as open: we would expect them to be vanishing except for those which combine multipoles which fulfill the Wigner selection rules. The correspondence between each needlet scale j and its multipole range is shown in Table 4.5.

Large Scales					
j	1	2	3	4	5
$[\ell_1, \ell_2]$	$[2, 3]$	$[3, 7]$	$[5, 15]$	$[9, 31]$	$[17, 63]$

Small Scales					
j	6	7	8	9	
$[\ell_1, \ell_2]$	$[33, 127]$	$[65, 255]$	$[132, 500]$	$[263, 500]$	-

Table 4.5: Correspondence between angular scale and needlet scale for $B = 2.0$.

On the full CMB sky, the χ^2 of the data is compatible with the distribution we obtain from 20,000 Gaussian simulations. When we calculate the χ^2 on the northern and southern hemispheres separately, we find a significant deviation from Gaussianity in the southern hemisphere while the northern hemisphere appears Gaussian, having a bispectrum generally somewhat smaller than expected (see Table 4.3.1). The results are shown in the histogram plots in Fig. 4.17. Furthermore, considering the triangle configurations as classified above, we found that this behaviour is concentrated in all triangle configurations separately except for the equilateral ones. The isosceles triangles are perhaps the most interesting ones since they probe the correlation between the large and the small angular scales (the so-called 'squeezed' configurations), which should reflect a non-local type of non-Gaussianity. A comparable degree of asymmetry is shown by scalene and open configurations, which confirm the global lack of power in the north hemisphere: the points in the northern hemisphere show a lower scatter. A similar asymmetric behaviour was found by Hansen et al. (2004); Land & Magueijo (2005); Eriksen et al. (2004) and recently confirmed by Hoftuft et al. (2009); Hansen et al. (2008); Groeneboom & Eriksen (2009b). In our analysis we already mask the big anomalous features present in

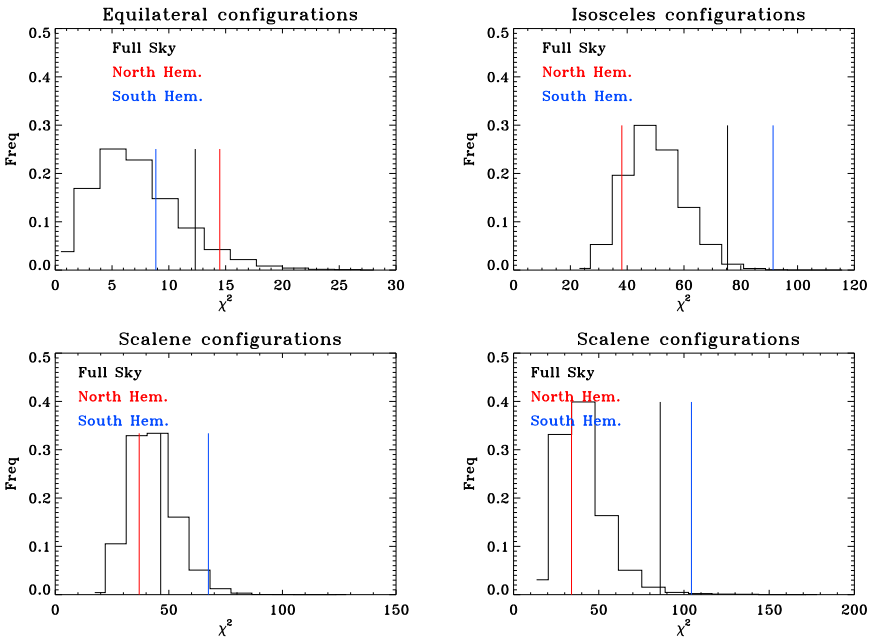

Figure 4.17: Needlet bispectrum χ^2 distribution of the three WMAP 5-year temperature data. The southern hemisphere is barely compatible with the Gaussian hypothesis, being the blue line which marks the real data χ^2 in the tail of the distribution.

the southern hemisphere (Sec. 4.1), responsible for about 50% of the power asymmetry in the angular power spectrum (Pietrobon et al., 2008). The results are summed in Table 4.3.1 and plotted in Fig. 4.18 where we plot the bispectrum as a function of the variable $X_{\rm var} \equiv 1/(j_1 j_2)^3 + 1/(j_3 j_2)^3 + 1/(j_1 j_3)^3$. Note that equilateral configurations

conf.	FULL SKY	NORTH	SOUTH
all (115)	29%	**96%**	**2%**
equi (9)	20%	11%	45%
iso (56)	5%	**96%**	**0.5%**
scal (50)	60%	**90%**	**7%**
open (50)	3%	**85%**	**2%**

Table 4.6: Percentage of the simulations with a χ^2 larger than WMAP 5-year data for the different triangular configurations of the needlets bispectrum. An asymmetry is present in each triangle configuration except for the equilateral, and is significant when all the configurations are combined.

are directly related to the skewness of the needlet coefficient distributions: the fact that on the whole sky we do not find a strong deviation from Gaussianity is in agreement with the previous literature, where only the kurtosis of the distributions showed an anomalous behaviour (see Vielva et al. (2004)).

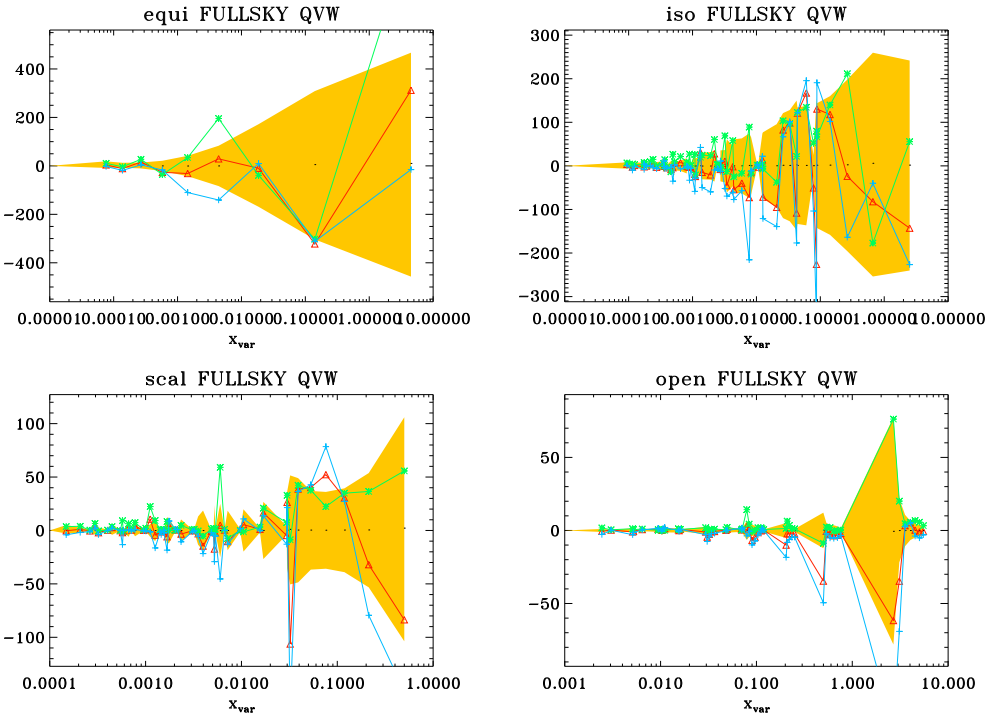

Figure 4.18: Needlet bispectrum for each triangle configuration: *equilateral* (top-left), *isosceles* (top-right), *scalene* (bottom-left) and *open* (bottom-right). The red triangles show the full sky analysis, the green crosses are the northern hemisphere and the light blue plusses are the south. The northern hemisphere shows a global lack of signal. The shadow region represents the 1-sigma level.

Large-Small Scale Analysis. Going more deeply, we focused on small and large angular scales separately. In particular, with the choice $B = 2$, we define the subset of needlets $j = 1$ to $j = 5$ as large scale, corresponding roughly to scales larger than 1 degree; while the subset $j = 6$ to $j = 9$ corresponds to the sub-degree scales (see Table 4.5). We then perform the same analysis we carried out the whole needlet set. The results are shown in Table 4.7. The isosceles configurations still show a large difference between the two hemispheres but the significance is lower than the whole set analysis. The open configuration result is still anomalous. No open configurations exist for the small scale subset $6 \leq j \leq 9$; however for the large scales these co-linear configurations are most significantly non-zero for the biggest contribution of the power. For the sub-degree set we did not find an high degree of anomaly, as summarised in Tab. 4.7, though the isosceles configurations are still significantly different between the two hemispheres. Dividing the analysis between the two sets at large and small scales, we miss the important contribution given by the correlation between the two, which is indeed crucial for the squeezed triangles. We then consider two more sets: one formed by a triangle which has one side $j_1 \leq 5$ and two sides belonging to the small scale set (j_2,$j_3 \geq 6$). We

conf.	Large Scales ($j \leq 5$)		
	FULL SKY	**NORTH**	**SOUTH**
all (28)	61%	93%	14%
equi (5)	86%	26%	45%
iso (16)	70%	90%	22%
scal (7)	37%	62%	15%
open (7)	3%	38%	2%

conf.	Small Scales ($j \geq 6$)		
	FULL SKY	**NORTH**	**SOUTH**
all (20)	11%	60%	21%
equi (4)	4%	10%	36%
iso (12)	5%	63%	8%
scal (4)	64%	61%	48%

Table 4.7: χ^2 for the WMAP 5-year QVW data compared to simulations. Top panel large scale study; bottom panel small scale one.

label this set as LSS and are predominantly squeezed. The second set, labelled as LLS, is formed by triangles which have j_1,$j_2 \leq 5$ and $j_3 \geq 6$ and are predominantly co-linear. We report the results in Tab. 4.8. The isosceles triangles belonging to the LSS set are

conf.	Correlation (L-S-S)		
	FULL SKY	**NORTH**	**SOUTH**
iso (20)	23%	78%	0.4%
scal (26)	76%	40%	51%
open (4)	32%	35%	54%

conf.	Correlation (L-L-S)		
	FULL SKY	**NORTH**	**SOUTH**
iso (8)	47%	94%	20%
scal (13)	62%	98%	15%
open (39)	3%	88%	2%

Table 4.8: χ^2 for the WMAP 5-year QVW data compared to simulations: correlation large-small scale. Top panel LSS set; bottom panel LLS set.

very anomalous in the south hemisphere. The LLS set in characterised by an anomaly in the open configurations. Interestingly the lack of signal in the northern hemisphere is evident in the LLS, while the LSS distribution appears more typical.

Influence on $f_{\rm NL}$ estimation. In the following section we address the issue of the effect of the sky asymmetries on the measure of the primordial non-Gaussianity parameter. A

complete review on the nature of this parameter may be found in Bartolo et al. (2004) and Fergusson & Shellard (2009); recent constraints from CMB experiments can be found in Smith et al. (2009); Curto et al. (2008); Komatsu et al. (2009); De Troia et al. (2007) while Slosar et al. (2008) constrained $f_{\rm NL}$ through the galaxy distribution. Limits on $f_{\rm NL}$ using wavelets are discussed in Curto et al. (2009); Cabella et al. (2004); Mukherjee & Wang (2004). In order to estimate $f_{\rm NL}$ we generate two sets of simulations. The first one consists in 20,000 Gaussian simulations consistent with the WMAP 5-year best fit angular power spectrum and the second one consists of primordial non Gaussian maps (Liguori et al., 2007). Both sets where then passed through the procedure described above. We then computed $f_{\rm NL}$ from the estimator introduced in Pietrobon et al. (2009):

$$f_{\rm NL} = \frac{X^{dT} C^{-1} X^{\rm th}}{X^{\rm th\,T} C^{-1} X^{\rm th}}. \tag{4.11}$$

Here X is a vector composed by the values of needlets bispectrum for a given triangular configuration according to Eq.3.16. The covariance matrix C is calculated from the Gaussian simulations since its dependency on $f_{\rm NL}$ is negligible (e.g. see Spergel & Goldberg (1999)). The theoretical non-Gaussian template X^{th} was calculated via Monte Carlo simulations over the 100 primordial non-Gaussian maps. Since we know the CMB sky is asymmetric, showing more non-Gaussianity in the southern hemisphere, we carried out the full sky analysis and also split north-south one to see if the asymmetry extends to differences in the $f_{\rm NL}$ estimate. In practice we computed $S_{j_1 j_2 j_3}$ on the pixels outside the extended "j_3-j_4"Kq75 mask in the northern and southern hemispheres. Recently Curto et al. (2009) targeted the same issue within the Spherical Mexican Hat Wavelets framework, finding no evidence of $f_{\rm NL}$ varying on the sky. The values shown in Table 4.9 do not indicate a significant deviation between the two hemispheres; the error bars become significantly larger due to the reduced number of pixels used to calculate the needlet bispectrum. It will be interesting to repeat the same test with the upcoming experiments like Planck where the error bars are expected to be drastically reduced. Combining all configurations we find $f_{\rm NL} = -25 \pm 75$ in the northern hemisphere and $f_{\rm NL} = 75 \pm 75$ in the south, which are consistent with the null hypothesis. Any differences compared to the results by Curto et al. (2009) are most likely primarily due to the broader mask: if we use the Kq75 mask provided by the WMAP team we obtain in the south $f_{\rm NL} = 25 \pm 75$. We stress that the fact we do not observe a sky asymmetry is not surprising since we do not expect such asymmetry for a primordial signal like the non-Gaussian one left over after inflation.

conf.	FULL SKY	NORTH	SOUTH
all	0 ± 45	-25 ± 75	75 ± 75
equi	-60 ± 200	-130 ± 260	-90 ± 260
iso	-20 ± 50	-30 ± 80	80 ± 85
scal	0 ± 55	-50 ± 80	110 ± 90
open	120 ± 400	-650 ± 600	770 ± 600

Table 4.9: $f_{\rm NL}$ estimates with the 1-sigma confidence levels for each triangle subset calculated from full sky, northern and southern hemispheres.

4.3.2 Conclusions

We used the needlets bispectrum to investigate the presence of anomalies in the WMAP 5-year data. For the first time we exploited the bispectrum formalism analysing the triangle configurations according to their shape. By splitting the χ^2 analysis of the needlets bispectrum for the northern and southern hemispheres we found that the southern sky is barely compatible with the Gaussian hypothesis while the northern hemisphere is characterised by a lack of global bispectrum signal. This is complementary to what found by applying different statistics: power spectra (Hansen et al., 2008), bispectrum (Land & Magueijo, 2005) and n-point correlation functions (Eriksen et al., 2005). We distinguished equilateral, isosceles, scalene and open configurations and compared the power present in the data to random Gaussian simulations. The most anomalous signals in the southern galactic hemisphere arise in the squeezed configurations (isosceles, large-small-small) and in the very co-linear configurations (open, large-large-small). This kind of information should be useful as a means to find out the physical origin of the anomalies. While the large squeezed signal hints at a local type of non-Gaussianity, this is not bourne out when a more optimal estimator tuned specifically to this type of non-Gaussianity is used. We investigated the effect of hemispherical asymmetry on the measurement of $f_{\rm NL}$ finding no significant discrepancy between north and south. It will be interesting to test with the next generation of CMB experiments, when the error bars on $f_{\rm NL}$ will be drastically reduced, to see if a north-south asymmetry arises in the $f_{\rm NL}$ estimates. As a consistency check, we performed the same tests (anomalies and $f_{\rm NL}$ estimates) with a different needlets parameter ($B = 3.5$) and for the channels Q,V and W separately and found consistent results.

4.4 Foreground Influence on Primordial non-Gaussianity Estimates: Needlets Analysis of WMAP 5-year Data

As we discussed in the previous sections, there has been considerable activity in constraining the amount of non-Gaussianity present in CMB data. This is motivated, on one side, by the theoretical interest into deviations from Gaussian statistics of primordial fluctuations – which is predicted in several implementations of the inflationary scenario, and then it can be used to rule out specific models; on the other hand, non-Gaussianity can be produced by undetected systematics, which may suggest problems in the dataset, or by late-time anomalies, which may point out inconsistency in the standard cosmological model.

The primordial non-Gaussianity produced by inflation is usually characterised by the $f_{\rm NL}$ parameter (see e. g. Luo (1994); Heavens (1998); Spergel & Goldberg (1999); Komatsu & Spergel (2001)). Since the release of the first year WMAP data (Bennett et al., 2003a; Komatsu et al., 2003), there has been a drastic reduction of the upper limits of $f_{\rm NL}$. The most recent constraints coming from different techniques can be found in Komatsu et al. (2009); Smith et al. (2009); Yadav & Wandelt (2008); Curto et al. (2009, 2008); De Troia et al. (2007); Pietrobon et al. (2009); Rudjord et al. (2009a); Natoli (2009); Rudjord et al. (2009b); Smidt et al. (2009)).

One particular class of non-Gaussian behaviours which is not primordial in nature, is the one expected from unremoved contamination from astrophysical sources, or foregrounds. When component separation techniques are applied to CMB data (e. g. Maino et al. (2002)), residual foregrounds can, albeit subdominant, be a source of non-Gaussianity, which can be confused with a primordial signature and affect the constraints on $f_{\rm NL}$. In this section we aim at generalising the needlet bispectrum estimator (Pietrobon et al., 2009) in the presence of such foreground residuals (Cabella et al., 2009).

4.4.1 Analysis

In constraining primordial non-Gaussianity, one can estimate $f_{\rm NL}$ by minimising the chi-square:

$$\chi^2(f_{\rm NL}) = Y^T \mathbf{C}^{-1} Y, \tag{4.12}$$

where $Y = Y^{obs} - \langle Y(f_{\rm NL})\rangle$ is the difference between an ordered array of data (Y^{obs}) and the corresponding theoretical prediction $Y(f_{\rm NL})$, as, for instance, the values of Minkowski functionals for the relatives thresholds (Hikage et al., 2006), the densities of lakes or hills when using the local curvature(Cabella et al., 2005) or finally the values of needlet bispectrum (Pietrobon et al., 2009; Rudjord et al., 2009a,b). In the presence of the expected

weak non-Gaussianity the covariance matrix $\mathbf{C}$ is calculated via Gaussian simulations with the same experimental setup of the data. It has been shown (Pietrobon et al., 2009; Rudjord et al., 2009a) that an unbiased estimator for $f_{\rm NL}$ is given by

$$f_{\rm NL} = \frac{\sum_{\mu\mu'} S^{\rm obs}_{\mu} \mathbf{C}^{-1}_{\mu\mu'} S^{\rm th}_{\mu'}}{\sum_{\mu\mu'} S^{\rm th}_{\mu} \mathbf{C}^{-1}_{\mu\mu'} S^{\rm th}_{\mu'}}, \tag{4.13}$$

where μ runs over the triplets $\{j_1 j_2 j_3\}$ and $S^{\rm th}_{\mu}$ stands for the ensemble average of primordial non-Gaussian realisations. Although the process of foreground reduction could make things more complicated, the minimum assumption that we can make is that the final map, contaminated by foreground residuals, can be modelled as:

$$\begin{aligned} T^{\rm sim}(\hat{\gamma}) &= T^{\rm G}(\hat{\gamma}) + f_{\rm NL} T^{\rm NG}(\hat{\gamma}) \\ &+ \alpha_{\rm td}\, D(\hat{\gamma}) + \alpha_{\rm ff}\, F(\hat{\gamma}) + \alpha_{\rm sync}\, S(\hat{\gamma}), \end{aligned} \tag{4.14}$$

where D, F and S mean thermal dust, free-free emission and synchrotron radiation map respectively. Eq. 4.12 can be easily generalised as follows:

$$\begin{aligned} \chi^2 &= \left(S^{obs}_{\mu} - S_{\mu}(f_{\rm NL}) - S^{i}_{\mu}(\alpha_i)\right) \mathbf{C}^{-1}_{\mu\mu'} \\ &\left(S^{obs}_{\mu'} - S_{\mu'}(f_{\rm NL}) - S^{i}_{\mu'}(\alpha_i)\right)^{T}, \end{aligned} \tag{4.15}$$

where i refers to the i-th foreground template with the Einstein summation convention assumed, and $S^{\rm i}_{\mu}$ is the needlet bispectrum of the relative foreground. Calculating the needlets coefficients from Eq. 4.14 we obtain

$$\beta_{jk} = \beta^{\rm G}_{jk} + \beta^{\rm N}_{jk} + f_{\rm NL}\beta^{\rm NG}_{jk} + \alpha_{\rm d}\beta^{\rm D}_{jk} + \alpha_{\rm f}\beta^{\rm ff}_{jk} + \alpha_{\rm s}\beta^{\rm S}_{jk}. \tag{4.16}$$

In Figure 4.20 we show the needlet coefficients in the case of $B = 2$ and $j = 6$ for the three foregrounds templates – dust, free-free and synchrotron – once they have been masked. The maps were converted into thermodynamic temperature for each channel and combined to form one single map. Each template was divided by a factor 10, which is the level of residuals expected. This factor, and then the leakage of the non-CMB component in the foreground reduced map we used, was estimated through a Monte Carlo Markov Chain. The angular power spectrum of the foreground reduced map have been compared to a linear combination of CMB, noise, synchrotron, free-free and Galactic dust. 100 realisations of CMB maps have been generated in order to take into account also the uncertainty due to the cosmic variance. We also created 100 realisations of noise with variance consistent with the data and then fitted the amplitude coefficients p_{γ} of each

component γ, such that

$$\mathcal{C}_\ell^{tot} = \sum_\gamma p_\gamma \mathcal{C}_\ell^\gamma + \mathcal{C}_\ell^{\rm CMB} + N_\ell,$$

where N_ℓ is the detector noise. We find $p_{\rm synch} < 0.1 \times 10^{-1}$, $p_{\rm dust} < 1.0 \times 10^{-1}$ and $p_{\rm ff} < 0.6 \times 10^{-1}$. The coefficients p_γ provide an indication of the power spectrum contamination percentage by the foreground residuals. The effect on the bispectrum is estimated to be of the order of $\sim 10^{-3}$. This is indeed confirmed by the best fit values of the amplitudes $\alpha_{\rm i}$ computed through Eq. 4.20, which are of the order of the unity.

If we compute the expectation value of the needlet bispectrum for a map ensemble as given in Eq. 4.14 we obtain:

$$\begin{aligned} S_{j_1 j_2 j_3} \;\sim\; & \sum_k \big(f_{\rm NL} \beta^{\rm NG}_{j1k} \beta^G_{j2k} \beta^G_{j3k} + \alpha^3_{\rm d} \beta^{\rm D}_{j1k} \beta^D_{j2k} \beta^D_{j3k} \\ + \; & \alpha^3_{\rm ff} \beta^{\rm F}_{j1k} \beta^F_{j2k} \beta^F_{j3k} + \alpha^3_{\rm sync} \beta^{\rm S}_{j1k} \beta^S_{j2k} \beta^S_{j3k} \big), \end{aligned} \tag{4.17}$$

where we kept the leading term of primordial non-Gaussianity expansion only and considered the correlations among foreground residuals negligible. We do not expect any correlation between the primordial non-Gaussianity and the distribution of the foregrounds residuals: this justifies why we ignored the terms like $\beta^{\rm NG}\beta^{\rm I_1}\beta^{\rm I_2}$ (I=$\{$D,F,S$\}$). The mixed contributions $\beta^{\rm I_1}\beta^{\rm I_2}\beta^{\rm I_3}$ have been considered as higher order corrections to our estimator $S_{j_1 j_2 j_3}$, because $\langle \beta^{\rm I} \rangle = 0$. If we were able to produce foregrounds maps we would expect these terms to vanish. Moreover, for the same reason, since we do not simulate different realisations of the foregrounds but we consider them as templates, we do not know the correlation matrix to properly model these cross-contributions. Finally we are interested in the foreground residuals whose correlation properties may be hidden by the CMB map cleaning procedure itself.

With this assumption the theoretical needlet bispectrum (S) in presence of foreground residuals can be linearly decomposed as follows:

$$S_{j_1 j_2 j_3} = f_{\rm NL} S^{\rm NG}_{j_1 j_2 j_3} + A_D S^{\rm D}_{j_1 j_2 j_3} + A_F S^{\rm F}_{j_1 j_2 j_3} + A_S S^{\rm S}_{j_1 j_2 j_3}, \tag{4.18}$$

where

$$\begin{aligned} S^{\rm NG}_{j_1 j_2 j_3} &= \sum_k \frac{\beta^{\rm G}_{j_1 k} \beta^{\rm G}_{j_2 k} \beta^{\rm NG}_{j_3 k}}{\sigma_{j_1} \sigma_{j_2} \sigma_{j_3}} + \text{perms}; \\ S^{\rm I}_{j_1 j_2 j_3} &= \sum_k \frac{\beta^{\rm I}_{j_1 k} \beta^{\rm I}_{j_2 k} \beta^{\rm I}_{j_3 k}}{\sigma_{j_1} \sigma_{j_2} \sigma_{j_3}}. \end{aligned}$$

Here for simplicity reason we have replaced $\alpha^3_{\rm i}$ with $A_{\rm i}$ for the foreground amplitudes.

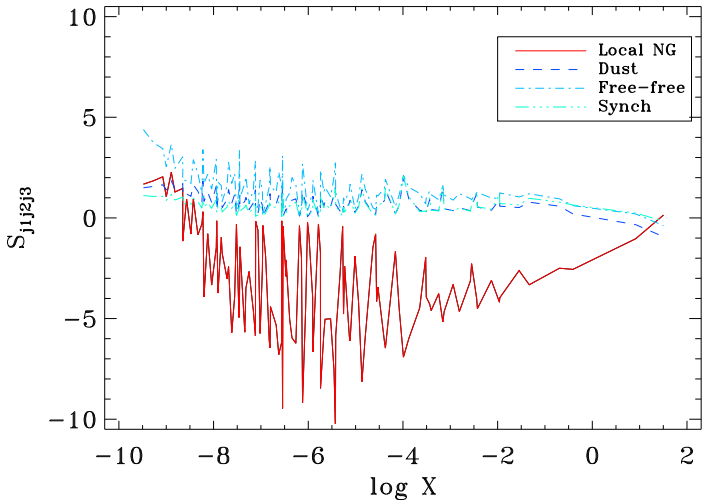

Figure 4.19: Bispectrum templates for the primordial non-Gaussian signal and the three WMAP data foregrounds normalised according to the procedure described by a factor 10^{-3}.

In Figure 4.19 we show the bispectrum for the primordial non-Gaussianity with $f_{\rm NL} = 50$ and for the foreground templates of WMAP data normalised according to prescription discussed previously. The bispectrum is shown as a function of the quantity $X = 1/j_1 j_2 + 1/j_1 j_3 + 1/j_3 j_2$.

Minimising Eq. 4.15 with respect to $x = (f_{\rm NL}, A_{\rm d}, A_{\rm f}, A_{\rm s})$ we obtain:

$$f_{\rm NL} = \frac{S_i^{\rm NG} \mathbf{C}_{ij}^{-1} S_j^{obs}}{S_i^{\rm NG} \mathbf{C}_{ij}^{-1} S_j^{\rm NG}} - \sum_I \frac{S_i^{\rm NG} \mathbf{C}_{ij}^{-1} S_j^{\rm I}}{S_i^{\rm NG} \mathbf{C}_{ij}^{-1} S_j^{\rm NG}} A_{\rm I} \qquad (4.19)$$

$$A_{\rm K} = \frac{S_i^{\rm K} \mathbf{C}_{ij}^{-1} S_j^{obs}}{S_i^{\rm K} \mathbf{C}_{ij}^{-1} S_j^{\rm K}} - \sum_I \frac{S_i^{\rm K} \mathbf{C}_{ij}^{-1} S_j^{\rm I}}{S_i^{\rm K} \mathbf{C}_{ij}^{-1} S_j^{\rm K}} A_{\rm I}$$

where $K = \{{\rm D}, {\rm F}, {\rm S}\}$.

The solution of the previous system provide us with the estimates of $f_{\rm NL}$ with the needlet bispectrum in presence of foreground residuals. In the following we present data and simulations where this estimator has been applied.

4.4.2 Data set, simulations and results

In the following, the needlets of the simulations and data will be calculated for B=2 unless specified otherwise. We used the *WMAP* 5-year data (Hinshaw et al., 2009) publicly available[6] combining all channels according to Eq. 4.6 (see Sec. 4.2.1). The foregrounds

[6] http://lambda.gsfc.nasa.gov/product/map/dr3/m_products.cfm

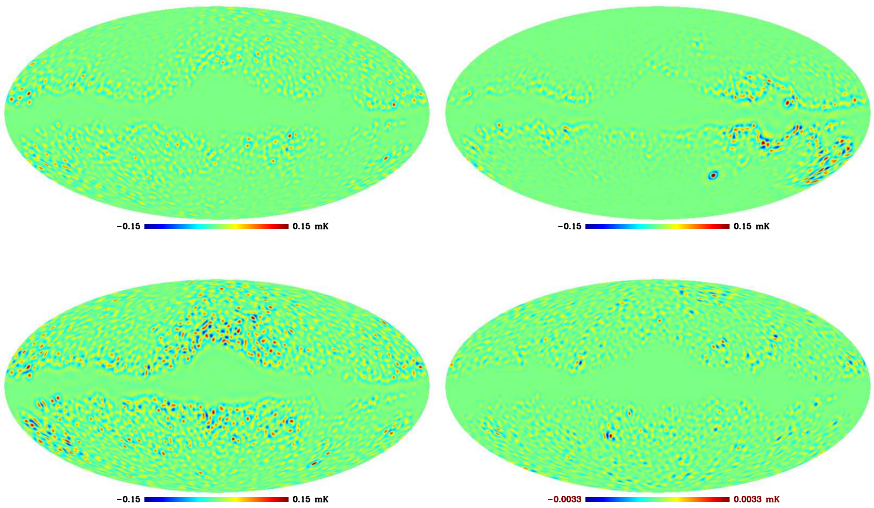

Figure 4.20: Thermal dust (top left) free-free (top right) synchrotron (bottom left) and non-Gaussian for $f_{\rm NL} = 100$ (bottom right) needlet coefficients for $B = 2$ and $j = 6$. The wide Kq75 mask is applied.

considered are the 3-year *WMAP* data templates of dust, free-free and synchrotron emission at the resolution of $N_{\rm side} = 256$, corrected by the conversion factors from antenna to thermodynamic temperature of the respective channel; we then combined them as in Eq. 4.6 to have one single map for each template. Data and foreground templates have been then masked with Kq75 mask (degraded as well to the same *HEALPix* resolution), which leaves uncovered roughly the 30% of the sky. We obtained our final constraints on $f_{\rm NL}$ by applying the estimator in its improved fashion to the *WMAP* 5-year data where:

- the covariance matrix $\mathbf{C}^{-1}$ was calibrated over 20,000 Gaussian simulations
- the needlet foreground bispectra $S^{\rm D}, S^{\rm F}, S^{\rm S}$ were calculated on the templates described above
- the primordial needlet bispectrum $S^{\rm NG}$ was calculated over 100 primordial non-Gaussian maps (Liguori et al., 2007) convolved with the beams and combined as done for the Gaussian simulations.

Figure 4.21 shows the data we used, superimposed to the one 68% confidence level region. The error bars on $f_{\rm NL}$ were computed through the distribution of its estimates for 20,000 Gaussian realizations.

In Figure 4.22 we show our results, where in each panel we reported the estimate of $f_{\rm NL}$ with and without marginalizing over the foreground templates. Without marginalizing, we found $f_{\rm NL} = 30 \pm 40, 80$ at 1σ and 2σ respectively. The marginalization over all foregrounds brings the constraint to $f_{\rm NL} = 36 \pm 47, 94$ with an increase of the error bars

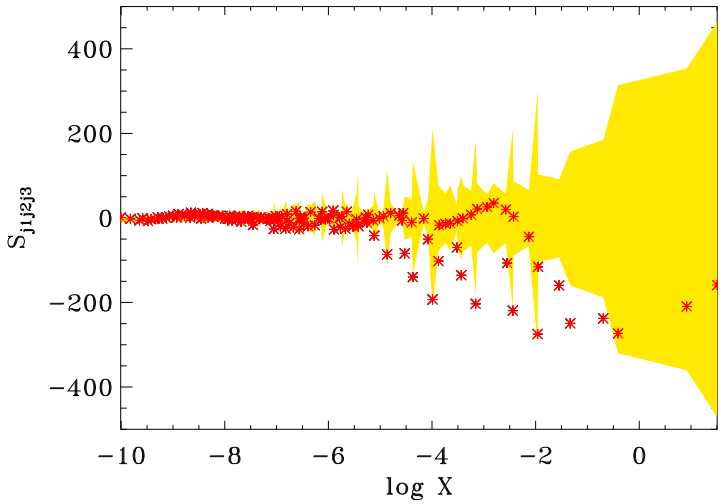

Figure 4.21: Needlets bispectrum measured from the WMAP 5-year temperature map. The yellow shaded region marks the 68% confidence level region computed from the 20,000 maps ensemble.

of about 15% and a positive shift of the mean value. This could be an hint of the reason for some positive detection present in literature (e. g. Yadav & Wandelt (2008); Rudjord et al. (2009a,b)).

More information can be obtained by looking at the estimates of $f_{\rm NL}$ marginalizing over the three foregrounds separately. The enlargement of the error bars due to each foreground is of the same order of magnitude, but the shift of the estimate seems to be due more to the dust component.

As a further check we carried out a Fisher analysis. So far we performed a maximum likelihood method to find a good estimate of $f_{\rm NL}$ in the presence of foreground contamination and quantified the scatter around this evaluation. In the limit of a large dataset, the maximum likelihood estimate is the one for which the Cramer-Rao inequality becomes an equality. Since the estimates of the parameters are evidently correlated, the latter can be written as $\sigma_\theta = 1/(F^{-1})_{ii}^{1/2}$, which is the marginal error and indeed the relevant error to quote. For a quick-start guide to the Fisher matrix see Coe (2009).

The Fisher matrix is defined as:

$$F_{ab} = \sum_{\mu\mu'} \frac{\partial S_\mu^{\rm T}}{\partial a} \mathbf{C}_{\mu\mu'}^{-1} \frac{\partial S_{\mu'}^{\rm T}}{\partial b} \tag{4.20}$$

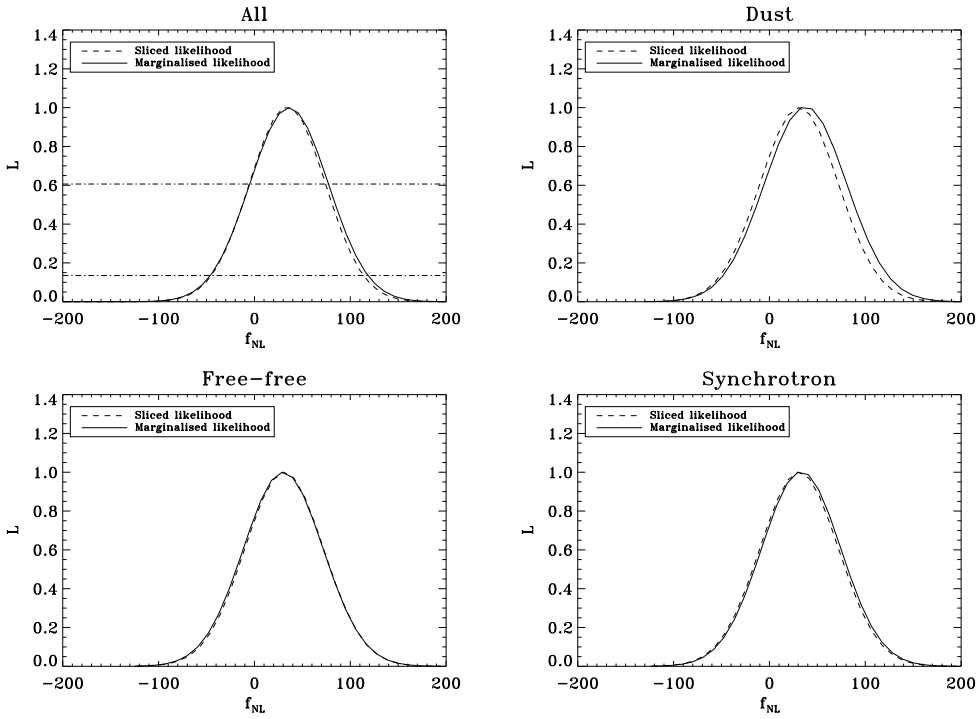

Figure 4.22: Unidimensional likelihood for the $f_{\rm NL}$ parameter. Solid lines represent marginalized likelihoods, whereas the dashed ones refer to the slice $A_{\rm foreg} = 0$. The top left panel shows the analysis including all the three foregrounds, while the others are derived for a two dimensional analysis where dust (top right), free-free (bottom left) and synchrotron (bottom right) emission are considered.

where S is the signal described in Eq. 4.18 and μ, μ', a and b run over the triplets $\{j_1, j_2, j_3\}$ and the parameter set $\{f_{\rm NL}, A_{\rm D}, A_{\rm F}, A_{\rm S}\}$. In detail we have:

$$F = \begin{pmatrix} S^{NG}\mathbf{C}^{-1}S^{NG} & S^{NG}\mathbf{C}^{-1}S^{\rm D} & S^{NG}\mathbf{C}^{-1}S^{\rm F} & S^{NG}\mathbf{C}^{-1}S^{\rm S} \\ S^{\rm D}\mathbf{C}^{-1}S^{NG} & S^{\rm D}\mathbf{C}^{-1}S^{\rm D} & S^{\rm D}\mathbf{C}^{-1}S^{\rm F} & S^{\rm D}\mathbf{C}^{-1}S^{\rm S} \\ S^{\rm F}\mathbf{C}^{-1}S^{NG} & S^{\rm F}\mathbf{C}^{-1}S^{\rm D} & S^{\rm F}\mathbf{C}^{-1}S^{\rm F} & S^{\rm F}\mathbf{C}^{-1}S^{\rm S} \\ S^{\rm S}\mathbf{C}^{-1}S^{NG} & S^{\rm S}\mathbf{C}^{-1}S^{\rm D} & S^{\rm S}\mathbf{C}^{-1}S^{\rm F} & S^{\rm S}\mathbf{C}^{-1}S^{\rm S} \end{pmatrix}$$

where we have omitted the sum over the triplets.

The marginal error on $f_{\rm NL}$ arising from this Fisher analysis is $\Delta f_{\rm NL} = 42$, very close to the limits obtained with the Monte Carlo approach; this confirms the efficiency of our estimation method. In Fig. 4.23 we show the 1σ and 2σ error ellipses together with the output from simulations; here each plot presents the significance regions in the case where the other parameters are fixed at their fiducial value (in this particular case the null hypothesis). It can be seen that the free-free component seems slightly anti-correlated with $f_{\rm NL}$, the cross-correlation coefficient being $\rho = -0.26$. The other foreground components, i.e. dust and synchrotron, show a positive correlation, represented by the orientation of the ellipses, with $\rho = 0.19$ and $\rho = 0.10$, respectively. The scatter of the over-plotted distribution of Gaussian simulations on the same $A_{\rm K}$-$f_{\rm NL}$ plane is in excellent agreement with the ellipses, which confirms again the consistency of our procedure.

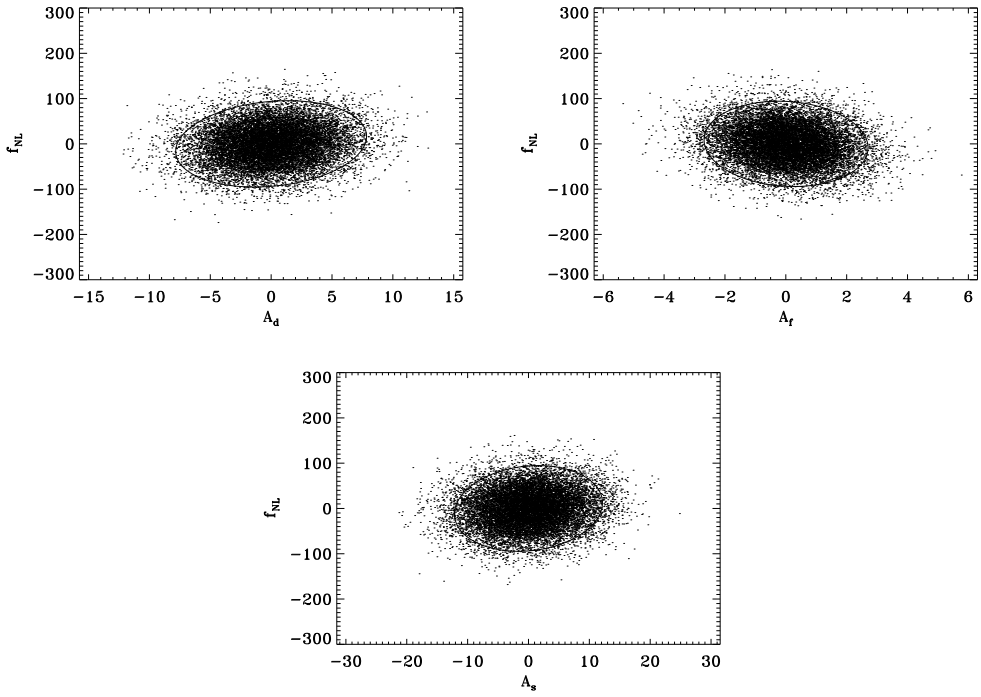

Figure 4.23: Scatter plots for a two dimensional analysis taking into account one foreground separately. The 1σ and 2σ confidence level derived from a Fisher matrix analysis are superimposed.

Notice that the three correlation coefficients nearly sum to zero, $+0.03$: this reflects the small positive shift in the mean value (from 30 to 36) and it is a consequence of the linear ansatz given by Eq. 4.18.

4.4.3 Conclusions

In this section we have presented a procedure to marginalize the residual foregrounds when estimating $f_{\rm NL}$ in the needlet bispectrum framework. However it is important to stress that this algorithm does not strictly rely on needlets properties and it can be easily applied to any linear estimator. With the foreground marginalization, we found, for WMAP 5-year data, that the estimate on $f_{\rm NL}$ is positively shifted by $\Delta f_{\rm NL} = 6$ and the error bars are enlarged of about 15% with respect to the estimate obtained without marginalizing. Foreground residuals can play different roles in different estimators of primordial non-Gaussianity. In fact, compared to other foreground analysis, our results seem to agree with those obtained by Yadav & Wandelt (2008), who argued that foregrounds negatively bias the $f_{\rm NL}$ value. However, Smith et al. (2009) draw another conclusion, showing that the sign of the bias could depend on the free choices of weighting in the construction of pipeline to estimate $f_{\rm NL}$. Since substantially needlets coefficients

are a rebinning of the filtered harmonic coefficients $a_{\ell m}$, this could explain the different behaviours. This study needs to be extended to each test of non-Gaussianity, since different tests act on different spaces (e.g. harmonic, pixel, wavelet), leading to the conclusion that the influence of foregrounds on estimating $f_{\rm NL}$ is not unique. Moreover, we have showed that each foreground has a different effect, when it is taken separately. A split analysis like this could be crucial, for instance, at high multipoles, where the foreground behaviour is currently poorly understood. All this reinforces the argument that a careful analysis combining different tests is crucial to discriminate between primordial non-Gaussianity and spurious effects.

Our procedure could be improved by taking into account the information on the intra-pixel covariance matrix of each single foreground residual and the cross correlation between them. This would allow a more accurate analysis via Monte Carlo realizations, instead of simply assuming a rigid pixel-independent foreground residual template. A similar approach could be fundamental for the next experiments, like Planck, for which the error bars on $f_{\rm NL}$ are expected to be drastically reduced ($\Delta f_{\rm NL} \sim 3-5$ Babich (2005)) and the uncertainties introduced by foregrounds become relevant.

Conclusions

In this chapter we have analysed in detail the Gaussianity properties of the CMB as measured by the WMAP team by means of needlets. Actually we focused on two complementary aspects of this topic. First, we analysed the map, detecting anomalous features at large scale structures, hot and cold spots, which determine a hemispherical asymmetry in the sky. We then checked the effect of such asymmetry on the needlets power spectrum and bispectrum. On the former, the spots account for roughly 50% of the total difference power, while on the latter we detect still a strong anomaly. This anomaly is particularly significant when looking at isosceles configurations.

Moreover, the bispectrum formalism allows us to set very promising constraints on the primordial non-Gaussianity parameter, in particular in view of the Planck experiments. Finally we included the effect of spurious unremoved foreground residuals in the CMB on the $f_{\rm NL}$ estimator, which is thought to be relevant for the next generation of cosmological experiments.

Chapter 5

Conclusions

Facts come in pairs at the very least,
for a single body is inconceivable
apart from a space in which it hangs.
Definition, setting bounds, delineation:
these are always acts of division
and thus of duality,
for as soon as a boundary is defined,
it has two sides.

("The way of Zen", A. Watts)

This work reviews the studies I carried out during my Ph. D. I focused on two main questions which still remain unanswered within the framework of the standard cosmological model: the characterisation of dark energy and the issue of non-Gaussianity.

Very recently we discovered that the Universe expansion is accelerating. This represents a challenging puzzle for theorists. The more likely explanation invokes a new fluid, dubbed dark energy, which has peculiar density-pressure properties. I investigated some of these properties assuming a few phenomenological models available in literature, and constrained their parameters combining the most recent CMB and large scale structure observations. Results are discussed in Chapter 2. I confirmed the ISW effect detection at more than 3σ level.

The study of the CMB anisotropies distribution requires sophisticated tools, which are continuously improved. I contributed to this active research topic introducing a new rendition of wavelets, needlets, which have nice properties, suitable to study fields on the sphere. Detailed discussion has been provided in Chapter 3 and needlet application to CMB data analysis is the underlying common ground of my Ph. D. project.

A crucial feature of the Big Bang scenario is the homogeneity and isotropy of the Universe, which results after the inflationary phase the Universe underwent in the very

early epoch of its evolution. Together with smoothness, inflation predicts small perturbations which follow a nearly Gaussian distribution. The tiny deviation from the normal distribution contains important details on the inflation process itself. Non-Gaussianity may reveal itself also in a different fashion due to more recent processes which leave a footprint on large scales. I have addressed this issue in Sec. 4.1, where a study of anomalous CMB spots and its consequences on CMB data analysis is performed. The power spectrum asymmetry itself is reduced by 50%, while the cosmological parameters are basically unaffected.

I spent lots of effort to characterise the primordial bispectrum of the CMB fluctuations, constraining its amplitude, namely the $f_{\rm NL}$ parameter finding $f_{\rm NL} = 30 \pm 40$ at 68% c.l. (Sec. 4.2), and its shape (Sec. 4.3). We found a striking asymmetry between the estimates of the bispectrum, measured in the northern and in the southern hemisphere. The former exhibits a general lack of power, whereas the latter as results are anomalous, especially in the isosceles configurations, **suggesting that perhaps the origin of this asymmetry depends upon a large-small scale correlation**. I also developed an estimator to measure such a bispectrum and improved it by describing a procedure to take into account unremoved foreground residuals (Sec. 4.4). As expected, the foregrounds residuals enlarge the error bars of a 15% and result mildly correlated to the primordial signal.

All these studies are particularly important in view of the new generation of upcoming experiments, which will provide datasets of extraordinary quality, which, as scientists, we have to skillfully combine to make the best of our theories. In the next decades, cosmology is going to be a fascinating but challenging field of research I am glad to belong to.

"We are at the very beginning of time for the human race. It is not unreasonable that we grapple with problems. But there are tens of thousands of years in the future. Our responsibility is to do what we can, learn what we can, improve the solutions, and pass them on."[1]

[1] R. Feynman, 'What Do You Care About What Other People Think?', 1988

Bibliography

Abazajian K. N., et al., 2009, ApJ, 182, 543

Abdalla E., Abramo L. R., Sodré L., Wang B., 2009, Phys. Lett. B, 673, 107

Ackerman L., Carroll S. M., Wise M. B., 2007, Phys. Rev. D, 75, 083502

Adriani O., et al., 2009, Nature, 458, 607

Afshordi N., 2004, Phys. Rev. D, 70, 083536

Afshordi N., Loh Y.-S., Strauss M. A., 2004, Phys. Rev. D, 69, 083524

Alabidi L., Lyth D., 2006, JCAP, 8, 6

Albrecht A., Steinhardt P. J., 1982, Phys. Rev. Lett., 48, 1220

Alpher R. A., Bethe H., Gamow G., 1948, Phys. Rev., 73, 803

Alpher R. A., Herman R., 1948, Nature, 162, 774

Alpher R. A., Herman R., 1988, Physics Today, 41, 24

Amendola L., 2000, Phys. Rev. D, 62, 043511

Amendola L., 2004, Phys. Rev. D, 69, 103524

Amendola L., Bellisai D., Occhionero F., 1993, Phys. Rev. D, 47, 4267

Amendola L., Quercellini C., 2003, Phys. Rev. D, 68, 023514

Amendola L., Quercellini C., 2004, Phys. Rev. D, 92, 181102

Amendola L., Tocchini-Valentini D., 2001, Phys. Rev. D, 64, 043509

Ananda K. N., Bruni M., 2006, Phys. Rev. D, 74, 023524

Ananda K. N., Bruni M., 2006, Phys. Rev. D, 74, 023523

Anestis A., 2007, Statistics Surveys (electronic), 1, 16

Antoine J.-P., Vandergheynst P., 1999, Appl. Comput. Harmon. Anal., 7, 262

Arrowsmith D. K., Place C. M., 1992, Differential Equations, Maps, and Chaotic Behaviour. Chapman and Hall, London

Babich D., 2005, Phys. Rev. D, 72, 043003

Balbi A., Bruni M., Quercellini C., 2007, Phys. Rev. D, 76, 103519

Baldi P., Kerkyacharian G., Marinucci D., Picard D., 2006, Annals of Statistics 2009, No. 3, 1150-1171, 37, 1150

Baldi P., Kerkyacharian G., Marinucci D., Picard D., 2007, Under revision for Bernoulli, arXiv: 0706.4169 (math)

Baldi P., Kerkyacharian G., Marinucci D., Picard D., 2008, arXiv: 0807.5059 (math ST)

Bardeen J. M., 1980, Phys. Rev. D, 22, 1882

Barrow J. D., Clifton T., 2006, Phys. Rev. D, 73, 103520

Bartolo N., Komatsu E., Matarrese S., Riotto A., 2004, Phys. Rep., 402, 103

Bartolo N., Matarrese S., Riotto A., 2006, JCAP, 6, 24

Bartolo N., Matarrese S., Riotto A., 2007, JCAP, 1, 19

Bean R., Dore O., 2004, Phys. Rev. D, 69, 083503

Bennett C., et al., 2003a, ApJ, 148, 97

Bennett C. L., et al., 2003b, ApJ, 148, 1

Bernabei R., et al., 2008, European Physical Journal C, pp 167–+

Bernui A., Mota B., Reboucas M. J., Tavakol R., 2007, Int. J. Mod. Phys. D, 16, 411

Bernui A., Reboucas M. J., 2009, Phys. Rev. D, 79, 063528

Böhmer C. G., Caldera-Cabral G., Lazkoz R., Maartens R., 2008, Phys. Rev. D, 78, 023505

Boldt E., 1987, Phys. Rep., 146, 215

Boubekeur L., Lyth D. H., 2006, Phys. Rev. D, 73, 021301

Boughn S., Crittenden R., 2004, Nature, 427, 45

Boughn S. P., Crittenden R. G., 2002, Phys. Rev. Lett., 88, 021302

Boughn S. P., Crittenden R. G., 2005, New Astron. Rev., 49, 75

Brown . M. L., et al., 2009, arXiv: 0906.1003 (astro-ph CO)

Bruni M., 1993, Phys. Rev. D, 47, 738

Bruni M., Ellis G. F. R., Dunsby P. K. S., 1992, Class. Quant. Grav., 9, 921

Bruni M., Matarrese S., Pantano O., 1995a, ApJ, 445, 958

Bruni M., Matarrese S., Pantano O., 1995b, Phys. Rev. Lett., 74, 1916

Bruni M., Piotrkowska K., 1994, MNRAS, 270, 630

Cabella P., Hansen F., Marinucci D., Pagano D., Vittorio N., 2004, Phys. Rev. D, 69, 063007

Cabella P., Hansen F. K., Liguori M., Marinucci D., Matarrese S., Moscardini L., Vittorio N., 2006, MNRAS, 369, 819

Cabella P., Kamionkowski M., 2004, arXiv: 0403392 (astro-ph CO)

Cabella P., Liguori M., Hansen F. K., Marinucci D., Matarrese S., Moscardini L., Vittorio N., 2005, MNRAS, 358, 684

Cabella P., Natoli P., Silk J., 2007, Phys. Rev. D, 76, 123014

Cabella P., Pietrobon D., Veneziani M., Balbi A., Crittenden R., de Gasperis G., Quercellini C., Vittorio N., 2009, arXiv: 0910.XXXX

Cabre A., Gaztanaga E., Manera M., Fosalba P., Castander F., 2006, MNRAS, 372, L23

Caldwell R. R., 2002, Phys. Lett. B, 545, 23

Caldwell R. R., Dave R., Steinhardt P. J., 1998, Phys. Rev. Lett., 80, 1582

Caldwell R. R., Kamionkowski M., Weinberg N. N., 2003, Phys. Rev. Lett., 91, 071301

Cayón L., Sanz J. L., Barreiro R. B., Martínez-González E., Vielva P., Toffolatti L., Silk J., Diego J. M., Argüeso F., 2000, MNRAS, 315, 757

Célérier M.-N., 2007, New Advances in Physics 1, 29 (2007), 1, 29

Cembranos J. A. R., de la Cruz-Dombriz A., Dobado A., Maroto A. L., 2008, JCAP, 10, 39

Chimento L. P., Forte M., Kremer G. M., 2009, Gen. Rel. Grav., 41, 1125

Coe D., 2009, arXiv: 0906.4123 (astro-ph CO)

Condon J. J., Cotton W. D., Greisen E. W., Yin Q. F., Perley R. A., Taylor G. B., Broderick J. J., 1998, ApJ, 115, 1693

Cooray A., 2002, Phys. Rev. D, 65, 103510

Cooray A., Sarkar D., Serra P., 2008, Phys. Rev. D, 77, 123006

Copeland E. J., Liddle A. R., Wands D., 1998, Phys. Rev. D, 57, 4686

Copeland E. J., Sami M., Tsujikawa S., 2006, Int. J. Mod. Phys. D, 15, 1753

Copi C., Huterer D., Schwarz D., Starkman G., 2007, Phys. Rev. D, 75, 023507

Copi C. J., Huterer D., Schwarz D. J., Starkman G. D., 2007, Phys. Rev. D, 75, 023507

Corasaniti P. S., Bassett B. A., Ungarelli C., Copeland E. J., 2003, Phys. Rev. Lett., 90, 091303

Corasaniti P.-S., Giannantonio T., Melchiorri A., 2005, Phys. Rev. D, 71, 123521

Creminelli P., Nicolis A., Senatore L., Tegmark M., Zaldarriaga M., 2006, JCAP, 5, 4

Crittenden R. G., Turok N., 1996, Phys. Rev. Lett., 76, 575

Cross N., et al., 2001, MNRAS, 324, 825

Cruz M., Cayón L., Martínez-González E., Vielva P., Jin J., 2007, ApJ, 655, 11

Cruz M., Martínez-González E., Vielva P., Cayón L., 2005, MNRAS, 356, 29

Cruz M., Martinez-Gonzalez E., Vielva P., Cayon L., 2005, MNRAS, 356, 29

Cruz M., Martínez-González E., Vielva P., Diego J. M., Hobson M., Turok N., 2008, MNRAS, 390, 913

Curto A., Aumont J., Macías-Pérez J. F., Martínez-González E., Barreiro R. B., Santos D., Désert F. X., Tristram M., 2007, A&A, 474, 23

Curto A., Macías-Pérez J. F., Martínez-González E., Barreiro R. B., Santos D., Hansen F. K., Liguori M., Matarrese S., 2008, A&A, 486, 383

Curto A., Martínez-González E., Barreiro R. B., 2009, ApJ, 706, 399

Curto A., Martinez-Gonzalez E., Mukherjee P., Barreiro R. B., Hansen F. K., Liguori M., Matarrese S., 2009, MNRAS, 393, 615

Davis T. M., et al., 2007, ApJ, 666, 716

de Bernardis P., et al., 2000, Nature, 404, 955

de la Macorra A., 2008, JCAP, 1, 30

de Oliveira-Costa A., Tegmark M., Gaensler B. M., Jonas J., Landecker T. L., Reich P., 2008, MNRAS, 388, 247

de Oliveira-Costa A., Tegmark M., Zaldarriaga M., Hamilton A., 2004, Phys. Rev. D, 69, 063516

De Troia G., et al., 2007, ApJ, 670, L36

Delabrouille J., Cardoso J.-F., Le Jeune M., Betoule M., Fay G., Guilloux F., 2009, A&A, 493, 835

Dicke R. H., Peebles P. J. E., Roll P. G., Wilkinson D. T., 1965, ApJ, 142, 414

Doran M., Müller C. M., Schäfer G., Wetterich C., 2003, Phys. Rev. D, 68, 063505

Dunkley J., et al., 2009, ApJ, 180, 306

Dunlop J. S., Peacock J. A., 1990, MNRAS, 247, 19

Dunsby P. K. S., Bruni M., Ellis G. F. R., 1992, ApJ, 395, 54

Durrer R., Maartens R., 2008, Gen. Rel. Grav., 40, 301

Durrer R., Maartens R., 2008, arXiv: 0811.4132 (astro-ph)

Einstein A., 1905, Annalen der Physik, 322, 891

Einstein A., 1916, Annalen der Physik, 354, 769

Eisenstein D. J., et al., 2005, ApJ, 633, 560

Enqvist K., Takahashi T., 2008, JCAP, 9, 12

Erickcek A. L., Kamionkowski M., Carroll S. M., 2008, Phys. Rev. D, 78, 123520

Erickcek A. L., Kamionkowski M., Carroll S. M., 2008, Phys. Rev. D, 78, 123520

Eriksen H. K., Banday A. J., Górski K. M., Hansen F. K., Lilje P. B., 2007, ApJ, 660, L81

Eriksen H. K., Banday A. J., Gorski K. M., Lilje P. B., 2005, ApJ, 622, 58

Eriksen H. K., Hansen F. K., Banday A. J., Gorski K. M., Lilje P. B., 2004, ApJ, 605, 14

Eriksen H. K., Hansen F. K., Banday A. J., Górski K. M., Lilje P. B., 2004, ApJ, 609, 1198

Eriksen H. K., O'Dwyer I. J., Jewell J. B., Wandelt B. D., Larson D. L., Górski K. M., Levin S., Banday A. J., Lilje P. B., 2004, ApJ, 155, 227

Fay G., et al., 2008, Phys. Rev. D, 78, 083013

Faÿ G., Guilloux F., 2008, arXiv: 0807.2162

Fergusson J. R., Shellard E. P. S., 2009, Phys. Rev. D, 80, 043510

Fixsen D. J., Cheng E. S., Gales J. M., Mather J. C., Shafer R. A., Wright E. L., 1996, ApJ, 473, 576

Fosalba P., Gaztanaga E., 2004, MNRAS, 350, L37

Fosalba P., Gaztanaga E., Castander F., 2003, ApJ, 597, L89

Freedman W. L., et al., 2001, ApJ, 553, 47

Friedmann A., 1922, Zeitschrift fr Physik A, 10, 377386

Gamow G., 1946, Phys. Rev., 70, 572

Gaztanaga E., Manera M., Multamaki T., 2006, MNRAS, 365, 171

Geller D., Hansen F. K., Marinucci D., Kerkyacharian G., Picard D., 2008, Phys. Rev. D, 78, 123533

Geller D., Lan X., Marinucci D., 2009, arXiv: 0907.3369 (astro-ph CO)

Geller D., Marinucci D., 2008, arXiv: 0811.2935 (math ST)

Geller D., Mayeli A., , 2007, Nearly Tight Frames and Space-Frequency Analysis on Compact Manifolds

Génova-Santos R., et al., 2008, MNRAS, 391, 1127

Giannantonio T., et al., 2008, Phys. Rev. D, 77, 123520

González-Nuevo J., Argüeso F., López-Caniego M., Toffolatti L., Sanz J. L., Vielva P., Herranz D., 2006, MNRAS, 369, 1603

Gorini V., Kamenshchik A. Y., Moschella U., Piattella O. F., Starobinsky A. A., 2008, JCAP, 0802, 016

Górski K. M., Hivon E., Banday A. J., Wandelt B. D., Hansen F. K., Reinecke M., Bartelmann M., 2005, ApJ, 622, 759

Granett B. R., Neyrinck M. C., Szapudi I., 2008, arXiv: 0805.2974 (astro-ph), 805

Groeneboom N. E., Eriksen H. K., 2009a, ApJ, 690, 1807

Groeneboom N. E., Eriksen H. K., 2009b, ApJ, 690, 1807

Guilloux F., Fay G., Cardoso J.-F., 2007, arXiv: 0706.2598 (math NA)

Guo Z.-K., Ohta N., Tsujikawa S., 2007, Phys. Rev. D, 76, 023508

Guth A. H., 1981, Phys. Rev. D, 23, 347

Hammond D. K., Wiaux Y., Vandergheynst P., 2009, MNRAS, 398, 1317

Hansen F. K., Banday A. J., Eriksen H. K., Górski K. M., Lilje P. B., 2006, ApJ, 648, 784

Hansen F. K., Banday A. J., Górski K. M., 2004, MNRAS, 354, 641

Hansen F. K., Banday A. J., Gorski K. M., Eriksen H. K., Lilje P. B., 2008, arXiv: 0812.3795 (astro-ph CO)

Hansen F. K., Cabella P., Marinucci D., Vittorio N., 2004, ApJ, 607, L67

Hansen F. K., Cabella P., Marinucci D., Vittorio N., 2004, ApJ, 607, L67

Hansen F. K., Eriksen H. K., Banday A. J., Gorski K. M., Lilje P. B., 2007, in Metcalfe N., Shanks T., eds, Cosmic Frontiers Vol. 379 of Astronomical Society of the Pacific Conference Series, Cosmic Microwave Background Challenges to the Standard Model. pp 16–+

Heavens A. F., 1998, MNRAS, 299, 805

Hernández E., Weiss G., 1996, A first course on wavelets. Studies in Advanced Mathematics, CRC Press, Boca Raton, FL

Hikage C., Komatsu E., Matsubara T., 2006, ApJ, 653, 11

Hinderks J. R., et al., 2009, ApJ, 692, 1221

Hinshaw G., et al., 2007, ApJ, 170, 288

Hinshaw G., et al., 2009, ApJ, 180, 225

Hivon E., Górski K. M., Netterfield C. B., Crill B. P., Prunet S., Hansen F., 2002, ApJ, 567, 2

Ho S., Hirata C., Padmanabhan N., Seljak U., Bahcall N., 2008, Phys. Rev. D, 78, 043519

Hoftuft J., Eriksen H. K., Banday A. J., Górski K. M., Hansen F. K., Lilje P. B., 2009, ApJ, 699, 985

Hu W., 1998, ApJ, 506, 485

Hu W., 2001, Phys. Rev. D, 64, 083005

Hu W., Scranton R., 2004, Phys. Rev. D, 70, 123002

Hu W. T., 1995, arXiv: astro-ph/9508126

Hubble E., 1929, Proceedings of the National Academy of Science, 15, 168

Ichikawa K., Suyama T., Takahashi T., Yamaguchi M., 2008, Phys. Rev. D, 78, 023513

Jarosik N., et al. 2007, ApJ, 170, 263

Jarrett T. H., et al., 2000, AJ, 119, 2498

Jeans J., 1943, Nature, 151, 490

Jeans J. H., ed. 1961, Astronomy and cosmogony. Dover, New York

Johnson B. R., et al. 2007, ApJ, 665, 42

Kamionkowski M., Kosowsky A., Stebbins A., 1997, Phys. Rev. D, 55, 7368

Kawasaki M., Nakayama K., Sekiguchi T., Suyama T., Takahashi F., 2008, JCAP, 11, 19

Kawasaki M., Nakayama K., Sekiguchi T., Suyama T., Takahashi F., 2009, JCAP, 1, 42

Kerkyacharian G., Petrushev P., Picard D., Willer T., 2007, Elec. Jour. of Stats., 1, 30

Khalil S., Munoz C., 2002, Contemp. Phys., 43, 51

Khoury J., 2002, PhD thesis, AA(PRINCETON UNIVERSITY)

Kolb E. W., Turner M. S., eds, 1990, The early universe. Addison-Wesley, Reading MA

Komatsu E., 2002, arXiv: 0206039 (astro-ph)

Komatsu E., et al., 2003, ApJ, 148, 119

Komatsu E., et al., 2009, ApJ, 180, 330

Komatsu E., Spergel D. N., 2001, Phys. Rev. D, 63, 063002

Komatsu E., Spergel D. N., Wandelt B. D., 2005, ApJ, 634, 14

Kowalski M., et al., 2008, ApJ, 686, 749

Kunz M., 2007, arXiv: 0702615 (astro-ph)

Lan X., Marinucci D., 2008a, arXiv: 0805.4154 (math ST)

Lan X., Marinucci D., 2008b, Elec. Jour. of Stats. 2008, Vol. 2, 332-367, 802

Land K., Magueijo J., 2005, MNRAS, 357, 994

Land K., Magueijo J., 2007, MNRAS, 378, 153

Langlois D., Vernizzi F., Wands D., 2008, JCAP, 0812, 004

Larson D. L., Wandelt B. D., 2004, ApJ, 613, L85

Lehners J.-L., Steinhardt P. J., 2008, Phys. Rev. D, 77, 063533

Lemaître G., 1931, MNRAS, 91, 483

Lew B., 2008, JCAP, 0809, 023

Lew B., 2008, JCAP, 9, 23

Lewis A., Bridle S., 2002, Phys. Rev. D, 66, 103511

Lewis A., Challinor A., Lasenby A., 2000, ApJ, 538, 473

Liddle A. R., Lyth D. H., eds, 2000, Cosmological Inflation and Large-Scale Structure. Cambridge University Press, Cambridge UK

Liguori M., Yadav A., Hansen F. K., Komatsu E., Matarrese S., Wandelt B., 2007, Phys. Rev. D, 76, 105016

Linde A., Mukhanov V., 2006, JCAP, 4, 9

Linde A. D., 1982, Phys. Lett. B, 108, 389

Luo X., 1994, ApJ, 427, L71

Lyth D. H., Rodriguez Y., 2005, Phys. Rev. Lett., 95, 121302

Lyth D. H., Ungarelli C., Wands D., 2003, Phys. Rev. D, 67, 023503

Lyth D. H., Wands D., 2002, Phys. Lett. B, 524, 5

Ma C.-P., Bertschinger E., 1995, ApJ, 455, 7

McEwen J. D., Vielva P., Hobson M. P., Martinez-Gonzalez E., Lasenby A. N., 2007, MNRAS, 373, 1211

Maddox S. J., Efstathiou G., Sutherland W. J., 1990, MNRAS, 242

Mainini R., Bonometto S., 2007, JCAP, 6, 20

Maino D., Farusi A., Baccigalupi C., Perrotta F., Banday A. J., Bedini L., Burigana C., De Zotti G., Górski K. M., Salerno E., 2002, MNRAS, 334, 53

Majerotto E., Sapone D., Amendola L., 2004, arXiv: 0410543 (astro-ph)

Malik K. A., Wands D., 2009, Phys. Rep., 475, 1

Manera M., Mota D. F., 2006, MNRAS, 371, 1373

Marinucci D., Pietrobon D., Balbi A., Baldi P., Cabella P., Kerkyacharian G., Natoli P., Picard D., Vittorio N., 2008, MNRAS, 383, 539

Martínez-González E., Gallegos J. E., Argüeso F., Cayón L., Sanz J. L., 2002, MNRAS, 336, 22

Masi S., et al. 2006, A&A, 458, 687

Masina I., Notari A., 2009, JCAP, 2, 19

Mather J. C., et al., 1990, ApJ, 354, L37

Mather J. C., et al., 1992, in Haubold H. J., Khanna R. K., eds, American Institute of Physics Conference Series Vol. 245 of American Institute of Physics Conference Series, Early results from the Cosmic Background Explorer (COBE). pp 266–278

Mayeli A., , 2008, Asymptotic Uncorrelation for Mexican Needlets

McEwen J. D., Hobson M. P., Lasenby A. N., 2006, arXiv: 0609159 (astro-ph)

McEwen J. D., Hobson M. P., Lasenby A. N., Mortlock D. J., 2008, MNRAS, 388, 659

McEwen J. D., Vielva P., Hobson M. P., Martínez-González E., Lasenby A. N., 2007, MNRAS, 376, 1211

Mizuno S., Koyama K., Vernizzi F., Wands D., 2008, in American Institute of Physics Conference Series Vol. 1040 of American Institute of Physics Conference Series, Primordial non-Gaussianities in new ekpyrotic cosmology. pp 121–125

Monteserín C., Barreiro R. B., Martínez-González E., Sanz J. L., 2006, MNRAS, 371, 312

Moudden Y., Cardoso J. F., Starck J. L., Delabrouille J., 2005, EURASIP J. Appl. Signal Process., 15, 2437

Mukherjee P., Wang Y., 2004, ApJ, 613, 51

Muller C. M., 2005, Phys. Rev. D, 71, 047302

Multamaki T., Sainio J., Vilja I., 2007, arXiv: 0710.0282, 710

Nakamura K., 2006, Phys. Rev. D, 74, 101301

Narcowich F. J., Petrushev P., Ward J. D., 2006, SIAM J. Math. Anal., 38, 574

Naselsky P. D., Christensen P. R., Coles P., Verkhodanov O., Novikov D., Kim J., 2007, arXiv: 0712.1118 (astro-ph), 712

Natoli P. e. a., 2009, arXiv: 0905.4301 (astro-ph CO)

Nitta D., Komatsu E., Bartolo N., Matarrese S., Riotto A., 2009, JCAP, 5, 14

Nolta M. R., et al., 2004, ApJ, 608, 10

Nolta M. R., et al., 2009, ApJ, 180, 296

Nolta M. R., et al., 2009, ApJ, 180, 296

Olivares G., Atrio-Barandela F., Pavón D., 2006, Phys. Rev. D, 74, 043521

Padmanabhan N., et al., 2005, Phys. Rev. D, 72, 043525

Padmanabhan T., 1993, Structure Formation in the Universe. Cambridge University Press, Cambridge UK

Park C.-G., 2004, MNRAS, 349, 313

Peebles P. J., Ratra B., 2003, Reviews of Modern Physics, 75, 559

Peebles P. J. E., ed. 1993, Principles of physical cosmology. Princeton University Press, Princeton NJ

Peebles P. J. E., Ratra B., 1988, ApJ, 325, L17

Penzias A. A., Wilson R. W., 1965, ApJ, 142, 419

Percival W. J., et al., 2007a, MNRAS, 381, 1053

Percival W. J., et al., 2007b, ApJ, 657, 51

Percival W. J., et al., 2009, arXiv: 0907.1660 (astro-ph CO)

Perlmutter S., et al., 1999, ApJ, 517, 565

Pettorino V., Baccigalupi C., 2008, Phys. Rev. D, 77, 103003

Piattella O. F., Bertacca D., Bruni M., Pietrobon D., 2010, Journal of Cosmology and Astro-Particle Physics, 1, 14

Pietrobon D., Amblard A., Balbi A., Cabella P., Cooray A., Marinucci D., 2008, Phys. Rev. D, 78, 103504

Pietrobon D., Balbi A., Bruni M., Quercellini C., 2008, Phys. Rev. D, 78, 083510

Pietrobon D., Balbi A., Marinucci D., 2006, Phys. Rev. D, 74, 043524

Pietrobon D., Cabella P., Balbi A., de Gasperis G., Vittorio N., 2009, MNRAS, 396, 1682

Pietrobon D., et al., 2009, arXiv: 0905.3702 (astro-ph CO)

Pietrobon D. e. o., 2009, In preparation

Planck M., 1901, Annalen der Physik, 309 (3), 553563

Pogosian L., Corasaniti P. S., Stephan-Otto C., Crittenden R., Nichol R., 2005, Phys. Rev. D, 72, 103519

Popa L. A., Mandolesi N., Caramete A., Burigana C., 2009, arXiv: 0907.5558 (astro-ph CO)

Pryke . C., et al., 2009, ApJ, 692, 1247

Quartin M., Calvão M. O., Jorás S. E., Reis R. R. R., Waga I., 2008, JCAP, 5, 7

Quercellini C., Bruni M., Balbi A., 2007, Class. Quant. Grav., 24, 5413

Quercellini C., Bruni M., Balbi A., Pietrobon D., 2008, Phys. Rev. D, 78, 063527

Raccanelli A., et al., 2008, MNRAS, 386, 2161

Reichardt C. L., et al., 2009, ApJ, 694, 1200

Riess A. G., et al., 1998, AJ, 116, 1009

Riess A. G., et al., 2004, ApJ, 607, 665

Riess A. G., et al., 2009, ApJ, 699, 539

Riess A. G. e. a., 2007, ApJ, 659, 98

Robertson H. P., 1935, ApJ, 82, 284

Rossmanith G., Raeth C., Banday A. J., Morfill G., 2009, arXiv: 0905.2854

Rudjord Ø., Hansen F. K., Lan X., Liguori M., Marinucci D., Matarrese S., 2009a, ApJ, 701, 369

Rudjord Ø., Hansen F. K., Lan X., Liguori M., Marinucci D., Matarrese S., 2009b, ArXiv e-prints

Sachs R. K., Wolfe A. M., 1967, ApJ, 147, 73

Sakai N., Inoue K. T., 2008, Phys. Rev. D, 78, 063510

Sandvik H., Tegmark M., Zaldarriaga M., Waga I., 2004, Phys. Rev. D, 69, 123524

Sandvik H. B., Tegmark M., Wang X.-M., Zaldarriaga M., 2004, Phys. Rev. D, 69, 063005

Sanz J. L., Argüeso F., Cayón L., Martínez-González E., Barreiro R. B., Toffolatti L., 1999, MNRAS, 309, 672

Sanz J. L., Herranz D., Lopez-Caniego M., Argueso F., 2006, arXiv: 0609351 (astro-ph CO)

Sato K., 1981, MNRAS, 195, 467

Schaefer B. M., Douspis M., Aghanim N., 2009, arXiv: 0903.4288 (astro-ph CO)

Scranton R., et al., 2003, arXiv: 0307335 (astro-ph)

Seljak U., Zaldarriaga M., 1996, ApJ, 469, 437

Serra P., Cooray A., 2008, Phys. Rev. D, 77, 107305

Serra P., Cooray A., Holz D. E., Melchiorri A., Pandolfi S., Sarkar D., 2009, arXiv: 0908.3186 (astro-ph CO)

Shafieloo A., Sahni V., Starobinsky A. A., 2009, arXiv: 0903.5141 (astro-ph CO)

Sievers J. L., et al. 2007, ApJ, 660, 976

Sievers J. L., et al., 2007, ApJ, 660, 976

Slosar A., Hirata C., Seljak U., Ho S., Padmanabhan N., 2008, JCAP, 8, 31

Smidt J., Amblard A., Serra P., Cooray A., 2009, arXiv: 0907.4051 (astro-ph CO)

Smith K. M., Huterer D., 2008, arXiv: 0805.2751 (astro-ph), 805

Smith K. M., Senatore L., Zaldarriaga M., 2009, arXiv: 0901.2572 (astro-ph CO)

Smith K. M., Zaldarriaga M., 2006, arXiv: 0612571 (astro-ph CO)

Smith R. E., Hernandez-Monteagudo C., Seljak U., 2009, arXiv: 0905.2408 (astro-ph CO)

Smoot G. F., et al., 1992, ApJ, 396, L1

Spergel D. N., et al., 2003, ApJ, 148, 175

Spergel D. N., et al., 2007, ApJ, 170, 377

Spergel D. N., Goldberg D. M., 1999, Phys. Rev. D, 59, 103001

Springel V., Frenk C. S., White S. D. M., 2006, Nature, 440

Springel V., Frenk C. S., White S. D. M., 2006, Nature, 440, 1137

Starck J.-L., Moudden Y., Abrial P., Nguyen M., 2006, A&A, 446, 1191

Steinhardt P. J., Turok N., 2002, Science, 296, 1436

Stewart J. M., 1990, Class. Quant. Grav., 7, 1169

Tauber J. A., 2001, in Harwit M., Hauser M. G., eds, The Extragalactic Infrared Background and its Cosmological Implications Vol. 204 of IAU Symposium, The Planck Mission. pp 493–+

Tegmark M., et al., 2004, Phys. Rev. D, 69, 103501

Tegmark M., et al., 2004, ApJ, 606, 702

Tonini C., 2009, arXiv: 09002.3433 (astro-ph GA)

Valiviita J., Majerotto E., Maartens R., 2008, JCAP, 0807, 020

Vielva P., Martínez-González E., Barreiro R. B., Sanz J. L., Cayón L., 2004, ApJ, 609, 22

Vielva P., Martínez-González E., Tucci M., 2006, MNRAS, 365, 891

Vielva P., Sanz J. L., 2008, arXiv: 0812.1756 (astro-ph CO)

Vielva P., Wiaux Y., Martínez-González E., Vandergheynst P., 2007, MNRAS, 381, 932

Visser M., 1997, Science, 276, 88

Wainwright J., Ellis G. F. R., 1997, Dynamical Systems in Cosmology. Cambridge University Press, Cambridge

Walker A. G., 1937, Proceedings of the London Mathematical Society, 2 42, 90127

Wands D., Copeland E. J., Liddle A. R., 1993, in Akerlof C. W., Srednicki M. A., eds, Texas/PASCOS '92: Relativistic Astrophysics and Particle Cosmology Vol. 688 of New York Academy Sciences Annals, Exponential Potentials, Scaling Solutions, and Inflation. pp 647–+

Wands D., Slosar A., 2009, arXiv: 0902.1084 (astro-ph CO)

Wang L., Caldwell R. R., Ostriker J. P., Steinhardt P. J., 2000, ApJ, 530, 17

Weinberg S., ed. 1972, Gravitation and Cosmology: Principles and Applications of the General Theory of Relativity. Wiley-VCH

Weinberg S., 1989a, Reviews of Modern Physics, 61, 1

Weinberg S., 1989b, Reviews of Modern Physics, 61, 1

Weinberg S., ed. 1993, The first three minutes : a modern view of the origin of the universe. Basic Books, New York

Weinberg S., ed. 2008, Cosmology. Oxford University Press, Oxford UK

Weller J., Lewis A. M., 2003, MNRAS, 346, 987

Wetterich C., 1988, Nucl. Phys. B, 302

Wetterich C., 1995, A&A, 301, 321

Wiaux Y., Jacques L., Vandergheynst P., 2005, ApJ, 632, 15

Wiaux Y., McEwen J. D., Vandergheynst P., Blanc O., 2008, MNRAS, 388, 770

Wiaux Y., McEwen J. D., Vielva P., 2007, Journal of Fourier Analysis and Applications, 13, 477

Wiaux Y., Vielva P., Barreiro R. B., Martínez-González E., Vandergheynst P., 2008, MNRAS, 385, 939

Wiaux Y., Vielva P., Martínez-González E., Vandergheynst P., 2006, Phys. Rev. Lett., 96, 151303

Wu E. Y. S., et al., 2009, Phys. Rev. Lett., 102, 161302

Yadav A. P. S., Komatsu E., Wandelt B. D., 2007, ApJ, 664, 680

Yadav A. P. S., Komatsu E., Wandelt B. D., Liguori M., Hansen F. K., Matarrese S., 2008, ApJ, 678, 578

Yadav A. P. S., Wandelt B. D., 2008, Phys. Rev. Lett., 100, 181301

York D. G., et al., 2000, AJ, 120, 1579

Yu B., Lu T., 2008, Phys. Rev. D, 78, 063008

Zhang Q.-J., Wu Y.-L., 2009, arXiv: 0905.1234 (astro-ph CO)

Appendix A

Beyond the Standard non-Gaussianity

"The third planet is incapable"
"of supporting life[...]"
"Our scientists have said"
"there's far too much oxygen in their atmosphere."

("The Martian Chronicles", R. Bradbury)

In the previous chapter we discussed the issue of non-Gaussianity, mainly from the point of view of the detection of a small deviation of the CMB fluctuation distribution from the Normal one. Such a small non-Gaussianity is indeed expected from theoretical arguments (Guth, 1981; Sato, 1981; Linde, 1982) and second order effects (Bartolo et al., 2004). Motivated by the upcoming cosmological experiments which will provide us with very precise datasets, and by the detection of a positive $f_{\rm NL}$ by Yadav & Wandelt (2008), a plethora of early Universe models has been proposed which may produce a measurable non-Gaussianity. See Lyth & Wands (2002); Linde & Mukhanov (2006); Alabidi & Lyth (2006); Mizuno et al. (2008); Khoury (2002); Steinhardt & Turok (2002); Lehners & Steinhardt (2008) for an incomplete list.

In this chapter we propose a new two fields inflationary model (Boubekeur & Lyth, 2006), which gets inspiration from the curvaton scenario (Lyth & Wands, 2002; Lyth et al., 2003), where the new degree of freedom, the auxiliary field, may significantly contribute to the cosmological perturbations, and then reflect into a high level of non-Gaussianity which does not violate the constraints of homogeneity and isotropy which are well satisfied by the dynamics of the standard inflaton field.

We first briefly describe the inflation formalism and then discuss the peculiarities of our model, focusing in particular on the 2- and 3-point correlation functions.

A.1 Motivation for the model

The local expectation values of canonical, weakly coupled scalar fields,

$$\phi_I(t,\mathbf{x}) = \bar{\phi}_I(t) + \delta\phi_I(t,\mathbf{x})\,, \tag{A.1}$$

whose effective mass is less than the Hubble scale during inflation, acquire an effectively classical distribution on large (super-Hubble) scales.

Quantum vacuum fluctuations on small scales ($k \gg aH$) lead to a distribution at Hubble-exit ($k_* = aH$) which is well described by independent Gaussian random fields

$$\langle \delta\phi_{I*}(\mathbf{k})\delta\phi_{J*}(\mathbf{k}')\rangle = (2\pi)^3\delta_{IJ}P_*(k)\delta^3(\mathbf{k}+\mathbf{k}')\,, \tag{A.2}$$

with a dimensionless power spectrum

$$\mathcal{P}_*(k) = \frac{4\pi k^3}{(2\pi)^3}P_*(k)\,. \tag{A.3}$$

During slow-roll inflation we have

$$\mathcal{P}_*(k) \simeq \left(\frac{H}{2\pi}\right)^2\,. \tag{A.4}$$

Non-linear evolution on large scales (after Hubble exit) leads to non-Gaussianity in the distribution of the scalar fields during inflation and as a result the primordial density perturbation during the radiation dominated era, which we will characterise by the dimensionless variable ζ. At linear order we have

$$\zeta = -\frac{H\delta\rho}{\dot{\rho}}\,, \tag{A.5}$$

where $\delta\rho$ is the density perturbation evaluated on spatially-flat hyper-surfaces. At non-linear order it is more convenient to define ζ in terms of the perturbation in the local integrated logarithmic expansion, $N = \int H dt$, from an initial spatially-flat hyper-surface during inflation to a uniform-density hyper-surface (Lyth & Rodriguez, 2005; Malik & Wands, 2009)

$$\zeta = \delta N\,. \tag{A.6}$$

Because the expansion on large (super-Hubble) scales is a function of the initial local value of the scalar fields at Hubble exit, the non-linear primordial density perturbation

can simply be expressed as a Taylor series expansion (Lyth & Rodriguez, 2005)

$$\zeta = \sum_I N_{,I}\delta\phi_{I*} + \frac{1}{2}\sum_{I,J} N_{,IJ}\delta\phi_{I*}\delta\phi_{J*} + \dots , \tag{A.7}$$

where $N_{,I} = \partial N/\partial\phi_{I*}$. It can be shown that the second (and higher) derivatives along the inflaton trajectory are suppressed by slow-roll parameters, $N''/N'^2 = \mathcal{O}(\epsilon)$. Non-Gaussianity generating during single-field, slow-roll inflation is thus suppressed.

It is informative to perform a rotation in field space along the inflaton trajectory during inflation (the adiabatic perturbations, $\delta\sigma$) and orthogonal directions (the entropy perturbations, δs_J). In the simplest case of two fields, Eq. A.7 reduces to (Langlois et al., 2008)

$$\zeta = N_{,\sigma}\delta\sigma_* + N_{,s}\delta s_* + \frac{1}{2}N_{,ss}\delta s_*^2 + \dots , \tag{A.8}$$

where we have dropped second-derivatives which involve adiabatic field perturbations as these are suppressed during slow-roll inflation. Any significant non-Gaussianity from slow-roll inflation is due to second order terms in ζ coming from entropy field perturbations during inflation, δs_*.

This δN-formalism can also be extended to describe non-linear isocurvature matter perturbations. To linear order we have

$$\mathcal{S} = \frac{\delta\rho_m}{\rho_m} - \frac{3}{4}\frac{\delta\rho_\gamma}{\rho_\gamma} . \tag{A.9}$$

Beyond linear order we define (Langlois et al., 2008)

$$\frac{1}{3}\mathcal{S} = \sum_I \Delta N_{,I}\delta\phi_{I*} + \frac{1}{2}\sum_{I,J}\Delta N_{,IJ}\delta\phi_{I*}\delta\phi_{J*} + \dots , \tag{A.10}$$

where ΔN describes the difference in the integrated expansion between uniform-matter-density hyper-surfaces and uniform-radiation-density hyper-surfaces. For adiabatic primordial perturbations the uniform-matter and uniform-radiation hyper-surfaces coincide and isocurvature perturbations vanish, $\mathcal{S} = 0$. Thus adiabatic field perturbations during inflation do not contribute to isocurvature matter perturbations, $\Delta N_\sigma = 0$, and in the simplest case of two fields we have (Langlois et al., 2008)

$$\frac{1}{3}\mathcal{S} = \Delta N_{,s}\delta s_* + \frac{1}{2}\Delta N_{,ss}\delta {s_*}^2 + \dots . \tag{A.11}$$

Observational constraints to date have focussed upon the case of adiabatic perturbations which are a local function of a single Gaussian random field, ζ_G, such that

$$\zeta = \zeta_G + \frac{3}{5} f_{\rm NL} \left(\zeta_G^2 - \langle \zeta_G^2 \rangle \right) . \tag{A.12}$$

This comes from a single fields model, where we have dropped the quadratic term in the number-of-efolds expansion.

$$\zeta_G = N_{,s} \delta s_* , \quad f_{\rm NL} = \frac{5}{6} \frac{N_{,ss}}{N_{,s}^2} . \tag{A.13}$$

This is a good description of the type of non-Gaussianity expected in models such as the original curvaton model where a single curvaton field decays some time after inflation to produce an adiabatic density perturbation. The curvaton model may also leave residual isocurvature perturbations (dependent upon the process of curvaton decay and the origin of the matter or CDM abundance) and these are correlated with the adiabatic density perturbation (Lyth et al., 2003).

However it is clear that at second order the non-linear expression (Eq. A.7) for ζ in the presence of more than one scalar field includes non-linear contributions from field perturbations which are independent of ζ_G. Similarly the isocurvature perturbation (Eq. A.10) contains non-linear terms some of which are uncorrelated with the first order curvature or isocurvature perturbation. In particular, if the first-order part of the adiabatic density perturbation is dominated by the adiabatic field perturbations during inflation, $\zeta_G = N_{,\sigma} \delta\sigma_*$, then this is uncorrelated with the entropy field perturbations during inflation which give rise to non-Gaussianity in the adiabatic density perturbation or isocurvature matter perturbations. Such a situation may occur in a mixed inflaton-curvaton model (Langlois et al., 2008).

In what follows we will consider the non-Gaussianity due to second-order perturbations in either the adiabatic density perturbation, ζ, or in the isocurvature perturbation, $\mathcal{S}$, which is uncorrelated with the first-order density perturbation, ζ_G:

$$\zeta = \zeta_G + \frac{3}{5} F_{\rm NL} \left(\chi_G^2 - \langle \chi_G^2 \rangle \right) , \tag{A.14}$$

$$\frac{1}{3} \mathcal{S} = F_{\rm NL}^{\rm iso} \left(\chi_G^2 - \langle \chi_G^2 \rangle \right) , \tag{A.15}$$

where we choose the normalisation of χ_G such that

$$P_{\chi_G} = P_{\zeta_G} . \tag{A.16}$$

In the extended δN-formalism we can identify

$$F_{\rm NL} = \frac{5}{6}\frac{N_{,ss}}{N_{,\sigma}^{\,2}}\,, \tag{A.17}$$

$$F_{\rm NL}^{\rm iso} = \frac{5}{6}\frac{\Delta N_{,ss}}{N_{,\sigma}^{\,2}}\,. \tag{A.18}$$

A simple example is provided by a scalar field, χ, whose mass is much less than the Hubble scale during inflation, $m_\chi \ll H_*$, which begins to oscillate some time after inflation, once the Hubble rate has dropped below the mass $H < m_\chi$. If the spatially averaged value of the field after inflation is small, $\bar{\chi} \ll H_*$, then the oscillating field has a highly non-Gaussian local energy density

$$\rho_\chi \simeq m_\chi^2 \delta\chi^2\,. \tag{A.19}$$

If it decays before primordial nucleosynthesis, and its decay products thermalise into full thermal equilibrium, then we have an adiabatic density perturbation at second-order of the form given in Eq. A.14. If the decay leaves a residual isocurvature perturbation then it will be of the form given in Eq. A.15.

This model can be seen as a particular case of a multi-field hybrid inflation described in Alabidi & Lyth (2006) with the choice $g = 0$ in the expression of the mass of the inflation driving field ψ (their Eq. 2, $m_\psi^2 = f\phi_e^2 + g\phi_e\chi + h\chi^2$).

A.2 Power spectrum

Within the setup discussed above, Eq. A.14 and Eq. A.15 become

$$\begin{aligned} \zeta(x) &= \zeta_G(x) + \frac{3}{5} f_{\rm NL}\left[\zeta_G^2(x) - \langle\zeta_G^2(x)\rangle\right] + \frac{3}{5} F_{NL}\left[\chi(x)^2 - \langle\chi^2(x)\rangle\right] \\ \frac{1}{3}S(x) &= F_{NL}^{iso}\left[\chi^2(x) - \langle\chi^2(x)\rangle\right] \end{aligned} \tag{A.20}$$

where ζ_G is the curvature, which up to a sign is equal to the gravitational potential Φ. In the following analysis we assume the variables to be defined within the comoving gauge.

We quote also the expression in k-space, where the quadratic term turns into a convolution integral:

$$\begin{aligned}\zeta(\mathbf{k}) &= \zeta_G(\mathbf{k}) + \frac{3}{5} f_{\rm NL}\Big[\int \frac{\mathrm{d}^3p}{(2\pi)^3}\zeta_G(\mathbf{p})\zeta_G(\mathbf{k}-\mathbf{p}) - (2\pi)^3\delta^{(3)}(\mathbf{k})\langle\zeta_G^2(x)\rangle\Big] \\ &+ \frac{3}{5} F_{NL}\Big[\int \frac{\mathrm{d}^3p}{(2\pi)^3}\chi(\mathbf{p})\chi(\mathbf{k}-\mathbf{p}) - (2\pi)^3\delta^{(3)}(\mathbf{k})\langle\chi^2(x)\rangle\Big] \qquad \text{(A.21)} \\ \frac{1}{3}S(\mathbf{k}) &= F_{NL}^{iso}\Big[\int \frac{\mathrm{d}^3p}{(2\pi)^3}\chi(\mathbf{p})\chi(\mathbf{k}-\mathbf{p}) - (2\pi)^3\delta^{(3)}(\mathbf{k})\langle\chi^2(x)\rangle\Big] \qquad \text{(A.22)}\end{aligned}$$

The additional χ field affects in the same way both the source of the adiabatic perturbations and that of the isocurvature ones; in terms of the density fluctuations the difference arises from the two proportionality factors, F_{NL} and F_{NL}^{iso} respectively, and the different evolutions described by the transfer functions.

The statistical properties of the fields are usually studied with the 2-point correlation function (2pcf) in harmonic space, the power spectrum. Based on the homogeneity assumption we write the auto-correlation function [1] as

$$\langle\chi^2\rangle \equiv \langle\chi(x_1)\chi(x_2)\rangle_E = \langle\chi(x)\chi(x+r)\rangle_E, \qquad \text{(A.23)}$$

which translated into Fourier space becomes

$$\begin{aligned}\langle\chi(x)\chi(x+r)\rangle_E &= \int \frac{\mathrm{d}^3k}{(2\pi)^3}e^{i\mathbf{k}\cdot x}\int \frac{\mathrm{d}^3k'}{(2\pi)^3}e^{i\mathbf{k}'\cdot(x+r)}\langle\chi(\mathbf{k})\chi(\mathbf{k}')\rangle_E \\ &\equiv \int \frac{\mathrm{d}^3k}{(2\pi)^3}e^{i\mathbf{k}r}P_\chi(\mathbf{k}) \qquad \text{(A.24)}\end{aligned}$$

where

$$\langle\chi(\mathbf{k})\chi(\mathbf{k}')\rangle_E \equiv (2\pi)^3\delta(\mathbf{k}+\mathbf{k}')P_\chi(\mathbf{k}) \qquad \text{(A.25)}$$

We define the power spectra for the two inflationary fields, according to the standard definition, as

$$\begin{aligned}P_{\zeta_G}(k) &= A_{\zeta_G}\Big|\frac{\mathbf{k}}{\mathbf{k}_0}\Big|^{n_{\zeta_G}-4} \qquad \text{(A.26)} \\ P_\chi(k) &= A_\chi\Big|\frac{\mathbf{k}}{\mathbf{k}_0}\Big|^{n_\chi-4}. \qquad \text{(A.27)}\end{aligned}$$

[1] Notice that the above definition reflects the ergodic limit that ensures

$$\frac{1}{V}\int \mathrm{d}^3x\chi(x)\chi(x+r) \to \langle\chi(x)\chi(x+r)\rangle_E$$

Since in principle the two fields are independent, we allow the spectral indices to be different and normalise the two power spectra to be equal at the scale k_0 interesting for the CMB. Adopting this convention we obtain a nearly constant power per logarithmic interval ($\mathcal{P}(k) = 4\pi k^3/(2\pi)^3 P(k)$) when $n_{\zeta_G/\chi} = 1$. We stress that since the two fields are independent the spectral indices are not bound to be equal; the latest constraints from WMAP 5-years Komatsu et al. (2009) apply to n_{ζ_G}, while n_χ could span the entire range. This actually is a specific and interesting feature of our model.

The 2pcf for the quantity ζ leads to a term proportional to the power spectrum of ζ_G and a second one which is a function of the power spectrum of χ^2. Any cross term vanishes since both the two primordial fields are chosen so that their ensemble average is zero. We are interested in evaluating the 2pcf for the $\delta\chi^2$ that represents the source for the matter density perturbations. Computing the 4pcf for the χ field in Fourier space and applying Wick's theorem we obtain the following result:

$$\begin{aligned}\left\langle \chi^2(x)\chi^2(x+r)\right\rangle &= 2\int \frac{\mathrm{d}^3k}{(2\pi)^3}\frac{\mathrm{d}^3k'}{(2\pi)^3}P(\mathbf{k})P(\mathbf{k}')e^{i(\mathbf{k}+\mathbf{k}')\cdot r} = \\ &= 2\int \frac{\mathrm{d}^3k}{(2\pi)^3}e^{i\mathbf{k}\cdot r}\int \frac{\mathrm{d}^3k'}{(2\pi)^3}P_\chi(\mathbf{k}')P_\chi(\mathbf{k}-\mathbf{k}') \qquad \text{(A.28)}\end{aligned}$$

According to the definition of the power spectrum, Eq. A.25, we identify the explicit form of the power spectrum for χ

$$P_{\chi^2}(\mathbf{k}) \equiv 2\int \frac{\mathrm{d}^3p}{(2\pi)^3}P_\chi(\mathbf{p})P_\chi(\mathbf{k}-\mathbf{p}) \qquad \text{(A.29)}$$

which results a convolution integral of the power spectrum of the primordial inflationary light field.

The curvature and the isocurvature sources seed directly the density field: indeed we can express the density in k-space as a superposition of adiabatic and isocurvature modes, each of those with the proper transfer function. Initial conditions for ζ and S are set in the early radiation epoch, while the matter density is generally defined in the matter domination era like

$$\delta_c(\mathbf{k},t) = \frac{2}{5}\left(\frac{k}{a\mathcal{H}}\right)^2\left(T^{curv}(\mathbf{k},t)\zeta(\mathbf{k}) + \frac{1}{3}T^{iso}(\mathbf{k},t)S(\mathbf{k})\right) \qquad \text{(A.30)}$$

where the subscript "c" reminds the comoving perturbation. Substituting Eqs.A.20 into Eq. A.30 we obtain the expression of the density as a function of the primordial sources:

$$\delta_c(\mathbf{k},t) = \frac{2}{5}\left(\frac{k}{a\mathcal{H}}\right)^2\left[T^{curv}(\mathbf{k},t)\left(\zeta_G(\mathbf{k}) + \frac{3}{5}f_{\mathrm{NL}}\zeta_G^2(\mathbf{k})\right) + \frac{3}{5}F_{NL}T^{mix}(\mathbf{k},t)\chi^2(\mathbf{k})\right] \qquad \text{(A.31)}$$

where we defined:

$$F_{NL}T^{mix}(\mathbf{k},t) \equiv [F_{NL}T^{curv}(\mathbf{k},t) + \frac{1}{3}\frac{5}{3}F_{NL}^{iso}T^{iso}(\mathbf{k},t)] \tag{A.32}$$

We explicitly factorise out the dependence on the scale factor and the Hubble parameter to match the usual normalisation of the transfer function on large scales, $T_{k\to 0}^{curv/iso} = 1$.

We simply mention that when dealing with matter density perturbations one complication arises since we do not measure the dark matter density directly, but only through a tracer which shows a bias in the growth of the perturbations. The bias may be scale dependent, making the full treatment much more challenging. In what follows we will ignore this contribution.

Once we compute the 2pcf for the primordial sources it is straightforward to write the power spectrum for the density field via Eq. A.31

$$P_{\delta_c}(\mathbf{k},t) = \frac{4}{25}\Big(\frac{k}{a\mathcal{H}}\Big)^4\Big[(T^{curv}(\mathbf{k},t))^2(P_{\zeta_G}(\mathbf{k})+\frac{9}{25}f_{\rm NL}P_{\zeta_G^2}(\mathbf{k}))+\frac{9}{25}F_{NL}^2(T^{mix}(\mathbf{k},t))^2P_{\chi^2}(\mathbf{k})\Big] \tag{A.33}$$

where $P_{\zeta_G^2}$ is defined analogously to Eq. A.29. Notice that the cross term between ζ_G and χ^2 vanishes because ζ_G is a Gaussian field with mean value vanishing.

In the next section we address the 3-point correlation function (3pcf) formalism.

A.3 Bispectrum

For a Normal distribution the odd moments are vanishing while the even ones can be given as function of the first and second moment, i.e. the mean value and the standard deviation. The first term one has to look at in order to measure deviation from the Gaussian distribution is the third moment.

The 3pcf for ζ picks up contributions both from ζ_G and χ, but none from the cross term. The reason can be found again in the zero mean value of the fields. The first non-linear bit is proportional to $f_{\rm NL}$ and has been first proposed by Komatsu & Spergel (2001) and it has become the standard approach in the literature.

For $F_{NL} = 0$ we obtain the standard non-Gaussian term, given by:

$$\begin{aligned}\big\langle\zeta(\mathbf{k}_1)\zeta(\mathbf{k}_2)\zeta(\mathbf{k}_3)\big\rangle &= 2(2\pi)^3\delta^{(3)}(\mathbf{k}_1+\mathbf{k}_2+\mathbf{k}_3)f_{\rm NL}[P_{\zeta_G}(k_1)P_{\zeta_G}(k_2)\\ &+ P_{\zeta_G}(k_1)P_{\zeta_G}(k_3)+P_{\zeta_G}(k_3)P_{\zeta_G}(k_2)]\end{aligned} \tag{A.34}$$

In order to help the comparison in the following, we report the non-linear correction to the shape of 3pcf for the density field in the standard scenario:

$$\begin{aligned}\langle\delta_c(\mathbf{k}_1)\delta_c(\mathbf{k}_2)\delta_c(\mathbf{k}_3)\rangle &= 2(2\pi)^3\delta^{(3)}(\mathbf{k}_1+\mathbf{k}_2+\mathbf{k}_3)\frac{8}{125}\left(\frac{\mathbf{k}_1}{a\mathcal{H}}\right)^2\left(\frac{\mathbf{k}_2}{a\mathcal{H}}\right)^2\left(\frac{\mathbf{k}_3}{a\mathcal{H}}\right)^2 f_{\rm NL}\\ &\times\ T^{curv}(\mathbf{k}_1)T^{curv}(\mathbf{k}_2)T^{curv}(\mathbf{k}_3)\big\langle\zeta_G(\mathbf{k}_1)\zeta_G(\mathbf{k}_2)\zeta_G(\mathbf{k}_3)\big\rangle \qquad \text{(A.35)}\end{aligned}$$

For $F_{NL}\neq 0$ and $f_{\rm NL}=0$ we need the 3-point correlation function for the χ^2 field. Once again we start with the 6-point correlation function for the primordial field χ and apply the Wick's theorem. Here we summarise the results.

$$\begin{aligned}\big\langle\zeta(\mathbf{k}_1)\zeta(\mathbf{k}_2)\zeta(\mathbf{k}_3)\big\rangle &= \frac{8}{125}F_{NL}^3\big\langle\chi^2(\mathbf{k}_1)\chi^2(\mathbf{k}_2)\chi^2(\mathbf{k}_3)\big\rangle =\\ &= (2\pi)^3\delta^{(3)}(\mathbf{k}_1+\mathbf{k}_2+\mathbf{k}_3)\frac{8}{3}\frac{8}{125}\Big(F_{NL}\Big)^3\int\frac{\mathrm{d}^3k}{(2\pi)^3}P_\chi(\mathbf{k})\\ &\times\ \big[P_\chi(\mathbf{k}_1+\mathbf{k})P_\chi(\mathbf{k}_2-\mathbf{k})+P_\chi(\mathbf{k}_2+\mathbf{k})P_\chi(\mathbf{k}_3-\mathbf{k})+\\ &+\ P_\chi(\mathbf{k}_3+\mathbf{k})P_\chi(\mathbf{k}_1-\mathbf{k})\big] \qquad \text{(A.36)}\end{aligned}$$

where we have explicitly symmetrised with respect to $\mathbf{k}_i$.

The main difference with respect to the standard non-Gaussian term arises from the convolution integral present in Eq. A.36 which makes the computation rather complicated. Moreover in the standard case the parameter $f_{\rm NL}$ appears linearly in the expression, while the 3pcf for χ^2 is proportional to F_{NL}^3.

It is possible to derive the 3pcf for the density field that results

$$\begin{aligned}\langle\delta_c(\mathbf{k}_1)\delta_c(\mathbf{k}_2)\delta_c(\mathbf{k}_3)\rangle &= \frac{8}{125}\left(\frac{k_1^2}{a^2\mathcal{H}^2}\right)\left(\frac{k_3^2}{a^2\mathcal{H}^2}\right)\left(\frac{k_3^2}{a^2\mathcal{H}^2}\right)\left(\frac{3}{5}\right)^3F_{NL}^3\\ &\times\ T^{mix}(\mathbf{k}_1)T^{mix}(\mathbf{k}_2)T^{mix}(\mathbf{k}_3)\big\langle\chi^2(\mathbf{k}_1)\chi^2(\mathbf{k}_2)\chi^2(\mathbf{k}_3)\big\rangle \qquad \text{(A.37)}\end{aligned}$$

Numerical Evaluation

Assuming for the power spectrum the shape $P_\chi(k)=A\big|k/k_0\big|^{n-4}$, we can approximate the integral over $\mathbf{k}$ in Eq. A.36, under the assumption that the most contribution comes from the poles, as

$$\begin{aligned}&\int\frac{\mathrm{d}^3k}{(2\pi)^3}P_\chi(\mathbf{k})P_\chi(\mathbf{k}_2-\mathbf{k})P_\chi(\mathbf{k}_3+\mathbf{k})\simeq\\ &\quad=(P_\chi(k_1)P_\chi(k_2)+P_\chi(k_1)P_\chi(k_3)+P_\chi(k_2)P_\chi(k_3))\int\frac{\mathrm{d}^3k}{(2\pi)^3}P_\chi(\mathbf{k})=\\ &\quad=\langle\chi^2(\mathbf{x})\rangle(P_\chi(k_1)P_\chi(k_2)+P_\chi(k_1)P_\chi(k_3)+P_\chi(k_2)P_\chi(k_3)) \qquad \text{(A.38)}\end{aligned}$$

where we used the result $\langle\chi^2(\mathbf{x})\rangle = \int \frac{\mathrm{d}^3k}{(2\pi)^3} P_\chi(k)$ (see Eq. **??**). It is worth stressing that this derivation is valid under the assumption of a *red* power spectrum, i.e. $n = 1-\varepsilon$ with $\varepsilon > 0$, that requires an infra-red (IR) cut-off in order to keep finite the two point correlation function, namely the mean value of the squared field. In this case the majority of the contribution to the integral comes from two poles, as long as the scales which we are interested in are greater than the IR cut-off. Notice that the divergence is present only at the level of the power spectrum, since the two-point and three-point correlation functions in χ^2 are finite, since they come from four-point and six-point correlation functions for the field χ. More interesting with this approximation we obtain an expression very close to Eq. A.34, allowing us to implement the standard estimator developed by Komatsu et al. (2005); Creminelli et al. (2006). This is the basic assumption on which most of the recent works Enqvist & Takahashi (2008); Ichikawa et al. (2008); Kawasaki et al. (2008, 2009) on non-Gaussianity are built. It is perfectly reasonable if the spectral index n_χ is bound to be close to n_{ζ_G}, which indeed has been tightly constrained from the WMAP 5-years data analysis Komatsu et al. (2009) to be $n_s = 0.960 \pm 0.013$.

Even in the case of a *blue* power spectrum, i.e. $n = 1+\varepsilon$ the divergence is present at the level of the power spectrum only, this time an ultra-violet (UV) divergence. We need a high-k cut-off in order to keep finite the two-point correlation function in χ.

It is possible to obtain a simple expression for the two-point correlation function in χ^2, given by

$$\begin{aligned}\langle\chi^2(\mathbf{k})\chi^2(\mathbf{k}_1)\rangle &\propto 2\int \frac{\mathrm{d}^3p}{(2\pi)^3} P_\chi(\mathbf{p}) P_\chi(\mathbf{k}_1-\mathbf{p}), \qquad n = 1+\varepsilon \\ &= 2\, k_1^{-2n+3} \int \frac{\mathrm{d}^3z}{(2\pi)^3} P_\chi(\mathbf{z}) P_\chi(\hat{\mathbf{k}}_1 - \mathbf{z}). \end{aligned} \tag{A.39}$$

where we used the rescaling $\mathbf{k} = \mathbf{z}k_1$. The integral in the equation above is simply a number that can be computed numerically, while the scale dependence is factorised.

Not as simple is the case of the 3-point correlation function, since we still factorise the dependence on one single scale, namely $\mathbf{k}_1$, but we are left with an integral function of the two angles α and β, as can be seen in the following expression:

$$\begin{aligned}\langle\chi^2(\mathbf{k}_1)\chi^2(\mathbf{k}_2)\chi^2(\mathbf{k}_3)\rangle &\propto \int \frac{\mathrm{d}^3k}{(2\pi)^3} P(\mathbf{k}) P(\mathbf{k}_2-\mathbf{k}) P(\mathbf{k}_3+\mathbf{k}) = \\ &= k_1^{3(n-4)+3} \times \int \frac{\mathrm{d}^3k}{(2\pi)^3} P(\mathbf{z}) P\Big(\frac{\sin\alpha}{\sin(\alpha+\beta)}\hat{\mathbf{k}}_2 - \mathbf{z}\Big) \\ &\quad P\Big(\frac{\sin\beta}{\sin(\alpha+\beta)}\hat{\mathbf{k}}_3 + \mathbf{z}\Big) \end{aligned} \tag{A.40}$$

where $\mathbf{k}_1$ is one of the three scales which build the triangle and α and β are the two angles that the other two scales form with $\mathbf{k}_1$. The formula above is actually rather complicated since the expressions of α and β are non-linear functions of $\mathbf{k}_i$, with the constraint $\alpha+\beta \neq 0, \pi$, that actually is anything else than the closed triangle requirement. Nevertheless, the limit $\alpha + \beta \lesssim \pi$ is particularly interesting, because it represents the squeezed configurations. The configuration in which the three ks are aligned is described by $\alpha = \beta = 0$, for which the expression above is well defined. It is possible to distinguish the *equilateral* configuration and the *squeezed* one. The former has $k_1 = k_2 = k_3$ and $\alpha = \beta = \gamma = \pi/3$; the latter is characterised by $k_1 << k_2 \sim k_3$, which is translated into $\alpha \sim \beta \lesssim \pi/2$. The case $\alpha \sim \gamma << \beta \lesssim \pi$ represents co-linear configurations.

α and r parameterisation In order to compute the integral (A.40) we choose a specific reference frame: the triangle lies in the $\hat{\mathbf{z}}_x - \hat{\mathbf{z}}_y$ plane, being $\mathbf{k}_1 = \hat{\mathbf{z}}_x$ along the horizontal axis. To completely describe the configuration it is necessary to specify the ratio between the two sides, namely $r \equiv k_3/k_1$. Using this parameterisation it is possible to span with continuity the whole parameter space.

In order to find which of the described configurations contributes mainly to the integral, we perform a numerical computation of Eq. A.38 using the above parameterisation. Results are shown for both our model and the standard non-Gaussianity in Fig. A.1. The two plots look pretty similar. In order to understand what is going on, we re-write

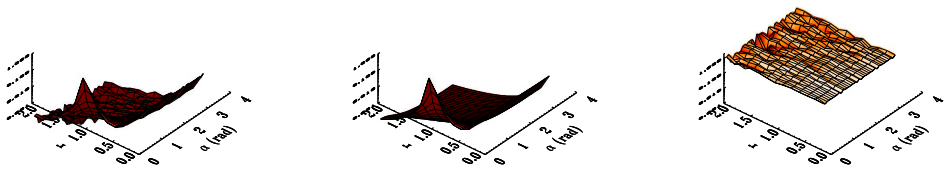

Figure A.1: Left panel: power of the *convolution integral*; middle panel: power of the 3pcf in *standard non-Gaussianity*. The two quantities are expressed as functions of α and r and computed for $n_s = 1.1$ (blue tilt). The third panel shows the ratio between the two: indeed it is very close to 1, with small deviations due to numerical accuracy.

Eq. A.34 in terms of the variables α and r:

$$\begin{aligned}\langle\zeta_G(\mathbf{k}_1)\zeta_G(\mathbf{k}_2)\zeta_G(\mathbf{k}_1)\rangle \;&\propto\; P_{\zeta_G}(k_1)P_{\zeta_G}(k_2) + P_{\zeta_G}(k_3)P_{\zeta_G}(k_2) + P_{\zeta_G}(k_1)P_{\zeta_G}(k_3)\\ &=\; P_{\zeta_G}^{2n-8}(k_1)[(1+r^2-2r\cos\alpha)^{(n-4)/2} + r^{n-4}\\ &+\; (r\sqrt{1+r^2-2r\cos\alpha})^{n-4}] \qquad \text{(A.41)}\end{aligned}$$

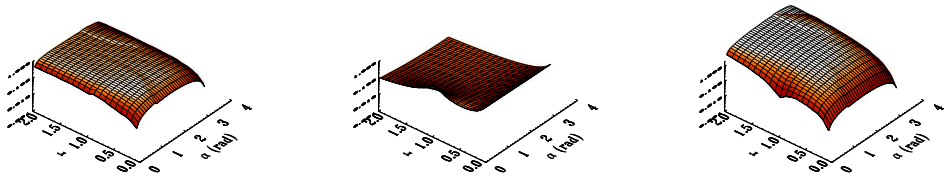

Figure A.2: Left panel: power of the *convolution integral*; middle panel: power of the 3pcf in *standard non-Gaussianity*. The two quantities are expressed as functions of α and r and computed for $n_s = 3.0$ (strong blue tilt). The third panel shows the ratio between the two which turns out to be quite far from 1 as expected.

The first important thing to notice is that the dependence on k_1 is different from ours, and they agree only in the peculiar case $n = 1$. Looking at the expression A.41 the behaviour for $r \simeq 1$ and $\alpha = 0$ becomes clear: two poles tend to coincide and then, even if we are studying a blue power spectrum that does not require an IR cut-off, the square of such a blue spectrum is red and needs an IR cut off. The higher power for r, independently of the angle α can be explained in the same way: two poles tend to coincide again. This explain also why the power is a little bit higher for $\alpha \gtrsim 0$ then for $\alpha \lesssim \pi$: the contribution from the third pole is slightly higher. Basically the effect we see is the contribution of the poles. Probably on smaller power intensity it is possible to distinguish specific features characteristic of the chosen spectral index.

A.4 $f_{\rm NL}$ estimator

The optimal estimator for a quantity $\mathcal{Q}^{th}$ is generically given by the product of $\mathcal{Q}$ by the observed quantity, $\mathcal{Q}^{obs}$ normalised to the square of the theoretical value. In the case of the non-linear parameter $f_{\rm NL}$ we can then write

$$f_{\rm NL} = \frac{\sum_{\mathbf{k}} \delta_c^{obs}(\mathbf{k}_1)\delta_c^{obs}(\mathbf{k}_2)\delta_c^{obs}(\mathbf{k}_3)\mathbf{Cov}^{-1}\langle\delta_c^{th}(\mathbf{k}'_1)\delta_c^{th}(\mathbf{k}''_2)\delta_c^{th}(\mathbf{k}'''_3)\rangle}{\sum_{\mathbf{k}} \delta_c^{th}(\mathbf{k}_1)\delta_c^{th}(\mathbf{k}_2)\delta_c^{th}(\mathbf{k}_3)\mathbf{Cov}^{-1}\langle\delta_c^{th}(\mathbf{k}'_1)\delta_c^{th}(\mathbf{k}''_2)\delta_c^{th}(\mathbf{k}'''_3)\rangle} \tag{A.42}$$

where o is a suitable observable, $\mathbf{Cov}$ is the covariance matrix given by the 6-point correlation function times the transfer function for the considered observable. The standard choices for o are the CMB fluctuations (Komatsu et al., 2005) and the baryon density ones (Slosar et al., 2008).

A.4.1 Primordial Bispectrum

We are interested in computing the bispectrum for non standard inflationary models, like the curvaton model Lyth & Wands (2002), in which the contribution to density pertur-

bations coming from the non linear potential con be large. In this context large means $f_{\rm NL} \sim 100$, that seems to be very exciting especially because it would be in agreement with the recent claim $f_{\rm NL} \sim 90$ stated by Yadav & Wandelt (2008).

The primordial scalar fluctuations can be constrained by the analysis of the Cosmic Microwave Background (CMB) radiation. This analysis is usually carried on expanding the relative temperature fluctuations on the Spherical Harmonics basis

$$\frac{\Delta T(\hat{\gamma})}{T_0} = \sum_{\ell m} a_{\ell m} Y_{\ell m}(\hat{\gamma}) a_{\ell m} = \int \mathrm{d}\Omega \frac{\Delta T(\hat{\gamma})}{T} Y^*_{\ell m}(\hat{\gamma}),$$

The coefficients of the expansion, $a_{\ell m}$ can be express in term of the primordial potential Φ of the inflationary fields that determines the primordial curvature perturbations, both adiabatic and isocurvature ones.

$$a_{\ell m} = 4\pi(-i)^\ell \int \frac{\mathrm{d}^3\mathbf{k}}{(2\pi)^3} \left[\zeta^{ad}(\mathbf{k}) g^{ad}_{T\ell} + S^{iso}(\mathbf{k}) g^{iso}_{T\ell} \right] Y^*_{\ell m}(\hat{\mathbf{k}}) \tag{A.43}$$

where $g^{ad/iso}_{T\ell}$ are the radiation transfer functions for adiabatic and isocurvature modes respectively.

The non-linear part of the potentials transfers into $a_{\ell m}$, introducing a non-Gaussian contribution into the temperature fluctuations. The CMB angular bispectrum is defined as

$$B^{m_1 m_2 m_3}_{\ell_1 \ell_2 \ell_3} \equiv \langle a_{\ell_1 m_1} a_{\ell_2 m_2} a_{\ell_3 m_3} \rangle, \tag{A.44}$$

It is useful to define the angular averaged bispectrum, given by

$$B_{\ell_1 \ell_2 \ell_3} = \sum_{\text{all } m} \begin{pmatrix} \ell_1 & \ell_2 & \ell_3 \\ m_1 & m_2 & m_3 \end{pmatrix} B^{m_1 m_2 m_3}_{\ell_1 \ell_2 \ell_3}, \tag{A.45}$$

where the matrix is the Wigner-$3j$ symbol. Since the bispectrum satisfies the triangle conditions and parity invariance: $m_1 + m_2 + m_3 = 0$, $\ell_1 + \ell_2 + \ell_3 = \text{even}$, and $|\ell_i - \ell_j| \leq \ell_k \leq \ell_i + \ell_j$ for all permutations of indexes, it basically consists of the Gaunt integral, $\mathcal{G}^{m_1 m_2 m_3}_{\ell_1 \ell_2 \ell_3}$ times an arbitrary real symmetric function of ℓ_1, ℓ_2 and ℓ_3, $b_{\ell_1 \ell_2 \ell_3}$:

$$B^{m_1 m_2 m_3}_{\ell_1 \ell_2 \ell_3} = \mathcal{G}^{m_1 m_2 m_3}_{\ell_1 \ell_2 \ell_3} b_{\ell_1 \ell_2 \ell_3}, \tag{A.46}$$

$$\mathcal{G}^{m_1 m_2 m_3}_{\ell_1 \ell_2 \ell_3} \equiv \int d^2\hat{\gamma} Y_{\ell_1 m_1}(\hat{\gamma}) Y_{\ell_2 m_2}(\hat{\gamma}) Y_{\ell_3 m_3}(\hat{\gamma}) \tag{A.47}$$

$\mathcal{G}^{m_1 m_2 m_3}_{\ell_1 \ell_2 \ell_3}$ is real, and satisfies all the rotational invariance conditions mentioned above. This allows us to focus on the so-called *reduced* bispectrum, $b_{\ell_1 \ell_2 \ell_3}$ Komatsu & Spergel

(2001). The angle-averaged bispectrum can be expressed in term of the reduced one as

$$B_{l_1 l_2 l_3} = \sqrt{\frac{(2l_1+1)(2l_2+1)(2l_3+1)}{4\pi}} \begin{pmatrix} l_1 & l_2 & l_3 \\ 0 & 0 & 0 \end{pmatrix} b_{l_1 l_2 l_3}, \tag{A.48}$$

where we used the relation **??**.

The bispectrum looks like

$$\begin{aligned} B^{m_1 m_2 m_3}_{\ell_1 \ell_2 \ell_3} &= \left\langle a^{\rm NL}_{\ell_1 m_1} a^{\rm NL}_{\ell_2 m_2} a^{\rm NL}_{\ell_3 m_3} \right\rangle \\ &= (4\pi)^3 (-i)^{\ell_1+\ell_2+\ell_3} \int \frac{{\rm d}^3\mathbf{k}_1}{(2\pi)^3} \int \frac{{\rm d}^3\mathbf{k}_2}{(2\pi)^3} \int \frac{{\rm d}^3\mathbf{k}_3}{(2\pi)^3} \\ & \quad g_{T\ell_1}(k_1) g_{T\ell_2}(k_2) g_{T\ell_3}(k_3) Y^*_{\ell_1 m_1}(\hat{\mathbf{k}}_1) Y^*_{\ell_2 m_2}(\hat{\mathbf{k}}_2) Y^*_{\ell_3 m_3}(\hat{\mathbf{k}}_3) \\ & \quad \left\langle \zeta(\mathbf{k}_1)\zeta(\mathbf{k}_2)\zeta(\mathbf{k}_3) \right\rangle \end{aligned} \tag{A.49}$$

where in the standard case the 3pcf for the curvature is given by Eq. A.34, while in our model it is given by Eq.A.36. By means of the Rayleigh's formula we can expand the $\delta^{(3)}$ function which is hidden in the 3pcf for the curvature perturbations in the expression above. The crucial step in performing the computation is expanding Dirac's delta in the Fourier basis, expressing the exponential in terms of the Bessel's functions and spherical harmonics. We can perform the integrals over the angular part which lead to three Gaunt's integrals. One of these describes the invariance property of the bispectrum under rotations and the requirements of parity symmetry and triangle relations imply (Eq.A.46), while the others take into account the coupling between k-modes, which in the standard case is vanishing. In this particular case, it is possible to simply further the expression of the bispectrum exploiting the orthogonality of the spherical harmonics. We obtained the usual form of the bispectrum:

$$\begin{aligned} B^{m_1 m_2 m_3}_{\ell_1 \ell_2 \ell_3} &= 2 f_{\rm NL} \mathcal{G}^{m_1 m_2 m_3}_{\ell_1 \ell_2 \ell_3} \int x^2 \, {\rm d}x \\ & \quad \left[\alpha_{\ell_1}(x) \beta_{\ell_2}(x) \beta_{\ell_3}(x) + {\rm perms} \right] \end{aligned} \tag{A.50}$$

where

$$\begin{aligned} \alpha_\ell(x) &\equiv \frac{2}{\pi} \int k^2 \, {\rm d}k g_{T\ell}(k) j_\ell(kx); \\ \beta_\ell(x) &\equiv \frac{2}{\pi} \int k^2 \, {\rm d}k \; g_{T\ell}(k) j_\ell(kx) P_{\zeta_G}(k) \end{aligned} \tag{A.51}$$

To make explicit the link with the formalism described above, we can identify the integral over the radial coordinate as the reduced bispectrum:

$$b_{\ell_1\ell_2\ell_3} = 2f_{\rm NL}\int x^2\,{\rm d}x\big[\alpha_{\ell_1}(x)\beta_{\ell_2}(x)\beta_{\ell_3}(x)+\beta_{\ell_1}(x)\alpha_{\ell_2}(x)\beta_{\ell_3}(x)+\beta_{\ell_1}(x)\beta_{\ell_2}(x)\alpha_{\ell_3}(x)\big]$$

In the model we are considering, due to the coupling between k-modes induced by the 3pcf of the perturbation sources, we obtain for the bispectrum the following expression:

$$\begin{aligned}B^{m_1m_2m_3}_{\ell_1\ell_2\ell_3} = \mathcal{G}^{m_1m_2m_3}_{\ell_1\ell_2\ell_3}\frac{8}{3}F^3_{NL}\int x^2\,{\rm d}x\int p^2\,{\rm d}pP(p)\Big[\sum_{\ell_2'\ell_3'L}\mathcal{F}^{\ell_1\ell_2\ell_3}_{\ell_2'\ell_3'L}\\ \frac{2}{\pi}\int k_1^2\,{\rm d}k_1 g_{T\ell_1}(k_1)j_{\ell_1}(k_1x)\\ \frac{2}{\pi}\int k_2^2\,{\rm d}k_2 g_{T\ell_2}(k_2)\tilde{P}^-_L(k_2,p)j_{\ell_2'}(k_2x)(-i)^{\ell_2-\ell_2'}\\ \frac{2}{\pi}\int k_3^2\,{\rm d}k_3 g_{T\ell_3}(k_3)\tilde{P}^+_L(k_3,p)j_{\ell_3'}(k_3x)(-i)^{\ell_3-\ell_3'}+{\rm perms}\Big]\end{aligned} \tag{A.52}$$

where we decomposed the power spectrum into spherical harmonics and $\mathcal{F}^{\ell_1\ell_2\ell_3}_{\ell_2'\ell_3'L}$ is defined in the Appendix and is function of $3j$ and $6j$ Wigner symbols. Notice that the three integrals over ${\rm d}k_i$ would reduce to $\alpha(x)$ if there was not k_i dependence of the quantities $\tilde{P}^\pm_L(k_i,p)$. This effect is due to the coupling between different modes introduced by the convolution integral in 3pcf. Nonetheless we are able to separate the dependence on m_i which would break the rotational invariance of the bispectrum.

Bispectrum estimator

Our aim is to find a computationally fast estimator for the bispectrum, following the one that was first proposed by Komatsu et al. (2005) and subsequently improved by Creminelli et al. (2006) taking into account anisotropic partial sky coverage, and finally extended to include properly CMB polarisation (see Yadav et al. (2007) and Yadav et al. (2008)).

We go through the fundamental steps again that lead to the fast cubic estimator in order to define quantities that will enter in our formalism later on. A very natural definition of $a_{\ell m}$ that comes straight-forwardly from the above calculations is the following

$$a_{\ell m} = w_\ell\int x^2\,{\rm d}x\big[\zeta_{\ell m}(x)\alpha^{ad}_\ell(x)+S_{\ell m}(x)\alpha^{iso}_\ell(x)\big]+n_{\ell m} \tag{A.53}$$

where $S_{\ell m}(x)$s are the harmonic coefficients of the fluctuations at given comoving distance $x=|\mathbf{x}|$, w_ℓ represents the beam effect and $n_{\ell m}$ the instrumental noise that for

simplicity reasons we assume to be approximate by $\langle n_{\ell m} n_{\ell' m'} \rangle \simeq \sigma_0^2 \delta_{\ell\ell'} \delta_{mm'}$. The functions αs are defined in Eq.A.51. Naively, an unbiased estimator of the angle-averaged bispectrum can be constructed by the observed $a_{\ell m}$ as follows:

$$\hat{B}_{\ell_1\ell_2\ell_3} = \sum_m \begin{pmatrix} \ell_1 & \ell_2 & \ell_3 \\ m_1 & m_2 & m_3 \end{pmatrix} a_{\ell_1 m_1} a_{\ell_2 m_2} a_{\ell_3 m_3} \tag{A.54}$$

For a full description of the estimator see Spergel & Goldberg (1999); Komatsu & Spergel (2001). The covariance matrix of the estimator can be computed by the six points correlation function for $a_{\ell m}$, provided that non-Gaussianity is weak, i.e. $\left\langle B_{\ell_1\ell_2\ell_3} \right\rangle \sim 0$, Luo (1994); Heavens (1998). The diagonal terms for $\ell_i \neq 0$ and $\ell_1 + \ell_2 + \ell_3 = \text{even}$ are

$$\begin{aligned} &\langle B^2_{\ell_1\ell_2\ell_3} \rangle = \langle C_{\ell_1} \rangle \langle C_{\ell_2} \rangle \langle C_{\ell_3} \rangle \Delta_{\ell_1\ell_2\ell_3} \\ &\Delta_{\ell_1\ell_2\ell_3} \equiv (1 + 2\delta_{\ell_1\ell_2}\delta_{\ell_2\ell_3} + \delta_{\ell_1\ell_2} + \delta_{\ell_2\ell_3} + \delta_{\ell_3\ell_1}). \end{aligned} \tag{A.55}$$

The variance is amplified by a factor of 2 or 6, when two or all l's are same, respectively. In presence of sky cuts the previous results for $\Delta_{\ell_1\ell_2\ell_3}$ do not hold anymore and a numerical simulation has to be performed in order to obtain realistic values for the coefficients in front of C_ℓs. Some hints can be found in Komatsu (2002).

Standard non-Gaussianity estimator. We are interested in the best estimator for the primordial non-Gaussianity bispectrum of which we know the specific shape. We can then think it as a Wiener filter that satisfies the relation

$$\frac{\partial}{\partial \mathcal{O}_\ell(x)} \langle |\mathcal{O}_\ell(x) a_{\ell m} - \zeta_{\ell m}(x)| \rangle = 0 \tag{A.56}$$

and we find

$$\mathcal{O}_\ell(x) = \frac{w_\ell \int \mathrm{d}x' x'^2 \alpha_\ell(x') \langle \zeta_{\ell m}(x') \zeta^*_{\ell m}(x) \rangle}{\mathcal{C}_\ell} \tag{A.57}$$

where $\zeta_{\ell m}(x)$ is the coefficient of the spherical harmonics expansion of the primordial curvature perturbation. In the simple case of standard non-Gaussianity we can express the 2pcf of $\zeta_{\ell m}(x)$ like

$$\langle \zeta_{\ell m}(x) \zeta^*_{\ell' m'}(x') \rangle = \delta_{\ell\ell'} \delta_{mm'} \frac{2}{\pi} \int k^2 \, \mathrm{d}k P(k) j_\ell(kx) j_\ell(kx') \equiv \delta_{\ell\ell'} \delta_{mm'} D(x, x') \tag{A.58}$$

which substituted back into Eq. A.57 gives

$$\mathcal{O}_\ell(x) = \frac{\beta_\ell(x) w_\ell}{\mathcal{C}_\ell}, \tag{A.59}$$

where the function $\beta_\ell(x)$ is given again by Eq.A.51 and we used the completeness relation of the Bessel's functions, Eq. **??**. A useful summary of the relations which link $\alpha_\ell(x)$, $\beta_\ell(x)$ and $D(x,x')$, which is the integral in Eq.A.58, are given in Babich (2005); Yu & Lu (2008).

Here we implicitly assume that adiabatic and isocurvature modes are not correlated and we can focus on one of the two separately. See Komatsu et al. (2005) for a detailed discussion.

We can recognise in the previous definitions some of the quantities present in the expression of the bispectrum, Eq. A.50. The *fast cubic estimator* is built filtering the measured $a_{\ell m}$ in order to obtain two maps, A and B, given by

$$A(x,\hat{\gamma}) \equiv \sum_{\ell m} \frac{\alpha_\ell(x) w_\ell}{\mathcal{C}_\ell} a_{\ell m} Y_{\ell m}(\hat{\gamma}) \tag{A.60}$$

$$B(x,\hat{\gamma}) \equiv \sum_{\ell m} \frac{\beta_\ell(x) w_\ell}{\mathcal{C}_\ell} a_{\ell m} Y_{\ell m}(\hat{\gamma}) \tag{A.61}$$

and computing the integral

$$\mathcal{S}_{\rm prim} \equiv 4\pi \int x^2\, {\rm d}x \int \frac{{\rm d}\Omega}{4\pi} A(x,\hat{\gamma}) B^2(x,\hat{\gamma}) \tag{A.62}$$

By direct inspection it can be verified that Eq. A.62 reduces to

$$\mathcal{S}_{\rm prim} = \sum_{\ell_1 \le \ell_2 \le \ell_3} \frac{\mathcal{B}^{\rm obs}_{\ell_1\ell_2\ell_3} B^{\rm prim}_{\ell_1\ell_2\ell_3}}{\mathcal{C}_{\ell_1}\mathcal{C}_{\ell_2}\mathcal{C}_{\ell_3}} \tag{A.63}$$

where $\mathcal{B}^{obs}_{\ell_1\ell_2\ell_3}$ is the observed bispectrum corrected for the beam effect, w_ℓ, and $B^{prim}_{\ell_1\ell_2\ell_3}$ is the theoretical one derived in Eq. A.50 averaged over m and computed for $f_{\rm NL} = 1$. The $\mathcal{C}_\ell$ at the denominator of Eq. A.63 are those extracted from the observed sky, given by $\mathcal{C}_\ell = w_\ell^2 C_\ell + \sigma_0^2$.

We can then derive the value of $f_{\rm NL}$ simply computing the ratio between the $S_{\rm prim}$ in Eq. A.63 and the theoretical expectation for the same quantity, as:

$$f_{\rm NL} = \frac{\mathcal{S}_{\rm prim}}{\sum_{\ell_1<\ell_2<\ell_3} \frac{(B^{\rm prim}_{\ell_1\ell_2\ell_3})^2}{\mathcal{C}_{\ell_1}\mathcal{C}_{\ell_2}\mathcal{C}_{\ell_3}}} \tag{A.64}$$

For a generalisation of this estimator which takes into account both temperature and polarisation see Yadav et al. (2007).

Estimator for the non-standard Term. In order to build a similar estimator for our model we have to compare Eq. A.52 with Eq. A.50. As already mentioned the three point correlation function for a curvaton-like model shows an angular dependence that prevents us computing the product of several spherical harmonics.

The above estimator is build following the prescription for a matching filter: basically the real signal is multiplied by the theoretical one and the product is weighted with the variance of the quantity under consideration, in this case the three point correlation function.

As a first step we can try to apply the standard estimator to our model to see how sensitive it is. Formally we simply substitute the theoretical bispectrum computed for $f_{\rm NL} = 1$ in Eq. A.64 with the one computed for the one underlying our theory for $F_{\rm NL} = 1$. We obtain

$$F^3_{\rm NL} = \frac{\sum_{\ell_1<\ell_2<\ell_3} \frac{\mathcal{B}^{\rm obs}_{\ell_1\ell_2\ell_3} B^{\rm prim}_{\ell_1\ell_2\ell_3}|_{F_{\rm NL}=1}}{\mathcal{C}_{\ell_1}\mathcal{C}_{\ell_2}\mathcal{C}_{\ell_3}}}{\sum_{\ell_1<\ell_2<\ell_3} \frac{(B^{\rm prim}_{\ell_1\ell_2\ell_3}|_{f_{\rm NL}=1})^2}{\mathcal{C}_{\ell_1}\mathcal{C}_{\ell_2}\mathcal{C}_{\ell_3}}} \tag{A.65}$$

We can not compute $F_{\rm NL}$ directly by means of $S_{\rm prim}$ because the $\alpha_\ell(r)$ and $\beta_\ell(r)$ functions have been obtained under the standard non-linear coupling assumptions. Nonetheless, if the approximation we discussed in Sec. A.3 lasts, it is possible to apply the fast cubic estimator, once replacing the power spectrum for ζ_G by $P_\chi(k)$.

A more rigorous approach would require the computation of the optimum filter $\mathcal{O}_\ell$ starting from the same definition given in Eq. A.56.

Flat sky and large scales (SW) approximations. The fast cubic estimator can be easily computed making use of temperature maps. Inspired by this consideration we try to build an estimator for our model in real space. We simplify further the system using the flat sky approximation under the assumption that the radiation transfer function is a Dirac delta in space. A bispectrum estimator, under the previous assumptions, looks like

$$\begin{aligned} S &= \int \mathrm{d}^2\mathbf{n} \int \mathrm{d}^2\mathbf{p} \int \mathrm{d}^2\mathbf{k} \int \mathrm{d}^2\mathbf{k}' \int \mathrm{d}^2\mathbf{k}'' e^{i(\mathbf{k}+\mathbf{k}'+\mathbf{k}'')\cdot\mathbf{n}} \\ &\quad P_\chi(p)\frac{\delta T_k}{C_k} P_\chi(|\mathbf{p}-\mathbf{k}'|)\frac{\delta T_{k'}}{C_{k'}} P_\chi(|\mathbf{p}+\mathbf{k}''|)\frac{\delta T_{k''}}{C_{k''}} + \text{perms} = \\ &= \int \mathrm{d}^2\mathbf{n} \int \mathrm{d}^2\mathbf{p} A(\mathbf{p},\mathbf{n}) B(\mathbf{p},\mathbf{n}) C(\mathbf{p},\mathbf{n}) \end{aligned} \tag{A.66}$$

where we defined

$$A(\mathbf{p},\mathbf{n}) \equiv \int \mathrm{d}^2\mathbf{k} e^{i\mathbf{k}\cdot\mathbf{n}} P_\chi(p)\frac{\delta T_k}{C_k}$$
$$B(\mathbf{p},\mathbf{n}) \equiv \int \mathrm{d}^2\mathbf{k}' e^{i\mathbf{k}'\cdot\mathbf{n}} P_\chi(|\mathbf{p}-\mathbf{k}'|)\frac{\delta T_{k'}}{C_{k'}}$$
$$C(\mathbf{p},\mathbf{n}) \equiv \int \mathrm{d}^2\mathbf{k}'' e^{i\mathbf{k}''\cdot\mathbf{n}} P_\chi(|\mathbf{p}+\mathbf{k}''|)\frac{\delta T_{k''}}{C_{k''}}$$

Now we recognise that it is possible to identify the above expressions as Fourier components:

$$A(\mathbf{y},\mathbf{n}) = \int \mathrm{d}^2\mathbf{p} A(\mathbf{p},\mathbf{n}) e^{i\mathbf{p}\cdot\mathbf{y}} = M(\mathbf{n})P'_\chi(\mathbf{y})$$
$$B(\mathbf{y},\mathbf{n}) = \int \mathrm{d}^2\mathbf{p} B(\mathbf{p},\mathbf{n}) e^{i\mathbf{p}\cdot\mathbf{y}} = M(\mathbf{n}+\mathbf{y})P'_\chi(\mathbf{y})$$
$$C(\mathbf{y},\mathbf{n}) = \int \mathrm{d}^2\mathbf{p} A(\mathbf{p},\mathbf{n}) e^{i\mathbf{p}\cdot\mathbf{y}} = M(\mathbf{n}-\mathbf{y})P'_\chi(\mathbf{y})$$

where $P'(\mathbf{y})$ is the Fourier transform of the power spectrum and $M(\mathbf{x})$ is real map weighted with its variance.

Now in order to simplify the computation we write the Fourier components Eqs. A.67 in terms of the Eqs. A.67. To clarify this we write only the first map

$$A(\mathbf{p},\mathbf{n}) = \int \mathrm{d}^2\mathbf{x} e^{-i\mathbf{p}\cdot\mathbf{x}} M(\mathbf{n})P'_\chi(\mathbf{x}) \tag{A.67}$$

Substituting into Eq. A.66 and using the resulting Dirac's delta function to perform one spatial integral we obtain

$$S = \int \mathrm{d}^2\mathbf{n} \int \mathrm{d}^2\mathbf{x} \int \mathrm{d}^2\mathbf{y} M(\mathbf{n})P'_\chi(\mathbf{x})M(\mathbf{n}+\mathbf{y})P'_\chi(\mathbf{y})M(\mathbf{n}+\mathbf{x}+\mathbf{y})P'_\chi(-\mathbf{x}-\mathbf{y}) \tag{A.68}$$

This basically is a product in real space of all possible combinations between pixels related by a triangle relation. This scales as the number of pixels cube and then is computationally challenging.

A.5 Conclusion

In this chapter we introduced a viable early Universe model based on a curvaton-like scenario and computed the two and three point correlation functions, both in real and k-space. Due to the quadratic term in the curvature expansion, the bispectrum estimators become rather complicated and their treatment in the CMB context is computationally

prohibitive. We studied these functions in a regime very close to the scale invariance, where the standard approach can be resembled. We tested its behaviour by means of a numerical code, which actually confirmed the theoretical intuition: when the power spectrum of the auxiliary field is far from being invariant, the approximations breaks down and a different analysis is necessary. We attempted to build an estimator suitable for this new model, but its numerical evaluation turns out to be extremely long. An improvement of such formalism is currently under investigation.